



**Swansea University**  
**Prifysgol Abertawe**

## **Chromate-Free Corrosion Protection of Zn-Al Alloy Coated Steels**

**Peter Morgan MSci**

Submitted to Swansea University in fulfilment of the requirements for the Degree of  
Doctor of Engineering

March 2025

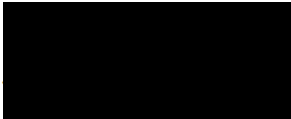


**Engineering and  
Physical Sciences  
Research Council**

# Declarations


---

This work has not previously been accepted in substance for any degree and is not being concurrently submitted in candidature for any degree.

Signed..  .....

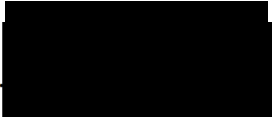
Date: 10/03/2025

This thesis is the result of my own investigations, except where otherwise stated. Other sources are acknowledged by footnotes giving explicit references. A bibliography is appended.

Signed..  .....

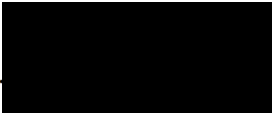
Date: 10/03/2025

I hereby give consent for my thesis, if accepted, to be available for electronic sharing.

Signed..  .....

Date: 10/03/2025

The University's ethical procedures have been followed and, where appropriate, that ethical approval has been granted.

Signed..  .....

Date: 10/03/2025

# Abstract

---

This thesis aimed to enhance the understanding of how bare and organically coated Zn-Al galvanised steels, specifically HDG, Galfan, and Zn55Al, corrode and develop corrosion protection using alternative inhibitors to hexavalent chromium. Hexavalent chromium poses significant health and environmental hazards.

The aqueous localised corrosion behaviour of Zn55Al, relative to HDG and Galfan, is poorly understood. Therefore, the corrosion behaviour of bare Zn55Al coated steel immersed in aqueous chloride was investigated using Scanning Vibrating Electrode Technique (SVET), Time-Lapse Microscopy (TLM), and Scanning Kelvin Probe Force Microscopy (SKPFM). It was found upon immersion that Zn55Al's zinc-rich interdendritic phase initially undergoes preferential anodic attack, but over time, the attack extended to aluminium-rich dendrites, causing more severe localised corrosion. High chloride concentrations yielded extensive local corrosion.

The inhibitory performance of the chromate-free corrosion inhibitor, 2-(1,3-benzothiazol-2-ylthio)succinic acid (BTSA), was evaluated against the aqueous localised corrosion of HDG, Galfan, and Zn55Al surfaces. Determined by SVET and Linear Polarisation Resistance (LPR), 10 mM of BTSA dosed in aqueous chloride electrolyte provided inhibitor efficiencies upwards of 90% for each substrate. BTSA provided mixed inhibition, but the magnitude of cathodic inhibition decreased as galvanised coating aluminium content increased.

The ability of in-coating BTSA to mitigate corrosion-driven organic coating failure of HDG steel was investigated. Time-lapse microscopy and SKP experiments showed that in-coating BTSA, added directly to a model coating or as a smart release exchangeable anion reduced the rate of cathodic delamination of HDG by up to a factor of 20. This performance was likely due to strong adsorption on the intact metal surface, stifling cathodic reduction of oxygen.

Finally, a novel accelerated test cell was developed to assess in-coating inhibitors against the anodic undermining of ZnAl galvanised substrates. The preliminary design showed a measurable anodic undermining of unpigmented PVB-coated Zn55Al within 20 hours of initiation.



# Acknowledgements

---

I would like to thank the funding contributions of the Engineering and Physical Sciences Research Council (EPSRC) through the Centre for Doctoral Training in Industrial Functional Coatings (COATED) scheme and the Materials and Manufacturing Academy (M2A), as well as Beckers Industrial Coatings Ltd.

Over the course of the EngD, I have been incredibly fortunate to be supported by so many kind and knowledgeable people. A special thanks to Professor Geraint Williams for spending so much time teaching me the electrochemistry underpinning this thesis... and for being such a calming and positive influence throughout. I would also like to thank Dr Natalie Wint for all her contributions to this work on a technical level and her efforts to help me improve everything outside of laboratory work, including writing and presenting. I also appreciate the efforts and support of the team from Beckers in Liverpool, especially Dr Sonny Ngo.

A special thanks to all my colleagues and newfound friends from the M2A – the camaraderie, support, and humour from my first day to my last have helped me get through even my most stressful moments. I would like to reserve a special thanks to Brendan Coles and Geraint Howells. Brendan - you possess an unrivalled ability to uplift and bring the best out of the people around you. Geraint – even if everything has gone wrong on a day, your humour helps me leave with a smile on my face.

Finally, I would like to thank my Mum and Dad for their unwavering support and belief in me.

# CONTENTS

|          |   |          |
|----------|---|----------|
| <b>1</b> | <b>Introduction and Literature review</b>               | <b>1</b> |
| 1.1      | Introduction . . . . .                                  | 2        |
| 1.2      | Corrosion Theory . . . . .                              | 5        |
| 1.2.1    | Thermodynamics of Corrosion . . . . .                   | 5        |
| 1.2.1.1  | Reference Electrodes and Measuring Electrode Potentials | 9        |
| 1.2.2    | Aqueous Corrosion . . . . .                             | 10       |
| 1.2.3    | Pourbaix Diagrams . . . . .                             | 11       |
| 1.2.4    | Polarisation and Corrosion Kinetics . . . . .           | 13       |
| 1.3      | Corrosion Prevention . . . . .                          | 17       |
| 1.3.1    | Metallic Coatings . . . . .                             | 17       |
| 1.3.1.1  | Hot-Dip Galvanised Steel (HDG) . . . . .                | 18       |
| 1.3.1.2  | Galfan . . . . .  | 19       |
| 1.3.1.3  | Zn55Al . . . . .  | 20       |
| 1.3.2    | Organic Coatings . . . . .                              | 21       |
| 1.3.2.1  | Pre-treatment . . . . .                                 | 22       |
| 1.3.2.2  | Primer . . . . .  | 22       |
| 1.3.2.3  | Top coat . . . . .                                      | 22       |
| 1.3.3    | Corrosion-driven Organic Coating Failure . . . . .      | 23       |
| 1.3.3.1  | Cathodic Delamination . . . . .                         | 23       |
| 1.3.3.2  | Anodic Undermining . . . . .                            | 24       |
| 1.3.4    | Corrosion Inhibitors . . . . .                          | 26       |
| 1.3.4.1  | Anodic Inhibitors . . . . .                             | 26       |
| 1.3.4.2  | Cathodic Inhibitors . . . . .                           | 27       |
| 1.3.5    | Anti-Corrosion Pigments . . . . .                       | 28       |
| 1.3.5.1  | Hexavalent Chromium . . . . .                           | 28       |
| 1.3.5.2  | Phosphate . . . . .                                     | 29       |
| 1.3.5.3  | Ion-Exchange Pigments and Hydrotalcite . . . . .        | 30       |

|          |  |           |
|----------|--|-----------|
| 1.3.5.4  | Corrosion Inhibition of ZnAl galvanised steel by Organic Azoles . . . . .                        | 33        |
| 1.4      | Electrochemical Techniques . . . . .   | 34        |
| 1.4.1    | Scanning Vibrating Electrode Technique (SVET) . . . . .  | 34        |
| 1.4.2    | Scanning Kelvin Probe (SKP) . . . . .  | 37        |
| 1.5      | References . . . . .   | 42        |
| <b>2</b> | <b>Experimental Methods</b>  | <b>53</b> |
| 2.1      | Materials . . . . .  | 54        |
| 2.1.1    | ZnAl Galvanised Steel Substrates . . . . .   | 54        |
| 2.1.2    | Substrate Preparation . . . . .  | 54        |
| 2.1.3    | Chemicals and Consumables . . . . .  | 55        |
| 2.2      | Methods . . . . .  | 56        |
| 2.2.1    | Assessment of Localised Corrosion by The Scanning Vibrating Electrode Technique (SVET) . . . . . | 56        |
| 2.2.1.1  | SVET Data Rendering and Manipulation . . . . .   | 60        |
| 2.2.1.2  | SVET Limitations . . . . .   | 61        |
| 2.2.2    | Assessment of Cathodic Delamination . . . . .  | 61        |
| 2.2.2.1  | Model Organic Coatings . . . . .   | 61        |
| 2.2.2.2  | Cathodic Delamination Preparation . . . . .  | 62        |
| 2.2.2.3  | Time-Lapse Photography Determination of Cathodic Delamination . . . . .                          | 63        |
| 2.2.2.4  | Scanning Kelvin Probe (SKP) Determination of Cathodic Delamination . . . . .                     | 64        |
| 2.2.2.5  | SKP Apparatus . . . . .  | 65        |
| 2.2.2.6  | SKP Operation . . . . .  | 66        |
| 2.2.2.7  | SKP Calibration . . . . .  | 66        |
| 2.2.3    | Electrochemical Measurements . . . . .   | 67        |
| 2.2.3.1  | Linear Polarisation Resistance . . . . .   | 68        |
| 2.3      | References . . . . .   | 69        |

|          |  |            |
|----------|--|------------|
| <b>3</b> | <b>Effect of Aqueous Chloride Concentration on the Localised Corrosion of Zn55Al Galvanised Steel</b>          | <b>71</b>  |
| 3.1      | Introduction . . . . .   | 72         |
| 3.2      | Experimental Details . . . . .   | 74         |
| 3.2.1    | Materials . . . . .  | 74         |
| 3.2.2    | Methods . . . . .  | 74         |
| 3.2.2.1  | Material Characterisation . . . . .  | 74         |
| 3.2.2.2  | Scanning Kelvin Probe Force Microscopy (SKPFM) . . . . .   | 74         |
| 3.2.2.3  | Scanning Vibrating Electrode Technique (SVET) . . . . .  | 75         |
| 3.2.2.4  | Time-Lapse Microscopy . . . . .  | 76         |
| 3.3      | Results . . . . .  | 77         |
| 3.3.1    | Material Characterisation . . . . .  | 77         |
| 3.3.2    | Scanning Kelvin Force Microscopy (SKPFM) . . . . .   | 79         |
| 3.3.3    | Scanning Vibrating Electrode Technique (SVET) . . . . .  | 81         |
| 3.3.3.1  | Position of Local Anodes . . . . .   | 81         |
| 3.3.3.2  | Percentage Anodic Area . . . . .   | 83         |
| 3.3.3.3  | Cumulative Anodic Current Density . . . . .  | 85         |
| 3.3.3.4  | Appearance of Post-SVET Surfaces . . . . .   | 86         |
| 3.3.4    | Time-Lapse Microscopy (TLM) . . . . .  | 89         |
| 3.3.5    | Discussion . . . . .   | 92         |
| 3.3.5.1  | Initial Immersion . . . . .  | 92         |
| 3.3.5.2  | Longer Immersion . . . . .   | 93         |
| 3.3.5.3  | Post-Immersion Surfaces . . . . .  | 94         |
| 3.3.5.4  | Mechanism of Zn55Al Localised Corrosion in Aqueous Chloride . . . . .  | 95         |
| 3.3.6    | Conclusion . . . . .   | 98         |
| 3.3.7    | References . . . . .   | 99         |
| <b>4</b> | <b>Localised Corrosion Inhibition of ZnAl Galvanised Steels by 2-(1,3-Benzothiazol-2-ylthio) succinic acid</b> | <b>104</b> |

|         |  |     |
|---------|--|-----|
| 4.1     | Introduction . . . . .   | 105 |
| 4.2     | Experimental Details . . . . .   | 107 |
| 4.2.1   | Materials . . . . .  | 107 |
| 4.2.2   | Methods . . . . .  | 107 |
| 4.2.2.1 | Scanning Vibrating Electrode Technique (SVET) . . . . .                      | 107 |
| 4.2.2.2 | Electrochemical Characterisation . . . . .                                   | 108 |
| 4.2.2.3 | Linear Polarisation Resistance (LPR) . . . . .                               | 108 |
| 4.2.2.4 | Open Circuit Potential (OCP) and Potentiodynamic Polarisation (PP) . . . . . | 108 |
| 4.3     | Results . . . . .  | 109 |
| 4.3.1   | HDG . . . . .  | 109 |
| 4.3.1.1 | SVET . . . . .   | 109 |
| 4.3.1.2 | LPR . . . . .  | 114 |
| 4.3.1.3 | OCP and PP . . . . .   | 116 |
| 4.3.2   | Galfan . . . . .   | 118 |
| 4.3.2.1 | SVET . . . . .   | 118 |
| 4.3.2.2 | LPR . . . . .  | 123 |
| 4.3.2.3 | OCP and PP . . . . .   | 124 |
| 4.3.3   | Zn55Al . . . . .   | 126 |
| 4.3.3.1 | LPR . . . . .  | 131 |
| 4.3.3.2 | OCP and PP . . . . .   | 132 |
| 4.4     | Discussion . . . . .   | 134 |
| 4.4.1   | Inhibition via Adsorption . . . . .  | 134 |
| 4.4.2   | Inhibition via Precipitation . . . . .                                       | 136 |
| 4.5     | Conclusion . . . . .   | 139 |
| 4.6     | References . . . . .   | 140 |

## **5 Inhibition of Corrosion-Driven Cathodic Delamination of HDG by in-coating**

|                            |            |
|----------------------------|------------|
| <b>BTSA Additives</b>      | <b>145</b> |
| 5.1 Introduction . . . . . | 146        |

|          |   |            |
|----------|---|------------|
| 5.2      | Experimental Details . . . . .  | 148        |
| 5.2.1    | Materials . . . . .   | 148        |
| 5.2.2    | Methods . . . . .   | 148        |
| 5.2.2.1  | Spectrophotometric Determination of BTSA . . . . .                        | 148        |
| 5.2.2.2  | Preparation of HT-BTSA . . . . .  | 149        |
| 5.2.2.3  | HT-BTSA Back-Exchange . . . . .   | 150        |
| 5.2.2.4  | Stratmann Cell Preparation . . . . .                                      | 151        |
| 5.2.2.5  | Cathodic Delamination Inhibition by in-coating BTSA<br>Species . . . . .  | 151        |
| 5.3      | Results and Discussion . . . . .  | 152        |
| 5.3.1    | Effects of in-coating BTSA . . . . .                                      | 152        |
| 5.3.2    | SKP Investigation of Unpigmented PVB . . . . .                            | 155        |
| 5.3.3    | SKP Investigation of HT-BTSA Pigmented PVB . . . . .                      | 159        |
| 5.3.4    | Mechanism of HT-BTSA Inhibition . . . . .                                 | 162        |
| 5.3.5    | Comparison of HT-BTSA to HT-Chromate . . . . .                            | 163        |
| 5.4      | Conclusions . . . . .   | 163        |
| 5.5      | References . . . . .  | 165        |
| <b>6</b> | <b>A Novel Accelerated Anodic Undermining Cell for ZnAl Coated Steels</b> | <b>170</b> |
| 6.1      | Introduction . . . . .  | 171        |
| 6.2      | Experimental Details . . . . .  | 173        |
| 6.2.1    | Materials . . . . .   | 173        |
| 6.2.2    | Method . . . . .  | 173        |
| 6.2.2.1  | FFC Assessment . . . . .  | 173        |
| 6.2.2.2  | Novel Anodic Undermining Cell . . . . .                                   | 173        |
| 6.3      | Results and Discussion . . . . .  | 176        |
| 6.3.1    | FFC . . . . .   | 176        |
| 6.3.2    | Novel Anodic Undermining Cell . . . . .                                   | 179        |
| 6.3.2.1  | Assessment by Time-Lapse Photography . . . . .                            | 180        |
| 6.3.2.2  | Assessment by SKP . . . . .   | 184        |

|          |                                    |            |
|----------|------------------------------------|------------|
| 6.3.2.3  | Mechanism . . . . .                | 186        |
| 6.4      | Conclusion . . . . .               | 189        |
| 6.5      | References . . . . .               | 190        |
| <b>7</b> | <b>Conclusions and Future Work</b> | <b>193</b> |

## LIST OF FIGURES

|      |   |    |
|------|---|----|
| 1.1  | Free energy vs reaction coordinate from ore, to pure metal, to corrosion products. $\Delta G$ is the enthalpy of a reaction, and $\Delta G^*$ is the activation energy. | 5  |
| 1.2  | Diagram of the Daniell Cell. . . . .  | 7  |
| 1.3  | Schematic representation of Evans' differential aeration cell. . . . .  | 11 |
| 1.4  | a) Pourbaix diagram of zinc, and b) Pourbaix diagram of aluminium. . . .  | 12 |
| 1.5  | Schematic representation of the Helmholtz model of the double layer. . .  | 14 |
| 1.6  | Schematic representation of Tafel analysis. . . . .   | 16 |
| 1.7  | A representative Evans diagram for a metal undergoing aqueous corrosion, where $\eta_a$ and $\eta_c$ are the anodic and cathodic overpotentials, respectively. . . . .  | 16 |
| 1.8  | Evans diagram of the sacrificial protection afforded by zinc-coated steel when a defect exposes the underlying steel to a corrosive environment. . .                    | 18 |
| 1.9  | The Al-Zn equilibrium diagram [21]. . . . .   | 18 |
| 1.10 | SEM images showing the microstructure of diamond-polished Galfan at (a) lower and (b) higher magnification [29]. . . . .  | 20 |
| 1.11 | A scanning electron microscope image of a cross-section of Zn55Al coated steel [33]. . . . .  | 21 |
| 1.12 | Schematic breakdown of a typical organic coating system for ZnAl coated steel cladding. . . . .   | 22 |
| 1.13 | Schematic diagram of the mechanism of cathodic delamination on a zinc surface organically coated with polyvinyl-butyrac-acetate (PVB). . . .                            | 24 |
| 1.14 | Schematic diagram of the propagation of FFC on aluminium alloy substrate.   | 25 |
| 1.15 | The change in the Evans diagram of aqueous corrosion upon adding an anodic precipitation inhibitor. . . . .   | 27 |
| 1.16 | The change in the Evans diagram for aqueous corrosion upon adding a cathodic precipitation inhibitor. . . . .   | 28 |
| 1.17 | Schematic representation of hydrotalcite modification and inhibitory action. . . . .  | 32 |



|      |   |    |
|------|---|----|
| 1.18 | The current flux and iso-potential lines that occur from local corrosion cells. The black lines indicate current flux, and the red lines are the resulting iso-potential lines. . . . .   | 35 |
| 1.19 | a) A photograph of the SKP apparatus, and b) A schematic representation of the SKP. . . . .   | 38 |
| 2.1  | Schematic representation of the SVET apparatus. . . . .   | 57 |
| 2.2  | The current flux and iso-potential lines that occur from local corrosion cells. The black lines indicate current flux, and the red lines are the resulting iso-potential lines. . . . .   | 58 |
| 2.3  | Schematic representation of the SVET calibration apparatus. . . . .   | 59 |
| 2.4  | An example calibration plot of a $0.86 \text{ mol dm}^{-3} \text{ NaCl}_{(\text{aq})}$ solution. . . . .  | 60 |
| 2.5  | Schematic diagram showing a) cathodic delamination sample preparation, and b) experimental procedure for a typical delamination experiment . . .  | 63 |
| 2.6  | An example of time-lapse photography determination of cathodic delamination. . . . .  | 64 |
| 2.7  | Schematic representation of the SKP apparatus. Recreated from [6] . . . .   | 66 |
| 3.1  | Schematic representation of the time-lapse optical microscopy apparatus. .  | 76 |
| 3.2  | Back-scatter electron SEM image of the Zn55Al surface. . . . .  | 78 |
| 3.3  | EDX maps of Zn55Al's surface Al (blue), Zn (red), and Si (yellow). . . .  | 78 |
| 3.4  | SKPFM-derived Volta potential map of the surface of Zn55Al. . . . .   | 80 |
| 3.5  | SVET current density maps at different intervals during immersion of $100 \text{ mm}^2$ of exposed Zn55Al in a near neutral solution of a) 5% w/v, b) 1% w/v, c) 0.2% w/v, and d) 0.04% w/v $\text{NaCl}_{(\text{aq})}$ for 24 hours. . . . .   | 82 |
| 3.6  | The SVET-derived time-dependent percentage anodic area of Zn55Al immersed in a pH 7 solution of a) 5% w/v, b) 1% w/v, c) 0.2% w/v, and d) 0.04% w/v $\text{NaCl}_{(\text{aq})}$ for 24 h. To enable clarity of trends, the plot is the mean result of experiments undertaken in triplicate with a calculated $\pm 5\%$ uncertainty. . . . . | 84 |

|      |   |     |
|------|---|-----|
| 3.7  | The SVET-derived cumulative anodic current density of 100 mm <sup>2</sup> of exposed Zn55Al immersed in a near neutral solution of a) 5% w/v, b) 1% w/v, c) 0.2% w/v, and d) 0.04% w/v NaCl <sub>(aq)</sub> for 24 h. To enable clarity of trends, the plot is the mean result of experiments undertaken in triplicate with a calculated $\pm 5\%$ uncertainty. . . . . | 85  |
| 3.8  | SVET current density maps at 24 hours alongside post-immersion images of 100 mm <sup>2</sup> of Zn55Al immersed in a near neutral solution of a) 5% w/v, b) 1% w/v, c) 0.2% w/v, and d) 0.04% w/v NaCl <sub>(aq)</sub> for 24 h. . . . .  | 87  |
| 3.9  | Optical microscope images of a) a white-stained area, and b) a black-stained area of Zn55Al post-immersion in 5% w/v NaCl <sub>(aq)</sub> for 24 h. . . .   | 88  |
| 3.10 | In-situ microstructural images taken at various times during exposure of Zn55Al to near neutral solutions of a) 5% w/v, and b) 0.04% w/v NaCl <sub>(aq)</sub> . . . .   | 91  |
| 3.11 | Proposed mechanism of aqueous localised corrosion of Zn55Al in NaCl <sub>(aq)</sub> . . . .   | 97  |
| 4.1  | <i>The chemical structure of 2-(1,3-benzothiazol-2-ylthio) succinic acid, BTSA.</i>   | 106 |
| 4.2  | SVET current density maps at various times during the immersion of a 100 mm <sup>2</sup> area of HDG in 1% w/v NaCl <sub>(aq)</sub> pH 7 containing BTSA concentrations of a) uninhibited, b) 1 mM, and c) 10 mM. . . . .   | 110 |
| 4.3  | Post-SVET photographs of the 100 mm <sup>2</sup> exposed surfaces of HDG immersed for 6h in 1% w/v NaCl <sub>(aq)</sub> pH 7 containing BTSA concentrations of a) uninhibited, b) 1 mM, and c) 10 mM. . . . .   | 111 |
| 4.4  | SVET current density maps of the immersed surface of HDG a) 0.5 h before, and b) 0.5 h after the addition at 3 h of 10 mM BTSA to an initial 1% w/v NaCl <sub>(aq)</sub> pH 7 solution. . . . .   | 113 |
| 4.5  | SVET-derived average anodic current density as a function of time of a 100 mm <sup>2</sup> exposed area of HDG immersed in 1% w/v NaCl <sub>(aq)</sub> pH 7 solution. After 3 h, 10 mM BTSA was added to the solution. . . . .  | 114 |
| 4.6  | The anodic-going and cathodic-going polarisation curves of HDG immersed in 1% w/v NaCl <sub>(aq)</sub> pH 7 containing BTSA concentrations of a) uninhibited, b) 1 mM, and c) 10 mM. . . . .  | 117 |

|      |   |     |
|------|---|-----|
| 4.7  | SVET current density maps at various times during the immersion of a 100 mm <sup>2</sup> area of Galfan in 1% w/v NaCl <sub>(aq)</sub> pH 7 containing BTSA concentrations of a) uninhibited, b) 1 mM, and c) 10 mM. . . . .      | 119 |
| 4.8  | Post-SVET photographs of the 100 mm <sup>2</sup> exposed surfaces of Galfan immersed in 1% w/v NaCl <sub>(aq)</sub> pH 7 containing BTSA concentrations of a) uninhibited, b) 1 mM, and c) 10 mM. . . . .                         | 120 |
| 4.9  | SVET current density maps of the immersed surface of Galfan a) 0.5 h before, and b) 0.5 h after the addition at 3 h of 10 mM BTSA to an initial 1% w/v NaCl <sub>(aq)</sub> pH 7 solution. . . . .                                | 122 |
| 4.10 | SVET-derived average anodic current density as a function of time of a 100 mm <sup>2</sup> exposed area of Galfan immersed in 1% w/v NaCl <sub>(aq)</sub> pH 7 solution. After 3 h, 10 mM BTSA was added to the solution. . . . . | 123 |
| 4.11 | The anodic and cathodic-going polarisation curves of Galfan immersed in 1% w/v NaCl <sub>(aq)</sub> pH 7 containing BTSA concentrations of a) uninhibited, b) 1 mM, and c) 10 mM. . . . .   | 125 |
| 4.12 | SVET current density maps at various times during the immersion of a 100 mm <sup>2</sup> area of Zn55Al in 1% w/v NaCl <sub>(aq)</sub> pH 7 containing BTSA concentrations of a) uninhibited, b) 1 mM, and c) 10 mM. . . . .      | 127 |
| 4.13 | Post-SVET photographs of the 100 mm <sup>2</sup> exposed surfaces of Zn55Al immersed in 1% w/v NaCl <sub>(aq)</sub> pH 7 containing BTSA concentrations of a) uninhibited, b) 1 mM, and c) 10 mM. . . . .                         | 128 |
| 4.14 | SVET current density maps of the immersed surface of Zn55Al a) 0.5 h before, and b) 0.5 h after the addition at 3h of 10 mM BTSA to an initial 1% w/v NaCl <sub>(aq)</sub> pH 7 solution. . . . .                                 | 130 |
| 4.15 | SVET-derived average anodic current density as a function of time of a 100 mm <sup>2</sup> exposed area of Zn55Al immersed in 1% w/v NaCl <sub>(aq)</sub> pH 7 solution. After 3h, 10 mM BTSA was added to the solution. . . . .  | 131 |
| 4.16 | The anodic-going and cathodic-going polarisation curves of Zn55Al immersed in 1% w/v NaCl <sub>(aq)</sub> pH 7 containing BTSA concentrations of a) uninhibited, b) 1 mM, and c) 10 mM. . . . .                                   | 133 |

|      |   |     |
|------|---|-----|
| 4.17 | The relative concentration of BTSA species as a function of pH [41]. . . .  | 135 |
| 4.18 | The adsorption of $\text{BTSA}^{2-}$ to ZnAl coated steel in near-neutral aqueous chloride solution. . . . .  | 135 |
| 4.19 | A proposed mechanism of inhibition of freely corroding ZnAl galvanised steel by BTSA in near-neutral aqueous chloride solution. . . . .   | 138 |
| 5.1  | Calibration plot of $\text{BTSA}^{2-}$ concentration vs optical absorbance ( $\lambda_{\text{max}} = 283 \text{ nm}$ ). All solutions were buffered to pH 7 through dropwise addition of $\text{NaOH}_{(\text{aq})}$ . . . . .                | 149 |
| 5.2  | The back-exchanged concentration of $\text{BTSA}^{2-}$ after four successive cycles in a) 1% w/v $\text{NaOH}_{(\text{aq})}$ , pH 10, and b) deionised water. . . . .   | 150 |
| 5.3  | Time lapse photography derived plots of delamination distance ( $X_{\text{del}}$ ) as a function of time for PVB films containing (a) 0 wt.%, b) 0.5 wt.%, c) 1 wt.% and d) 2 wt.% BTSA. . . . .  | 153 |
| 5.4  | Time lapse photography derived plots of delamination distance ( $X_{\text{del}}$ ) as a function of time for PVB films containing a $\Phi_{\text{HT-BTSA}}$ of (a) 0, b) 0.05, c) 0.1, d) 0.2 and e) 0.3. . . . .                             | 153 |
| 5.5  | Time-lapse derived rate of cathodic delamination ( $k_{\text{del}}$ ) as a function of HT-BTSA $\Phi$ and BTSA wt.% for a) PVB coatings containing HT-BTSA and b) PVB coatings containing BTSA. . . . .                                       | 154 |
| 5.6  | SKP derived $E_{\text{corr}}$ as a function of distance from defect profile for the delamination of unpigmented PVB coating on HDG steel shown at a) 2h, b) 4h, c) 6h, d) 8h, e) 10h, f) 12h, g) 14h, h) 16h, and i) 18h. . . . .             | 156 |
| 5.7  | SKP derived $E_{\text{corr}}$ as a function of distance from defect for the delamination of a PVB film on HDG steel with 10 mM BTSA doped into the well electrolyte shown at a) 14h, b) 16h, c) 18h, d) 20h, e) 22h, and f) 24h. . .          | 158 |
| 5.8  | SKP derived $E_{\text{corr}}$ as a function of distance from defect for the delamination of a PVB film containing a $\Phi_{\text{HT-BTSA}}$ of 0.05 on HDG steel shown at a) 12h, b) 14h, c) 16h, d) 18h, e) 20h, f) 22h, and g) 24h. . . . . | 161 |

|      |   |     |
|------|---|-----|
| 5.9  | SKP derived $E_{\text{corr}}$ as a function of distance from defect for the delamination of a PVB film containing a $\Phi_{\text{HT-BTSA}}$ of 0.2 on HDG steel shown at a) 14h, b) 16h, c) 18h, d) 20h, e) 22h, and f) 24h. . . . .              | 161 |
| 5.10 | Schematic representation of the inhibitory influence of in-coating BTSA on the underfilm corrosion-delamination cell. . . . .   | 163 |
| 6.1  | Preparation of the novel anodic undermining cell. . . . .   | 175 |
| 6.2  | Optical images of the FFC experiment on Zn55Al over a 4-week period. Underfilm corrosion was initiated by injection of 2 $\mu\text{L}$ of 4 mol $\text{dm}^{-3}$ into a scribed defect that penetrated to the underlying steel substrate. . . . . | 176 |
| 6.3  | Time-lapse photography derived plot of underfilm corroded area as a function of $t^{1/2}$ for the preliminary FFC experiment on Zn55Al. . . . .   | 177 |
| 6.4  | Photo of the anodic undermining cell for Zn55Al. . . . .  | 180 |
| 6.5  | Time-lapse photos at selected intervals of the novel anodic undermining cell of unpigmented PVB on Zn55Al. . . . .  | 181 |
| 6.6  | Time lapse photography derived plot of delamination distance ( $X_{\text{del}}$ ) as a function of $t^{1/2}$ , for an unpigmented PVB coated Zn55Al sample using the accelerated anodic undermining cell. . . . .                                 | 183 |
| 6.7  | SKP derived time-dependent profiles of $E_{\text{corr}}$ as a function of distance from the defect for an unpigmented PVB coated Zn55Al sample using the accelerated anodic undermining cell. The profiles are shown at 2h intervals. . . . .     | 184 |
| 6.8  | SEM image and corresponding EDX elemental maps of the post-SKP underfilm Zn55Al surface. . . . .  | 186 |
| 6.9  | Schematic of the anodic undermining produced by the test cell, overlaid with representative SKP $E_{\text{corr}}$ vs distance profiles and the noteworthy regions marked. . . . .   | 188 |

## LIST OF TABLES

|     |   |     |
|-----|---|-----|
| 1.1 | Selected half cell reactions and their standard electrode potentials. . . . .   | 7   |
| 2.1 | Suppliers and descriptions of the ZnAl coated galvanised steel substrates<br>used in this work. . . . .   | 54  |
| 2.2 | The chemicals and consumables used in this work. . . . .  | 55  |
| 3.1 | A summary of transient anode behaviour seen in SVET current density<br>maps of the surface of Zn55Al immersed in near neutral solutions of vary-<br>ing [NaCl] concentration. . . . .   | 83  |
| 4.1 | SVET-derived time-dependent values of cumulative $J_a$ and corresponding<br>inhibitor efficiency, $\eta$ of HDG immersed in 1% w/v $\text{NaCl}_{(\text{aq})}$ pH 7 con-<br>taining BTSA concentrations of a) uninhibited, b) 1 mM, and c) 10 mM. .                               | 112 |
| 4.2 | LPR-derived time-dependent values of polarisation resistance, $R_p$ , and<br>corresponding inhibitor efficiency, $\eta$ , of HDG immersed in 1% w/v $\text{NaCl}_{(\text{aq})}$<br>pH7 containing BTSA concentrations of a) uninhibited, b) 1 mM, and c)<br>10 mM. . . . .        | 115 |
| 4.3 | SVET-derived time-dependent values of cumulative $J_a$ and corresponding<br>inhibitor efficiency, $\eta$ , of Galfan immersed in 1% w/v $\text{NaCl}_{(\text{aq})}$ at pH 7<br>containing BTSA concentrations of a) uninhibited, b) 1 mM, and c) 10 mM.                           | 121 |
| 4.4 | LPR-derived time-dependent values of polarisation resistance, $R_p$ , and<br>corresponding inhibitor efficiency, $\eta$ , of Galfan immersed in 1% w/v $\text{NaCl}_{(\text{aq})}$<br>at pH 7 containing BTSA concentrations of a) uninhibited, b) 1 mM, and<br>c) 10 mM. . . . . | 124 |
| 4.5 | SVET-derived time-dependent values of cumulative anodic $J_a$ and corre-<br>sponding inhibitor efficiency, $\eta$ , of Zn55Al immersed in 1% w/v $\text{NaCl}_{(\text{aq})}$<br>at pH 7 containing BTSA concentrations of a) uninhibited, b) 1 mM, and<br>c) 10 mM. . . . .       | 129 |

|     |  |     |
|-----|--|-----|
| 4.6 | LPR-derived time-dependent values of polarisation resistance, $R_p$ , and corresponding inhibitor efficiency, $\eta$ , of Zn55Al immersed in 1% w/v $\text{NaCl}_{(\text{aq})}$ at pH 7 containing BTSA concentrations of a) uninhibited, b) 1 mM, and c) 10 mM. . . . . | 132 |
|-----|--|-----|

# **Chapter 1**

## **Introduction and Literature review**



## 1.1 Introduction

One of the most widely used materials in the world is steel, an alloy of iron and carbon. In 2021 alone, over 1.95 billion tonnes of crude steel were produced globally, and this is likely to increase in the future [1]. Its demand arises because in addition to a low cost of production, steel provides the desirable mechanical properties of strength, malleability, and ductility. As such, it is suitable for various applications, including construction, transportation, energy, and manufacturing [2].

Unfortunately, steel is susceptible to corrosion, an electrochemical reaction that occurs in the presence of electrolyte which changes its physical properties and appearance. The corrosion costs to the industries mentioned can be high, as materials must often be repaired or replaced. In 2013, the estimated global cost of corrosion was a vast US\$2.5 trillion, equating to 3.4% of the global Gross Domestic Product (GDP) in that year [3]. To mitigate these losses, steel products are often hot-dip coated (galvanised) with ZnAl coatings, which provide sacrificial corrosion protection to the underlying steel, thus maintaining its favourable physical properties and extending product lifetime. Even so, ZnAl galvanised steels can still be susceptible to highly damaging localised corrosion [4], which can penetrate the interior of the coating and sometimes to the base steel. As mitigation, galvanised steel products are often directly coated with organic layers containing corrosion-inhibiting pigments that can leach out of the organic coating and slow down corrosion reactions [5].

For decades, the most effective anti-corrosive pigments were those containing hexavalent chromium; however, due to its acute toxicity and carcinogenicity, hexavalent chromium has been subject to Registration, Evaluation, Authorisation and Restriction of Chemicals (REACH) legislation [6–10]. Subsequently, many industries have not been able to use or have had to minimise the use of hexavalent chromium since the sunset date of September 2017 [7]. This change has significantly impacted the industrial coating industry, including Beckers Group, the sponsor of this research. Beckers Group, known for providing chromate-free corrosion-inhibiting coatings to the galvanised steel and aluminium industries, has faced challenges in matching the performance of previous chromate-containing systems. Consequently, there's a pressing need to discover and investigate new and effec-

tive chromate-free inhibitors.

To this end, the work conducted in this thesis aims to:

- a) Determine the localised corrosion mechanism in aqueous chloride of Zn55Al, a type of ZnAl galvanised steel.
- b) Identify a non-toxic chromate-free inhibitor that can inhibit the aqueous localised corrosion of ZnAl galvanised steels, namely HDG, Galfan and Zn55Al.
- c) Incorporate the identified inhibitor into model coatings systems for testing its effectiveness against cathodic delamination, a corrosion-driven organic coating failure of HDG.
- d) Determine an accelerated method of reproducibly producing anodic undermining, a corrosion-driven organic coating failure observed ZnAl galvanised steels. Such a method is required so that the performance of in-coating inhibitors against anodic undermining can be assessed on an accelerated time-scale in the future.

The thesis is structured as follows:

- **Chapter 1**, after this introduction offers a review of the literature pertinent to this research.
- **Chapter 2** details the materials and methods used in this work.
- **Chapter 3** explains the results of work focused on the aqueous localised corrosion mechanism of Zn55Al when exposed to various chloride concentrations. This chapter utilises the Scanning Vibrating Electrode Technique (SVET) and in situ Time Lapse Microscopy (TLM) to time-dependently monitor localised corrosion events.
- **Chapter 4** assesses the effectiveness of 2-(1,3-Benzothiazol-2-ylthio) succinic acid (BTSA) in inhibiting the aqueous localised corrosion of three common ZnAl galvanised steels: HDG, Galfan, and Zn55Al. This evaluation uses SVET and Linear

Polarization Resistance (LPR) to determine BTSA's efficiency in aqueous solutions, with polarisation studies aiding in understanding its inhibitory mechanism.

- **Chapter 5** assesses the performance of in-coating BTSA and a newly synthesised smart-release BTSA inhibitor a preventing corrosion-driven organic coating failure of HDG, namely cathodic delamination. It is conducted visually through time-lapse photography and electrochemically via Scanning Kelvin Probe (SKP) techniques.
- **Chapter 6** introduces a novel accelerated test cell that may provide a future avenue for rapid performance screening of in-coating inhibitors (e.g. BTSA) against anodic undermining, a common corrosion-driven coating failure associated with ZnAl galvanised steel substrates. The preliminary design is used on Zn55Al and compared to the anodic undermining produced by a modified Lockheed Filiform Corrosion Test. Again, time-lapse photography and SKP methods are employed.
- **Chapter 7** provides research conclusions and suggestions for future work.

## 1.2 Corrosion Theory

### 1.2.1 Thermodynamics of Corrosion

Most metals are less thermodynamically stable than their corrosion products and therefore tend to not occur naturally in their pure form. Instead, they must be extracted from their metal ore. For example, iron is derived from ores such as haematite ( $\text{Fe}_2\text{O}_3$ ) and magnetite ( $\text{Fe}_3\text{O}_4$ ) by heating them in a blast furnace with a source of carbon (coke) as a reducing agent [11]. This extraction results in a positive change in Gibbs free energy ( $\Delta G$ ) meaning that the metal (iron in this example) moves to a higher free energy state compared to its ore. This state is thermodynamically unfavourable, hence the metal will react with the environment wherever possible in a corrosion process so it can return to a lower energy state. For iron, this results in oxidised iron corrosion products. The thermodynamic pathway from metal ore to pure metal, followed by corrosion leading to more stable products is illustrated in Figure 1.1.

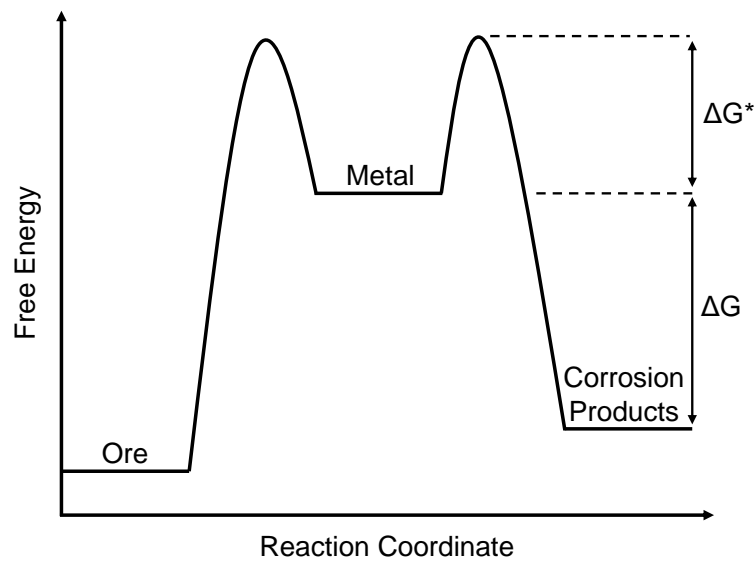


**Figure 1.1:** Free energy vs reaction coordinate from ore, to pure metal, to corrosion products.  $\Delta G$  is the enthalpy of a reaction, and  $\Delta G^*$  is the activation energy.

The rate at which a metal undergoes these corrosion reactions is determined by the energy required to overcome the activation energy barrier and is calculated by the Arrhenius equation (Equation 1.1):

$$k = Ae^{-\frac{\Delta G^*}{RT}} \quad (1.1)$$

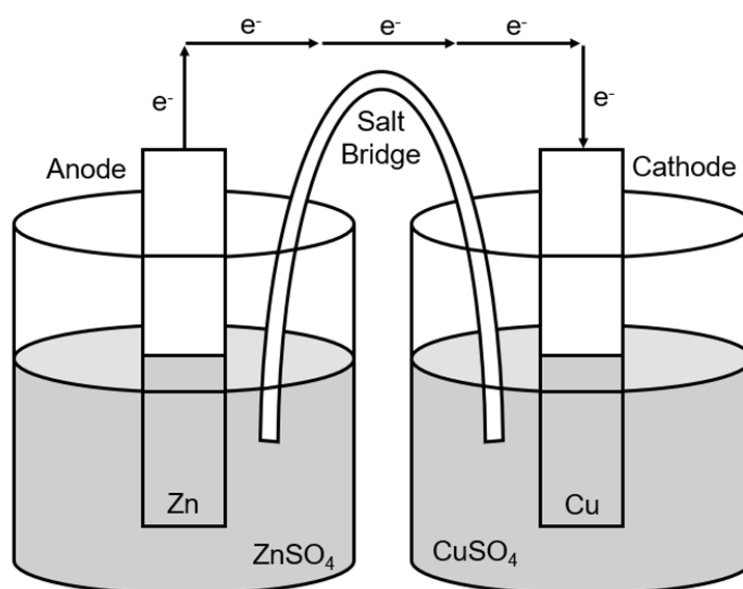
where  $k$  is the rate constant,  $A$  is the frequency at which atoms and molecules collide in a way that leads to a reaction,  $\Delta G^*$  is the activation energy,  $R$  is the molar gas constant, and  $T$  is the temperature. Due to the exponential function of Equation 1.1, a small  $\Delta G^*$  will result in rapid corrosion rates, but a large  $\Delta G^*$  will produce a low corrosion rate.

Four components are essential for corrosion to occur: an anode, where a metal oxidizes into metal ions through the loss of electrons; a cathode, where electrons are gained and used to reduce an ion or molecule; a conductor, which facilitates the rapid transport of electrons between the anode and cathode; and an electrolyte, enabling ion movement to complete the electrochemical cell. In an electrochemical cell with two connected metals, the flow of electrons is governed by the difference in their standard electrode potentials. The standard electrode potential quantifies the tendency of an oxidised species to gain electrons and undergo reduction. Pertinent standard electrode potentials for the research presented in this thesis are listed in Table 1.1.

When two metals are connected, the metal with the higher standard electrode potential will receive electrons from the one with the lower potential. This principle is exemplified by the Daniell Cell, depicted schematically in Figure 1.2 [12–14]. As shown, Zn and Cu electrodes are immersed in aqueous solutions of  $\text{ZnSO}_4$  and  $\text{CuSO}_4$ , respectively. An external circuit and a saline bridge connect them electrochemically.

**Table 1.1:** Selected half cell reactions and their standard electrode potentials.

| Reduction Half-Reaction   | $E_{red}^0$ vs SHE |
|---|--------------------|
| $\text{Cr}_2\text{O}_7^{2-} + 14\text{H}^+ + 6\text{e}^- \rightarrow 2\text{Cr}^{3+} + 7\text{H}_2\text{O}$ | +1.36              |
| $\text{O}_2 + 2\text{H}_2\text{O} + 4\text{e}^- \rightarrow 4\text{OH}^-$                                   | +0.40              |
| $2\text{H}^+ + 2\text{e}^- \rightarrow \text{H}_2$  | 0.00               |
| $\text{Fe}^{2+} + 2\text{e}^- \rightarrow \text{Fe}$  | -0.44              |
| $\text{Zn}^{2+} + 2\text{e}^- \rightarrow \text{Zn}$  | -0.76              |
| $\text{Al}^{3+} + 3\text{e}^- \rightarrow \text{Al}$  | -1.68              |

**Figure 1.2:** Diagram of the Daniell Cell.

The standard electrode potentials ( $E_{red}^0$ ) for the reduction of  $\text{Zn}^{2+}$  ions to Zn and  $\text{Cu}^{2+}$  to Cu is -0.76 V and 0.34 V, respectively. Consequently, as  $\text{Zn}^{2+}$  reduction has the more negative  $E_{red}^0$ , the Zn electrode becomes the anode and undergoes dissolution to  $\text{Zn}^{2+}$  ions via Equation 1.2:



The electrons produced from Zn dissolution are received via the external circuit by the Cu cathode, being used to reduce  $\text{Cu}^{2+}$  ions to metallic copper that plates out onto the Cu cathode (Equation 1.3):



The circuit is completed by a saline bridge that contains a solution of  $\text{K}^+$  and  $\text{NO}_3^-$ . When power is provided by the cell, the  $\text{NO}_3^-$  anion diffuses towards the anode to relieve positive charge, and the  $\text{K}^+$  cation diffuses to the cathode to relieve negative charge. By combining the two half-cell reactions, an overall electrochemical reaction is produced (Equation 1.4):



Convention dictates that the half-cell of the reduced species ( $\text{Cu}^{2+}$ ) is considered the left-hand side equation (LHE), and the half-cell containing the oxidised species (Zn) is the right-hand side equation (RHE) [15]. The electromotive force, EMF for the complete cell ( $E_{\text{cell}}$ ) is given by Equation 1.5:

$$E_{\text{cell}} = E_{\text{RHE}}^0 - E_{\text{LHE}}^0 \quad (1.5)$$

where  $E_{\text{RHE}}^0$  and  $E_{\text{LHE}}^0$  are the standard potential values of the oxidised and reduced species, respectively. In the case of the Daniell cell,  $E_{\text{cell}}$  is 1.10 V.  $E_{\text{cell}}$  is related to  $\Delta G$  by Equation 1.6:

$$\Delta G = -nFE_{\text{cell}} \quad (1.6)$$

where  $n$  is the number of electrons transferred, and  $F$  is the Faraday constant ( $96485 \text{ C mol}^{-1}$ ). The more negative the value of  $\Delta G$ , the more likely the reaction will occur spontaneously, therefore the more positive the value of  $E_{\text{cell}}$  the more negative the value of  $\Delta G$ , thereby giving a stronger thermodynamic driving force.

In practice, electrochemical reactions will generally not be exposed to standard conditions (1 mol dm<sup>-3</sup> concentration of ions, 1 atm pressure, and 25 °C temperature). Electrode potentials can change due to the influence of temperature and the changing concentrations of reactants and products. This is accounted for in the Nernst equation (Equation 1.7) [16]:

$$E_{\text{cell}} = E_{\text{cell}}^0 - \frac{RT}{nF} \ln \frac{[\text{reduced}]}{[\text{oxidised}]} \quad (1.7)$$

where R is the universal gas constant (8.31 J mol<sup>-1</sup>), [reduced] refers to the concentration of reactants from the reduction reaction, and [oxidised] refers to the concentration of products from the oxidation reaction.

### 1.2.1.1 Reference Electrodes and Measuring Electrode Potentials

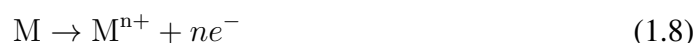
Electrode potentials can be measured relative to a reference electrode. The electrode under investigation is connected to the reference electrode using a salt bridge and an external circuit. The standard electrode potential of the reference ( $E_{\text{ref}}$ ) electrode must be consistent and reproducible such that electrode potentials of the sample under investigation can be referenced to it. The reference electrodes cited in this work are:

- The **Standard Hydrogen Electrode (SHE)**, consisting of a platinum wire immersed in 1 mol dm<sup>-3</sup> solution of H<sup>+</sup>, where hydrogen gas is introduced at a pressure of one atmosphere and a temperature of 298 K (25 °C). The reduction of H<sup>+</sup> to H<sub>2</sub> gas at this electrode defines the zero point on the standard electrochemical potential scale. To measure an unknown electrode potential, the test electrode is placed in a solution containing its ions, and the potential difference from the SHE measured. The SHE is given the value of 0 V. If the potential of another reference electrode is known with respect to the SHE, the value of test electrode potentials using that reference electrode can be converted to a value against the SHE.
- The **Standard Calomel Electrode (SCE)**, +0.241 V vs. SHE), which consists of mercury (Hg) in contact with mercury chloride (Hg<sub>2</sub>Cl<sub>2</sub>, calomel) and a saturated aqueous solution of KCl.



### 1.2.2 Aqueous Corrosion

The Daniell cell presented in Section 1.2.1 is an example of a galvanic corrosion cell as it occurs between two metals of differing standard electrode potential. However, it is typical for anodic and cathodic activity to occur on single metal surfaces, producing either ‘general’ or ‘localised’ aqueous corrosion. During general corrosion, deterioration of the metal occurs uniformly over the entire surface as anodic and cathodic sites are small, numerous, spatially inseparable and change places at short time intervals. This means that all areas of the exposed metal surface will corrode at the same rate. However, in localised corrosion, the anodic and cathodic sites are large, less numerous, spatially distinct, and tend to remain in the same place over time. As such, anodic activity is focused on a few discrete areas, meaning the metal will deteriorate very quickly in those areas via metal dissolution (Equation 1.8):



The electrons released in the anodic reaction are transported through the metal and consumed at cathodic sites. In aerated neutral or alkaline electrolytes, the predominant cathodic reaction is oxygen reduction (Equation 1.9), while in acidic conditions, the cathodic reaction is predominantly hydrogen evolution (Equation 1.10):



An example of localised aqueous corrosion is differential aeration, which results from differences in the concentration of oxygen that gains access a metal surface. An example is Evans’ drop experiment (Figure 1.3 ), which involves adding a drop of aqueous saline solution (e.g. NaCl or KCl) on a clean, polished Fe surface [17–19]. On the periphery of the droplet, the metal surface has access to a higher oxygen concentration than the centre,

meaning the rate of oxygen reduction is faster at the droplet periphery. This difference forces Fe dissolution to the droplet centre, leading to a central ring of corrosion product.

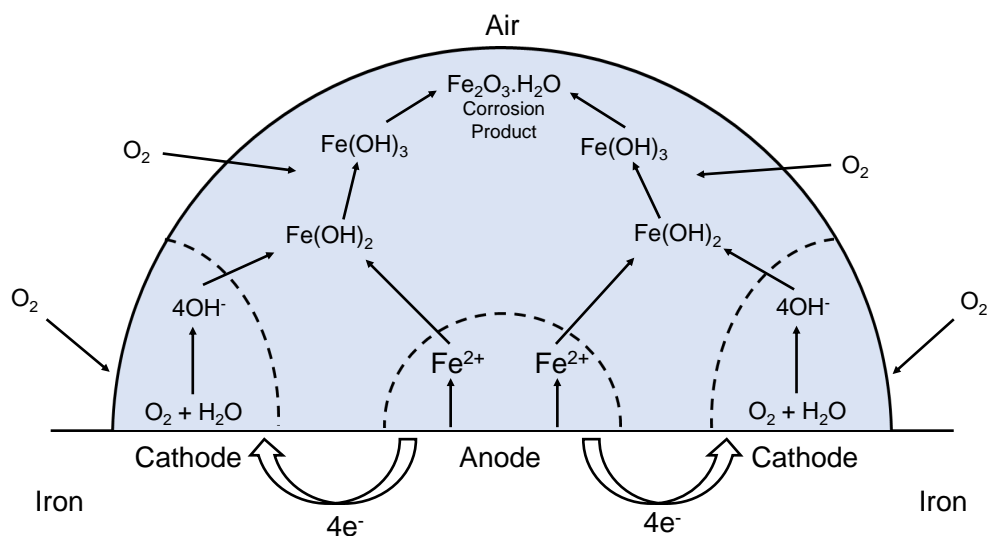


**Figure 1.3:** Schematic representation of Evans' differential aeration cell.

### 1.2.3 Pourbaix Diagrams

Pourbaix diagrams, commonly known as potential-pH diagrams, graphically illustrate the thermodynamic stability of various metallic ions in aqueous environments, based on solution pH and potential. These diagrams are helpful tools for analysing the corrosion behaviour of metals and metal alloys. Within the scope of this thesis, the focus is on ZnAl coatings, and hence, the Pourbaix diagrams for Zn and Al are presented in Figure 1.4. The diagrams are based upon a condition whereby the concentration of metal ions (generated by metal dissolution) is more than  $1 \times 10^{-6} \text{ mol dm}^{-3}$  in solution, the metal is undergoing corrosion; however, below that concentration, the material is considered immune.

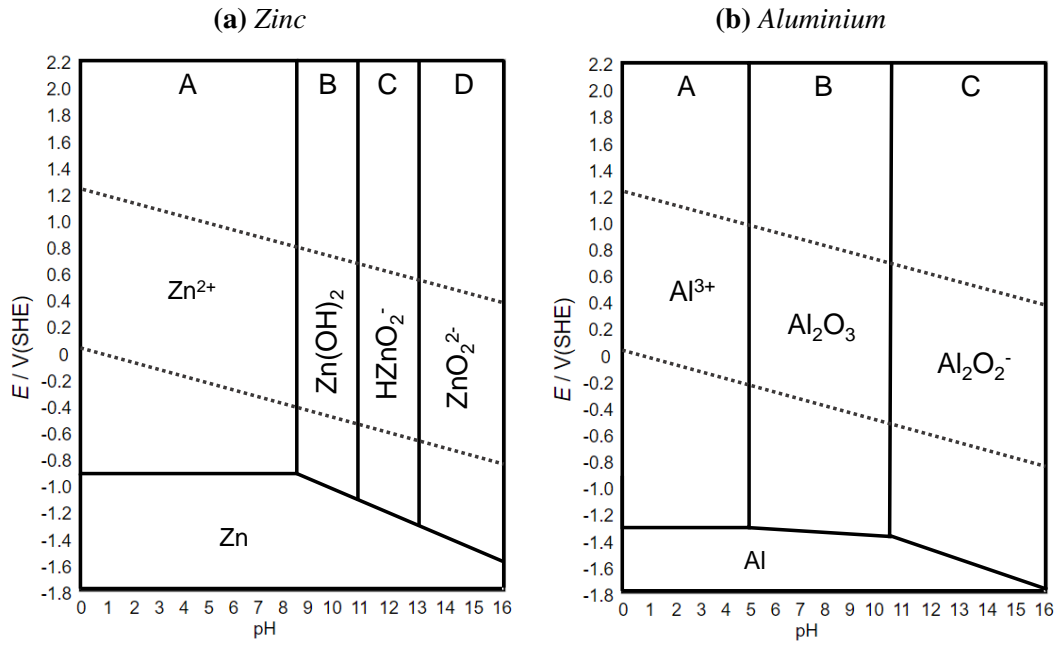
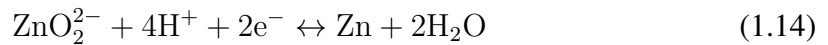
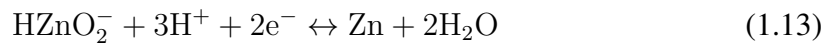
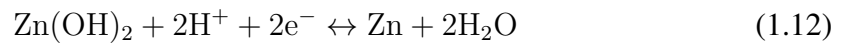


**Figure 1.4:** a) Pourbaix diagram of zinc, and b) Pourbaix diagram of aluminium.

For Zn immersed in water (Figure 1.4a), there are four equilibrium reactions:



Equation 1.11 is independent of pH and corresponds to the horizontal line on the Pourbaix diagram, whereas Equations 1.12-1.14 vary linearly with pH. The vertical lines are independent of potential; they show the predominant oxidised species in solution at a given

pH. In this case, within three of the regions (labelled A, C and D), the oxidised Zn species is soluble in solution, and corrosion proceeds. However in region B, the corrosion product  $\text{Zn(OH)}_2$  is insoluble so creates a barrier to corrosion and renders the surface passive.

In the case of Al (Figure 1.4b) the Pourbaix diagram is dominated by region B (between pH 4-10), where the predominant oxidised Al species is  $\text{Al}_2\text{O}_3$ , an insoluble surface film that renders Al passive. Only in very acidic (region A) or very alkaline (region C) aqueous solutions is the passive film broken down and corrosion of Al proceeds.

### 1.2.4 Polarisation and Corrosion Kinetics

If a metal electrode, M, is placed in a solution of its own ions,  $\text{M}^{n+}$ , the reversible reaction (1.15) occurs whereby a forward reduction of  $\text{M}^{n+}$  ions to M is reversed by a backwards dissolution of M to  $\text{M}^{n+}$ .



Values of current density are associated with both reactions and are directly related to corrosion rate. The current density of the reduction (cathodic) reaction is denoted  $i_c$  and the current density of the oxidation (anodic) reaction is denoted  $i_a$ .

When corrosion initiates, a charge separation at the interface between the metal electrode and the solution forms that balances  $i_c$  and  $i_a$ . This charge separation forms the electrical double layer (EDL) and is illustrated in Figure 1.5. At equilibrium, the values of  $i_c$  and  $i_a$  are equal and opposite, allowing an exchange current,  $i_0$  to be determined by Equation 1.16:

$$i_a = -i_c = i_0 \quad (1.16)$$

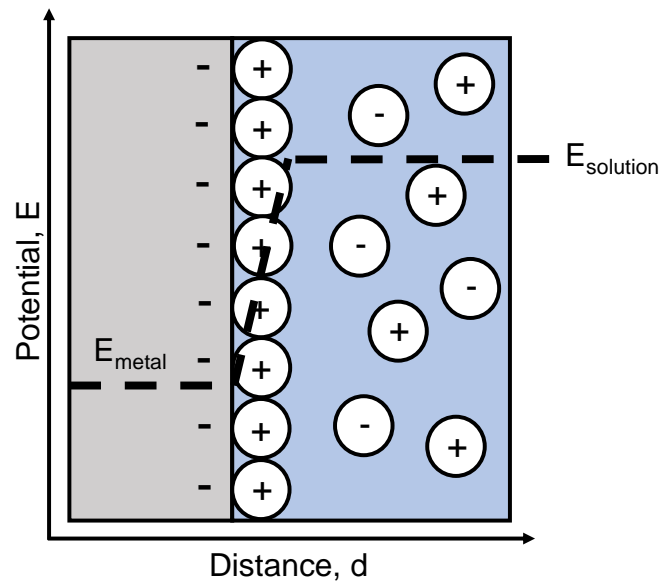


**Figure 1.5:** Schematic representation of the Helmholtz model of the double layer.

Under these equilibrium conditions, the Nernst equation can be used to calculate the equilibrium potential ( $E_e$ ). However, this equilibrium is highly dependent on factors such as the substrate and the concentration of solution. As such, if conditions vary, and therefore non-equilibrium conditions are established, net current may flow as  $i_a$  and  $i_c$  differ. As a result, the electrode becomes polarised either anodically or cathodically.

Any deviation from  $E_e$  through the application of an applied potential,  $E$  is defined as the overpotential,  $\eta$  (Equation 1.17).

$$\eta = E - E_e \quad (1.17)$$

The reaction rates for the anodic and cathodic reactions are given by Equation 1.18 and Equation 1.19, respectively.

$$k_a = k'_a \exp\left(\frac{\Delta G^0}{RT}\right) \quad (1.18)$$

$$k_c = k'_c \exp\left(\frac{-\Delta G^0}{RT}\right) \quad (1.19)$$

where  $k'_a$  and  $k'_c$  are rate constants for the anodic and cathodic reactions, respectively. By taking the anodic reaction at equilibrium and combining Faraday's Law, Equation 1.16 and Equation 1.18, Equation 1.20 is derived:

$$i_0 = zFk_a = zFk'_a \exp\left(\frac{-\Delta G^0}{RT}\right) \quad (1.20)$$

If an overpotential,  $\eta$  is applied in the anodic direction, the activation energy of the reaction is reduced to  $(\Delta G - \alpha_a zF\eta)$ , where  $\alpha_a$  is the anodic transfer coefficient and an Equation 1.21 is derived:

$$i_a = i_0 \exp\left(\frac{\alpha_a zF\eta}{RT}\right) \quad (1.21)$$

If an overpotential,  $\eta$  is applied in the cathodic direction, the activation energy of the reaction is decreased by  $(1 - \alpha_c)zF\eta$ , where  $\alpha_c$  is the cathodic transfer coefficient and an Equation 1.22 is derived:

$$i_c = i_0 + \exp\left(\frac{(1 - \alpha_c) zF\eta}{RT}\right) \quad (1.22)$$

Equations 1.21 and 1.22 are Tafel equations from which the values of  $\alpha$  can be experimentally measured. A Tafel plot can be made by taking the natural log of anodic and cathodic currents, an example of which is given in Figure 1.6

In the case of aqueous corrosion, Tafel curves are often provided as an Evans diagram (Figure 1.7). From this diagram, the free corrosion potential,  $E_{\text{corr}}$  and free corrosion current  $I_{\text{corr}}$  are extracted from the intersection of the lines associated with the anodic and cathodic reactions.

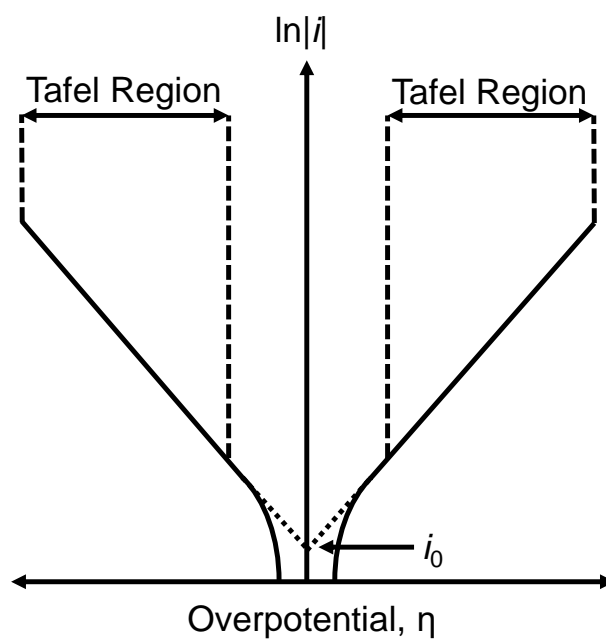


**Figure 1.6:** Schematic representation of Tafel analysis.

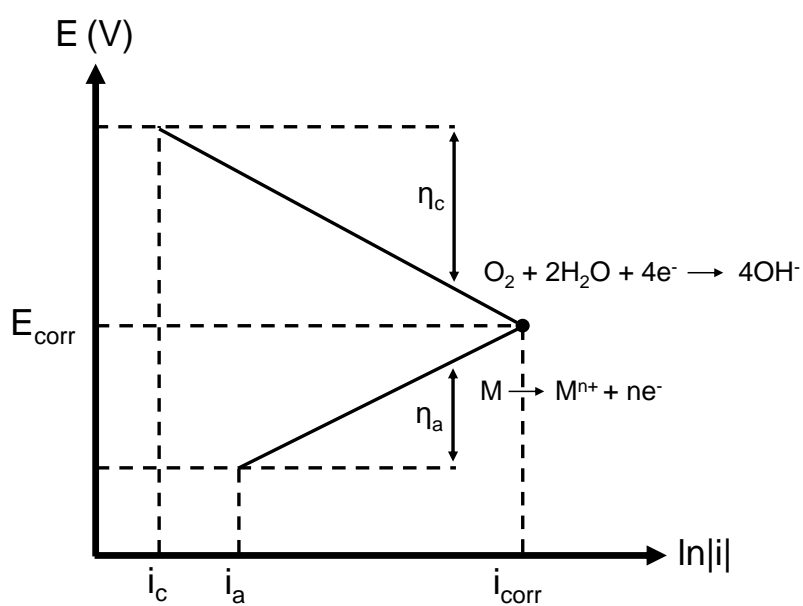


**Figure 1.7:** A representative Evans diagram for a metal undergoing aqueous corrosion, where  $\eta_a$  and  $\eta_c$  are the anodic and cathodic overpotentials, respectively.

## 1.3 Corrosion Prevention

### 1.3.1 Metallic Coatings

As discussed in Section 1.1, the favourable properties and cost-effectiveness of steel has established it as an important material within the automotive, construction and appliance industries. However the inherent corrosion susceptibility of iron means that without treatment, bare steel products often have limited lifetimes in these industries. To combat this, Zn and Zn-alloy coated steels are increasingly utilized as defence against corrosion. The primary protective mechanism is sacrificial: when the underlying steel becomes exposed to the environment due to damage or manufacturing defects (i.e. cut edges) Zn will corrode in preference to steel because it has a more active (negative) standard electrode potential (see Table 1.1). A secondary protection mechanism involves the formation of a passive barrier that impedes further corrosion by the environment [20].

Zn sacrificial protection of steel is illustrated in the Evans diagram shown in Figure 1.8. For an intact Zn coating, the corrosion rate ( $i_{\text{corr-Zn}}$ ) is less than that of steel ( $i_{\text{corr-Fe}}$ ) due to a significantly lower exchange current density of dissolved oxygen on Zn than iron (given by  $i_{\text{oc-Zn}}$  and  $i_{\text{oc-Fe}}$ , respectively). At a defect where steel becomes exposed to a corrosive environment, the electrode potential of iron becomes equal to that of Zn. As such, the corrosion rate of iron ( $i_{\text{corr-Fe-Exposed}}$ ) becomes significantly reduced than if not in combination with the Zn coating.

The metallic coatings for steel that are the focus of this work include Hot-Dip Galvanised (HDG), Galfan, and Zn55Al. These coatings are all Zn coatings alloyed with various compositions of Al and created using the hot-dip galvanising process, where steel is dipped into a molten bath of the specific alloy and allowed to cool. The microstructure of these substrates can be analysed through an Al-Zn equilibrium diagram [21], as illustrated in Figure 1.9. The following sections will examine each coating's microstructure and corrosion behaviour.



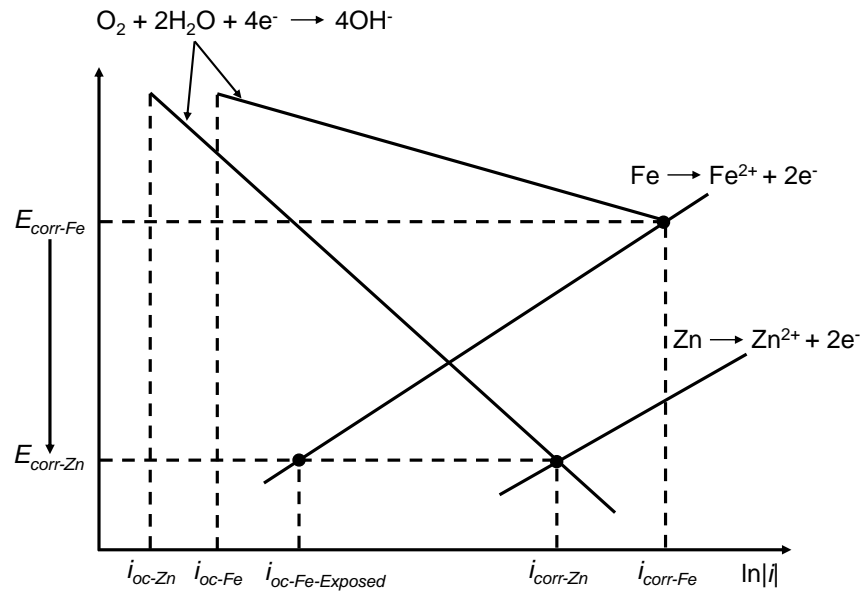


**Figure 1.8:** Evans diagram of the sacrificial protection afforded by zinc-coated steel when a defect exposes the underlying steel to a corrosive environment.

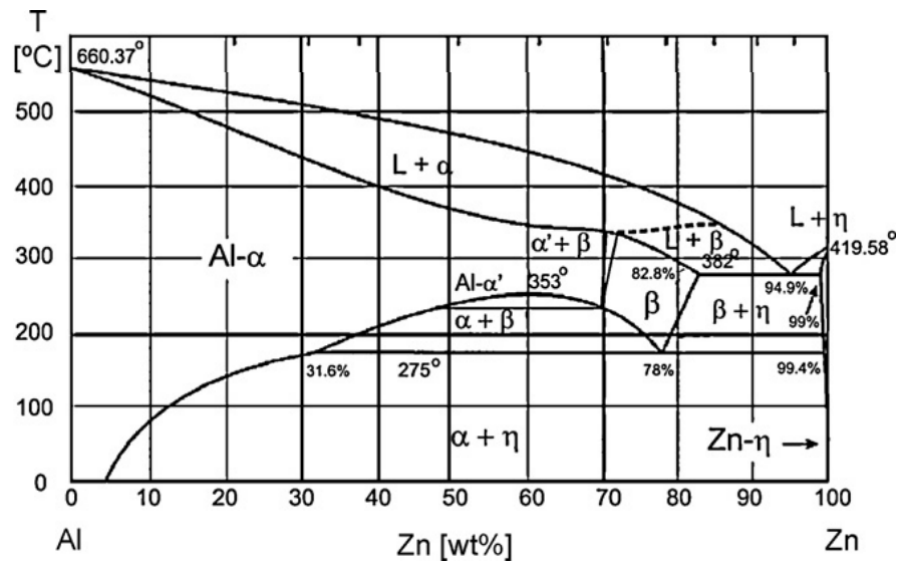


**Figure 1.9:** The Al-Zn equilibrium diagram [21].

### 1.3.1.1 Hot-Dip Galvanised Steel (HDG)

HDG is considered the benchmark in terms of galvanised coating. Its composition is predominantly Zn, but with a small 0.15-0.25 wt.% addition of aluminium. The Al

addition drastically improves the mechanical properties of the galvanised sheet due to the rapid formation of an Al-Fe intermetallic ( $\text{Fe}_2\text{Al}_5$  or Fe-Al-Zn) between the coating and the substrate which provides better coating weight control, formability, and adhesion to the underlying steel substrate [20, 22-25].

Previous studies have investigated the atmospheric corrosion of HDG in various environments and over extended periods. For instance, in a world-wide study, Persson et al. [26] examined the atmospheric corrosion of HDG over two years in marine, urban, and industrial environments. It was found that localised pitting is a prominent corrosion mechanism for the substrate, evidenced through a clear separation of corrosion products between localised anodic sites (basic sulfate and chloride salts) and surrounding cathodic sites (zinc hydroxy carbonate).

### 1.3.1.2 Galfan

For commercial steel makers, in addition its susceptibility to corrosion pure zinc can be costly (approximately US\$2800 per tonne). To reduce corrosion rates while reducing commercial costs, Zn is often alloyed with additions of aluminium; Al-alloyed galvanised coatings provide better corrosion resistance and are cheaper because of Al's lower cost (US\$1100 per tonne).

One such product is Galfan<sup>TM</sup>, a Zn coating alloyed with approximately 4.5 wt.% Al and trace amounts (0.05 wt.%) of mischmetal (cerium and lanthanum) [20]. Since its introduction over 30 years ago, Galfan's superior corrosion resistance relative to HDG has been empirically established. For instance, studies by Zoccola et al. [27] showed improved performances of Galfan during 5 year exposure in severe marine and industrial sites, while Uchima et al. [28] confirmed its lower corrosion rate in cyclic modified salt spray tests.

After hot-dipping, solidification of Galfan results in an essentially two-phase microstructure (Figure 1.10) that is made up of a Zn-rich proeutectoid phase surrounded by a eutectic phase consisting of  $\beta$ -Al (5-25 wt.% Al) and  $\eta$ -Zn lamellas (<5 wt.% Al) [20, 24]. During

the initial stages of atmospheric corrosion, the eutectic phase is more susceptible to attack, with it likely starting at the  $\eta$ -Zn phase adjacent to the  $\beta$ -Al. In marine atmospheres, this attack results in Zn and/or ZnAl corrosion products such as simonkolleite, LDH and gordaite [29, 30].

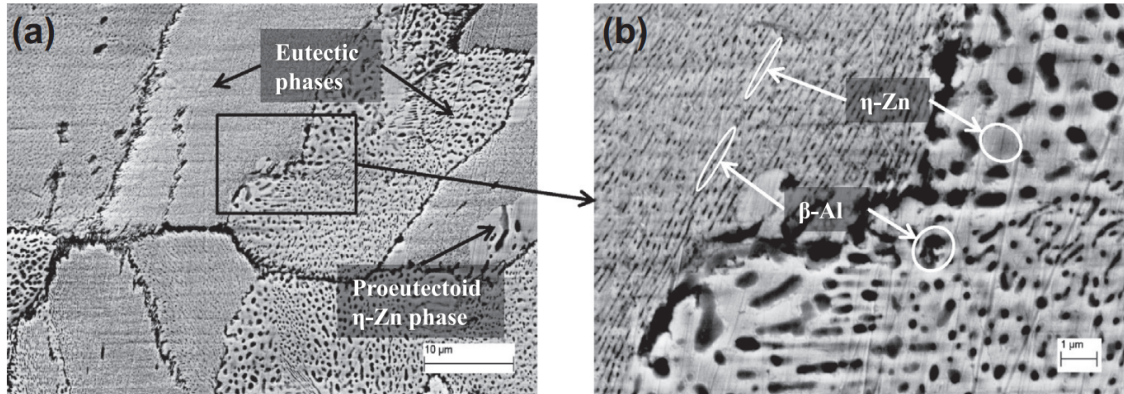


**Figure 1.10:** SEM images showing the microstructure of diamond-polished Galfan at (a) lower and (b) higher magnification [29].

### 1.3.1.3 Zn55Al

Zn55Al, known commercially as Galvalume<sup>TM</sup> and Aluzinc has an even greater Al content than Galfan, containing 55 wt.% Al. Zn55Al has the best intrinsic corrosion resistance of the ZnAl coated steels described, possessing up to four time better corrosion resistance than HDG in marine and industrial atmospheres [31,32]. Its enhanced performance is attributed to its two-phase microstructure (Figure 1.11) of primary Al-rich dendrites (approx. 80 wt.% Al) that occupy approximately 80% by volume of the coating separated by a Zn-rich interdendritic (approx. 78 wt.% Zn). While Zn maintains sacrificial protection to the underlying steel, the large surface coverage of the Al-rich dendrites enables a strongly passive Al (hydro)oxide layer to form and cover much of the surface, thereby acting as a barrier to corrosive electrolyte [20, 33].

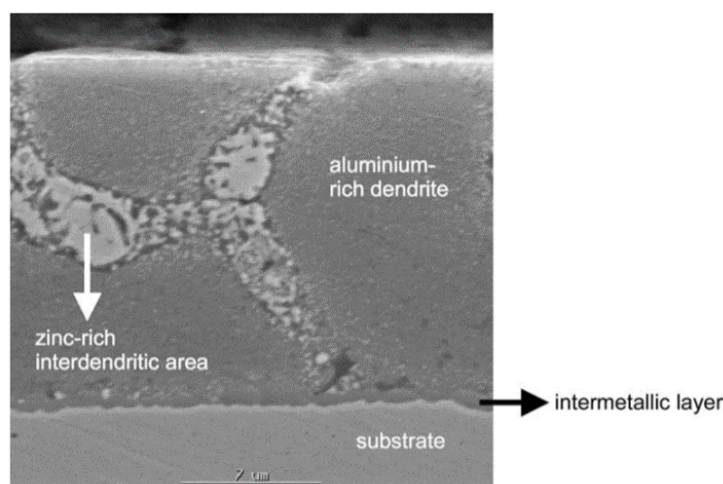


**Figure 1.11:** A scanning electron microscope image of a cross-section of Zn55Al coated steel [33].

Previous work into the initial atmospheric corrosion of Zn55Al suggests that the passive layer described can be broken down locally by contact with chloride and gradually replaced by Zn-rich corrosion products that include zinc aluminium hydroxy carbonate, zinc chloro sulfate, zinc hydroxy chloride, and zinc hydroxy carbonate [34, 35]. This has led to the conclusion that during the initial exposure, Zn-rich interdendritic regions undergo preferential anodic attack [32, 36-38].

### 1.3.2 Organic Coatings

Organic coating systems are often used to further enhance the corrosion-resistance of ZnAl coated steels. For instance, in 2021, 5 million metric tonnes of hot-dipped coated steel produced in European Union countries were organically coated [39]. Their use is popular as not only do they protect the substrate from the environment, but they also provide more pleasing aesthetics. As such, organically coated ZnAl coated steels are ideal for cladding and roofing in the construction industry. A schematic of a typical coating system for a pre-finished ZnAl coated steel cladding product is shown in Figure 1.12. The organic components consist of a pre-treatment, primer, and top-coat [40].

### 1.3.2.1 Pre-treatment

The pre-treatment coating, often referred to as a ‘conversion’ coating, is a thin layer ( $< 1 \mu\text{m}$ ) used to promote the adhesion of subsequent organic coatings by reducing the effects of metallic surface roughness. In addition, it acts as a barrier to corrosion of the underlying ZnAl coated steel, providing a small degree of corrosion protection.

### 1.3.2.2 Primer

The primer layer is thicker than the pre-treatment, possessing a typical thickness of 5-12  $\mu\text{m}$ . It usually contains corrosion-inhibiting pigments that can leach out of the coating and suppress corrosion activity on the ZnAl coated steel substrate.

### 1.3.2.3 Top coat

The top coat is the thickest layer in the coating system, possessing a typical thickness between 18-200  $\mu\text{m}$ . It is the most significant barrier to the environment, protecting the underlying coatings from UV degradation and water ingress, while providing the product its colour.

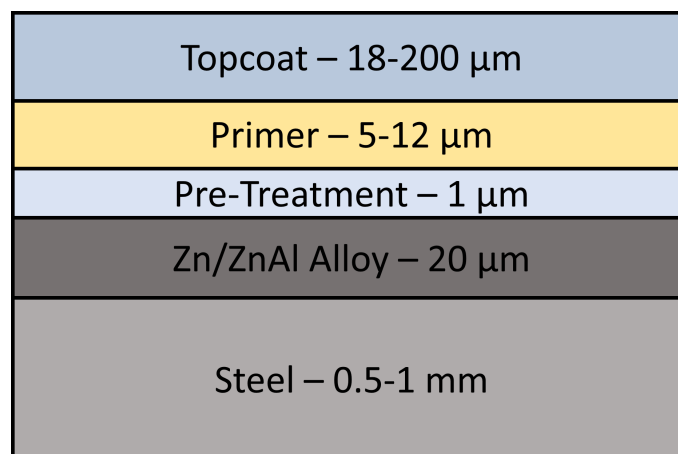


**Figure 1.12:** Schematic breakdown of a typical organic coating system for ZnAl coated steel cladding.

### 1.3.3 Corrosion-driven Organic Coating Failure

Although organic coatings on ZnAl galvanised steel reduce corrosion of the substrate, defects that expose the underlying metal surface to electrolytes can lead to corrosion-induced failures of the organic coating. The following sections detail the prevalent failure mechanisms for ZnAl galvanised steels, namely cathodic delamination and anodic undermining.

#### 1.3.3.1 Cathodic Delamination

A common mechanism of corrosion-driven organic coating failure is cathodic delamination, a failure mechanism of iron, steel and HDG substrates [41-49] that occur at coating defects. It is characterised by an ingress of electrolyte that couples anodic dissolution at a defect site to cathodic oxygen reduction occurring underneath an organic coating [49-52]. The outcome is an alkaline environment in cathodic regions, leading to the delamination of the organic coating. A schematic illustration of cathodic delamination arising on zinc surfaces (such as HDG) is shown in Figure 1.13 delamination is attributed to a combination of three phenomena that can occur in alkaline environments – dissolution of the metal oxide film, coating displacement and base-catalysed polymer degradation.

Firstly, in alkaline environments, passive oxide films of the metal surface can be destroyed, damaging the interface between the metal surface and the organic coating. For example, in the case of zinc, its zinc oxide layer is amphoteric; therefore, the alkaline pH generated from the cathodic reduction reaction can dissolve the layer and thus destroy the coating–zinc interface [53,54].

Secondly, regarding coating displacement, it is thought that alkaline electrolytes can physically displace the organic coating at the substrate-coating interface. An electrode's 'wettability' increases with decreasing electrolyte-electrode interfacial energy and will reach a maximum value at the potential of zero charge. As such, the affinity of water for an oxide-covered metal will increase as the pH shifts from the isoelectric point of the oxide; hence, displacement of the coating ensues as pH rises [53,55-58].

Thirdly, it is possible that alkaline electrolyte directly reacts with the polymer of the organic coating, breaking bonds within the coating or between the substrate and the coating. Many polymers are susceptible to alkaline hydrolysis, including polyesters, epoxy esters, and polymers that possess urethane and urea linkages [59-61].

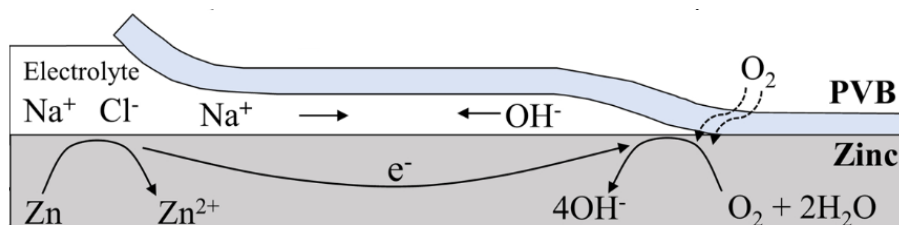


**Figure 1.13:** Schematic diagram of the mechanism of cathodic delamination on a zinc surface organically coated with polyvinyl-butyrac-co-acetate (PVB).

### 1.3.3.2 Anodic Undermining

In contrast to cathodic delamination, in anodic undermining the leading front that leads to coating failure undergoes anodic dissolution instead of oxygen reduction. Examples of this process include filiform corrosion (FFC) and cut-edge corrosion.

FFC was first reported in 1944 by Sharman and predominantly affects organically coated steel and aluminium surfaces. It initiates at penetrative defects and progresses as characteristic thread-like under-film deposits of corrosion products [62]. The mechanism of FFC, as schematically illustrated in Figure 1.14 consists of two main features, an electrolyte-filled head containing aggressive metal cations and anions (such as  $\text{Cl}^-$ ) and a tail of dry, porous corrosion products. The driving force for filament advancement is differential aeration of the filament head, arising from a facile mass transport of gaseous  $\text{O}_2$  through the tail. As such, the back of the filament head becomes the principal site of oxygen reduction, while anodic metal dissolution occurs towards the leading edge of the filament head. The dissolution products become trapped at the back end of the head, becoming part of the tail. Throughout the process, chloride-containing electrolyte is maintained in the filament head so FFC, once established, can propagate for several months or even years [53,62-64].

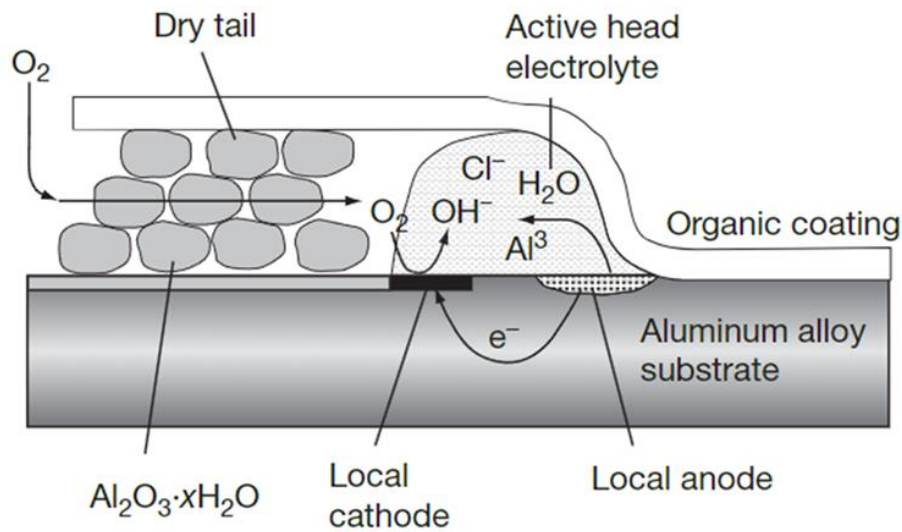


**Figure 1.14:** Schematic diagram of the propagation of FFC on aluminium alloy substrate.

Unlike the in-service defects such as scratches that can propagate FFC, cut-edge corrosion originates from manufacturing defects, specifically the cut-edges introduced when the pre-finished product is cut to size for its application. These cut-edges are cross-sections of the whole product, meaning all metallic substrates and organic coatings are exposed to the environment at once. In such a circumstance, the ZnAl layer undergoes sacrificial anodic dissolution to provide cathodic protection to the exposed steel. Considering ZnAl coatings usually have a maximum thickness of 30  $\mu\text{m}$  and the steel it is protecting has a thickness of up to 1 mm, the cathode-to-anode ration is large. Consequently, expedited rates of ZnAl anodic dissolution must occur to ensure adequate electron transfer to the steel for cathodic oxygen reduction. Subsequently, the organic coating system adhered to the ZnAl layer delaminates as the ZnAl layer rapidly undergoes dissolution.

Comparing HDG, Galfan and Zn55Al, the material that probably suffers most from cut-edge corrosion and its associated organic coating failure is Zn55Al, as sacrificial zinc-rich regions only occupy approximately 30% of the coating volume, therefore its cathode-to-anode ratio is the largest.



### 1.3.4 Corrosion Inhibitors

To inhibit metallic corrosion, inhibiting compounds are often incorporated into the organic coating system, functioning by leaching out from coatings and reducing the rate of either the anodic or cathodic reaction, or in some cases both simultaneously. The specific types of inhibitor relevant to this thesis are discussed in the subsequent sections.

#### 1.3.4.1 Anodic Inhibitors

Anodic inhibitors act to reduce the rate of the anodic half of the corrosion process and operate either through precipitation or cathodic depolarisation. Anodic precipitation inhibitors are anions that react with metal ions from anodic dissolution to form insoluble precipitates. These precipitates serve as a protective layer that hinder access of corrosive ions to the metal surface, thus hindering further corrosion. Chromates ( $\text{CrO}_4^{2-}$ ), molybdates ( $\text{MoO}_4^{2-}$ ), phosphates ( $\text{PO}_4^{3-}$ ), and silicates ( $\text{SiO}_4^{4-}$ ) exemplify this type [65,66], working by shifting the anodic dissolution curve to a more noble (positive) potential as shown in the Evans diagram of Figure 1.15. This moves the intercept with the cathodic curve to higher  $E_{\text{corr}}$  but reduces the corrosion current,  $i_{\text{corr}}$ , thus reducing corrosion rates. The efficiency of anodic precipitation inhibitors is dependent on their ability to adequately cover all anodic sites. An incomplete coverage in combination with an increase in  $E_{\text{corr}}$  could lead to situations where small sites that are anodically polarised couple with large cathodic areas and highly damaging localised corrosion ensues. Thus, a sufficient quantity of the anodic inhibitor is important in mitigating the risk of localised corrosion [67].

In the case of cathodic depolarisers, strong oxidising agents that provide an alternative pathway for cathodic reactions other than oxygen reduction, the metal becomes anodically polarised to a potential that favours the formation of passivating layers such as oxides or hydroxides that shield the metal from further corrosion. Chromates are particularly effective cathodic depolarizers [65].

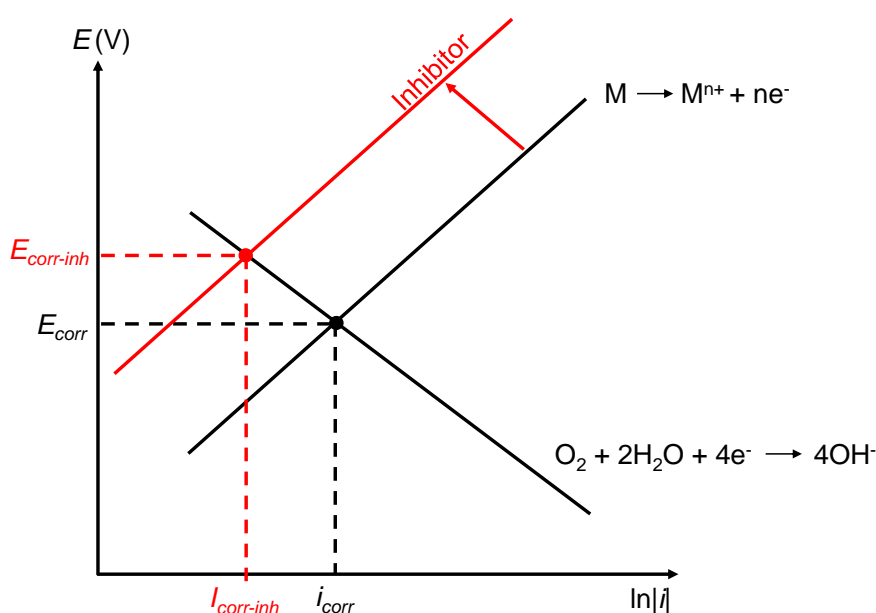


**Figure 1.15:** The change in the Evans diagram of aqueous corrosion upon adding an anodic precipitation inhibitor.

### 1.3.4.2 Cathodic Inhibitors

Cathodic inhibitors act to reduce the rate of the cathodic half of the corrosion process and operate either through precipitation or cathodic poisoning. Cathodic precipitation inhibitors are ions that can react with the products of the cathodic reaction to form insoluble oxides and hydroxides that act as barriers to further reaction. Examples include  $\text{Ca}^{2+}$ ,  $\text{Ce}^{3+}$ ,  $\text{Sr}^{2+}$ ,  $\text{Zn}^{2+}$ ,  $\text{Mg}^{2+}$  and  $\text{CrO}_4^{2-}$ . As demonstrated in the Evans diagram in Figure 1.16, cathodic precipitation inhibitors work by shifting the cathodic curve to more negative potentials. This moves the intercept with the anodic curve to a lower  $i_{\text{corr}}$ , thus reducing corrosion rates. In addition, as  $E_{\text{corr}}$  is also reduced, accelerated localised anodic attack is not observed when insufficient inhibitor concentrations are used; therefore, they are generally safer than anodic inhibitors.

Cathodic poisoning acts upon hydrogen evolution reactions. Elements such as arsenic (As), bismuth (Bi) and antimony (Sb) prevent bonds from being made between adjacent adsorbed hydrogen atoms on the metal surface. This means that they are retained on the

surface, and the kinetics of the cathodic reaction is retarded. Unfortunately, however, cathodic poisoning can lead to hydrogen atoms diffusing into the metal substrate, causing hydrogen embrittlement.

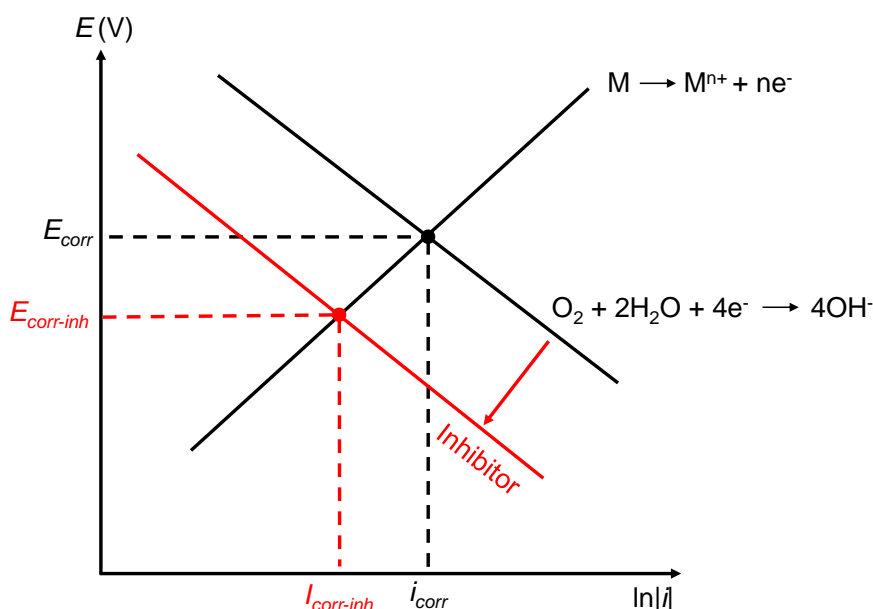


**Figure 1.16:** The change in the Evans diagram for aqueous corrosion upon adding a cathodic precipitation inhibitor.

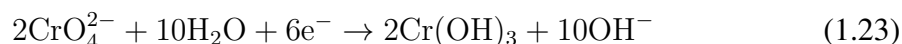
## 1.3.5 Anti-Corrosion Pigments

### 1.3.5.1 Hexavalent Chromium

Historically, the common corrosion-inhibiting pigments employed by the organic coatings industry to guarantee long and robust product lifetimes were based on hexavalent chromium and chromate ( $\text{CrO}_4^{2-}$ ) derivatives. The most effective were based on sparingly soluble chromate species, namely that of strontium chromate ( $\text{SrCrO}_4$ ) and zinc chromate ( $\text{ZnCrO}_4$ ), which act as anodic precipitators and cathodic depolarisers.

Chromate pigments have been shown to be effective at preventing the corrosion-driven organic coating failures discussed in Section 1.3.3.1 and Section 1.3.3.2. In the case of cathodic delamination, it was shown by Williams et al. [66] that  $\text{SrCrO}_4$  could effectively

inhibit the cathodic delamination of HDG, as  $\text{CrO}_4^{2-}$  could diffuse beneath the organic coating and compete with the oxygen reduction reaction, ultimately forming an insoluble  $\text{Cr}(\text{OH})_3$  precipitate (Equation 1.23), which blocked further oxygen reduction [66,68,69].



Regarding the cut-edge corrosion and subsequent anodic undermining of Zn55Al, Chiba et al. outlined the protection mechanism afforded by chromates contained in primer coatings. When the cut-edge of organically coated Zn55Al products are exposed to atmospheric electrolyte,  $\text{CrO}_4^{2-}$  can leach out and migrate to the exposed cut-edge. There, it slows the kinetics of oxygen reduction occurring directly on the exposed steel as outlined in Equation 1.23, ultimately decreasing the dissolution rate of the Zn55Al coating that is required for sacrificial protection. Zin et al. conducted a separate study that found an additional benefit of  $\text{CrO}_4^{2-}$ : it can directly inhibit the anodic dissolution of the sacrificial coating, thus passivating the entire cut-edge [70-72].

Despite the high effectiveness of hexavalent chromium in corrosion inhibition, its application has been significantly curtailed by REACH regulations due to its toxicological profile. Acute and chronic health issues, including skin ulcers, laryngeal inflammation, nasal septum perforation, and damage to the kidneys and lungs, have been linked to exposure. Moreover, compounds containing hexavalent chromium are recognized carcinogens with the potential to damage DNA [73,74].

### 1.3.5.2 Phosphate

Phosphates are another widely used type of inhibitor pigment used with the organic coating industry, with species such as zinc phosphate ( $\text{Zn}_3(\text{PO}_4)_2$ ), aluminium phosphate ( $\text{AlPO}_4$ ) and strontium phosphate ( $\text{Sr}_3(\text{PO}_4)_2$ ) commonly employed. These compounds release phosphate ions that serve as anodic inhibitors for Zn-alloy coatings by forming an insoluble precipitate with zinc ions (Reaction 1.24) that act as a barrier to further corrosion.



To date, phosphate-containing pigments have not been able to match the efficacy of chromate-containing pigments in preventing corrosion-induced organic coating failures [75,76]. For example, in accelerated cathodic delamination experiments over 24h, it was found that model coatings containing  $\text{SrCrO}_4$  completely prevented delamination. In contrast, model coatings containing an equal pigment loading of zinc phosphate  $\text{Zn}_3(\text{PO}_4)_2$  managed to reduce delamination rates by only 66% [66]. Unlike chromates, phosphates do not suppress rates by competing with oxygen at cathodic sites; rather, they can only migrate to the defect to provide anodic inhibition. Given the low solubility of phosphates, not enough of active inhibitor can migrate to the defect site to fully suppress the anodic reaction. As a result, the anodic reaction can continue, allowing cathodic delamination to continue progression.

### 1.3.5.3 Ion-Exchange Pigments and Hydrotalcite

In an effort to improve the delivery of active inhibitor species to corroding sites, organic coating systems containing "smart-release" pigments are receiving greater attention. Of particular prominence are ion-exchange pigments, which are inorganic clay materials that electrostatically hold corrosion inhibiting anions and cations within their structure [77]. Upon contact with electrolyte, ion-exchangers sequester ions such as  $\text{Na}^+$ ,  $\text{OH}^-$  and  $\text{Cl}^-$  through an exchanged of their contained inhibitor. This gives them a distinct advantage over sparingly soluble salts in that their contained inhibitor ions are released only upon interaction with a corrosive electrolyte, resulting in more controlled inhibitor depletion.

The ion exchanger used in this work is hydrotalcite (HT), which has the general formula  $\text{Mg}_6\text{Al}_2\text{CO}_3(\text{OH})_{16} \cdot 4(\text{H}_2\text{O})$ . Its structure consists of positively charged layers containing aluminium and magnesium that are balanced electrostatically by weakly bonded anions, usually carbonate ( $\text{CO}_3^{2-}$ ) [78,79]. HT's advantage is its "memory effect", which allows anionic inhibitor species to be intercalated into its layered structure. As shown schematically in Figure 1.17, when HT is calcined at 450 °C, it loses its contained carbonates as

carbon dioxide and water leading to the disruption of the HT structure. However, when this calcined HT is introduced to a deaerated solution containing aqueous inhibitor anions, it "remembers" its layered structure and reincorporates the inhibitor anions. When the HT-Inhibitor species is used within a coating system, it can sequester electrolyte ions and release its contained inhibitor into solution and migrate to sites of corrosion [79-82].

The effectiveness of HT pigments against cathodic delamination and anodic undermining in coating systems have been previously studied. For instance, Ansell et al. [83] investigated how HT, intercalated with various inorganic and organic inhibitors, inhibited the cathodic delamination of model PVB coatings. It was found that benzotriazole (BTA) was the most effective organic inhibitor, rivalling the best inorganic inhibitor, chromate at equivalent pigment loadings. The inhibition mechanism of HT-BTA involved sequestering  $\text{Cl}^-$  and  $\text{OH}^-$  from the underfilm electrolyte, with  $\text{BTA}^-$  then strongly adsorbing onto the under-film HDG surface and preventing further cathodic reduction of oxygen. Regarding anodic undermining, it has been shown that HT pigments exchanged with various organic and inorganic species can inhibit the FFC of AA2024 aluminium alloy surfaces. As-received HT was moderately effective, mainly by sequestering  $\text{Cl}^-$ . However, inhibition was enhanced when inhibitors were intercalated into HT [83-86].

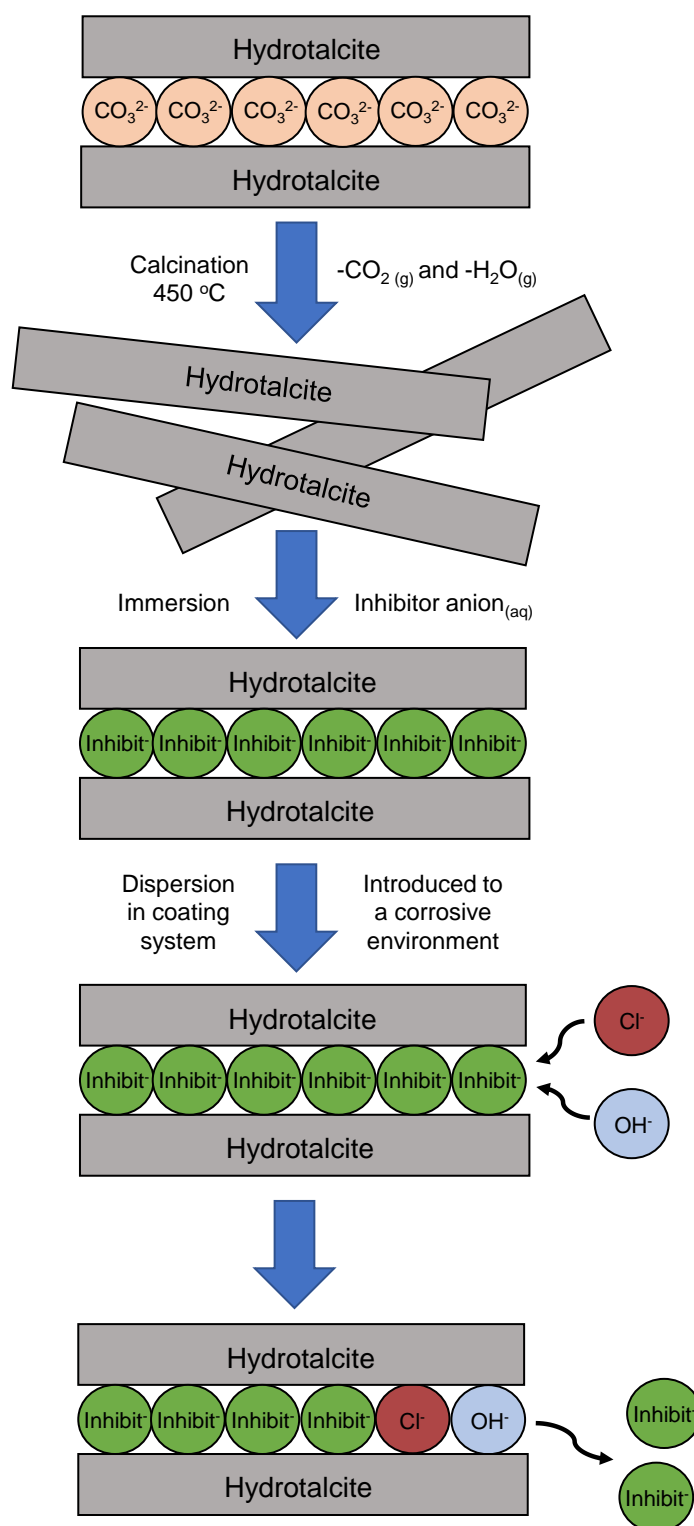


**Figure 1.17:** Schematic representation of hydrotalcite modification and inhibitory action.

#### 1.3.5.4 Corrosion Inhibition of ZnAl galvanised steel by Organic Azoles

For Zn-alloy galvanised steel, the main form of corrosion protection is the incorporation of corrosion inhibitors/pigments into organic coating systems. In addition to the chromate, phosphate, and ion-exchange type inhibitors described earlier in this section, many other alternative inhibitors have been assessed for their anti-corrosion performance.

One promising inhibitor type is the use of organic molecules containing azole groups, which have been identified as effective, non-toxic inhibitors for galvanised steel. Azoles are aromatic five-membered rings that include nitrogen along with at least one other heteroatom, such as oxygen or sulphur [87]. These heteroatoms are electron-rich, allowing the molecules to interact strongly with metal surfaces, forming a protective barrier that mitigates corrosion, even in chloride-rich environments [88]. For instance, benzotriazole (BTA) has been found to interact with HDG, leading to the formation of polymeric  $[\text{Zn}(\text{BTA})_2]_n$  complexes, which slow down the corrosion process [89-92]. In addition, 2-amino-4-methylthiazole (2AT-Me) was reported to lower anodic and cathodic reaction currents of HDG subjected to immersion in 100 mM NaCl environment [88], while 2-mercaptobenzothiazole (MBT) and 5-amino-1,3,4-thiadiazole-2-thiol (ATT) have also been found to reduce corrosion rates in 50 mM NaCl solution over several days [93]. Both studies suggested that the electron-rich heteroatoms of the azole ring acted as areas of adsorption to the HDG surface [93-94].



## 1.4 Electrochemical Techniques

The following sections will detail the electrochemical techniques that underpin this work, namely the Scanning Vibrating Electrode Technique (SVET) for assessment of localised corrosion, and the Scanning Kelvin Probe (SKP) for assessment of organic coating failure.

### 1.4.1 Scanning Vibrating Electrode Technique (SVET)

SVET is a non-destructive method that allows for the spatial resolution and mapping of localised corrosion on metallic surfaces submerged in corrosive electrolytes [95-97]. It operates by measuring the potential gradients in electrolyte that originate from ionic current flow between distinct sites of anodic and cathodic activity. These gradients can be represented in terms of iso-electric lines that lie normal to current flux lines, as illustrated in Figure 1.18. A key benefit of the SVET is its ability to monitor corrosion over time without perturbing the metal surface. As such, the SVET offers a means to time-dependently observe localised corrosion events occurring on a metal at its open circuit potential (OCP).

For a corroding surface, the Laplace equation can be used to calculate the distribution of potential and ionic current Equation (1.25):

$$\nabla^2 E = 0 \quad (1.25)$$

where  $\nabla^2$  is the Laplace operator, and  $E$  is the electrical potential, as seen in Ohm's Law (Equation 1.26):

$$i = -\kappa \nabla E \quad (1.26)$$

where  $i$  is the current and  $\kappa$  is the solution conductance. Solutions to this equation are non-trivial with no analytical solution possible. However, solutions can be obtained when

considering the simplest case of a point current source.

The SVET technique makes use of a scanning micro-tip electrode which is vibrated mechanically at a constant amplitude and frequency above the sample. An alternating potential is therefore detected when scanning above a sample which is corroding. The potential in the direction of vibration is proportional to the electric field strength ( $F$ ) or potential gradients ( $dE/dZ$ ) that occur as a result of ionic currents. As such, the SVET signal can be related to the ionic current in the electrolyte lying in the direction of the probe, and therefore normal to the sample surface. The microtip resides at a set distance above the surface and thus the signal measured is not proportional to the surface current density but the vector component of the current density in the electrolyte at the height of the probe. The numerical manipulation of SVET signals to values of current density are described in more detail in the calibration procedure of Section 2.2.1.

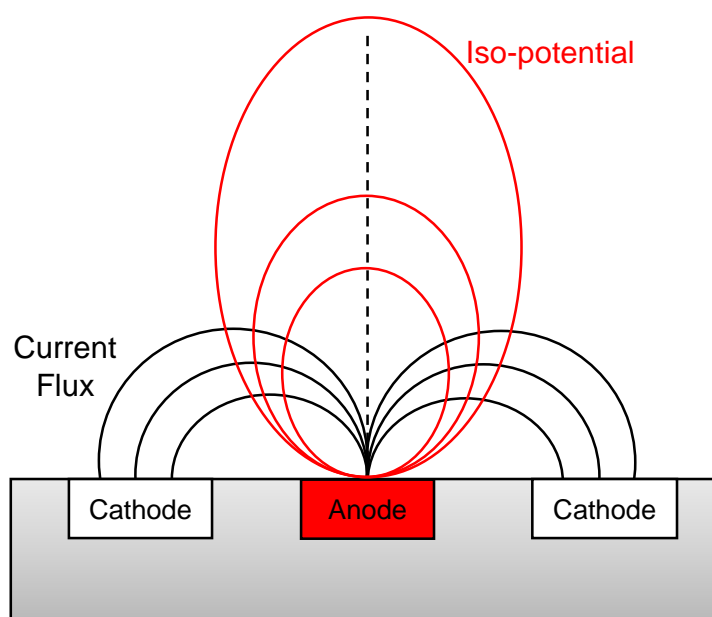


**Figure 1.18:** *The current flux and iso-potential lines that occur from local corrosion cells. The black lines indicate current flux, and the red lines are the resulting iso-potential lines.*

The SVET has been used extensively to understand the localised corrosion behaviour of various metallic surfaces. For instance, Williams et al. [98] observed that blackened areas of corrosion on unpolarised magnesium in sodium chloride electrolyte featured a cathod-

ically active centre encircled by a ring of anodic activity. It was found that emanating anodic current density was directly proportional to the radius of the local cathode. In the case of ZnAl galvanised steels, Worsley et al. [4] explored how the varying aluminium content of HDG, Galfan, and Zn55Al influenced the localisation and intensity of corrosion on their surfaces when immersed in 0.1% w/v sodium chloride solution. By calibrating and integrating the outputted SVET data, the total anodic current emanating from the surface for the 24h tests was determined and converted to total metal loss using Faraday's Law. The findings indicated that galvanised steels with higher aluminium content are more resistant to chloride electrolyte as they showed less zinc loss over the total immersion time (i.e. Zn55Al < Galfan < HDG).

The SVET has also been used to measure the performance of corrosion inhibitors at preventing localised corrosion on zinc and ZnAl surfaces. For instance, Wint et al. [99] showed that the localised corrosion of unpolarised zinc immersed in 1% w/v sodium chloride solutions of varying pH can be mitigated by an addition of 10 mM L-tryptophan into the test solution. At pH 2, the addition resulted in an 88% decrease in zinc mass loss, as measured by gravimetric mass loss and SVET, while efficiencies of 80% and 64% were observed at pH 11 and pH 7, respectively. Furthermore, SVET was employed by Glover et al. [100] to observe the inhibition effect of phenylphosphonic acid (H<sub>2</sub>PP) on HDG immersed in a 5% w/v sodium chloride solution. It was found that H<sub>2</sub>PP, at a concentration of 50 mM almost completely inhibited the localised corrosion of HDG steel, achieving a 96% efficiency over the 24 h immersion period.

### 1.4.2 Scanning Kelvin Probe (SKP)

Although the Scanning Kelvin Probe (SKP) was first developed as a method of measuring the work function of surfaces [101-102], it has become of significant use in for corrosion research as it provides an in-situ method of investigating corrosion-driven organic coating failures on from metal substrates. It is an electrochemical, non-perturbing technique that determines the potential of bare metals covered in electrolyte films or metals underneath organic coatings, indicating underfilm corrosion phenomena [103].

Figure 1.19 shows a picture of the SKP apparatus (Figure 1.19a) alongside a schematic representation (Figure 1.19b). It comprises a gold reference probe that vibrates near the metal surface under investigation. The two metals are connected through an external circuit, and both are enclosed within a Faraday cage to control temperature and humidity. The gold reference probe and the metal under investigation form one-half each of a parallel plate capacitor. When electrically connected, electrons flow from the capacitor with a higher work function, as dictated by its fermi level, to the metal with the lower work function. The capacitance,  $C$ , is given by Equation 1.27:

$$C = \frac{\epsilon\epsilon_0 A}{d} \quad (1.27)$$

where  $\epsilon$  is the capacitor dielectric medium (air or polymer/air),  $\epsilon_0$  is the permittivity of free space,  $A$  is the area of the plate capacitor and  $d$  is the distance between the two plates. The gold reference probe is vibrated sinusoidally at a specific frequency. Thus, the fluctuating distance to the sample surface is given by Equation 1.28:

$$d = d_0 + d_1 \sin(\omega t) \quad (1.28)$$

where  $d_0$  is the mean separation of both plates,  $d_1$  is the maximum amplitude of vibration,  $\omega$  is the vibration frequency, and  $t$  is the time. The Volta potential difference that develops between the vibrating reference probe and the sample  $\Delta\Psi_{\text{sample}}^{\text{ref}}$  produces an alternating current, ( $i_{\text{ac}}$ ) (Equation 1.29:

$$i_{ac} = \Delta \Psi_{sample}^{ref} \frac{dC}{dt} \quad (1.29)$$

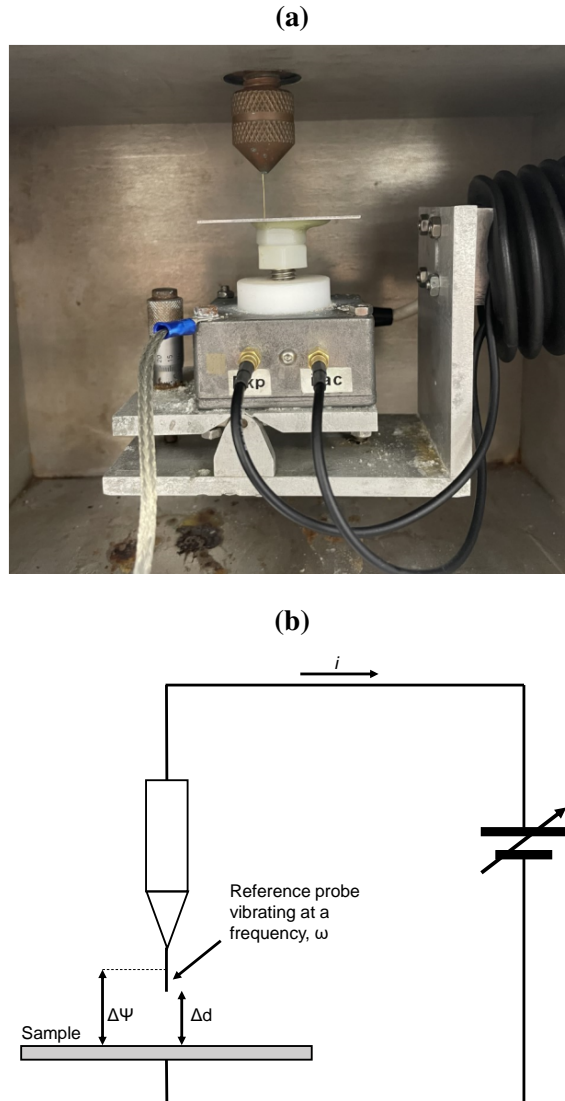


**Figure 1.19:** a) A photograph of the SKP apparatus, and b) A schematic representation of the SKP.

Substitution of Equations 1.27, 1.28 and 1.29 yield Equation 1.30:

$$i_{ac} = \varepsilon \varepsilon_0 A \cdot \Delta \Psi_{sample}^{ref} \frac{d_1 \omega \cos(\omega t)}{d_0^2} \quad (1.30)$$

From which  $\Delta\Psi_{\text{sample}}^{\text{ref}}$  can be calculated. However, this calculation is more complex due to the number of variables. Instead, the current is amplified and detected by a lock-in amplifier, but is decreased to zero by applying a direct current nulling voltage,  $E$ . Therefore:

$$E_{i=0} = -\Delta\Psi \quad (1.31)$$

which is often termed the Kelvin probe potential,  $E_{\text{KP}}$ :

$$-E = E_{\text{KP}} = \Delta\Psi \quad (1.32)$$

Several contributing potential differences will affect the measured value of  $E_{\text{KP}}$ . Considering a metal substrate, it may develop a surface oxide and or form an electrolyte layer. Fortunately, these will remain constant under constant temperature, humidity, and gas composition. As such, if the adsorbed electrolyte is thicker than the electrical double layer and ionic flow is absent [45,66], then  $E_{\text{KP}}$  can be related to the free corrosion potential,  $E_{\text{corr}}$  of the metal by Equation 1.33:

$$E_{\text{KP}} = E_{\text{corr}} + \text{constant} \quad (1.33)$$

For a bare metal surface covered by an electrolyte solution, the half-cell potential,  $E_{1/2}$  of the metal-solution interface is given by Equation 1.34 :

$$E_{1/2} = \frac{W_{\text{ref}}}{F} - \chi_{\text{gas}}^{\text{sol}} + \Delta\psi_{\text{sol}}^{\text{ref}} \quad (1.34)$$

where  $W_{\text{ref}}$  is the work function of the reference material,  $F$  is Faraday's constant,  $\chi_{\text{gas}}^{\text{sol}}$  is the dipole potential of the solution/gas interface, and  $\Delta\psi_{\text{sol}}^{\text{ref}}$  is the measured Volta potential difference between the solution surface and the reference probe. An identical relationship can be applied for the polymer coated metal surfaces by Equation 1.35:

$$E_{1/2} = \frac{W_{\text{ref}}}{F} - \chi_{\text{gas}}^{\text{pol}} + \Delta\psi_{\text{pol}}^{\text{ref}} \quad (1.35)$$

where  $\chi_{\text{gas}}^{\text{pol}}$  is the dipole potential of the polymer-gas interface and  $\Delta\psi_{\text{pol}}^{\text{ref}}$  is the Volta potential difference between the polymer surface and the reference probe. In the scenario of cathodic delamination, when electrolyte ingresses underneath the polymer coating and accesses the metal surface, Equation 1.35 can be written as Equation 1.36:

$$E_{1/2} = \Delta\varphi_D + \frac{W_{\text{Ref}}}{F} - \chi_{\text{gas}}^{\text{pol}} + \Delta\psi_{\text{pol}}^{\text{ref}} \quad (1.36)$$

where  $\Delta\varphi_D$  is the Donnan potential and is equal to the Galvani potential between the ingressing electrolyte and the polymer coating. Considering the SKP chamber keeps the temperature, humidity, and uniform gas composition constant,  $W_{\text{ref}}$  and  $\chi_{\text{gas}}^{\text{pol}}$  will remain constant. For polymers exhibiting a fixed charge in contact with a 1:1 electrolyte,  $\Delta\varphi_D$  can be expressed by Equation 1.37:

$$\Delta\varphi_D = \frac{RT}{F} \ln \left( \frac{x}{2} + \sqrt{1 + \left(\frac{x}{2}\right)^2} \right) \quad (1.37)$$

where  $R$  is the universal gas constant,  $T$  is the temperature in units of Kelvin, and  $x$  is the ratio of membrane fixed charge density to the electrolyte concentration. In this work, the polymer selected for studies of inhibitor pigments with organic coatings was polyvinyl butyral-co-vinyl alcohol-co-vinyl acetate, PVB, because it does not possess functional groups that are susceptible to hydrolysis and therefore does not develop significant charge current densities. Using PVB alongside a high concentration of electrolyte (5% w/v  $\text{NaCl}_{(\text{aq})}$ ),  $x \ll 1$ ; hence  $\Delta\varphi_D$  is approximately zero. As such, the  $E_{\text{corr}}$  for a metal covered in electrolyte and a polymer-coated metal can be expressed by Equations 1.38 and 1.39, respectively:

$$E_{\text{corr}} = A + \Delta\psi_{\text{sol}}^{\text{ref}} \quad (1.38)$$

$$E_{\text{corr}} = B + \Delta\psi_{\text{pol}}^{\text{ref}} \quad (1.39)$$

where  $A$  and  $B$  are constants that are determined by measuring  $E_{\text{corr}}$  and  $\Delta\psi_{\text{sol}}^{\text{ref}}$  or  $\Delta\psi_{\text{pol}}^{\text{ref}}$ ,

respectively using the SKP. This procedure is described in further detail by Williams et al [66] and in Chapter 2.



## 1.5 References

1. World Steel in Figures 2022 - worldsteel.org. <https://worldsteel.org/steel-topics/statistics/world-steel-in-figures-2022/> (accessed March 28, 2023).
2. Steel: characteristics, properties and uses - Ulma Forged Solutions. <https://www.ulmaforge.com/en/characteristics-properties-and-uses/> (accessed January 7, 2024).
3. Assessment of the global cost of corrosion. <http://impact.nace.org/economic-impact.aspx> (accessed March 28, 2023).
4. D.A. Worsley, H.N. McMurray, J.H. Sullivan, I.P. Williams, Quantitative Assessment of Localized Corrosion Occurring on Galvanized Steel Samples Using the Scanning Vibrating Electrode Technique, *Corrosion*. 60 (2004) 437–447.
5. P.J. Denissen, A.M. Homborg, S.J. Garcia, Requirements for corrosion inhibitor release from damaged primers for stable protection: A simulation and experimental approach using cerium loaded carriers, *Surf. Coat. Technol.* 430 (2022) 127966.
6. A. Sheffett, I. Thind, A.M. Miller, D.B. Louria, Cancer mortality in a pigment plant utilizing lead and zinc chromates, *Arch. Environ. Health*. 37 (1982) 44–52.
7. Substances restricted under REACH - ECHA. <https://echa.europa.eu/substances-restricted-under-reach> (accessed March 28, 2023).
8. J.M. Davies, Lung cancer mortality among workers making lead chromate and zinc chromate pigments at three English factories, *Br. J. Ind. Med.* 41 (1984) 158–169.
9. H. Gibb, C. Chen, Evaluation of issues relating to the carcinogen risk assessment of chromium, *Science of the Total Environment*, The 86 (1989) 181–186.
10. S.A. Katz, H. Salem, The toxicology of chromium with respect to its chemical speciation: a review, *J. Appl. Toxicol.* 13 (1993) 217–224.
11. A. Babich, D. Senk, Coke in the iron and steel industry, *New Trends in Coal Conversion: Combustion, Gasification, Emissions, and Coking* (2019) 367–404.

12. A. Boulabiar, K. Bouraoui, M. Chastrette, M. Abderrabba, A historical analysis of the Daniell cell and electrochemistry teaching in French and Tunisian textbooks, *J. Chem. Educ.* 81 (2004) 754–757.
13. G.F. Martins, Why the Daniell cell works, *J. Chem. Educ.* 67 (1990) 482–482.
14. X. Dong, Y. Wang, Y. Xia, Re-building Daniell Cell with a Li-ion exchange Film, *Scientific Reports*. 4 (2014) 1–6.
15. E.E. Stansbury, R.A. Buchanan, R.M. Condra, *Fundamentals of Electrochemical Corrosion*. (2000).
16. A.C. Fisher, *Electrode Dynamics*, Oxford University Press, 2009.
17. L.C. Bannister, U.B. Evans, CLXXVII.—The passivity of metals. Part V. The potential–time curves of some iron alloys, *Journal of the Chemical Society (Resumed)* (1930) 1361–1374.
18. Y.-C. Chang, R. Woollam, M.E. Orazem, Mathematical Models for Under-Deposit Corrosion, *J. Electrochem. Soc.* 161 (2014) C321–C329.
19. D.J. Blackwood, A. Sainz-Rosales, X. Ocampo-Lazcarro, A. Hernández-Pérez, A. Gabriela González-Gutiérrez, E.R. Larios-Durán, C. Ponce De León, F.C. Walsh, M. Bárcena-Soto, N. Casillas, Classic Evans Drop Corrosion Experiment Investigated in Terms of a Tertiary Current and Potential Distribution, *Corrosion and Materials Degradation*. 3, (2022) 270–280.
20. A.R. Marder, The metallurgy of zinc-coated steel, *Prog. Mater. Sci.* 45 (2000) 191–271.
21. J.L. Murray, The Al-Zn (Aluminum-Zinc) system, *Bulletin of Alloy Phase Diagrams* 4 (1983) 55–73.
22. S. Feliu, V. Barranco, XPS study of the surface chemistry of conventional hot-dip galvanised pure Zn, galvanneal and Zn–Al alloy coatings on steel, *Acta. Mater.* 51 (2003) 5413–5424.

23. G. Vourlias, N. Pistofidis, G. Stergioudis, E. Pavlidou, D. Tsipas, Influence of alloying elements on the structure and corrosion resistance of galvanized coatings, *Physica. Status. Solidi. A. Appl. Res.* 201 (2004) 1518–1527.
24. J. Elvins, J.A. Spittle, D.A. Worsley, Microstructural changes in zinc aluminium alloy galvanising as a function of processing parameters and their influence on corrosion, *Corros. Sci.* 47 (2005) 2740–2759.
25. T. Kato, K. Nunome, K. Kaneko, H. Saka, Formation of the  $\delta$  phase at an interface between an Fe substrate and a molten 0.2 mass
26. D. Persson, D. Thierry, O. Karlsson, Corrosion and corrosion products of hot dipped galvanized steel during long term atmospheric exposure at different sites worldwide, *Corros. Sci.* 126 (2017) 152–165.
27. Zoccola JC, Townsend HE, Borzillo AR, Atmospheric factors affecting the corrosion of engineering metals, STP 646. Philadelphia: American Society for Testing and Materials (1978) 165–184.
28. Uchima Y, Hasaka M, Koga H. GALVATECH '89, Tokyo. The Iron and Steel Institute of Japan; (1989) 545.
29. X. Zhang, C. Leygraf, I. Odnevall Wallinder, Atmospheric corrosion of Galfan coatings on steel in chloride-rich environments, *Corros. Sci.* 73 (2013) 62–71.
30. D. Thierry, D. Persson, A. Le Gac, N. LeBozec, A. Peltola, P. Väisänen, Long-term atmospheric corrosion of Zn–5%Al-coated steel and HDG during outdoor worldwide exposures, *Corrosion Engineering, Science and Technology.* 55 (2020) 520–530.
31. E. Palma, J.M. Puente, M. Morcillo, The atmospheric corrosion mechanism of 55%Al-Zn coating on steel, *Corros Sci.* 40 (1998) 61–68.
32. H. Townsend, T.C. Consultants, Thirty year atmospheric corrosion performance of 55% aluminum-zinc alloy- coated sheet steel. (2015).

33. J.H. Selverian, M.R. Notis, A.R. Marder, The microstructure of 55 w/o Al-Zn-Si (Galvalume) hot dip coatings, *Journal of Materials Engineering*. 9 (1987) 133–140.
34. X. Zhang, T.N. Vu, P. Volovitch, C. Leygraf, K. Ogle, I.O. Wallinder, The initial release of zinc and aluminum from non-treated Galvalume and the formation of corrosion products in chloride containing media, *Appl. Surf. Sci.* 258 (2012) 4351–4359.
35. D. Persson, D. Thierry, N. LeBozec, Corrosion product formation on Zn55Al coated steel upon exposure in a marine atmosphere, *Corros. Sci.* 53 (2011) 720–726.
36. A.R. Moreira, Z. Panossian, P.L. Camargo, M.F. Moreira, I.C. Da Silva, J.E. Ribeiro De Carvalho, Zn/55Al coating microstructure and corrosion mechanism, *Corros. Sci.* 48 (2006) 564–576.
37. K.G. Watkins, R.D. Jones, P.G. Beahan, Electrochemical investigation of the corrosion rate of 55 aluminium-zinc alloy coated steel, *Mater. Lett.* 8 (1989) 26–30.
38. T. Guo, C. Liu, C. Ran, X. Dong, Effects of spangle size on performances of hot-dip 55%Al-Zn alloy coating, *Int. J. Electrochem. Sci.* 13 (2018) 9505–9519.
39. European Steel in Figures 2022, <https://www.eurofer.eu/publications/brochures-booklets-and-factsheets/european-steel-in-figures-2022/> (accessed April 5, 2023).
40. B. Popov, Corrosion Inhibitors, in: B. Popov (Ed.), *Corrosion Engineering*, 581–597.
41. C.M. Griffiths, N. Wint, G. Williams, H.N. McMurray, The contribution of Zn(II) and phosphate anions to the inhibition of organic coating cathodic disbondment on galvanised steel by zinc phosphate pigment, *Corros. Sci.* 198 (2022) 110111.
42. W. Fürbeth, M. Stratmann, Delamination of polymeric coatings from electrogalvanized steel - a mechanistic approach. Part 2: Delamination from a defect down to steel, *Corros. Sci.* 43 (2001) 229.

43. P. Ansell, L. Berry, J. McGettrick, J. Searle, N. Wint, H.N. McMurray, G. Williams, Role of Smart-Release Pigments in Preventing Corrosion Driven Cathodic Disbondment of Organically Coated Hot Dip Galvanised Steel, *J. Electrochem. Soc.* 170 (2023) 011502.
44. S.J. Caraguay, T.S. Pereira, R.O. Giacomelli, A. Cunha, M. Pereira, F.A. Xavier, The effect of laser surface textures on the corrosion resistance of epoxy coated steel exposed to aggressive environments for offshore applications, *Surf. Coatings Technol.* 437 (2022) 128371.
45. A. Leng, H. Streckel, M. Stratmann, The delamination of polymeric coatings from steel. Part 1: Calibration of the Kelvinprobe and basic delamination mechanism, *Corros. Sci.* 41 (1998) 547.
46. E.L. Koehler, The Oxide Film on Steel and Cathodic Disbondment of a Protective Organic Coating, *J. Electrochem. Soc.* 40 (1984) 1982.
47. A. Leng, H. Streckel, M. Stratmann, The delamination of polymeric coatings from steel. Part 2: First stage of delamination, effect of type and concentration of cations on delamination, chemical analysis of the interface, *Corros. Sci.* 41 (1998) 579.
48. A. Leng, H. Streckel, K. Hofmann, M. Stratmann, The delamination of polymeric coatings from steel Part 3: Effect of the oxygen partial pressure on the delamination reaction and current distribution at the metal/polymer interface, *Corros. Sci.* 41 (1998) 599.
49. N.W. Khun, G.S. Frankel, Effects of surface roughness, texture and polymer degradation on cathodic delamination of epoxy coated steel samples, *Corros. Sci.* 67 (2013) 152.
50. H. Leidheiser, W. Wang, L. Igetoft, The mechanism for the cathodic delamination of organic coatings from a metal surface, *Prog. Org. Coat.* 11 (1983) 19.
51. M. Stratmann, R. Feser, A. Leng, Corrosion protection by organic films, *Electrochim. Acta.* 39 (1994) 1207.

52. E.L. Koehler, The Oxide Film on Steel and Cathodic Disbondment of a Protective Organic Coating, *J. Electrochem. Soc.* 132 (1985) 1005–1009.
53. H.N. McMurray, G. Williams, Under Film/Coating Corrosion, *Shreir's Corrosion* (2010) 988–1004.
54. W. Fürbeth, M. Stratmann, The delamination of polymeric coatings from electro-galvanised steel – a mechanistic approach.: Part 1: delamination from a defect with intact zinc layer, *Corros. Sci.* 43 (2001) 207–227.
55. E.L. Koehler, The Influence of Contaminants on the Failure of Protective Organic Coatings on Steel, *Corrosion*. 33 (1977) 209–217.
56. F.M. Fowkes, M.A. Mostafa, Acid-Base Interactions in Polymer Adsorption, *Industrial and Engineering Chemistry Product Research and Development*. 17 (1978) 3–7.
57. U.R. Evans, *The Corrosion and Oxidation of Metals*, 1960.
58. T.P. Hoar, Double layer and electrode kinetics, *Electrochim. Acta*. 11 (1966) 945.
59. J.S. Hammond, J.W. Holubka, J.E. deVries, R.A. Dickie, The application of x-ray photo-electron spectroscopy to a study of interfacial composition in corrosion-induced paint de-adhesion, *Corros. Sci.* 21 (1981) 239–253.
60. O.Ø. Knudsen, A. Forsgren, Degradation of Paint by Corrosion, *Corrosion Control Through Organic Coatings* (2017) 163–182.
61. R.A. Dickie, Paint adhesion, corrosion protection, and interfacial chemistry, *Prog. Org. Coat.* 25 (1994) 3–22.
62. C.F. Sharman, Filiform Underfilm Corrosion of Lacquered Steel Surfaces, *Nature*. 153, 3890 (1944) 621–622.
63. R.T. Ruggeri, T.R. Beck, An Analysis of Mass Transfer in Filiform Corrosion, *Corrosion*. 39 (1983) 452–465.

64. A. Bautista, Filiform corrosion in polymer-coated metals, *Prog. Org. Coat.* 28 (1996) 49–58.
65. E. Mattsson, *Basic Corrosion Concepts*, Horwood, 1996. <https://www.routledge.com/Basic-Corrosion-Technology-for-Scientists-and-Engineers/Mattsson/p/book/9781861251381> (accessed June 23, 2023).
66. G. Williams, H.N. McMurray, Chromate Inhibition of Corrosion-Driven Organic Coating Delamination Studied Using a Scanning Kelvin Probe Technique, *J. Electrochem. Soc.* 148 (2001) B377.
67. .M. Powell, H.N. McMurray, D.A. Worsley, Use of the Scanning Reference Electrode Technique for the Evaluation of Environmentally Friendly, Nonchromate Corrosion Inhibitors, *Corrosion.* 55 (1999) 1040–1051.
68. Y.I. Kuznetsov, I.L. Rozenfeld, T.A. Agalarova, Protection of steel in sea water by chromate inhibitors in conjunction with cathodic polarization, *Protection of Metals.* 18 (1982) 438–441.
69. J. Zhao, G. Frankel, R.L. McCreery, Corrosion Protection of Untreated AA-2024-T3 in Chloride Solution by a Chromate Conversion Coating Monitored with Raman Spectroscopy, *J. Electrochem. Soc.* 145 (1998) 2258–2264.
70. A. Chiba, I. Muto, N. Hara, Cut Edge Corrosion Inhibition by Chromate in Primer of Prepainted 55% Al-Zn Alloy Coated Steel, *J. Electrochem. Soc.* 158 (2011) C42–C47.
71. I.M. Zin, V.I. Pokhmurskii, J.D. Scantlebury, S.B. Lyon, Model electrochemical cell study of cut-edge corrosion inhibition on coil-coated steel sheet by chromate, phosphate, and calcium-containing pigments, *J. Electrochem. Soc.* 148 (2001) B293–B298.
72. I.M. Zin, Efficiency of certain chromate-free pigments for the corrosion protection of galvanized steel, *Materials Science.* 36 (2000) 450–453.

73. S.A. Katz, The analytical biochemistry of chromium, *Environ. Health. Perspect.* 92 (1991) 13–16.
74. Z.J. Fang, M. Zhao, H. Zhen, L.F. Chen, P. Shi, Z.W. Huang, Genotoxicity of Tri- and Hexavalent Chromium Compounds In Vivo and Their Modes of Action on DNA Damage In Vitro. 9 (2014).
75. P. Puomi, H.M. Fagerholm, A. Sopanen, Parameters affecting long-term performance of painted galvanised steels, *Anti-Corrosion Methods and Materials.* 48 (2001) 160–170.
76. P. Puomi, H.M. Fagerholm, J.B. Rosenholm, K. Jyrkäs, Comparison of different commercial pretreatment methods for hot-dip galvanized and Galfan coated steel, *Surf. Coat. Technol.* 115 (1999) 70–78.
77. M.F. Montemor, Functional and smart coatings for corrosion protection: A review of recent advances, *Surf. Coat. Technol.* 258 (2014) 17–37.
78. S.J. Mills, A.G. Christy, J.-M.R. Génin, T. Kameda, F. Colombo, Nomenclature of the hydrotalcite supergroup: natural layered double hydroxides, *Mineral Mag* 76 (2012) 1289–1336.
79. S. Miyata, Anion-exchange properties of hydrotalcite-like compounds, *Clay. Miner.* 31 (1983) 305–311.
80. F. Kovanda, E. Kováčsová, D. Koloušek, Removal of Anions from Solution by Calcined Hydrotalcite and Regeneration of Used Sorbent in Repeated Calcination-Rehydration-Anion Exchange Processes, *Chem. Commun.* 64 (1999) 1517–1528.
81. D.G. Evans, X. Duan, Preparation of layered double hydroxides and their applications as additives in polymers, as precursors to magnetic materials and in biology and medicine, *Chemical Communications.* (2006) 485–496.
82. F. Cavani, F. Trifirò, A. Vaccari, Hydrotalcite-type anionic clays: Preparation, properties and applications, *Catal. Today.* 11 (1991) 173–301.



83. P. Ansell, L. Berry, J. McGettrick, J. Searle, N. Wint, H.N. McMurray, G. Williams, Role of Smart-Release Pigments in Preventing Corrosion Driven Cathodic Disbondment of Organically Coated Hot Dip Galvanised Steel, *J. Electrochem. Soc.* 170 (2023) 11502.
84. G. Williams, H.N. McMurray, Inhibition of filiform corrosion on organic-coated AA2024-T3 by smart-release cation and anion-exchange pigments, *Electrochim. Acta.* 69 (2012) 287.
85. G. Williams, H.N. McMurray, Inhibition of filiform corrosion on polymer coated AA2024-T3 by hydrotalcite-like pigments incorporating organic anions, *Electrochem. Solid-State. Lett.* 7 (2004) B13.
86. G. Williams, H.N. McMurray, Anion-exchange inhibition of filiform corrosion on organic coated AA2024-T3 aluminum alloy by hydrotalcite-like pigments, *Electrochem. Solid-State Lett.* 6 (2003) B9.
87. T. Eicher, S. Hauptmann, A. Speicher, *The Chemistry of Heterocycles.* (2003).
88. Q. Deng, S. Jeschke, B.J. Murdoch, S. Hirth, P. Eiden, J.N. Gorges, P. Keil, X.B. Chen, I. Cole, In-depth insights of inhibitory behaviour of 2-amino-4-methylthiazole towards galvanised steel in neutral NaCl solution, *Corros. Sci.* 199 (2022) 110206.
89. K. Aramaki, Effects of organic inhibitors on corrosion of zinc in an aerated 0.5 M NaCl solution, *Corros. Sci.* 43 (2001) 1985–2000.
90. T. Kosec, D.K. Merl, I. Milosev, Impedance and XPS study of benzotriazole films formed on copper, copper–zinc alloys and zinc in chloride solution, *Corros. Sci.* 50 (2008) 1987–1997.
91. A.M. Fenelon, C.B. Breslin, An electrochemical study of the formation of benzotriazole surface films on copper, zinc and a copper-zinc alloy, *J. Appl. Electrochem.* 31 (2001) 509–516.
92. V. Sirtori, F. Zambon, L. Lombardi, XPS and ellipsometric characterization of zincBTA complex, *J. Electron. Mater.* 29 (2000) 463–467.

93. I.A. Kartsonakis, S.G. Stanciu, A.A. Matei, R. Hristu, A. Karantonis, C.A. Charitidis, A comparative study of corrosion inhibitors on hot-dip galvanized steel, *Corros. Sci.* 112 (2016) 289–307.
94. Q. Deng, S. Jeschke, M.R. Jakeria, P. White, S. Hirth, P. Eiden, J.N. Gorges, X.B. Chen, P. Keil, I. Cole, Synergistically and sustainably performed inhibitors for galvanized steel against aqueous corrosion, *Corros. Sci.* 213 (2023) 110984.
95. Y. Ishikawa, H.S. Isaacs, Electrochemical Behavior of Pits Developed on Aluminum in a Dilute Chloride Solution, *CORROSION ENGINEERING*. 33 (1984) 147–152.
96. H. Isaacs, Applications of current measurement over corroding metallic surfaces, *Prog. Clin. Biol. Res.* (1986).
97. H. S. Isaacs and Y. Ishikawa, Applications of the Vibration Probe to Localized Current Measurements, *Proc. NACE Corrosion*, 1985.
98. G. Williams, N. Birbilis, H.N. McMurray, The source of hydrogen evolved from a magnesium anode, *Electrochem. Commun.* 36 (2013) 1–5.
99. N. Wint, J.H. Sullivan, D.J. Penney, The Role of pH on the Inhibition of Aqueous Zinc Corrosion by L-tryptophan, *J. Electrochem. Soc.* 164 (2017) C356–C366.
100. C.F. Glover, G. Williams, Inhibition of Localized Corrosion of Hot Dip Galvanized Steel by Phenylphosphonic Acid, *J. Electrochem. Soc.* 164 (2017) C407–C417.
101. M. Stratmann, The investigation of the corrosion properties of metals, covered with adsorbed electrolyte layers—A new experimental technique, *Corros. Sci.* 27 (1987) 869–872.
102. M. Stratmann, H. Streckel, On the atmospheric corrosion of metals which are covered with thin electrolyte layers—I. Verification of the experimental technique, *Corros. Sci.* 30 (1990) 681–696.

103. W. Furbeth, M. Stratmann, Scanning Kelvin Probe investigations on the delamination of polymeric coatings from metallic surfaces, *Prog. Org. Coat.* 39 (2000) 23–29.

## **Chapter 2**

# **Experimental Methods**

## 2.1 Materials

### 2.1.1 ZnAl Galvanised Steel Substrates

The commercial metallic-coated steel substrates used throughout this work were supplied in sheets derived from roll-to-roll processes. Each substrate is a commercially available, hot-dip galvanised product consisting of 0.7 mm gauge mild steel metallurgically coated on both sides with a ZnAl coating. The suppliers and descriptions of all substrates are summarised in Table 2.1.

**Table 2.1:** *Suppliers and descriptions of the ZnAl coated galvanised steel substrates used in this work.*

| Sample ID     | Description   | Supplier                       |
|---------------|---|--------------------------------|
| <b>HDG</b>    | Commercial Product: “GI”<br>Process: Hot-dip galvanising<br>Coating Composition: 99.8 wt.% Zn, 0.2 wt.% Al<br>Coating Thickness: 20 $\mu\text{m}$                                 | Tata Steel, UK                 |
| <b>Galfan</b> | Commercial Product: “Galfan”<br>Process: Hot-dip galvanising<br>Coating Composition: 95.5 wt.% Zn, 4.5 wt.% Al<br>Coating Thickness: 18 $\mu\text{m}$                             | Tata Steel, UK                 |
| <b>Zn55Al</b> | Commercial Product: “Galvalume”, “Zincalume”<br>Process: Hot-dip galvanising<br>Coating Composition: 55 wt.% Al, 43.6 wt.% Zn, 1.4 wt.% Si<br>Coating Thickness: 16 $\mu\text{m}$ | Becker Industrial Coatings, UK |

### 2.1.2 Substrate Preparation

Sheets of HDG, Galfan and Zn55Al were cut into 50 x 50 mm coupons using a guillotine, degreased with acetone, and rinsed with deionised water. The coupons were polished

using an aqueous slurry of 5  $\mu\text{m}$  alumina powder to remove oxide layers and contaminants during manufacture. Residual alumina was washed off with deionised water and the metallic substrates were dried by a hair dryer after a wash in ethanol. When microstructural imaging was required, samples were mounted in conductive resin, polished to a 1  $\mu\text{m}$  finish and its microstructure revealed by a 2% Nital etch.

### 2.1.3 Chemicals and Consumables

**Table 2.2:** *The chemicals and consumables used in this work.*

| Chemical/Consumable ID                                       | Grade, Description                               | Supplier |
|--|--|----------|
| Sodium Chloride, NaCl  | $\geq 99\%$                                      | Merck    |
| Hydrochloric Acid, HCl                                       | $\geq 99\%$                                      | Merck    |
| Sodium Hydroxide, NaOH                                       | $\geq 99\%$                                      | Merck    |
| 2-(1,3-Benzothiazol-2-ylthio)<br>succinic acid, BTSA         | $\geq 99\%$                                      | Merck    |
| Poly(vinyl butyral-co-vinyl<br>alcohol-co-vinyl acetate, PVB | $\geq 99\%$                                      | Merck    |
| Hydrotalcite, HT   | $\geq 99\%$                                      | Merck    |
| 5 $\mu\text{m}$ Alumina Powder                               | $\geq 99\%$                                      | Buehler  |
| Acetone  | $\geq 99\%$                                      | Merck    |
| Ethanol  | $\geq 99\%$                                      | Merck    |
| Silicone Rubber  | White, Non-corrosive                             | RS       |
| Electrical Tape  | 30 $\mu\text{m}$ thickness, 19<br>mm wide, Black | RS       |
| Scotch Tape  | 19 mm wide                                       | RS       |
| PTFE Tape  | 25 mm wide,<br>waterproof                        | RS       |

## 2.2 Methods

### 2.2.1 Assessment of Localised Corrosion by The Scanning Vibrating Electrode Technique (SVET)

The SVET apparatus (made in situ at Swansea University) can measure, at an open circuit, the potential gradients in the solution above a corroding metallic sample, thereby indicating areas of anodic activity and regions of cathodic activity. The output from SVET experimentation are semi-quantitative, time-dependent maps of current density that show localised corrosion events. In this thesis, it is used in Chapter 3 to provide insights into the effects of aqueous chloride concentration on the localised corrosion of Zn55Al, and it was used in Chapter 4 to determine inhibitor efficiencies and provide mechanistic insights into the inhibition of HDG, Galfan and Zn55Al surfaces by BTSA.

A schematic representation of the SVET apparatus is shown in Figure 2.1 The SVET utilises a platinum wire microtip, 125  $\mu\text{m}$  in diameter, sealed in a borosilicate glass sheath. As determined by a micro manipulator stage in conjunction with a PC, the probe microtip scans over an electrolyte immersed sample in x and y directions, and at a constant height (100  $\mu\text{m}$  in this case). In order to take measurements along the scan area, the probe vibrates normal to the surface at a frequency of 140 Hz, and at an amplitude of 25  $\mu\text{m}$ , as governed by a lock-in amplifier (EG&G Instruments 7265) in conjunction with a vibrator driver amplifier. Additionally, the lock-in amplifier detects and enhances the SVET voltage signal at each point via digital signal averaging (typically of 10 successive measurements).

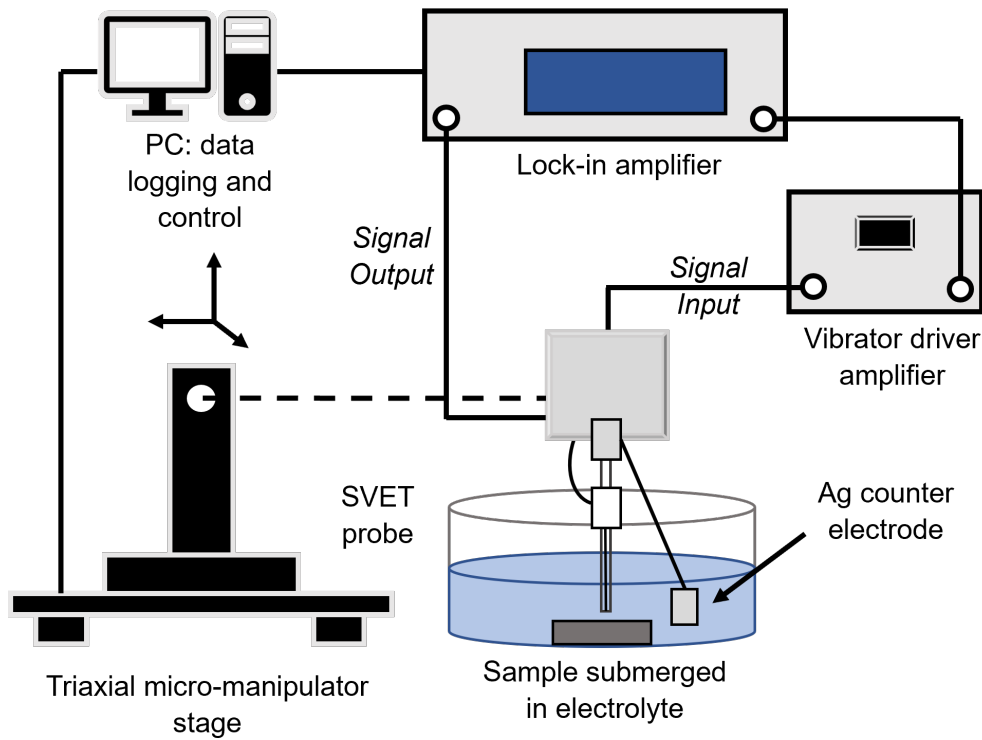


**Figure 2.1:** Schematic representation of the SVET apparatus.

The SVET measures the potential gradients in solution that arise ohmically from ionic current flux from distinguishable sites of anodic and cathodic activity. The ohmic potential gradients can be described in terms of iso-electronic lines that lie normal to ionic current flux lines, as shown in Figure 2.2. Considering an anodic point source with, the potential,  $E$ , at a point  $(x,y,z)$  in an electrolyte of conductivity,  $\kappa$  is given by:

$$E = \frac{i}{2\pi\kappa\sqrt{x^2 + y^2 + z^2}} \quad (2.1)$$

The normal electrical field strength,  $F$ , measured by vibrating the microtip perpendicular to the surface, is given by differentiating  $E$  with respect to vibrating distance,  $z$ :

$$F = \frac{dE}{dz} = -\frac{iz}{2\pi\kappa(x^2 + y^2 + z^2)^{1.5}} \quad (2.2)$$

As such, the maximum electrical field strength measured will be at the origin of a point



current source.

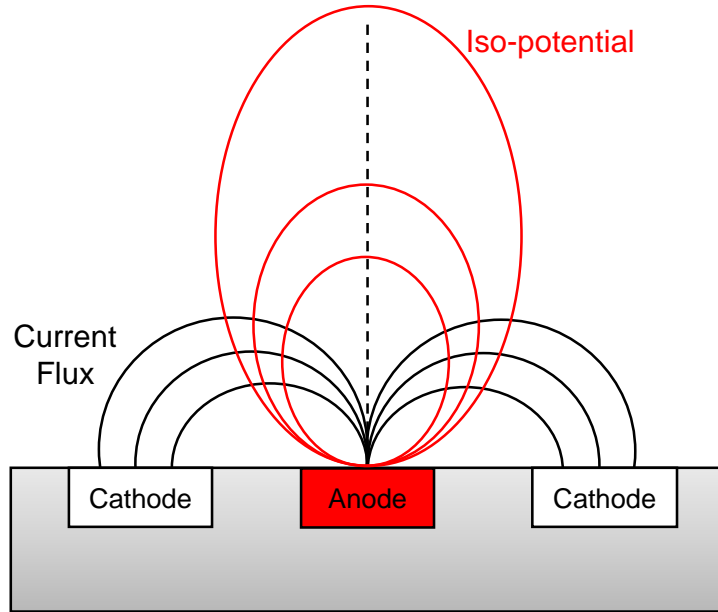


**Figure 2.2:** The current flux and iso-potential lines that occur from local corrosion cells. The black lines indicate current flux, and the red lines are the resulting iso-potential lines.

A calibration procedure using a point current source is performed before an SVET experiment so measured voltage signals (in nV) can be converted to values of current density (in  $\text{A m}^{-2}$ ). Under conditions that abide to Ohm's Law, the peak-to-peak SVET voltage signal ( $V_{pp}$ ) is related to current flux density along the direction of probe vibration ( $j_z$ ). Since current emerges from a point source from its centre and with a hemispherical profile,  $j_z$  can be calculated by dividing the applied current by the hemispherical surface area:

$$j_z = \frac{i}{2\pi z^2} \quad (2.3)$$

where  $i$  is applied current, and  $z$  is the height of the SVET probe over the point current source. A plot of  $V_{pp}$  vs  $j_z$  gives the linear equation:

$$V_{pp} = j_z \frac{A_{pp}}{\kappa} \quad (2.4)$$

where  $A_{pp}$  is the peak-to-peak vibration amplitude and  $\kappa$  is solution conductivity such that

a quantity  $G = \kappa/A_{pp}$  may be defined as the SVET calibration factor.

Calibration measurements are conducted with use of a two-compartment cell, a schematic of which is given in Figure 2.3. Both cell compartments contain a  $1\text{ cm}^2$  Pt electrode and are filled with the electrolyte to be used for the SVET experiment. They are linked by a vertically orientated glass tube of length 7 cm and of 5 mm internal diameter. Via manual positioning, the SVET probe is inserted into the opening of the tube and a range of currents are applied using a nano-galvanostat. For each applied current, the associated current flux density,  $j_z$  can be calculated via Equation 2.3 and then plotted against the measured  $V_{pp}$  output. The outputted calibration plot, an example of which is shown in Figure 2.4 gives rise to a linear trendline of gradient,  $G$  that is the calibration factor. After the SVET experiment, division of data points by  $G$  provides a value for current density in the plane of scan.

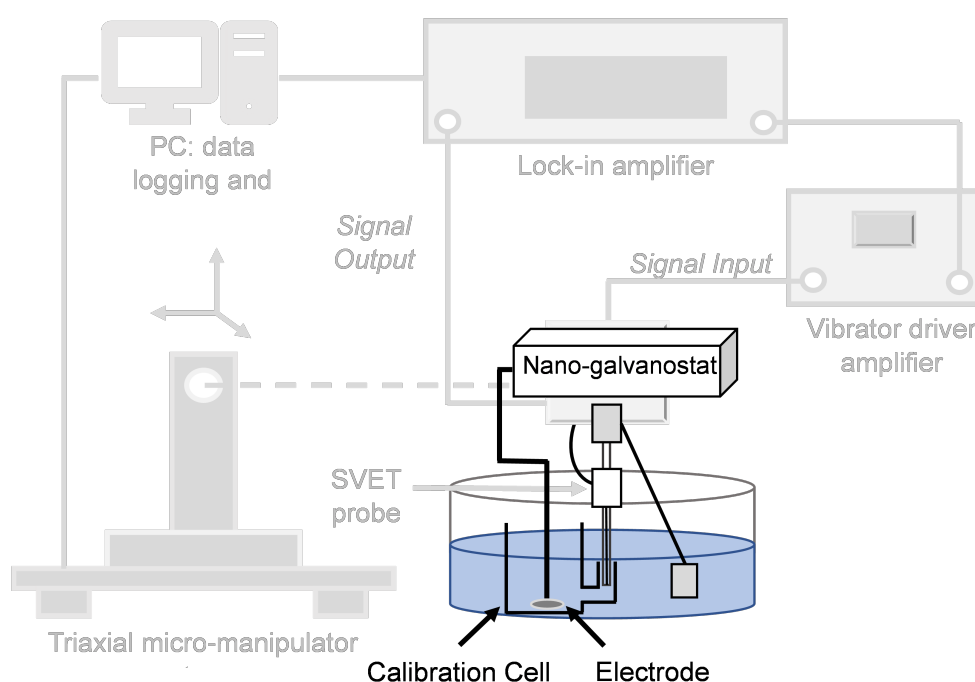


**Figure 2.3:** Schematic representation of the SVET calibration apparatus.

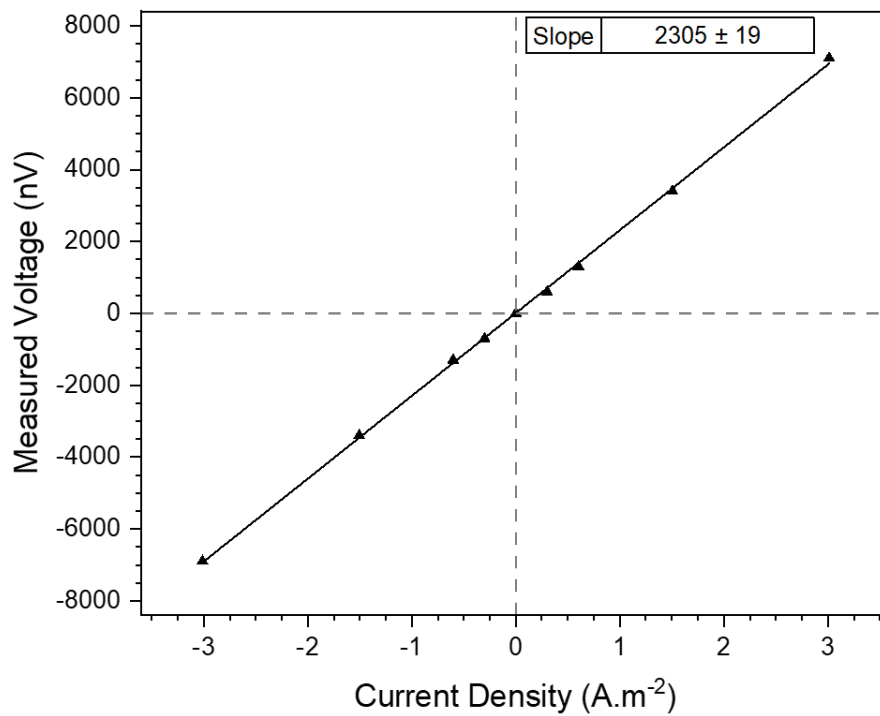


**Figure 2.4:** An example calibration plot of a  $0.86 \text{ mol dm}^{-3} \text{ NaCl}_{(aq)}$  solution.

### 2.2.1.1 SVET Data Rendering and Manipulation

In this thesis, all raw SVET data was calibrated and then visualised through creation of current density maps using the Origin data visualisation software provided by OriginLabs. Colours are superimposed on the maps - areas of anodic activity possess positive current density and are presented as red, while areas of cathodic activity possess negative current density and are presented as blue. The intensity of the colours are referenced to a scale bar that donates the magnitude of current density.

In addition to being used qualitatively to visualise areas of anodic and cathodic activity, for each current density distribution ( $j_z$ ) map, a semi-quantitative estimate of the area-averaged anodic current density ( $J_{a_t}$ ) and time-dependent anodic current ( $I_{a_t}$ ) can be produced by numerical integration:

$$I_{a_t} = A J_{a_t} \geq \int_0^X \int_0^Y [j_{z(x,y)} > 0] \, dx \, dy \quad (2.5)$$

where  $A$  is the sample area, and  $x$  and  $y$  are the length and width of the SVET scan.

### 2.2.1.2 SVET Limitations

The SVET can be limited by its spatial resolution meaning that on occasions where localise corrosion features are very close in proximity, they cannot be independently resolved. The theoretical spatial resolution of the SVET is determined by the Gaussian distribution of the normal electrical field strength from the point source origin, and the full-width half-maximum (whm) value of the signal peak. Considering a scan height of  $100\text{ }\mu\text{m}$  used throughout the presented work, the SVET has a theoretical spatial resolution of  $153\text{ }\mu\text{m}$  [1]. As such, the SVET would be unable to distinguish between localised corrosion features separated by a distance less than  $153\text{ }\mu\text{m}$ .

Additionally, the SVET can have issues due to its detection limit. If the ionic flux lines in solution between anodes and cathodes do not spread far enough out of the surface, then the probe of the SVET may not pass through them and so are undetected. This would be the case metallic substrates that are either undergoing general corrosion or are effectively inhibited by a corrosion inhibitor. In both cases, areas of anodic and cathodic activity are small and not spatially defined.

## 2.2.2 Assessment of Cathodic Delamination

### 2.2.2.1 Model Organic Coatings

To test the performance of in-coating inhibitors on corrosion-induced organic coating failure (Chapter 5), inhibitive pigments were dispersed or dissolved in a model coating system based upon poly(vinyl butyral-co-vinyl alcohol-co-vinyl acetate, PVB. PVB was used as it air dries within 30 minutes, leaving a strongly adhered film. Additionally, because PVB only mechanically bonds to the substrate, the coating fails when exposed to corrosive electrolyte in a timeframe conducive to accelerated testing, usually within 24 hours.

The PVB solution used in this work was an ethanolic solution of 15.5% w/w PVB. Powdered PVB (Mw 70,000-100,000) was added incrementally to ethanol and mixed using an IKA high-shear mixer. The resulting ethanolic solution was degassed in an ultrasonic bath for 30 minutes. The pigment volume fraction,  $\Phi_{\text{pig}}$  of inhibitors dispersed in model PVB coatings was calculated by:

$$\Phi_{\text{pig}} = \left( 1 + \frac{M_{\text{PVB}} \cdot \rho_{\text{pig}}}{M_{\text{pig}} \cdot \rho_{\text{PVB}}} \right)^{-1} \quad (2.6)$$

where  $M_{\text{PVB}}$  is the mass of PVB used in the coating formulation,  $M_{\text{pig}}$  is the mass of the inhibitor pigment,  $\rho_{\text{pig}}$  is the density of the inhibitor pigment, and  $\rho_{\text{PVB}}$  is the density of PVB ( $0.8 \text{ g.cm}^{-3}$ ).

#### 2.2.2.2 Cathodic Delamination Preparation

Chapter 5 describes the ability of BTSA and a BTSA-derived smart-release pigment to inhibit cathodic delamination. Cathodic delamination is a corrosion-driven coating failure that initiates when defects of an organic coating expose the metal surface to an aqueous electrolyte.

The accelerated cathodic delamination experiments carried out in Chapter 3 are based on the sample preparation designed by Stratmann et al [2-4]. Generally, the method allows for an electrolyte containing penetrative defect to be made that acts as an initiation point for coating delamination. The preparation of the Stratmann cell is described schematically in Figure 2.5. In brief, 50 mm x 50 mm galvanised steel coupons were prepared as described in Section 2.1.2. Scotch tape was used to cover a 15 mm x 50 mm area of the HDG coupon perpendicular to the rolling direction. Electrical tape (145  $\mu\text{m}$  thick) was then stuck on both edges normal to the scotch tape, covering 10 mm x 50 mm of the surface on both sides. Using the electrical tape as height guides, PVB or inhibitor-containing PVB solutions (as described in Section 2.2.2.1) were then bar cast onto the substrate and allowed to dry in air. After 30 minutes, a 30  $\mu\text{m}$  thick dry film was produced, as measured by a micrometre screw gauge. The scotch tape was cut along the electrical tape sections

and peeled back to the area where PVB coated the metal surface, thus creating an interface between exposed metal (defect) and PVB-coated metal. Non-corrosive silicone was used on the perimeter of the bare metal area to create a reservoir for aqueous electrolyte. In all experiments, delamination was initiated by adding 2 mL of  $0.86 \text{ mol dm}^{-3} \text{ NaCl}_{(\text{aq})}$  at pH 7 to the reservoir. The samples were contained in an enclosed, air-containing environment of constant relative humidity (96%). The progress of cathodic delamination was followed using either time-lapse photography or by the Scanning Kelvin Probe (SKP).

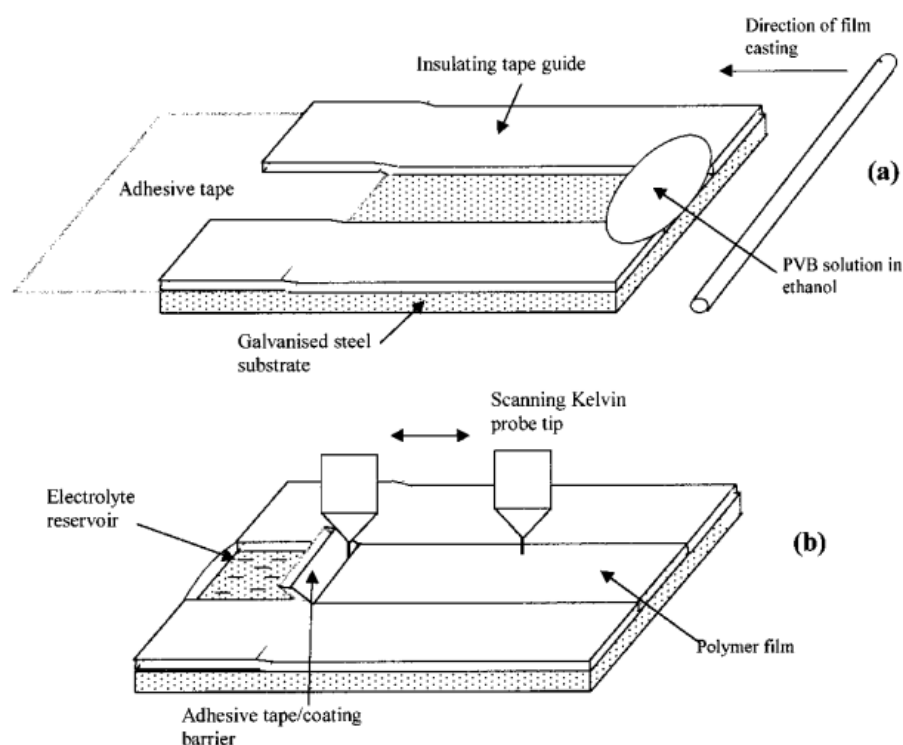


**Figure 2.5:** Schematic diagram showing a) cathodic delamination sample preparation, and b) experimental procedure for a typical delamination experiment

### 2.2.2.3 Time-Lapse Photography Determination of Cathodic Delamination

For time-lapse photography determination of cathodic delamination, Stratmann cells were prepared, initiated, and contained as described in Section 2.2.2.2. The humidity chamber was itself placed in an Ortery Photosimile 200 software-operated photography studio in which the lighting conditions were controlled. A transparent window in the container

allowed images of the samples to be taken using a Canon EOS 600D SLR camera. Photos were taken immediately after initiation and at hourly intervals for up to 72 hours. A dark corrosion product was visible during cathodic delamination; therefore, the delamination front was measured as a function of distance from the defect ( $X_{\text{del}}$ ) using pixel value analysis in ImageJ. An example of this methodology is given in figure 2.6. In a few cases, the delamination front was not uniform, hence ( $X_{\text{del}}$ ) varied across the delamination front. In these instances, the geometry of the delamination front was found not to change; therefore, three measurements were taken at different points along the delamination front and averaged [5]. Time-lapse photography is employed in Chapter 5 to measure the effect of BTSA and smart-release BTSA pigments at inhibiting cathodic delamination.

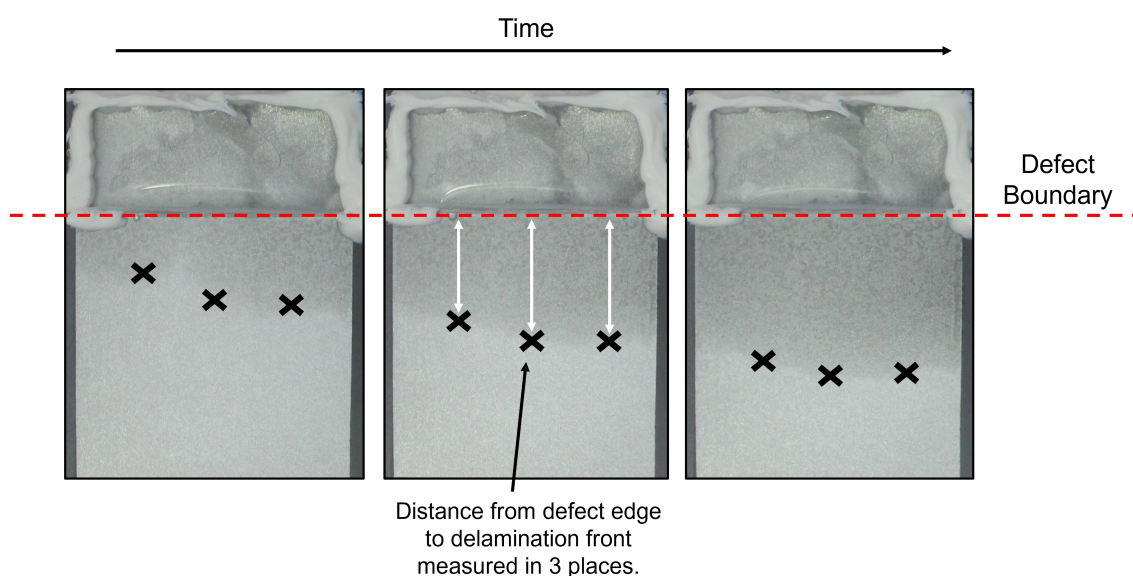


**Figure 2.6:** An example of time-lapse photography determination of cathodic delamination.

#### 2.2.2.4 Scanning Kelvin Probe (SKP) Determination of Cathodic Delamination

In this thesis, the SKP is complementarily used alongside the time-lapse photography method in Chapter 5 to give electrochemical insights into the action of BTSA and smart-release BTSA pigments at inhibiting cathodic delamination. In short, the SKP can measure the free corrosion potential ( $E_{\text{corr}}$ ) of metal surfaces underneath organic coatings.

In the Stratmann cell set-up described in Section 2.2.2.2, scanning from the defect and across the coating over time allows for time-dependent values of  $E_{\text{corr}}$  to be determined as a function of distance. This allows the underfilm conditions to be followed over time and thereby show the movement of a delamination front.

### 2.2.2.5 SKP Apparatus

Figure 2.7 shows a schematic of the SKP apparatus. The SKP probe is a gold wire (125  $\mu\text{m}$  diameter) that is vibrated vertically 100  $\mu\text{m}$  from the coated sample surface. A vibrational amplitude of 40  $\mu\text{m}$  and the vibrational frequency of 280 Hz is achieved by fixing the gold probe to a glass tube connected to an audio loudspeaker driven by an EG&G 7265 lock-in amplifier. The probe, sample, and sample holder are confined inside a stainless-steel chamber so that external electrical noise interference is minimised. Petri dishes containing 0.86  $\text{mol dm}^{-3}$   $\text{NaCl}_{(\text{aq})}$  are placed inside the sealed chamber to maintain a relative humidity of 95%. The probe is held in a stationary position, but the sample holder is connected to a tri-axial motor stage, allowing manual or automatic movement to be controlled and recorded on a PC.

The variation in capacitance between the sample and reference plates produces an AC current that is amplified and converted to an AC voltage. Where the DC bias voltage nulls the AC current, the DC output is applied, resulting in the Galvani potentials of the sample and reference plates equalising. The lock-in amplifier then converts the reverse bias value to a digital signal recorded as a measurement by the PC.



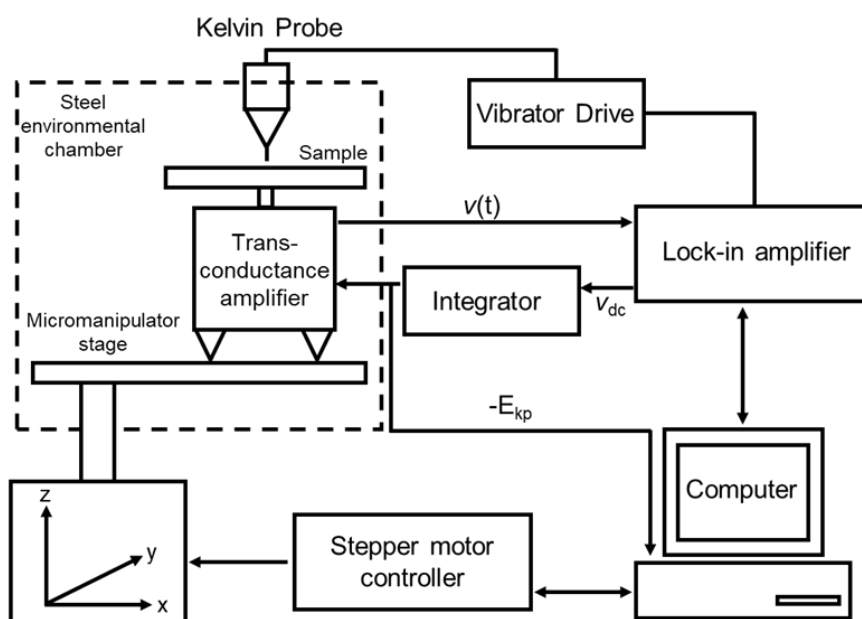


**Figure 2.7:** Schematic representation of the SKP apparatus. Recreated from [6]

### 2.2.2.6 SKP Operation

The sample under investigation is fastened to the SKP stage and levelled through a combination of the micromanipulator stage and triaxial micromanipulator. The sample is at the desired proximity from the gold reference probe when the the overload signal of the lock-in amplifier approaches a maximum value. This is performed at several points along the sample surface and the stage moved accordingly so that the sample is level. The sample is then moved 100  $\mu\text{m}$  below the probe. In this case, through movement of the sample stage under the SKP reference probe, measurements of  $E_{\text{corr}}$  were made every 0.05 mm along a 12 mm line normal to the defect-coating boundary. Scans were conducted immediately after initiation and then at hourly intervals for up to 72 hours.

### 2.2.2.7 SKP Calibration

The SKP is calibrated using metal/aqueous metal couples such as  $\text{Ag}/\text{Ag}^+$ ,  $\text{Cu}/\text{Cu}^{2+}$ ,  $\text{Fe}/\text{Fe}^{2+}$  and  $\text{Zn}/\text{Zn}^{2+}$ . To make calibration cells, a 8 mm diameter, 1 mm deep well is machined into the centre of 15 mm diameter, 5 mm thick disks of the relevant metal. The

wells are filled with a  $0.5 \text{ mol dm}^{-3}$  aqueous solution of the respective metal chloride salt (nitrate for  $\text{Ag}^+$ ). The SKP probe tip is positioned  $100 \mu\text{m}$  above the electrolyte meniscus in the centre of the well, and the value of  $E_{\text{KP}}$  is logged. A solartron I280 potentiostat is used to measure the electrode potential vs. SCE simultaneously for each  $\text{M}/\text{M}^{2+}$  coupling. Considering this work utilizes the SKP for the determination of  $E_{\text{corr}}$  of organically coated substrates, the effect of the PVB coating must be taken into account. The effect of the PVB polymer on SKP calibration is determined by placing a self-supporting  $30 \mu\text{m}$  thick PVB film over each calibration disk and in contact with the electrolyte meniscus. The polymer is then allowed to equilibrate with the electrolyte for 6 h and  $E_{\text{KP}}$  values obtained as before. It has been shown previously that PVB accounts for an offset of  $-220 \text{ mV}$  [6]. The calibration equation is:

$$E_{\text{corr}} = E_{\text{KP}} + \text{constant} \quad (2.7)$$

The  $\text{Cu}/\text{Cu}^{2+}$  redox couple used for calibration in this work has a known  $E_{\text{corr}}$  value of  $298 \text{ mV}$ . If a value of  $240 \text{ mV}$  is determined during calibration then Equation 2.7 becomes:

$$298 \text{ mV } (E_{\text{corr}}, \text{Cu}/\text{Cu}^{2+}) = -240 \text{ mV } (E_{\text{KP}}, \text{Cu}/\text{Cu}^{2+}) + \text{constant} \quad (2.8)$$

$$538 \text{ mV} = \text{constant} \quad (2.9)$$

$$538 \text{ mV} - 220 \text{ mV (PVB Offset)} = 318 \text{ mV} \quad (2.10)$$

The final value of  $318 \text{ mV}$  can be added to  $E_{\text{KP}}$  values to give  $E_{\text{corr}}$  values for each measured point.

### 2.2.3 Electrochemical Measurements

In addition to SVET experiments in Chapter 4, electrochemical measurements are made on uninhibited and inhibited HDG, Galfan and Zn55Al substrates immersed in aqueous

electrolyte (NaCl) and in conjunction with a Gamry Reference 620 potentiostat. For open circuit potential (OCP) measurements, a standard 2-electrode set up was employed with a 100 mm<sup>2</sup> square exposed area of the examined substrate constituting the working electrode (WE), and a saturated calomel electrode (SCE) being the reference electrode. The working electrode's OCP was recorded every 30 seconds for 60 minutes. For potentiodynamic polarisation (PP) experiments, the working electrode was left at open circuit for 10 minutes before being polarised by 300 mV either cathodically or anodically. The anodic and cathodic branches were acquired separately at a scan rate of 0.1667 mV s<sup>-1</sup>.

### 2.2.3.1 Linear Polarisation Resistance

As described in Section 2.2.1.2, the SVET is semi-quantitative; it has resolution and sensitivity limits that mean in highly inhibited systems, results should be corroborated with other methods. As such, in Chapter 4, Linear Polarisation Resistance (LPR) was used in combination with the SVET. LPR is a method for determining corrosion rates, having previously been employed to follow the time-dependent performance of inhibitors for ZnAl galvanised steel surfaces as it does not perturb the sample surface [7-9]. In LPR, a small amplitude excitation potential is applied ( $\pm 10$  mV in this case) to the inspected sample and the current density response is measured. A value of polarisation resistance ( $R_p$ ) is calculated from the slope of the potential versus the current density slope around the corrosion potential ( $E_{\text{corr}}$ ). The  $R_p$  value is used to determine the corrosion rate ( $i_{\text{corr}}$ ) of the material through the Stern-Geary relationship:

$$i_{\text{corr}} = \frac{B}{R_p} \quad (2.11)$$

where  $B$  is the Stern-Geary coefficient. The relationship of  $i_{\text{corr}}$  to  $R_p$  is inversely proportional, hence, the higher the  $R_p$  value, the lower the corrosion rate.

## 2.3 References

1. H. N. McMurray, D. A. Worsley, in *Research in Chemical Kinetics Volume IV*, R. Compton and G. Hancock, Amsterdam; New York: Wiley-Blackwell, 1997, 256.
2. A. Leng, H. Streckel, M. Stratmann, The delamination of polymeric coatings from steel. Part 1: Calibration of the Kelvinprobe and basic delamination mechanism, *Corros. Sci.* 41 (1998) 547.
3. A. Leng, H. Streckel, M. Stratmann, The delamination of polymeric coatings from steel. Part 2: First stage of delamination, effect of type and concentration of cations on delamination, chemical analysis of the interface, *Corros. Sci.* 41 (1998) 579.
4. A. Leng, H. Streckel, K. Hofmann, M. Stratmann, The delamination of polymeric coatings from steel Part 3: Effect of the oxygen partial pressure on the delamination reaction and current distribution at the metal/polymer interface, *Corros. Sci.* 41 (1998) 599.
5. N. Wint, P. Ansell, J. Edy, G. Williams, H.N. McMurray, A Method for Quantifying the Synergistic Inhibitory Effect of Corrosion Inhibitors When Used in Combination: A ‘Chromate Generating Coating’, *J. Electrochem. Soc.* 166 (2019) C580–C588.
6. G. Williams, H.N. McMurray, Chromate Inhibition of Corrosion-Driven Organic Coating Delamination Studied Using a Scanning Kelvin Probe Technique, *J. Electrochem. Soc.* 148 (2001) B377.
7. I.A. Kartsonakis, S.G. Stanciu, A.A. Matei, R. Hristu, A. Karantonis, C.A. Charitidis, A comparative study of corrosion inhibitors on hot-dip galvanized steel, *Corros. Sci.* 112 (2016) 289–307.
8. L.A. Hernandez-Alvarado, L.S. Hernandez, J.M. Miranda, O. Dominguez, The protection of galvanised steel using a chromate-free organic inhibitor, *Anti-Corrosion Methods and Materials.* 56 (2009) 114–120.

9. L.A. Hernandez-Alvarado, L.S. Hernandez, S.L. Rodriguez-Reyna, Evaluation of corrosion behavior of galvanized steel treated with conventional conversion coatings and a chromate-free organic inhibitor, *International Journal of Corrosion*. (2012).

## **Chapter 3**

# **Effect of Aqueous Chloride Concentration on the Localised Corrosion of Zn55Al Galvanised Steel**

### **3.1 Introduction**

Hot-dip zinc galvanised steel (HDG) has been used in the construction, automotive and appliance industries for decades due to its low production cost and good mechanical properties. However, for some uses that require long service lifetimes whilst being exposed to the atmosphere, such as facades and roofs for buildings, HDG can suffer from corrosion. As such, because of their superior corrosion resistance, ZnAl alloy coated steels have gained greater prominence within the construction industry [1,2]. Two coatings are commonly used: Galfan, which contains 5 wt.% Al, and Zn55Al (i.e., *Galvalume<sup>TM</sup>*), which contains 55 wt.% Al. Of the two, Zn55Al has the greatest intrinsic corrosion resistance, possessing up to four times better general corrosion resistance than HDG in marine and industrial atmospheres [3,4]. The increased performance is attributed to Zn55Al's microstructure, which is essentially two-phase consisting of primary dendrites rich in Al (approximately 80 wt.%) approximately 80% by volume of the coating, with the remainder consisting of interdendritic areas rich in Zn (approximately 78 wt.%). Because much of the surface coverage is occupied by dendrites and Al is passive between pH 4 and 9, a strongly passive Al hydr(oxide) layer covers much of the surface, acting as a barrier to corrosive electrolytes, while Zn still maintains sacrificial protection to the underlying steel [5,6]. Zn55Al also contains a small addition of Si (approx. 1.6 wt.%) that limits the extent of alloying of the ZnAl matrix to the steel substrate by forming a well-adhered Fe-Al-Si-Zn intermetallic layer at the coating-steel interface [5].

Unfortunately, for ZnAl galvanised steels, chloride-containing atmospheres present the problem of localised corrosion, a highly damaging phenomena that reduces their lifetime and aesthetics [3,7–9]. For HDG and Galfan, the mechanism of chloride-induced localised corrosion has been researched extensively [10–16]. However, Zn55Al has received less attention.

Previous research into the initial atmospheric corrosion of Zn55Al suggests that the passive Al hydr(oxide) layer is destroyed locally in contact with chloride and gradually replaced by Zn-rich corrosion products [17]. These initial products include zinc aluminium hydroxy carbonate, zinc chloro sulfate, zinc hydroxy chloride, and zinc hydroxy carbon-

ate [18]. These products have similarly been observed in accelerated salt spray testing and during exposure to wet storage conditions [19,20]. Regarding its corrosion mechanism, it is believed that initial anodic dissolution begins in the Zn-rich interdendritic phase of the coating [2,4,9,21]. However, after longer-term exposure anodic attack may extend into Al-rich dendrites, giving a more significant and damaging local attack. As discussed by Palma et al., the extension of localised attack is sensitive to atmospheric chloride concentration and time of wetness (ToW), with regions of high atmospheric chloride concentration and longest ToW being the most aggressive [3].

Currently, there is limited discussion about the impact of chloride concentration on the localised corrosion behaviour of Zn55Al. This is because previous studies have largely focused on short immersion times in dilute aqueous chloride solutions. Therefore, it is not appropriate to correlate this data with long-term atmospheric studies. To better complement outdoor exposure data and gain greater insights into the corrosion mechanism of Zn55Al, longer immersion tests with higher concentrations of chloride-containing media are needed.

To this end, this chapter provides a mechanistic insight into the effect of varying aqueous chloride concentrations (5% w/v – 0.04% w/v NaCl<sub>(aq)</sub>) on the localised corrosion of Zn55Al. In doing so, the Scanning Vibrating Electrode Technique (SVET) is employed to identify time-dependent changes in anodic and cathodic activity over 24 hours of immersion. The SVET has previously evaluated localised corrosion activity on the surfaces of Zn-alloys and other metals [22–25]. Pertinent to this work, it has also assessed the effect of aqueous chloride concentration on localised corrosion behaviour. For example, using the SVET, Wint et al. [26] showed that in dilute NaCl<sub>(aq)</sub> (<0.01%) the total (area averaged) corrosion current density of zinc varies with approximately the square root of NaCl<sub>(aq)</sub>. Further to the SVET, Scanning Kelvin Probe Force Microscopy (SKPFM) is used to determine the relative nobility of microstructural phases, and in-situ time-lapse microscopy (TLM) is used to monitor and visualise selective chloride-induced anodic attack at a microstructural level [27].



## **3.2 Experimental Details**

### **3.2.1 Materials**

55 wt.% Al, 43.4 wt.% Zn and 1.6 wt.% Si coated steel (Zn55Al) was supplied by Becker Industrial Coatings. It consisted of 0.7 mm gauge carbon steel coated with a 16  $\mu\text{m}$  thick ( $150 \text{ gm}^{-2}$ ) Zn55Al layer on each side. 50 mm x 50 mm coupons were cut from a large sheet and cleaned using an aqueous slurry of 5  $\mu\text{m}$  polishing alumina, rinsed with deionised water, degreased in ethanol, and allowed to dry in air. Chemicals, including acetone ( $(\text{CH}_3)_2\text{CO}$ ), ethanol ( $\text{C}_2\text{H}_5\text{OH}$ ), nitric acid ( $\text{HNO}_3$ ), and sodium hydroxide ( $\text{NaOH}$ ), were purchased from Merck at analytical grade.  $\text{NaCl}_{(\text{aq})}$  solutions were buffered to pH 7 by adding  $\text{NaOH}_{(\text{aq})}$  dropwise.

### **3.2.2 Methods**

#### **3.2.2.1 Material Characterisation**

Microstructural and compositional information about the Zn55Al surface was obtained. A 15 mm<sup>2</sup> Zn55Al sample was mounted in Conducto-Mount (Metprep Ltd) conductive phenolic resin and polished with a 1  $\mu\text{m}$  diamond slurry. The sample was etched using 2 wt.% Nital and rinsed with water and ethanol. Microstructural and compositional images were obtained using a Hitachi TM4000Plus SEM with a Bruker Energy Dispersive X-ray Spectroscopy (EDX) module.

#### **3.2.2.2 Scanning Kelvin Probe Force Microscopy (SKPFM)**

The relative potential difference between microstructural phases of Zn55Al was recorded using a JPK NanoWizard3 atomic force microscope (AFM) with a Scanning Kelvin Probe (SKP) equipped with an FM-50 193 Pointprobe tip. The sample was prepared in the same way as for microstructural analysis. Measurements were performed in AC (tapping) mode 20 nm from the sample surface. The scan speed was 20  $\mu\text{m s}^{-1}$ .

### 3.2.2.3 Scanning Vibrating Electrode Technique (SVET)

The SVET was used to spatially resolve the time-dependent corrosion behaviour of Zn55Al immersed in varying concentrations of NaCl<sub>(aq)</sub>. Details about the SVET instrumentation and operating procedure can be found in Chapter 2 and elsewhere [28–33]. The SVET samples were prepared the same way as for microstructural analysis, except they were mounted in non-conductive phenolic resin. PTFE tape was used to expose a 100 mm<sup>2</sup> area of the Zn55Al surface to SVET solutions containing either 5% w/v, 1% w/v, 0.2% w/v, or 0.04% w/v NaCl<sub>(aq)</sub> at pH 7 (all concentrations in % w/v will be given as “% [NaCl]” from this point forward). Measurements were taken every 100 µm in both x and y directions, scanning immediately after immersion and then at 30-minute intervals for 24 h. It was assumed that the dissolved carbon dioxide and oxygen concentrations within the electrolyte were at the equilibrium concentration values for air-saturated water (1.32 x 10<sup>-5</sup> mol dm<sup>-3</sup> and 2.8 x 10<sup>-4</sup> mol dm<sup>-3</sup>, respectively) [34]. After 24 h, the sample was removed from the electrolyte, washed with deionised water, rinsed with acetone, and air-dried. Photographs of the exposed area were then taken. The outputted dataset consisted of 10,000 V<sub>pp</sub> values for each of the 48 total scans, which were converted to current density values, j<sub>z</sub>, using a calibration method described in Chapter 2. The values of j<sub>z</sub> were then plotted as current density contour maps for each time interval using OriginLab Origin data analysis and graphing software. Further, the total anodic current (I<sub>a(t)</sub>) and area-averaged total anodic current density (J<sub>a(t)</sub>) associated with corrosion for each scan interval was obtained through numerically integrating all the positive j<sub>z</sub> values present in each scan using Equation 3.1.

$$I_{a_t} = A \cdot J_{a_t} \geq \int_0^X \int_0^Y [j_{z(x,y)} > 0] dx dy \quad (3.1)$$

where A is the sample area (100 mm<sup>2</sup>) and x and y are the length and width of the SVET scan respectively.

#### **3.2.2.4 Time-Lapse Microscopy**

Time-lapse optical microscopy (TLM) was used to observe aqueous corrosion occurring on the surface of Zn55Al at a microstructural level. The experimental setup shown in Figure 3.1 is an iteration of previous methodologies [35,36]. In brief, the technique involved fitting a cylindrical PET waterproof shroud to the lens of a Meiji Techno MT7100 metallurgical microscope and monitoring the sample of interest under immersion conditions. The samples were prepared in the same way as for SVET experimentation. PTFE tape was used to expose a 0.78 mm<sup>2</sup> circular area of the Zn55Al surface, and the whole sample was secured to the base of a petri dish. The sample was then immersed in pH 7 solutions of either 5% or 0.04% [NaCl]. An Infinity 2 digital camera attachment captured images every two minutes for up to 18h. The images were assembled into time-lapse videos using Microsoft Movie Maker software.

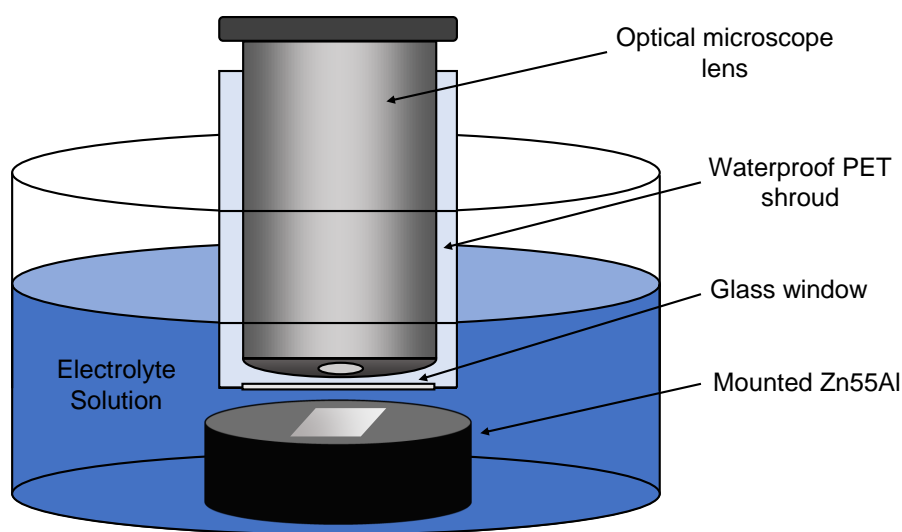


**Figure 3.1:** *Schematic representation of the time-lapse optical microscopy apparatus.*

## **3.3 Results**

### **3.3.1 Material Characterisation**

Figure 3.2 presents a back-scattered electron (BSE) scanning electron microscope (SEM) image of the Zn55Al microstructure. The microstructure comprises three primary features: large dendrites (10-40  $\mu\text{m}$  wide), interdendritic regions (<10  $\mu\text{m}$  wide), and fine, thread-like features. Based on measurements from five distinct sample areas, the average area ratio of dendrites to interdendritic regions is approximately 2:1.

In the BSE image, the large dendrites appear dull, while some areas of the interdendritic region are bright, indicating compositional variation. In BSE imaging, atoms with higher atomic numbers scatter more electrons toward the detector, resulting in increased signal intensity and a brighter appearance. Since Zn has a higher atomic number than Al, the bright regions likely correspond to areas with a higher Zn content.

Energy dispersive X-ray (EDX) analysis, shown in Figure 3.3, confirms this compositional variation. The EDX maps for Al (red), Zn (blue), and Si (yellow) reveal that dendrites are Al-rich (approx. 65% Al), while interdendritic regions are Zn-rich (approx. 79% Zn). The small, thread-like structures contain neither Al nor Zn but are instead Si particles.

The BSE image (Figure 3.2) and EDX mapping (Figure 3.3) further suggest that multiple phases exist within the interdendritic regions. Some interdendritic areas appear bright and Zn-rich, while others show a fine, intermixed pattern of dull (Al-rich) and bright (Zn-rich) material, indicating phase separation.

Overall, the observed microstructure is consistent with rapid, non-equilibrium cooling after hot-dipping, where  $\alpha$ -Al dendrites solidify first, followed by an interdendritic eutectic containing primary  $\eta$ -Zn and metastable  $\beta$ -Zn. The  $\beta$ -Zn phase subsequently undergoes eutectoid transformation upon further cooling into a fine mixture of  $\alpha$ -Al and  $\eta$ -Zn within the interdendritic. This microstructural evaluation agrees with previous reports for commercial Zn55Al coated steel [37].

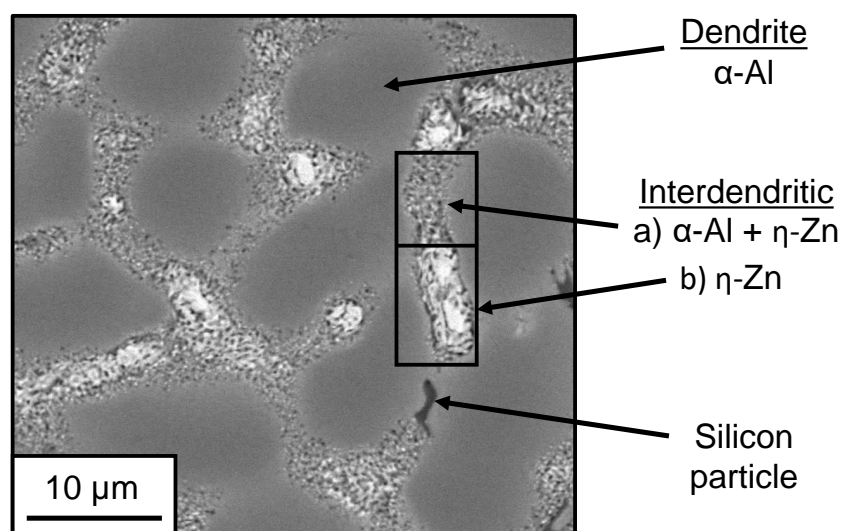


**Figure 3.2:** Back-scatter electron SEM image of the Zn55Al surface.

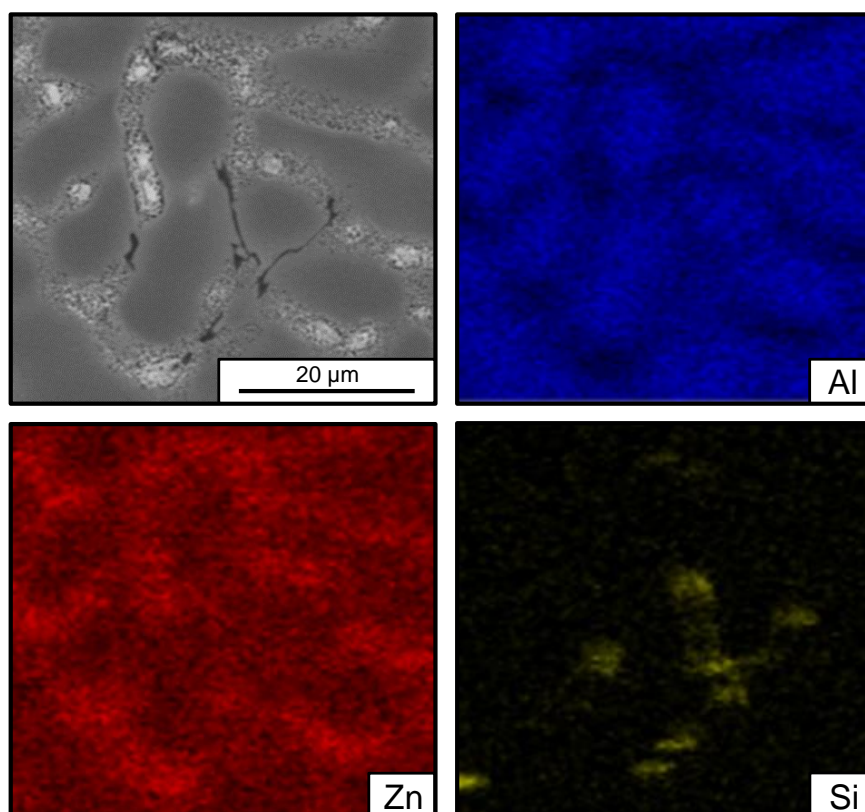


**Figure 3.3:** EDX maps of Zn55Al's surface Al (blue), Zn (red), and Si (yellow).

### **3.3.2 Scanning Kelvin Force Microscopy (SKPFM)**

Volta potential measurements were performed before immersion in aqueous chloride to compare the initial relative thermodynamic likelihood of a microstructural phase undergoing an electrochemical reaction. Figure 3.4 shows the SKPFM-derived Volta potential map of a  $400\text{ }\mu\text{m}^2$  area of the Zn55Al surface. As Volta potential mapping gives a value of relative nobility, not absolute values of potential, the Volta potential map has been normalised so that 0 V corresponds to the highest potential observed.

Upon visual comparison of the appearance of the Volta potential map and the SEM image in Figure 3.2, it can be observed that the areas with the more positive Volta potentials generally correspond to  $\alpha$ -Al dendrites, while the regions with more negative Volta potentials correspond to interdendritic areas. Notably, however, is that the lowest relative potentials (approx. -0.5 V) is associated with  $\eta$ -Zn of the eutectic interdendritic (primary  $\eta$ -Zn and  $\eta$ -Zn of the eutectoid transformation of metastable  $\beta$ -Zn).

It has been previously shown for other Zn-alloy galvanised steels that phases that possess lower volta potentials possess greater intrinsic reactivity [38]. As such, in this case, SKPFM predicts that the  $\eta$ -Zn phases of the eutectic interdendritic are the most intrinsically reactive (less noble) phases of the Zn55Al microstructure.

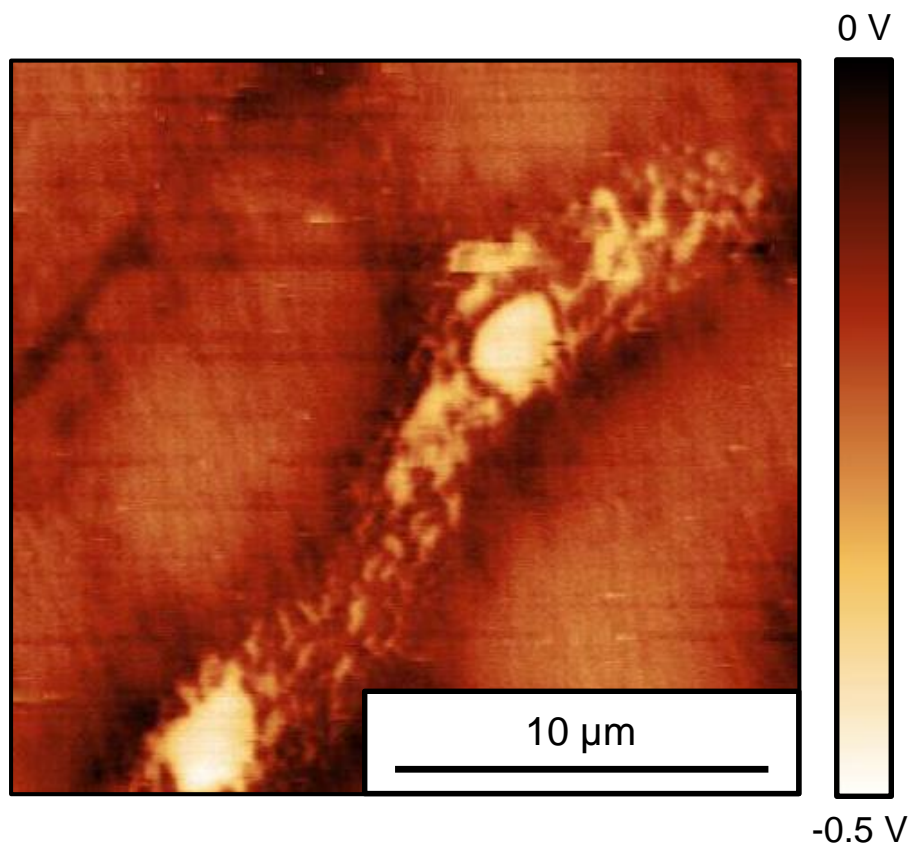


**Figure 3.4:** *SKPFM-derived Volta potential map of the surface of Zn55Al.*

### **3.3.3 Scanning Vibrating Electrode Technique (SVET)**

The SVET was used to understand the mechanism of localised corrosion and to provide a semi-quantitative evaluation of the effect of aqueous chloride concentration. Figure 3.5 displays SVET-derived current density maps measured at different intervals during immersion of 100 mm<sup>2</sup> of exposed Zn55Al in varying [NaCl]. The blue areas on each map represent negative  $j_z$  values, corresponding to net cathodic activity, while. In contrast, red areas represent positive  $j_z$  values corresponding to net anodic activity. As shown by the maps at 1 h of immersion in all [NaCl], Zn55Al showed spatially distinct localised anodic sites set against a background net cathodic activity. However, at longer immersion times, differences regarding local anode position, total area occupied, and cumulative magnitude are observed. Each difference will be discussed in turn:

#### **3.3.3.1 Position of Local Anodes**

Regarding the position of localised anodes, the current density maps for all [NaCl] in Figure 3.5 shows that anodes are either transient (i.e., passivate between scans and move to an adjacent position) or are of fixed position (i.e., largely stationary in nature);

**5% [NaCl] (Figure 3.5a);** local anodes are exclusively transient during the first 4 h of immersion, moving outward from the bottom left corner of the exposed area to the top right corner. However, between 4 h and 5 h, the active transient anodes in the top right corner stabilise and are subsequently observed as stationary anodes that remain active for the rest of immersion.

**1% [NaCl] (Figure 3.5b);** transient and stationary activity is observed during the first 1 h of immersion, with some transient anodes leaving behind stationary anodes at early scan intervals. By 7 h of immersion, all anodic activity is stationary and remains active for the rest of immersion.

**0.2% [NaCl] (Figure 3.5c);** localised anodes are constrained to the top left corner of the exposed sample for the first hour. However, transient anodes move outward between 1 h and 2 h, leaving behind stationary anodes that are observed for the remainder of



immersion. A transition to entirely stationary anodic activity is not seen; instead transient anodic activity continues throughout immersion.

**0.04% [NaCl] (Figure 3.5d);** anodic activity is almost exclusively transient throughout immersion, with the only stationary activity beginning immediately after immersion but passivating by 4 h.

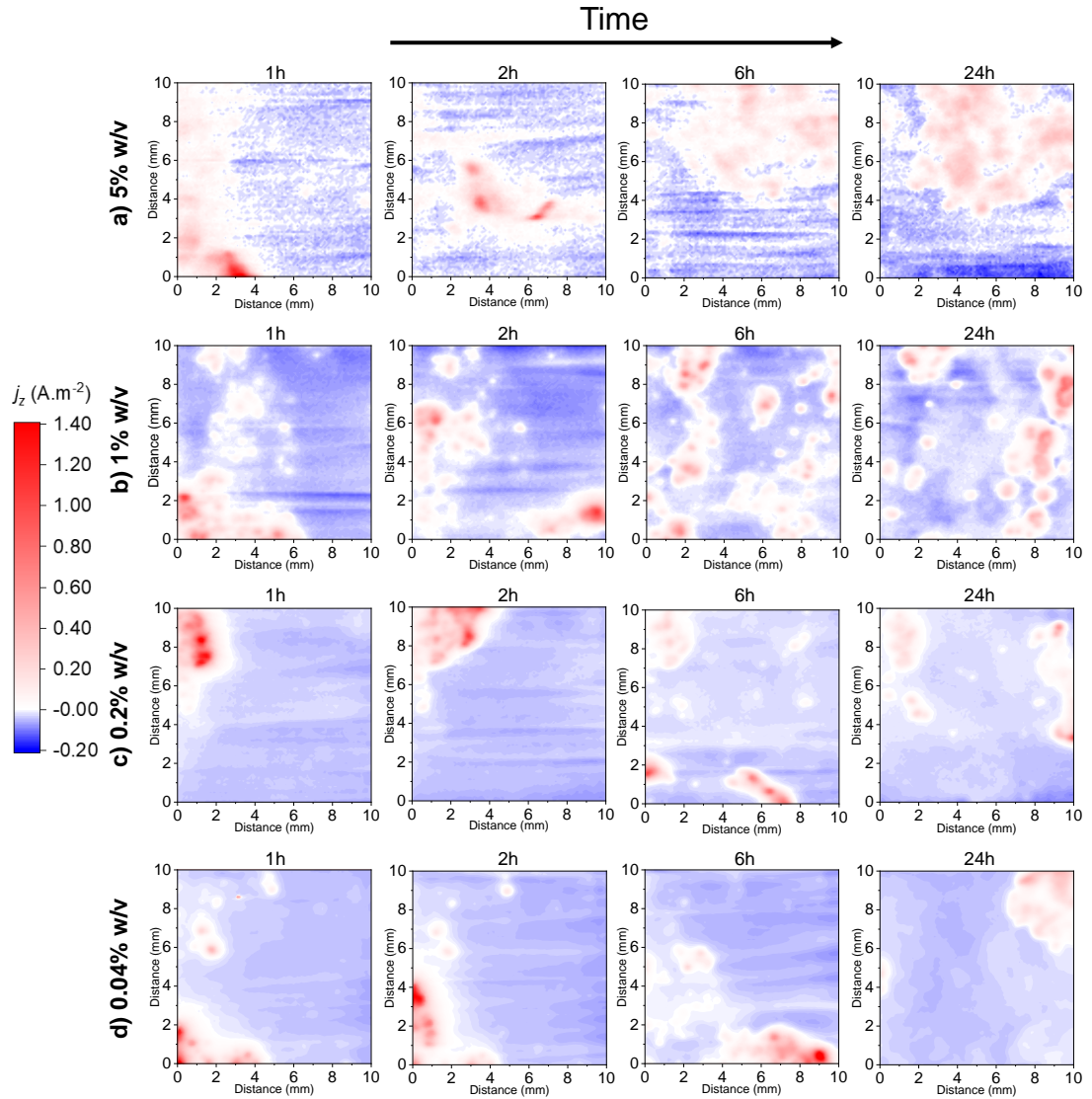


**Figure 3.5:** SVET current density maps at different intervals during immersion of 100 mm<sup>2</sup> of exposed Zn55Al in a near neutral solution of a) 5% w/v, b) 1% w/v, c) 0.2% w/v, and d) 0.04% w/v NaCl<sub>(aq)</sub> for 24 hours.

Table 3.1 details the average speed of transient anodes and the time taken for all transient anodes to stabilise (if applicable) for each [NaCl] concentration. The average speed of transient anodes is calculated by averaging the distance travelled scan-to-scan by the transient anode with the highest  $j_z$  value. In general, an increase in [NaCl] concentration leads to faster movement of transient anodes. For instance, the most prominent anode observed in 5% [NaCl] (Figure 3.5a) moves more than three times faster over the exposed Zn55Al surface compared to 0.04% [NaCl] (Figure 3.5d). Moreover, higher [NaCl] concentrations are more likely to exhibit a complete transition to stationary anodic activity, whereas this change is not observed in lower [NaCl] concentrations.

**Table 3.1:** *A summary of transient anode behaviour seen in SVET current density maps of the surface of Zn55Al immersed in near neutral solutions of varying [NaCl] concentration.*

| [NaCl]   | 5% w/v | 1% w/v | 0.2% w/v      | 0.04% w/v     |
|--|--------|--------|---------------|---------------|
| <i>Average Transient Anode Speed (<math>\text{mm h}^{-1}</math>)</i>           | 7.98   | 6.51   | 4.51          | 2.50          |
| <i>Time of transition from transient anodes to fully stationary anodes (h)</i> | 5      | 7      | No Transition | No Transition |

### 3.3.3.2 Percentage Anodic Area

Figure 3.6 displays the percentage change anodically active area of Zn55Al's exposed surface, as derived from SVET current density maps (Figure 3.5) for each [NaCl] concentration. The anodic area percentage is calculated by totalling the number of positive (anodic)  $j_z$  data points for each scan and calculating a percentage from the total number of data points. In general, increasing [NaCl] concentration leads to a greater anodic area. For instance, at 24 h, only 12% of the surface is anodically active in 0.04% [NaCl], whereas 50% of the surface is anodically active in 5% [NaCl].

Additionally, from Figure 3.6 the two modes of anodic activity can be compared by tracking the change in the anodic area at each scan interval. In the case of 5% and 1% [NaCl],

during transient anodic activity (0–7 h), the percentage of anodic area scan-to-scan varies significantly – between 30–60% and 15–40%, respectively, reflecting the dynamic nature of the moving anodes. However, after 7 h when stationary activity becomes the primary current density source, anodic activity scan-to-scan becomes less changeable, and the range of anodic areas narrows to between 40–60% and 30–40%, respectively. In contrast, in 0.2% and 0.04% [NaCl], where transient activity predominates throughout immersion, similar changes in area range is not recorded. Instead, the anodic area ranges between 10–25% and 8–25% for the immersion time.

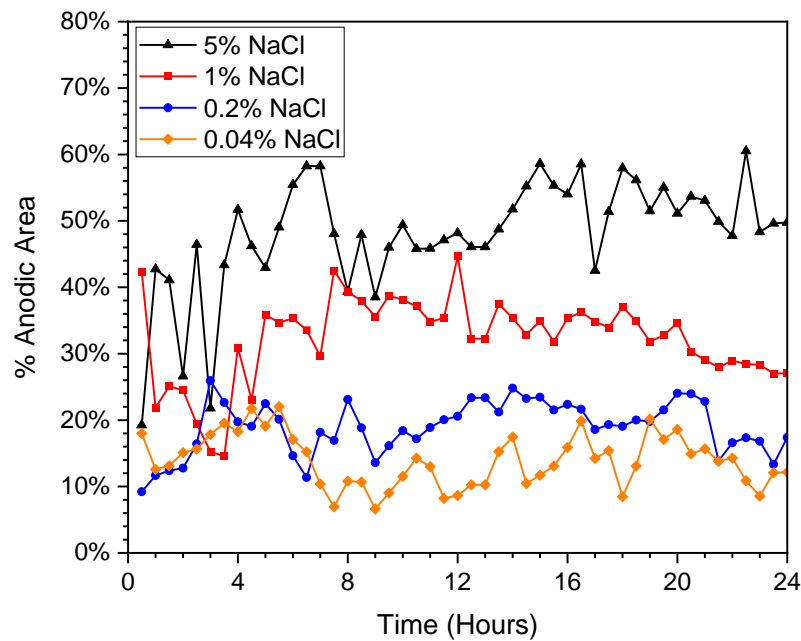


**Figure 3.6:** *The SVET-derived time-dependent percentage anodic area of Zn55Al immersed in a pH 7 solution of a) 5% w/v, b) 1% w/v, c) 0.2% w/v, and d) 0.04% w/v  $\text{NaCl}_{(aq)}$  for 24 h. To enable clarity of trends, the plot is the mean result of experiments undertaken in triplicate with a calculated  $\pm 5\%$  uncertainty.*

### 3.3.3.3 Cumulative Anodic Current Density

Figure 3.7 is a plot of the cumulative area-averaged anodic current density ( $j_a$ ) recorded for Zn55Al immersed in various [NaCl] solutions. Cumulative  $j_a$  values are calculated by adding the  $j_{a(t)}$  for each scan. The plot reveals that there is a steady increase in cumulative  $j_a$  as the [NaCl] concentration increases. During the initial stages of immersion, when transient activity dominates, there is a linear correlation between cumulative  $j_a$  and time. For 0.2% and 0.04% [NaCl], the linear trendline remains constant for the remainder of the immersion, but for 5% and 1% [NaCl], the gradient increases slightly, coinciding with the onset of stationary localised activity. Since the lowest concentrations do not display a transition from transient to stationary anodes in their current density maps (Figure 3.5), it is probable that stationary anodes produce greater anodic current density than transient anodes and are more damaging to the Zn55Al surface.

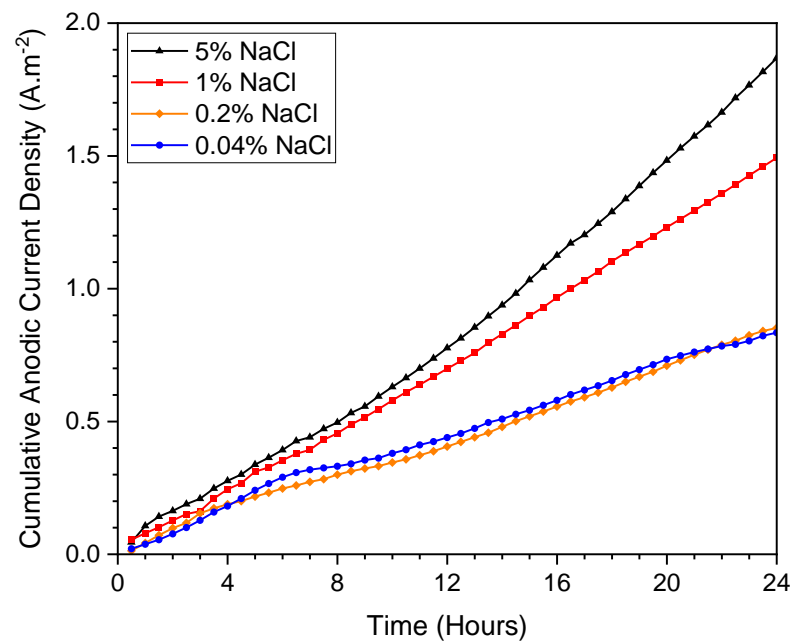


**Figure 3.7:** The SVET-derived cumulative anodic current density of 100 mm<sup>2</sup> of exposed Zn55Al immersed in a near neutral solution of a) 5% w/v, b) 1% w/v, c) 0.2% w/v, and d) 0.04% w/v NaCl<sub>(aq)</sub> for 24 h. To enable clarity of trends, the plot is the mean result of experiments undertaken in triplicate with a calculated  $\pm 5\%$  uncertainty.

### **3.3.3.4 Appearance of Post-SVET Surfaces**

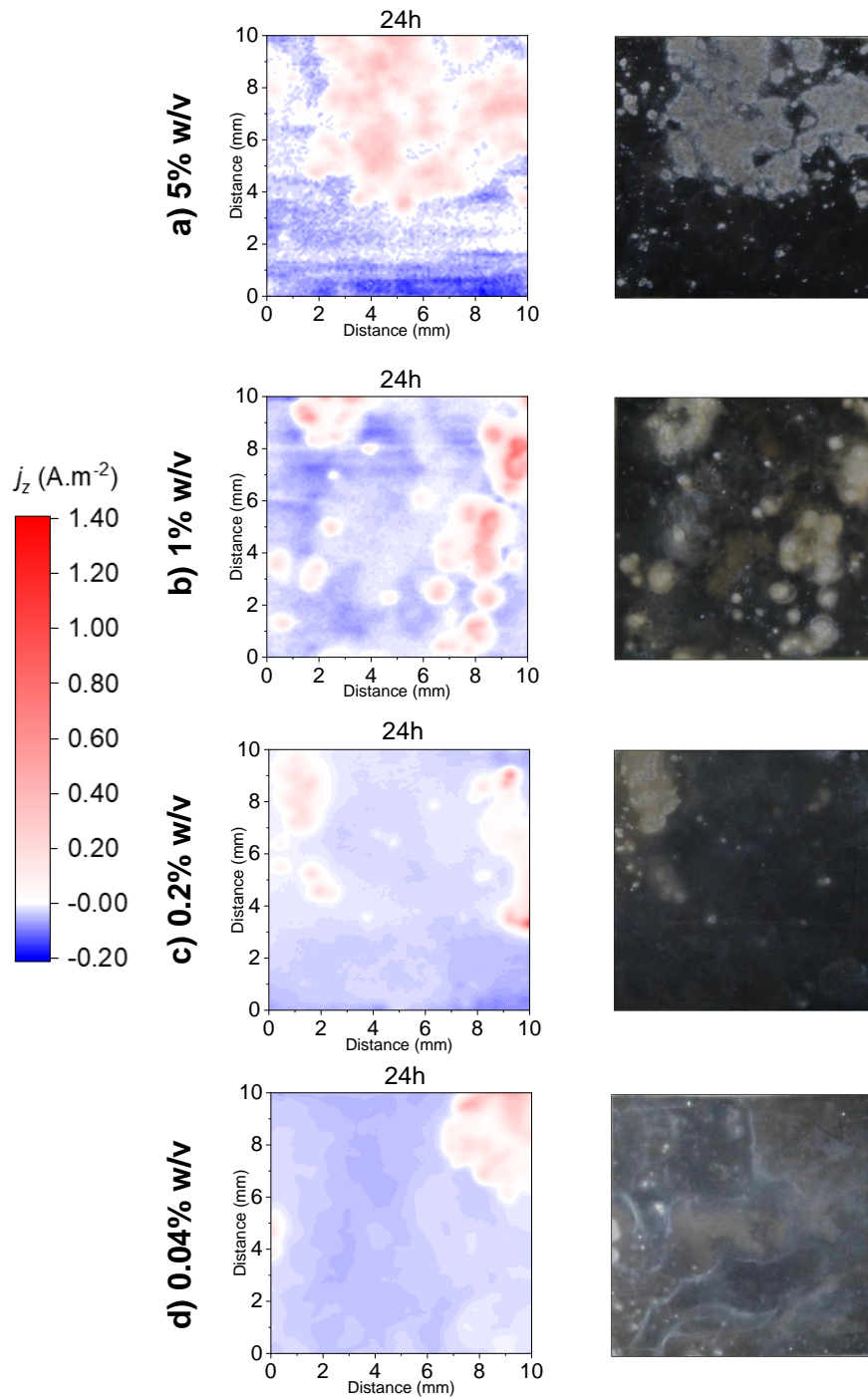
Figure 3.8 shows the post-immersion photographs and corresponding SVET-derived current density maps at 24h for Zn55Al immersed in each [NaCl]. In all cases, the images show white-stained regions set against a black-stained background.

**5% and 1% [NaCl] (Figures 3.8a and 3.8b);** the white and black-stained regions are in the same position on the 24 h current density maps as local anodes and the background cathode, respectively. Given that the anodic activity observed for both concentrations at 24 h is stationary, the white-stained regions likely arise from stationary anodic attack of the surface.

**0.2% [NaCl] (Figure 3.8c);** both stationary (top-left corner) and transient (middle-right) anodes are visible in the current density map at 24 h. However, only the stationary anodes in the top-left corner appear as white-stained regions in the post-immersion image.

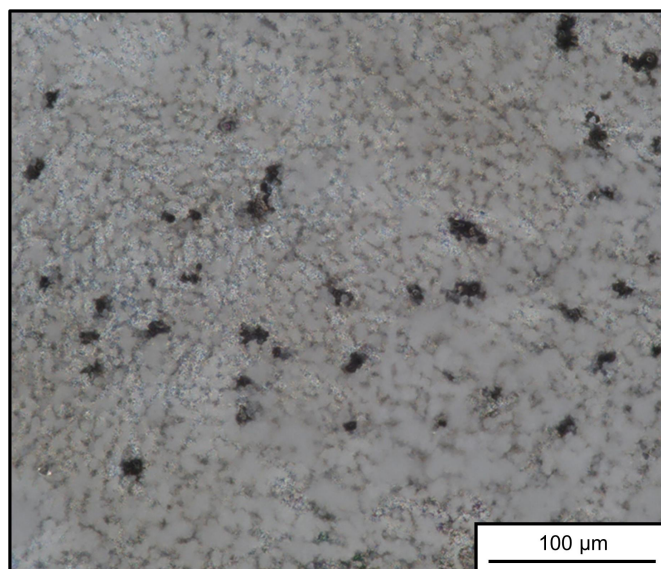
**0.04% [NaCl] (Figure 3.8d);** the post-immersion surface is almost entirely black-stained, albeit for a few white-stained areas. Notably, any white-stained areas are not shown as active anodes in their corresponding current density map at 24 h, hence those areas are likely due to stationary anodes of earlier immersion times repassivating by 24 h.

Figure 3.9a shows optical microscope images of a white-stained area (Figure 3.9a) and a black-stained area (Figure 3.9b) of the Zn55Al surface after immersion in 5% [NaCl]. In white-stained regions, several small local pits are observed, consistent with stationary anodic activity in those areas in current density maps (Figure 3.5a). The pits are approximately 10-40  $\mu\text{m}$  in diameter, larger than the size of interdendritic regions; thereby suggesting a contribution of anodic attack of the larger  $\alpha$ -Al dendrites either exclusively or in addition to the attack of interdendritic areas. Moreover, the pits are surrounded by solid, white corrosion products that provide the observed white-stained appearance in those areas. In black-stained regions, selective darkening of  $\alpha$ -Al dendrites is observed, while the interdendritic regions appear intact. Overlying solid precipitates are not seen in black-stained areas.



**Figure 3.8:** SVET current density maps at 24 hours alongside post-immersion images of 100 mm<sup>2</sup> of Zn55Al immersed in a near neutral solution of a) 5% w/v, b) 1% w/v, c) 0.2% w/v, and d) 0.04% w/v NaCl<sub>(aq)</sub> for 24 h.

**(a)** *White-Stained Area*



**(b)** *Black-Stained Area*

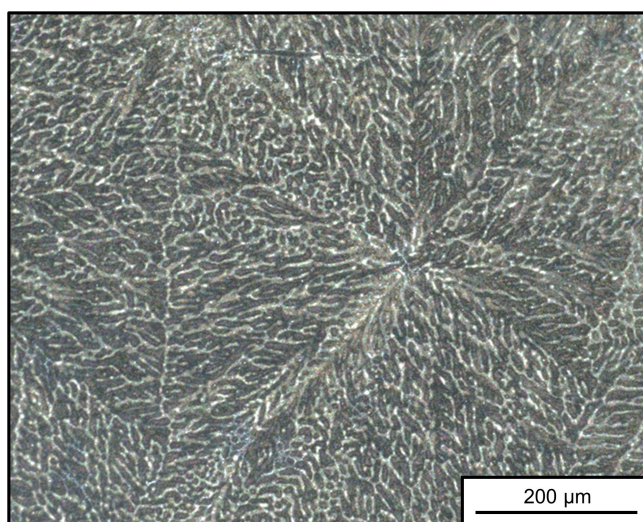


**Figure 3.9:** Optical microscope images of a) a white-stained area, and b) a black-stained area of Zn55Al post-immersion in 5% w/v  $\text{NaCl}_{(aq)}$  for 24 h.



### **3.3.4 Time-Lapse Microscopy (TLM)**

To gain extra information on the mechanism of chloride-induced localised corrosion and the effect of [NaCl] concentration, a TLM technique was used to provide an in-situ observation of the microstructure of Zn55Al during immersion in the extremes of [NaCl] concentration. Figure 3.10 shows the microstructural images taken at various times during immersion of Zn55Al in 5% and 0.04% [NaCl].

The image taken upon immersion in 5% [NaCl] (Figure 3.10a) resembles the microstructure shown in Figure 3.2: large, bright  $\alpha$ -Al dendrites separated by a dark interdendritic. However, as immersion time progresses, three main features are seen: a) multiple fixed localised areas of surface darkening (attack) that radially expand outwards during immersion; b) a separate, general background black-staining of the surface; and c) a region of apparent bright and uncorroded coating separating the local and general darkening regions.

The sites of localised darkening occur over both interdendritic and dendritic regions, consistent with the white-stained post-immersion photograph of Zn55Al (Figure 3.9a), which shows an anodic attack of dendrites. This suggests that the localised radial darkening is due to an anodic attack of the surface in those areas. The background black staining is consistent with the black staining in Figure 3.9b, suggesting that these are sites of cathodic activity. The sites of uncorroded coating between the localised attack and general black staining are visually consistent with areas of net zero  $j_z$  (white) in current density maps (Figure 3.5), suggesting that they possess neither anodic nor cathodic activity.

The activity described for 5% [NaCl] (Figure 3.10a) occurs quickly upon immersion. By 4 h, several extended localised anodes can be identified. Unfortunately, its fast rate of occurrence makes it difficult to determine how the localised anodes initiate. However, in the case of 0.04% [NaCl] (Figure 3.10b), the process is slower, so the initiation of stationary anodes is more easily observed. Initially, as for 5% [NaCl], the microstructure upon immersion in 0.04% [NaCl] resembles that seen in Figure 3.2. However, at 6 h, an attack of the interdendritic region can be seen. Later, at 12 h, it is observed that the attack has ex-



tended to an  $\alpha$ -Al dendrite adjacent to an area of interdendritic dissolution. Subsequently, as for 5% [NaCl], the site radially extends outwards for the remaining immersion time. At the end of immersion (18 h), only one area of the surface is occupied by a stationary anode, consistent with the current density map findings (Figure 3.5) of a decreasing propensity for stationary anodic activity to occur at lower [NaCl] concentrations.

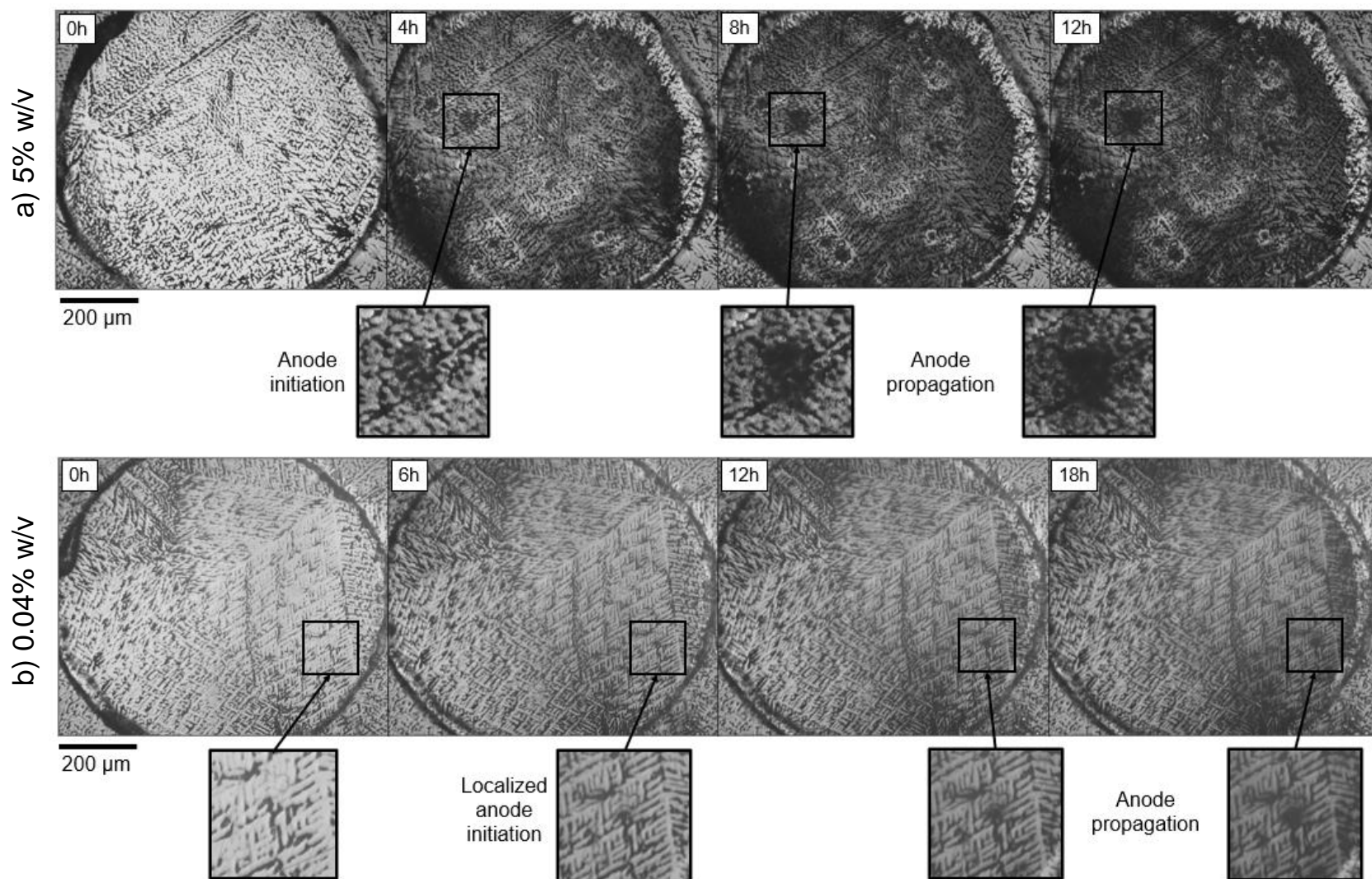


**Figure 3.10:** In-situ microstructural images taken at various times during exposure of Zn55Al to near neutral solutions of a) 5% w/v, and b) 0.04% w/v  $\text{NaCl}_{(aq)}$ .

### 3.3.5 Discussion

#### 3.3.5.1 Initial Immersion

For ZnAl galvanised steels in contact with near-neutral aqueous chloride solutions, the predominant anodic reactions that can occur are Zn and Al dissolution via Reactions 6.2 and 6.3, respectively [39].



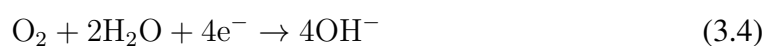
Upon immersion in aqueous chloride, it might be expected that areas rich in Al such as  $\alpha$ -Al dendrites would be preferentially attacked owing to its standard electrode potential being 0.9 V more negative (active) than Zn. However, the Volta potential map (Figure 3.4) shows that pre-immersion,  $\alpha$ -Al dendrites are up to 0.3 V more positive (inert) than the primary  $\eta$ -Zn phase of interdendritic, instead predicting an initial preferential attack of  $\eta$ -Zn. The difference can be ascribed to the nature of the oxides of Zn55Al's surface; the strong oxidation tendency of Al allows an Al hydr(oxide) film to form over dendrites, differentiating its oxide from the Zn hydr(oxide) film that forms over interdendritic regions [18]. Considering Al hydr(oxide) provides stronger passivity than Zn hydr(oxide), the  $\alpha$ -Al dendrites are less likely to undergo an electrochemical reaction, so they have a more positive (inert) relative Volta potential.

Indeed, as predicted by Volta potential mapping, the TLM results show that upon immersion in [NaCl], anodic attack occurs preferentially in interdendritic regions, most likely in  $\eta$ -Zn phases. An initial selective attack of the interdendritic is in agreement with several previous reports of Zn55Al exposed to aqueous and atmospheric chloride [17,18].

By comparing the TLM and SVET results, the dezincification process is most likely represented in current density maps as transient anodic activity. For example, in both cases, dezincification (TLM) and transient anodic activity (SVET) are seen immediately after

immersion. Additionally, it is shown in the TLM images for 0.04% [NaCl] that interdendritic attack occurs more slowly, akin to the trend of slower-moving and longer-living transient anodes seen at lower [NaCl] concentrations in current density maps. Regarding that trend, it is possible that in high concentration [NaCl] solutions, a local anode can couple to a larger surrounding cathodic area due to the solution's greater ionic conductivity ("throwing power"). As such, the rate of dissolution in an active interdendritic site is more rapid so corrosion products are deposited more quickly and block expansion of corrosion into the interior of the coating. This means that the anode must move onward to an adjacent and more anodically susceptible interdendritic area at a higher rate [21].

The SVET current density maps (Figure 3.5) show that localised anodic activity is set against a background of cathodic activity. The predominant cathodic reaction for ZnAl galvanised steels in contact with near-neutral aqueous chloride solutions is oxygen reduction via Reaction 3.4 [11]:



The surface of Al-rich phases are generally considered to be poor electrocatalysts for cathodic oxygen reduction [40]. For this reason, Zn-rich interdendritic areas of Zn55Al are more favourable sites for oxygen reduction than Al-rich dendrites and are the likely source of cathodic current density. Evidence for this is that not all areas of the immersed surface are anodically attacked in current density maps, meaning there is intact interdendritic where cathodic activity can occur. Additionally, the post-immersion photograph of a net cathodic area in Figure 3.9b shows a seemingly intact interdendritic phase.

### 3.3.5.2 Longer Immersion

At longer immersion times, a change in the mode of localised corrosion occurs. For example, the TLM shows an extension of anodic attack from interdendritic areas into dendrites, followed by a stable radial expansion. Likewise, the SVET shows that transient anodes can stabilise in one place. In both experimental methods, a higher [NaCl] concentration

causes the change to occur more quickly and gives rise to more localised anodic features. As such, the extension of anodic attack into dendrites is likely shown as the transition of transient anodes to stationary anodes in SVET current density maps. Regarding that transition, the selective interdendritic attack may leave areas of the Zn55Al surface porous, with subsequent metal ion hydrolysis acidifying the pore [41-43]. If the resulting pH is significantly low ( $< \text{pH } 4$ ), the passive oxide of  $\alpha$  dendrites can be destroyed, rendering the dendrite active and allowing stabilised anodic attack to proceed.

Generally, the results show that higher  $[\text{NaCl}]$  concentrations lead to a greater number of stable anodes that remain active. As initial corrosion of  $\eta$ -Zn of the Zn55Al surface leave areas enriched in Al (Al-rich dendrites remain), the trend could be described in terms of Al pitting, in which chloride concentration is pivotal in initiating and maintaining pit growth. In short, at a constant pH, the pitting potential ( $E_{\text{pit}}$ ) varies linearly with the logarithm of chloride concentration, indicating that higher  $[\text{NaCl}]$  concentrations correlate with a lower  $E_{\text{pit}}$  value [43,44]. Should  $E_{\text{pit}}$  be decreased so that it equates to  $E_{\text{corr}}$  then spontaneous pitting will occur, thus higher chloride concentrations increase the probability of pit initiation. Upon pitting, Al dissolves, releasing  $\text{Al}^{3+}$  ions which then hydrolyse, leading to an acidic environment that further drives dissolution. Meanwhile,  $\text{Cl}^-$  ions migrate into the developing pit to preserve charge neutrality. If the availability of  $\text{Cl}^-$  ions fall below a critical threshold, the pit may become passivated. This may explain why stationary anodes do not persist at lower  $[\text{NaCl}]$  concentrations, owing to the limited supply of chloride ions [45,46].

### **3.3.5.3 Post-Immersion Surfaces**

The SVET current density mapping and post-SVET photographs show that white staining is associated with areas of stationary anodic activity, and black staining is associated with background cathodic activity. A possible reason for the difference in appearance could be the variation in local solution conditions related to each half-cell reaction. For instance, due to the production of  $\text{H}^+$  by metal hydrolysis, areas undergoing stationary anodic attack are locally acidic. In contrast, due to the production of hydroxide ions from

oxygen reduction, areas of cathodic activity are locally alkaline. Previously, it has been shown that differences in solution pH can affect the appearance of Zn55Al surfaces. As demonstrated by Wallinder et al., Zn55Al surfaces are white-stained after immersion in deionised water at pH 1 due to the formation of Zn-rich corrosion products. However, they appear black-stained when exposed to deionised water at pH 13 due to the formation of bayerite,  $\text{Al}(\text{OH})_3$  [20].

The TLM of Zn55Al immersed in 5% [NaCl] (Figure 3.10a) reveals an area of intact coating between cathodic areas (high pH) and local anodes (low pH). It is possible that due to an inevitable pH gradient between the separated cathodic and anodic regions, the intact area has a near-neutral local pH and remains passive, as confirmed by SVET current density maps showing zero net current density between sites of anodic and cathodic activity.

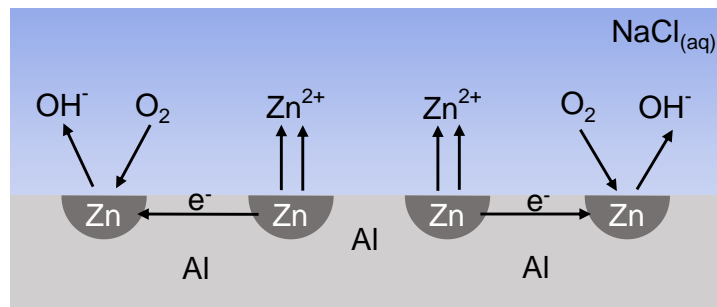
Based on the above, the deposition of white corrosion products could tentatively be attributed to localised anodes creating a locally acidic pH from which Zn-rich white corrosion products such as  $\text{Zn}_5(\text{OH})_8\text{Cl}_2$  are stable [21]. About black staining, it is possible that upon immersion in [NaCl], ejection of  $\text{Al}^{3+}$  and  $\text{Zn}^{2+}$  from anodic sites towards cathodic sites results in the selective precipitation of crystalline  $\text{Al}(\text{OH})_3$  on top of dendrite's oxide layer, but amorphous  $\text{Zn}(\text{OH})_2$  over interdendritic regions; the amorphous nature of  $\text{Zn}(\text{OH})_2$  allowing net cathodic activity on interdendritic areas to continue, keeping the phase intact (Figure 3.9b) [12,20]. However, the local alkaline conditions produced at those cathodic sites enable a degree of breakdown of the oxide layer of nearby dendrites, rendering them active. Consequently, dissolved particles can become embedded into the dendrite corrosion product layer, making the layer appear black via particle-embedded optical effects, as first described by Mie et al [47,48].

#### **3.3.5.4 Mechanism of Zn55Al Localised Corrosion in Aqueous Chloride**

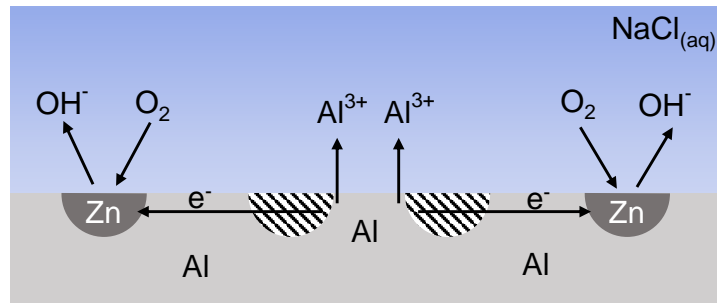
A proposed mechanism of Zn55Al localised corrosion in near-neutral aqueous chloride is provided in Figure 3.11. Upon immersion (Figure 3.11a), anodic dissolution occurs preferentially in  $\eta$ -Zn phases of the interdendritic and is coupled to cathodic oxygen re-

duction at other interdendritic sites. The activity is transient (i.e. moves position around the surface), leaving parts of the coating porous and enriched in Al. At later immersion times (Figure 3.11b), if the pH of an attacked interdendritic area is significantly low ( $< \text{pH } 4$ ), the oxide layer of Al-rich dendrites may be destroyed and allow anodic dissolution to extend into them, producing stationary, localised anodes. This process is most prevalent at higher  $[\text{NaCl}]$  concentrations due to the greater availability of chloride ions in solution to assist in initiating and maintaining the local anode (Figure 3.11c).

(a) Interdendritic dissolution



(b) Dendrite dissolution



(c) Anode Stabilisation

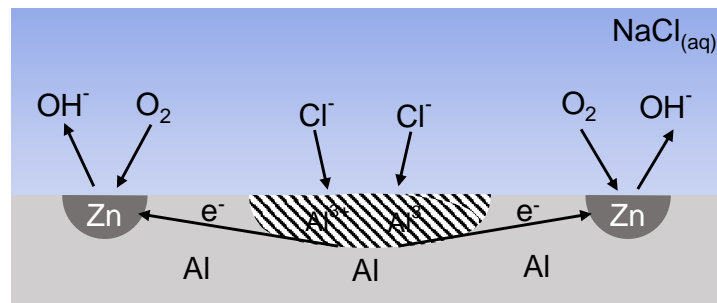


**Figure 3.11:** Proposed mechanism of aqueous localised corrosion of Zn55Al in  $NaCl_{(aq)}$ .



### **3.3.6 Conclusion**

A combination of SKPFM, SVET, optical microscopy, and TLM was used to propose a mechanism for the localised corrosion of Zn55Al in near-neutral aqueous chloride. Before immersion, the  $\eta$ -Zn phases of the interdendritic areas of the Zn55Al microstructure were more susceptible to anodic attack than  $\alpha$ -Al phases, as shown by SKPFM. Indeed, TLM results showed that Zn-rich regions were preferentially attacked at the early stages of immersion, while the SVET showed that the attack may be associated with transient (moving) anodes. At later immersion times, as demonstrated by TLM and optical microscopy, the anodic attack extended into dendrites, leading to an advanced local attack; this transition likely being shown by the SVET as transient anodes becoming stationary anodes of fixed position.

Regarding the appearance of the Zn55Al surface post-immersion, areas of the surface that underwent stationary anodic attack were associated with surface white staining, while areas of the surface that were net cathodes were associated with surface black staining. The difference probably resulted from a difference in local solution pH, with local anodes of acidic pH forming white corrosion products and net cathodes giving an alkaline pH that enabled the formation of a layer of  $\text{Al}(\text{OH})_3$  embedded with light-scattering particles.

Furthermore, the effect of aqueous chloride concentration on the mechanism was examined using the SVET. It was found that higher concentrations of sodium chloride stabilise anodic attack at an earlier immersion time and over a larger surface area. As a result, higher cumulative anodic current density values were recorded. It was tentatively suggested that due to early attack of  $\eta$ -Zn, areas of the surface become enriched in Al, resulting in stationary anode initiation and maintenance similar to that of pure Al.

### 3.3.7 References

1. H.E. Townsend, L. Allegra, R.J. Dutton, S.A. Kriner, Hot-dip coated sheet steel: a review, *Mater. Perform.* 25 (1986) 36–46.
2. A.R. Moreira, Z. Panossian, P.L. Camargo, M.F. Moreira, I.C. Da Silva, J.E. Ribeiro De Carvalho, Zn/55Al coating microstructure and corrosion mechanism, *Corros. Sci.* 48 (2006) 564–576.
3. E. Palma, J.M. Puente, M. Morcillo, The atmospheric corrosion mechanism of 55%Al-Zn coating on steel, *Corros. Sci.* 40 (1998) 61–68.
4. H. Townsend, T.C. Consultants, Thirty year atmospheric corrosion performance of 55 % aluminum-zinc alloy- coated sheet steel, (2015).
5. A.R. Marder, The metallurgy of zinc-coated steel, *Prog. Mater. Sci.* 45 (2000) 191–271.
6. J.H. Selverian, M.R. Notis, A.R. Marder, The microstructure of 55 w/o Al-Zn-Si (Galvalume) hot dip coatings, *Journal of Materials Engineering.* 9 (1987) 133–140.
7. H.N. McMurray, Localised corrosion behavior in aluminum-zinc alloy coatings investigated using the scanning reference electrode technique, *Corrosion.* 57 (2001) 313–322.
8. C.I. Elsner, P.R. Seré, A.R. di Sarli, B.M. Rosales, Atmospheric Corrosion of Painted Galvanized and 55%Al-Zn Steel Sheets: Results of 12 Years of Exposure, *International Journal of Corrosion.* 2012 (2012) 16.
9. K.G. Watkins, R.D. Jones, P.G. Beahan, Electrochemical investigation of the corrosion rate of 55 aluminium-zinc alloy coated steel, *Mater. Lett.* 8 (1989) 26–30.
10. C.F. Glover, G. Williams, Inhibition of Localised Corrosion of Hot Dip Galvanized Steel by Phenylphosphonic Acid, *J. Electrochem. Soc.* 164 (2017) C407–C417.
11. D.A. Worsley, H.N. McMurray, J.H. Sullivan, I.P. Williams, Quantitative Assessment of Localised Corrosion Occurring on Galvanized Steel Samples Using the Scanning Vibrating Electrode Technique, *Corrosion.* 60 (2004) 437–447.

12. H.N. McMurray, Localised Corrosion Behavior in Aluminum-Zinc Alloy Coatings Investigated Using the Scanning Reference Electrode Technique, *Corrosion*. 57 (2001) 313–322.
13. N.C. Barnard, S.G.R. Brown, H.N. McMurray, Modelling the Localised corrosion effects experienced by zinc-4.5wt.% aluminium steel coatings in 5% NaCl solution, in: C.A. Brebbia, V.G. DeGiorgi, R.A. Adey, *Simulation of Electrochemical Processes*. (2005) 99–108.
14. D. Thierry, D. Persson, N. Le Bozec, Atmospheric corrosion of zinc and zinc alloyed coated steel, in: *Encyclopedia of Interfacial Chemistry: Surface Science and Electrochemistry*, Elsevier, (2018) 55–78.
15. S. Thomas, N. Birbilis, M.S. Venkatraman, I.S. Cole, Corrosion of Zinc as a Function of pH, *Corrosion*. 68 (2012) 015009–1.
16. C. Cachet, R. Wiart, Reaction mechanism for zinc dissolution in chloride electrolytes, *J. Electroanal. Chem. Interfacial. Electrochem.* 129 (1981) 103.
17. X. Zhang, T.N. Vu, P. Volovitch, C. Leygraf, K. Ogle, I.O. Wallinder, The initial release of zinc and aluminum from non-treated Galvalume and the formation of corrosion products in chloride containing media, *Appl. Surf. Sci.* 258 (2012) 4351–4359.
18. D. Persson, D. Thierry, N. LeBozec, Corrosion product formation on Zn55Al coated steel upon exposure in a marine atmosphere, *Corros. Sci.* 53 (2011) 720–726.
19. P.R. Seré, M. Zapponi, C.I. Elsner, A.R. di Sarli, Comparative corrosion behaviour of 55Aluminium-Zinc alloy and Zinc hot-dip coatings deposited on low carbon steel substrates, *Corros. Sci.* 40 (1998) 1711–1723.
20. I.O. Wallinder, W. He, P.E. Augustsson, C. Leygraf, Characterization of black rust staining of unpassivated 55% Al–Zn alloy coatings. Effect of temperature, pH and wet storage, *Corros. Sci.* 41 (1999) 2229–2249.
21. T. Guo, C. Liu, C. Ran, X. Dong, Effects of spangle size on performances of hot-dip 55%Al-Zn alloy coating, *Int. J. Electrochem. Sci.* 13 (2018) 9505–9519.

22. J. Elvins, J.A. Spittle, D.A. Worsley, Relationship between microstructure and corrosion resistance in Zn–Al alloy coated galvanised steels, *Corrosion Engineering, Science and Technology*. 38 (2013) 197–204.
23. D.A. Worsley, H.N. McMurray, J.H. Sullivan, I.P. Williams, Quantitative Assessment of Localised Corrosion Occurring on Galvanized Steel Samples Using the Scanning Vibrating Electrode Technique, *Corrosion*. 60 (2004) 437–447.
24. A.P. dos Santos, S.M. Manhabosco, J.S. Rodrigues, L.F.P. Dick, Comparative study of the corrosion behavior of galvanized, galvanealed and Zn55Al coated interstitial free steels, *Surf. Coat. Technol.* 279 (2015) 150–160.
25. K.B. Deshpande, Validated numerical modelling of galvanic corrosion for couples: Magnesium alloy (AE44)–mild steel and AE44–aluminium alloy (AA6063) in brine solution, *Corros. Sci.* 52 (2010) 3514–3522.
26. N. Wint, K. Khan, J.H. Sullivan, H.N. McMurray, Concentration Effects on the Spatial Interaction of Corrosion Pits Occurring on Zinc in Dilute Aqueous Sodium Chloride, *J. Electrochem. Soc.* 166 (2019) C3028–C3038.
27. J. Sullivan, S. Mehraban, J. Elvins, In situ monitoring of the microstructural corrosion mechanisms of zinc-magnesium-aluminium alloys using time lapse microscopy, *Corros. Sci.* 53 (2011) 2208–2215.
28. S. Böhm, H.N. McMurray, S.M. Powell, D.A. Worsley, Photoelectrochemical investigation of corrosion using scanning electrochemical techniques, *Electrochim. Acta*. 45 (2000) 2165–2174.
29. G. Williams, H. Neil McMurray, Localised Corrosion of Magnesium in Chloride-Containing Electrolyte Studied by a Scanning Vibrating Electrode Technique, *J. Electrochem. Soc.* 155 (2008) C340.
30. A.C. Bastos, M.C. Quevedo, O. v Karavai, M.G.S. Ferreira, On the Application of the Scanning Vibrating Electrode Technique (SVET) to Corrosion Research, *J. Electrochem. Soc.* 164 (2017) C973–C990.

31. H.S. Isaacs, The Effect of Height on the Current Distribution Measured with a Vibrating Electrode Probe, *J. Electrochem. Soc.* 138 (1991) 722–728.
32. H.N. McMurray, S.M. Powell, D.A. Worsley, Mechanistic changes in cut edge corrosion induced by variation of inhibitor pigmentation in organically coated galvanised steel, *Corrosion Engineering, Science and Technology.* 36 (2013) 42–48.
33. D.A. Worsley, H.N. McMurray, A. Belghazi, Determination of localised corrosion mechanisms using a scanning vibrating reference electrode technique, *Chemical Communications.* (1997) 2369–2370.
34. G.W.C. Kaye, T.H. Laby, *Tables of Physical and Chemical Constants*, Longman, London, 1986.
35. J. Sullivan, S. Mehraban, J. Elvins, In situ monitoring of the microstructural corrosion mechanisms of zinc–magnesium–aluminium alloys using time lapse microscopy, *Corros. Sci.* 53 (2011) 2208–2215.
36. J. Sullivan, N. Cooze, C. Gallagher, T. Lewis, T. Prosek, D. Thierry, In situ monitoring of corrosion mechanisms and phosphate inhibitor surface deposition during corrosion of zinc-magnesium-aluminium (ZMA) alloys using novel time-lapse microscopy, *Faraday. Discuss.* 180 (2015) 361–379.
37. A.R. Marder, The metallurgy of zinc-coated steel, *Prog. Mater. Sci.* 45 (2000) 191–271.
38. N. Wint, D. Eaves, E. Michailidou, A. Bennett, J.R. Searle, G. Williams, H.N. McMurray, The kinetics and mechanism of filiform corrosion occurring on zinc-aluminium-magnesium coated steel, *Corros. Sci.* 158 (2019) 108073.
39. H.N. McMurray, S.R. Magill, B.D. Jeffs, Scanning reference electrode technique as tool for investigating localised corrosion phenomena in galvanised steels, *Iron-making and Steelmaking.* 23 (1996) 183–188.
40. H. Dafydd, D.A. Worsley, H.N. McMurray, The kinetics and mechanism of cathodic oxygen reduction on zinc and zinc–aluminium alloy galvanized coatings, *Corros. Sci.* 47 (2005) 3006–3018.

41. T. Hagyard, J.R. Williams, Potential of aluminium in aqueous chloride solutions. Part 1, Transactions of the Faraday Society. 57 (1961) 2288–2294.
42. D.A. Vermilyea, Concerning the Critical Pitting Potential, J Electrochem Soc. 118 (1971) 529.
43. J.R. Galvele, Transport Processes and the Mechanism of Pitting of Metals, J. Electrochem. Soc. 123 (1976) 464–474.
44. E. McCafferty, The electrode kinetics of pit initiation on aluminum, Corros. Sci. 37 (1995) 481–492.
45. G.S. Frankel, Pitting Corrosion of Metals: A Review of the Critical Factors, J. Electrochem. Soc. 145 (1998) 2186–2198.
46. E. McCafferty, Sequence of steps in the pitting of aluminum by chloride ions, Corros. Sci. 45 (2003) 1421–1438.
47. X.D. Wang, Z.X. Cui, H.J. Zhang, X. Zheng, B. Chen, Z.S. Wang, A new proof of Mie effect in light scattering, Optik. 124 (2013) 6194–6196.
48. G. Mie, Beiträge zur Optik trüber Medien, speziell kolloidaler Metallösungen, Ann Phys. 330 (1908) 377–445.

## **Chapter 4**

# **Localised Corrosion Inhibition of ZnAl Galvanised Steels by 2-(1,3-Benzothiazol-2-ylthio) succinic acid**

## 4.1 Introduction

As shown in Chapter 3, even ZnAl galvanised steels with high Al content, such as Zn55Al, are susceptible to severe localised corrosion when exposed to chloride-containing electrolytes. This poses a significant challenge for industries such as construction that require their ZnAl galvanised steel products to have long lifetimes of up to 30 years or more [1,2]. Therefore, ZnAl galvanised steel products are often protected by organic coating systems incorporating primer layers containing corrosion inhibitors.

In the past, the corrosion inhibitors used in such systems were based on sparingly soluble hexavalent chromium salts, primarily strontium chromate and zinc chromate [3–7]. However, the use of hexavalent chromium has become limited under the REACH directive due to its acute toxicity and carcinogenicity [8–11]. Unfortunately, the efficacy of chromate-free systems has not yet matched that of previous chromate-containing systems. Hence, the identification of effective chromate-free alternatives is essential.

Recently, organic molecules, particularly those containing azole moieties, have been identified as potential alternatives due to their reduced toxicity. Azole moieties are five-membered aromatic rings with a nitrogen atom and at least one other heteroatom, such as a nitrogen, oxygen, or sulphur atom [12]. The N, O, or S heteroatoms are electron-rich, enhancing the molecule-to-molecule interactions required for protective film formation on metal surfaces [13–16].

Several azole compounds have been shown to protect galvanised steel surfaces in aqueous chloride solutions [16,17]. Kartsonakis et al. demonstrated the promising efficiency of 2-mercaptobenzothiazole (MBT) and 5-amino-1,3,4-thiadiazole-2-thiol (ATT) towards HDG immersed in 50 mM NaCl over seven days [18]. Similarly, 2-amino-4-methylthiazole (2AT-Me) has been shown to reduce the anodic and cathodic current densities of HDG in 100 mM NaCl [16,17]. Both studies suggested that the electron-rich heteroatoms of the azole ring acted as areas of adsorption to the HDG surface. Elsewhere, benzotriazole (BTA) has been shown to form polymeric  $[\text{Zn}(\text{BTA})_2]_n$  complexes with HDG, thus reducing its corrosion rate [19–22].



Considering the promise of azole compounds as corrosion inhibitors for ZnAl galvanised steels, this chapter investigates another azole compound, namely 2-(1,3-benzothiazol-2-ylthio) succinic acid (BTSA). BTSA is a non-toxic, environmentally friendly organic molecule selected due to its unique chemical structure (Figure 4.1) that contains a succinic acid group in addition to its electron-rich sulphur-containing azole moiety. The succinic acid group is a diprotic acid that ionises readily in aqueous solution, giving the succinate (dicarboxylate) anion of BTSA,  $\text{BTSA}^{2-}$ . Consequently, BTSA has increased aqueous solubility compared to azole-only organic compounds and is therefore more compatible with water-based coating systems. In addition, previous studies have shown that succinate can inhibit metal surface corrosion in aqueous chloride solutions, potentially enhancing inhibition in this case [23].

Given the potential of BTSA as a non-toxic corrosion inhibitor, this chapter describes an investigation into its inhibitory performance towards the localised corrosion of HDG (0.15-0.25 wt.% Al), Galfan (4.5 wt.% Al) and Zn55Al surfaces (55 wt.% Al) in 1% w/v  $\text{NaCl}_{(\text{aq})}$ . In doing so, the scanning vibrating electrode technique (SVET) and linear polarisation resistance (LPR) methods provide time-dependent inhibitor efficiencies of BTSA dosed at varying concentrations into the aqueous chloride electrolyte. Furthermore, possible inhibition mechanisms are postulated based on open-circuit potential (OCP) results and potentiodynamic polarisation (PP) experiments.

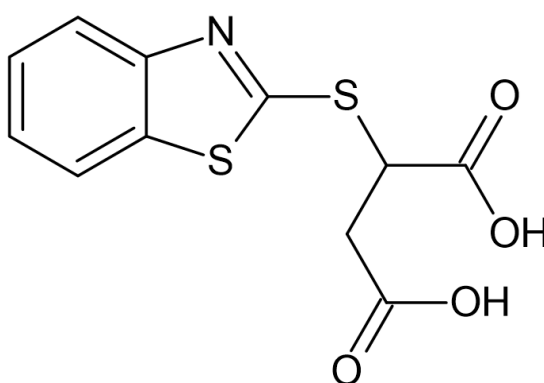


**Figure 4.1:** *The chemical structure of 2-(1,3-benzothiazol-2-ylthio) succinic acid, BTSA.*

## 4.2 Experimental Details

### 4.2.1 Materials

Hot dip galvanised steel (HDG) and Galfan substrates were supplied by TATA Steel UK, and Zn55Al substrate was supplied by Becker Industrial Coatings Ltd. In each case, the substrate consisted of 0.7 mm thick mild steel with a 20  $\mu\text{m}$  Zn-based coating applied to each side. In the case of HDG, the coating included 0.15 wt.% Al. For Galfan, the coating included 4.5 wt.% Al, and for Zn55Al 55 wt.% Al. The as received substrates were cut into 50 mm x 50 mm coupons and cleaned using an aqueous slurry of 5  $\mu\text{m}$  polishing alumina. They were then rinsed with deionised water, degreased in ethanol, and air-dried. 1% w/v  $\text{NaCl}_{(\text{aq})}$  was used to initiate corrosion. Varying concentrations of BTSA were added to 1% w/v  $\text{NaCl}_{(\text{aq})}$  solution. Before each experiment, the solutions were buffered to pH 7 by adding  $\text{NaOH}_{(\text{aq})}$  dropwise.

### 4.2.2 Methods

#### 4.2.2.1 Scanning Vibrating Electrode Technique (SVET)

The SVET was used to provide temporally and spatially resolved corrosion current density data associated with the localised corrosion of each substrate immersed in 1% w/v  $\text{NaCl}_{(\text{aq})}$  solutions containing varying concentrations of BTSA. Details about the SVET instrumentation and operating procedure can be found in Section 2.2.1 and elsewhere [24-29]. In brief, PTFE tape was used to expose a 100 mm<sup>2</sup> square area of the sample under investigation. Data was obtained at 100  $\mu\text{m}$  intervals in both the x and y direction immediately after immersion and at 30-minute intervals thereafter. The dissolved carbon dioxide and oxygen concentrations within the electrolyte were taken to be those associated with the equilibrium concentration values for air-saturated water ( $1.32 \times 10^{-5} \text{ mol dm}^{-3}$  and  $2.8 \times 10^{-4} \text{ mol dm}^{-3}$ , respectively) [30]. After 6 h, the sample was removed from the electrolyte, washed with deionised water, rinsed with acetone, and air-dried. Photographs of the exposed area were taken to correlate the surface corrosion product's presence with the

current density values recorded. The outputted dataset consisted of 10,000  $V_{pp}$  values for each of the 12 scans. These were converted to current density values,  $j_z$ , using a calibration method described in Section 2.2.1.  $J_z$  values were then plotted to produce current density maps for each time interval using OriginLab's Origin data analysis and graphing software.

#### **4.2.2.2 Electrochemical Characterisation**

Electrochemical measurements were performed in 1% w/v  $\text{NaCl}_{(aq)}$  solutions containing BTSA of varying concentrations using a 3-electrode arrangement in conjunction with a Gamry Reference 620 potentiostat. A 100 mm<sup>2</sup> square exposed area of HDG, Galfan or Zn55Al constituted the working electrode. The potential was varied with respect to a saturated calomel reference electrode (SCE). A platinum foil counter electrode was used to complete the circuit.

#### **4.2.2.3 Linear Polarisation Resistance (LPR)**

To compliment SVET results, LPR was used to determine time-dependent inhibitor efficiency values for each substrate. Samples were polarised by  $\pm 15$  mV concerning the OCP at a scan rate of 0.1667 mV. Polarisation resistance ( $R_p$ ) values were calculated between  $\pm 5$  mV of the OCP at each time interval. Subsequently, time-dependent inhibitor efficiency ( $\eta$ ) values were calculated every 30 minutes for 6 h.

#### **4.2.2.4 Open Circuit Potential (OCP) and Potentiodynamic Polarisation (PP)**

OCP and PP experiments were conducted to obtain information about BTSA's inhibition mechanism. In OCP experiments, the working electrode's OCP was recorded every 30 seconds for 60 minutes. In the PP experiments, the working electrode was left at an open circuit for 10 minutes before being polarised by 0.3 V either cathodically or anodically at a scan rate of 0.1667 mV s<sup>-1</sup>.

## 4.3 Results

### 4.3.1 HDG

#### 4.3.1.1 SVET

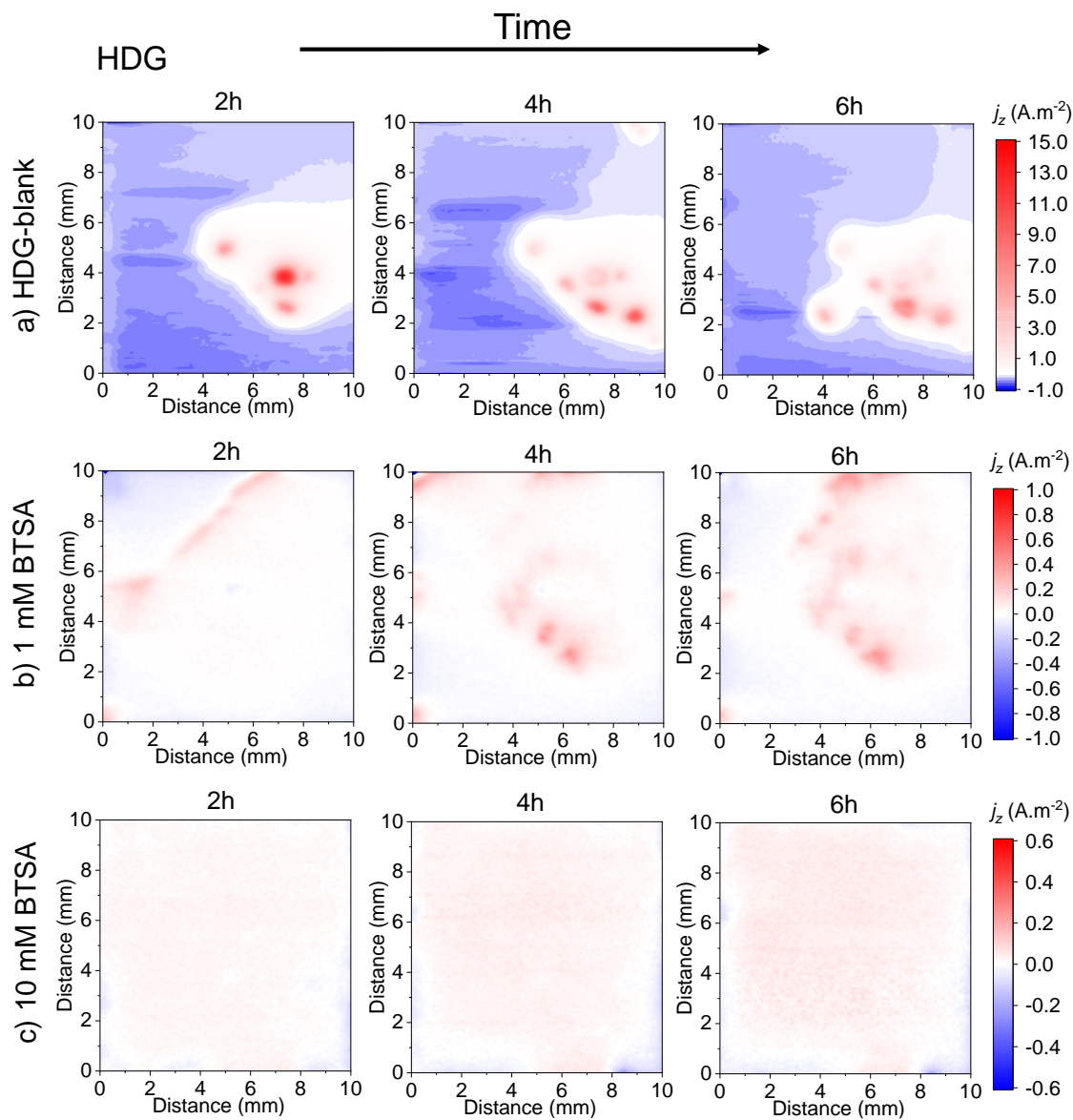
To provide a qualitative and semi-quantitative assessment of the inhibitory performance of BTSA, the SVET was used to follow the localised corrosion behaviour of each ZnAl substrate in aqueous chloride dosed with varying concentrations of BTSA.

Figure 4.2 shows SVET-derived current density maps at 2 h, 4 h and 6 h during immersion of HDG in 1% w/v NaCl<sub>(aq)</sub> containing BTSA concentrations of a) uninhibited, b) 1 mM BTSA, and c) 10 mM BTSA. The maps of uninhibited-HDG (Figure 4.2a) show intense areas of stationary localised anodic activity (red) in the centre of the exposed area set against a background of cathodic activity (blue). Consistent with previous reports for uninhibited-HDG [31,32], at each time interval the number of stationary anodes observed increases. Additionally, once initiated, the anodes remain active for the remaining immersion time. Regarding their magnitude, peak anodic  $j_z$  values of approximately 14 A m<sup>-2</sup> are recorded after 2 h. The background general cathodic activity possesses cathodic  $j_z$  values ranging between -0.5 A m<sup>-2</sup> and -1.0 A m<sup>-2</sup>.

In the presence of 1 mM BTSA (Figure 4.2b), the SVET current density maps again show localised anodic activity against background cathodic activity; however, the peak anodic  $j_z$  values recorded (approximately 1 A m<sup>-2</sup>) are more than one order of magnitude lower than that of uninhibited-HDG. In addition, the corresponding background cathodic activity possesses cathodic  $j_z$  values up to five times less than uninhibited-HDG (approximately -0.2 A m<sup>-2</sup>). This concurrent reduction in anodic and cathodic  $j_z$  is expected because, in open circuit conditions, anodic and cathodic currents are equal. Therefore, if the current density of one-half reaction decreases, the other must also decrease.

Finally, in the case of 10 mM BTSA (Figure 4.2c) a complete suppression of localised corrosion is observed. Instead, the current density maps show low-magnitude general corrosion throughout the immersion time. As a result, a peak anodic  $j_z$  value of 0.01 A m<sup>-2</sup>

is recorded, two orders of magnitude lower than that of uninhibited-HDG. Subsequently, the corresponding cathodic  $j_z$  values recorded are approximately  $-0.1 \text{ A m}^{-2}$ , up to 10 times lower than for uninhibited-HDG.



**Figure 4.2:** SVET current density maps at various times during the immersion of a  $100 \text{ mm}^2$  area of HDG in  $1\% \text{ w/v NaCl}_{(aq)}$  pH 7 containing BTSA concentrations of a) uninhibited, b)  $1 \text{ mM}$ , and c)  $10 \text{ mM}$ .

Figure 4.3 shows photographs of the exposed HDG surfaces after each SVET experiment. For both uninhibited-HDG (Figure 4.3a) and 1 mM BTSA (Figure 4.3b), the post-immersion photos show localised areas of white corrosion product set against an apparent uncorroded background; the white regions corresponding to the position of localised anodes in SVET current density maps, and the uncorroded background corresponding to background cathodic activity. The post-immersion photograph of 10 mM BTSA (Figure 4.3c) shows only a few, very small localised areas of white corrosion product in an otherwise feature free surface and consistent with the absence of localised anodes in its SVET current density maps (Figure 4.2c). The few small local white areas are likely due to very short-lived anodes which may have not measured if they occurred while the SVET was not scanning.

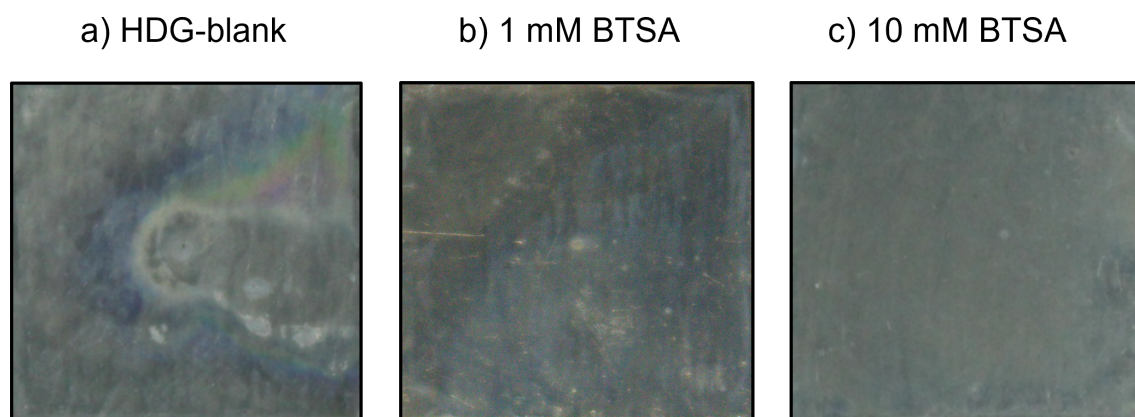


**Figure 4.3:** Post-SVET photographs of the 100 mm<sup>2</sup> exposed surfaces of HDG immersed for 6h in 1% w/v NaCl<sub>(aq)</sub> pH 7 containing BTSA concentrations of a) uninhibited, b) 1 mM, and c) 10 mM.

Table 4.1 shows time-dependent cumulative area averaged anodic current density ( $J_a$ ) values and corresponding inhibitor efficiency ( $\eta$ ) values derived from the SVET current density maps (Figure 4.2). Cumulative  $J_a$  values are calculated by summing the total anodic current density ( $J_{a(t)}$ ) recorded between scans, while  $\eta$  at time,  $t$  is calculated by:

$$\eta_{(t)} = \left( 1 - \left( \frac{CJ_{a(BTSA)}}{CJ_{a(0)}} \right) \right) \times 100 \quad (4.1)$$

where  $CJ_{a(BTSA)}$  is the cumulative  $J_a$  of a BTSA-inhibited sample, and  $CJ_{a(0)}$  is the cumulative  $J_a$  of an uninhibited sample.

As shown in the table, BTSA additions decrease the cumulative  $J_a$  of HDG. During the initial 2 h of immersion in the presence of 1 mM and 10 mM BTSA,  $\eta$  values above 90% are recorded. However,  $\eta$  values decrease at longer immersion times to 78% and 87%, respectively, after 6 h. This decline might indicate a breakdown of inhibition over time.

**Table 4.1:** SVET-derived time-dependent values of cumulative  $J_a$  and corresponding inhibitor efficiency,  $\eta$  of HDG immersed in 1% w/v  $NaCl_{(aq)}$  pH 7 containing BTSA concentrations of a) uninhibited, b) 1 mM, and c) 10 mM.

| HDG SVET | Uninhibited   | 1 mM BTSA   |            | 10 mM BTSA  |            |
|----------|---|---|------------|---|------------|
| Time / h | Cumulative<br>anodic current<br>density / A m <sup>-2</sup> | Cumulative<br>anodic current<br>density / A m <sup>-2</sup> | $\eta$ / % | Cumulative<br>anodic current<br>density / A m <sup>-2</sup> | $\eta$ / % |
| 0.5      | 0.18  | 0.01  | 93         | 0.01  | 93         |
| 1.0      | 0.41  | 0.03  | 93         | 0.03  | 93         |
| 1.5      | 0.62  | 0.05  | 92         | 0.05  | 91         |
| 2.0      | 0.82  | 0.08  | 91         | 0.08  | 90         |
| 2.5      | 1.06  | 0.12  | 89         | 0.11  | 90         |
| 3.0      | 1.32  | 0.17  | 87         | 0.14  | 90         |
| 3.5      | 1.51  | 0.23  | 85         | 0.16  | 89         |
| 4.0      | 1.70  | 0.29  | 83         | 0.21  | 88         |
| 4.5      | 1.87  | 0.35  | 81         | 0.24  | 87         |
| 5.0      | 2.06  | 0.41  | 80         | 0.27  | 87         |
| 5.5      | 2.24  | 0.48  | 79         | 0.29  | 87         |
| 6.0      | 2.43  | 0.54  | 78         | 0.32  | 87         |

A further SVET experiment was conducted to follow the performance of BTSA in inhibiting active localised corrosion of HDG. Initially, HDG was immersed in a near-neutral solution of 1% w/v  $NaCl_{(aq)}$  to initiate localised corrosion, with SVET scans conducted

every 30 minutes for 3 h. However, after 3 h, 10 mM BTSA was added to the solution, and any changes to localised corrosion were followed by further scans every 30 minutes for 3 h.

The SVET current density maps of the HDG surface before and after the addition of BTSA are presented in Figure 4.4. The map obtained 30 minutes before the addition of BTSA shows several areas with intense localised anodic activity (red) and  $j_z$  values greater than  $4.0 \text{ A m}^{-2}$ . However, upon adding the BTSA (10 mM), these localised anodes are no longer visible in the current density map. Instead, the anodic activity becomes more general with maximum anodic  $j_z$  values of  $0.5 \text{ A m}^{-2}$  recorded; the change demonstrating that BTSA quickly passivates local anodes.

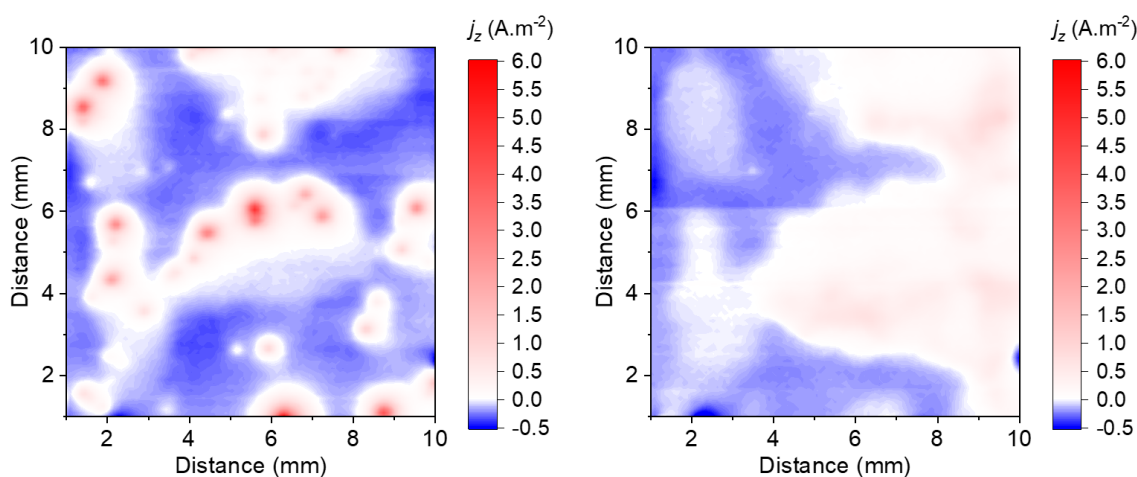


**Figure 4.4:** SVET current density maps of the immersed surface of HDG a) 0.5 h before, and b) 0.5 h after the addition at 3 h of 10 mM BTSA to an initial 1% w/v  $\text{NaCl}_{(aq)}$  pH 7 solution.

To compare the magnitude of anodic activity before and after the BTSA addition, a plot of average anodic  $j_z$  against time is provided in Figure 4.5. The average  $j_z$  values are calculated by adding all positive (anodic)  $j_z$  data points and then dividing by the total number of  $j_z$  data points of the scan. During the first 2.5 h of uninhibited immersion, the average anodic  $j_z$  steadily increases to a maximum of  $0.55 \text{ A m}^{-2}$ . However, upon the



addition of BTSA, the average anodic  $j_z$  drops sharply to  $0.12 \text{ A m}^{-2}$ , a 78% reduction that suggests an immediate inhibition by BTSA toward the freely locally corroding HDG surface. Further, inhibition is maintained for the remaining immersion time, with the average anodic  $j_z$  recorded at 6 h ( $0.22 \text{ A m}^{-2}$ ) being 60% lower than before the addition.

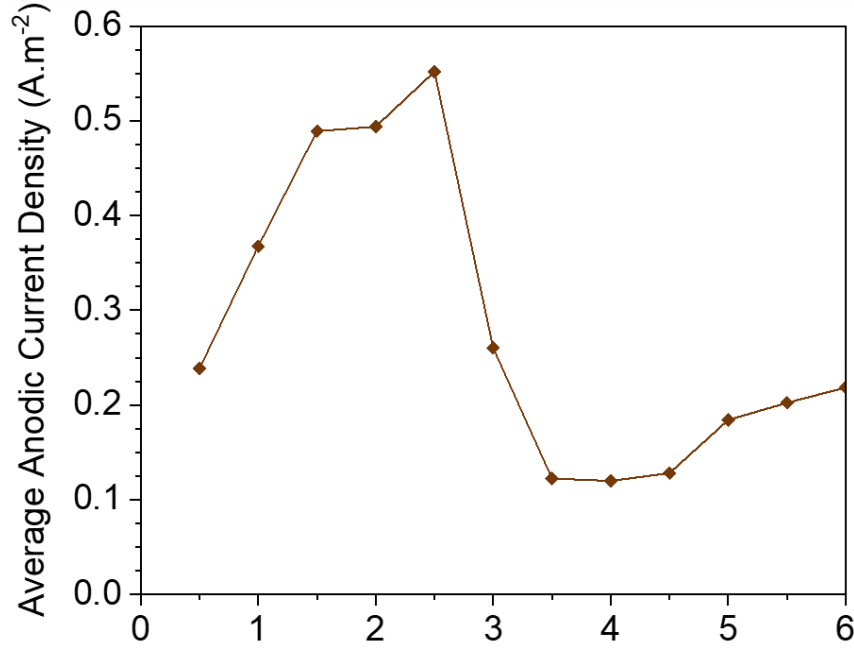


**Figure 4.5:** SVET-derived average anodic current density as a function of time of a  $100 \text{ mm}^2$  exposed area of HDG immersed in 1% w/v  $\text{NaCl}_{(\text{aq})}$  pH 7 solution. After 3 h, 10 mM BTSA was added to the solution.

#### 4.3.1.2 LPR

For comparison to the SVET results, the time-dependent inhibitor performance of BTSA was also assessed through the LPR method described in Chapter 2. Table 4.2 displays measurements of polarisation resistance ( $R_p$ ) recorded at 30 minute intervals for HDG immersed in 1% w/v  $\text{NaCl}_{(\text{aq})}$  pH 7 solutions containing varying concentrations of BTSA. Values of  $\eta$ , at time,  $t$ , are calculated from  $R_p$  values using Equation 4.2:

$$\eta_{(t)} = \frac{R_{p,i} - R_{p,0}}{R_{p,i}} \times 100 \quad (4.2)$$

where  $R_{p,0}$  is the polarisation resistance without inhibitor (uninhibited) and  $R_{p,i}$  is the polarisation resistance with inhibitor present.  $R_p$  is inversely proportional to corrosion rate, hence a higher  $R_p$  indicates slower rates.

In agreement with the SVET results, HDG's corrosion resistance improves in the presence of BTSA, with  $R_p$  values approximately one order of magnitude greater than those obtained without BTSA. As such, time-averaged  $\eta$  values of  $89 \pm 3\%$  and  $93 \pm 2\%$  are calculated for 1 mM BTSA and 10 mM BTSA, respectively. The low uncertainty associated with both values demonstrates that the inhibition is maintained throughout immersion.

**Table 4.2:** LPR-derived time-dependent values of polarisation resistance,  $R_p$ , and corresponding inhibitor efficiency,  $\eta$ , of HDG immersed in 1% w/v  $\text{NaCl}_{(aq)}$  pH7 containing BTSA concentrations of a) uninhibited, b) 1 mM, and c) 10 mM.

| HDG LPR  | Uninhibited                               | 1 mM BTSA                                 |             | 10 mM BTSA                                |             |
|----------|---|---|-------------|---|-------------|
| Time / h | $R_p / \text{k}\Omega\cdot\text{cm}^{-2}$ | $R_p / \text{k}\Omega\cdot\text{cm}^{-2}$ | $\eta / \%$ | $R_p / \text{k}\Omega\cdot\text{cm}^{-2}$ | $\eta / \%$ |
| 0.5      | 1.07                                      | 7.60                                      | 86          | 18.92                                     | 94          |
| 1.0      | 1.11                                      | 8.24                                      | 87          | 20.26                                     | 95          |
| 1.5      | 0.99                                      | 10.67                                     | 91          | 16.31                                     | 94          |
| 2.0      | 0.90                                      | 8.48                                      | 89          | 15.64                                     | 94          |
| 2.5      | 0.90                                      | 10.51                                     | 91          | 15.22                                     | 94          |
| 3.0      | 0.85                                      | 10.38                                     | 92          | 11.79                                     | 93          |
| 3.5      | 0.81                                      | 9.63                                      | 92          | 11.56                                     | 93          |
| 4.0      | 0.86                                      | 8.95                                      | 90          | 10.67                                     | 92          |
| 4.5      | 0.76                                      | 8.22                                      | 91          | 10.12                                     | 93          |
| 5.0      | 0.80                                      | 7.73                                      | 90          | 10.12                                     | 92          |
| 5.5      | 0.84                                      | 7.17                                      | 88          | 9.26                                      | 91          |
| 6.0      | 0.84                                      | 6.94                                      | 88          | 9.14                                      | 91          |

#### 4.3.1.3 OCP and PP

OCP and PP measurements were conducted to understand better how BTSA inhibits HDG. In OCP measurements, the presence of an inhibitor can shift values to either more positive or negative potentials. A positive potential shift indicates inhibition of anodic reactions, while a negative potential change indicates inhibition of cathodic reactions.

The OCP of uninhibited-HDG was  $-1.009 \pm 0.012$  V vs SCE after 1 h of immersion in 1% w/v NaCl<sub>(aq)</sub>, within the expected range of freely corroding zinc. In the presence of BTSA, the OCP after 1 h modestly decreased to  $-1.002 \pm 0.010$  V vs SCE and  $-0.985 \pm 0.016$  V vs SCE for 1 mM BTSA and 10 mM BTSA, respectively. Although the OCP values decrease, the change in OCP in the presence of BTSA is comparable to the uncertainty value of each OCP. Therefore, it cannot be stated whether there is a net positive or negative change in OCP in the presence of BTSA. When there is no definitive anodic or cathodic bias in OCP, an inhibitor can either provide mixed inhibition through simultaneous suppression of anodic and cathodic activity or it may not provide inhibition at all. Given the previous SVET and LPR results that show significant inhibition of corrosion of HDG by BTSA, the OCPs suggest mixed inhibition.

Additional evidence of the influence of BTSA on both anodic and cathodic kinetics of HDG may be obtained by PP. Figure 4.6 shows the PP curves obtained for HDG immersed in 1% w/v NaCl<sub>(aq)</sub> in the presence of varying concentrations of BTSA. Compared to uninhibited-HDG, the presence of BTSA results in lower current densities for both the anodic and cathodic-going curves. For the anodic branch at applied potentials approximately 0.1 V higher than the OCP of uninhibited HDG, the presence of BTSA seems to decrease the anodic current density by at least a factor of 8. Correspondingly, for the cathodic branch the presence of BTSA results in a decrease of cathodic current density by at least a factor of 2. These reductions suggest that BTSA inhibits both the anodic and cathodic reactions, further evidence of mixed inhibition.

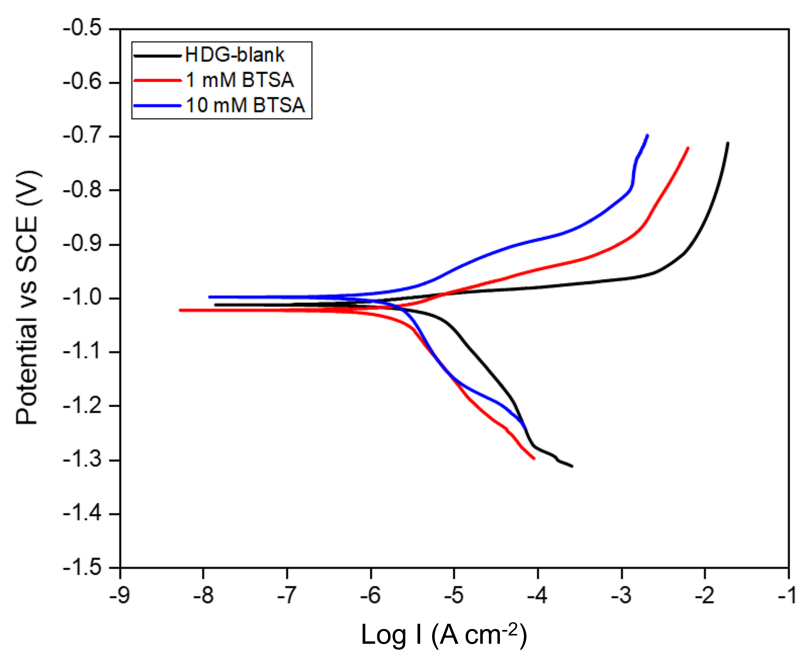


**Figure 4.6:** The anodic-going and cathodic-going polarisation curves of HDG immersed in 1% w/v NaCl<sub>(aq)</sub> pH 7 containing BTSA concentrations of a) uninhibited, b) 1 mM, and c) 10 mM.

## 4.3.2 Galfan

### 4.3.2.1 SVET

Figure 4.7 shows SVET-derived current density maps at 2 h, 4 h and 6 h of Galfan immersed in 1% w/v  $\text{NaCl}_{(\text{aq})}$  containing BTSA concentrations of a) uninhibited, b) 1 mM BTSA, and c) 10 mM BTSA. For uninhibited-Galfan (Figure 4.7a), immersion initiates several distinct local anodes set against a background of cathodic activity. As time progresses, additional anodes are initiated. By the conclusion of the 6 h immersion period, all previously observed anodes remain detectable on the current density map; however, there is a notable reduction in peak anodic  $j_z$  values from approximately  $9.0 \text{ A m}^{-2}$  at 2h to  $3.0 \text{ A m}^{-2}$  at 6h. This decrease suggests the passivation of anodic areas over time and is consistent with previous SVET results obtained for Galfan in aqueous chloride [32].

In the presence of 1 mM BTSA (Figure 4.7b), the current density maps again show localised anodic activity against background cathodic activity; however, compared to uninhibited-Galfan, the number of anodes is reduced, with only two anodes (top-left corner and bottom right corner) observed throughout immersion. Additionally, the maximum peak  $j_z$  value is  $0.7 \text{ A m}^{-2}$ , more than one order of magnitude lower than uninhibited-Galfan. Cathodic  $j_z$  values are approximately  $-0.5 \text{ A m}^{-2}$ , half that of the uninhibited experiment.

Finally, in the presence of 10 mM BTSA (Figure 4.7c), localised corrosion is not observed for the whole immersion time, with the current density maps instead showing low-magnitude anodic activity that is homogeneously distributed over the scanned area. As such, the anodic  $j_z$  values recorded are approximately  $0.05 \text{ A m}^{-2}$  across the surface, two orders of magnitude lower than uninhibited-Galfan. In addition, cathodic current densities are reduced to a maximum value of  $0.5 \text{ A m}^{-2}$  during immersion.

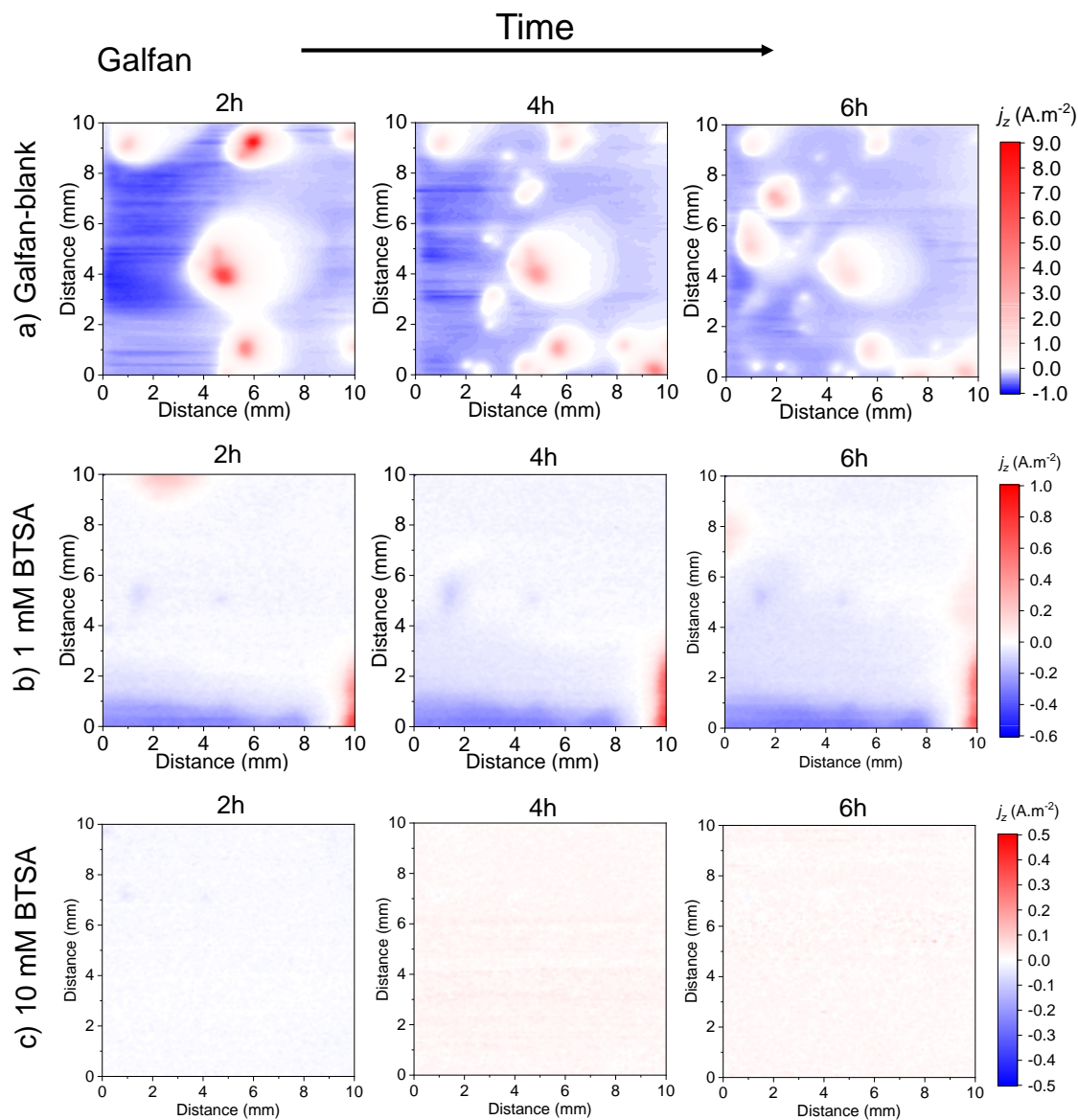


**Figure 4.7:** SVET current density maps at various times during the immersion of a 100 mm<sup>2</sup> area of Galfan in 1% w/v NaCl<sub>(aq)</sub> pH 7 containing BTSA concentrations of a) uninhibited, b) 1 mM, and c) 10 mM.

Figure 4.8 shows photographs of the Galfan surfaces taken following the immersion period. For uninhibited-Galfan (Figure 4.8a), the darker grey areas correspond to the areas of localised anodic activity in its current density maps. In contrast, the lighter grey hue relates to areas of net cathodic activity. For samples immersed in aqueous chloride containing 1 mM BTSA (Figure 4.8b) and 10 mM BTSA (Figure 4.8c), no obvious visible localised damage is seen for each surface, this being consistent with the general absence of local anodes in Figure 4.7b and Figure 4.7c, respectively.

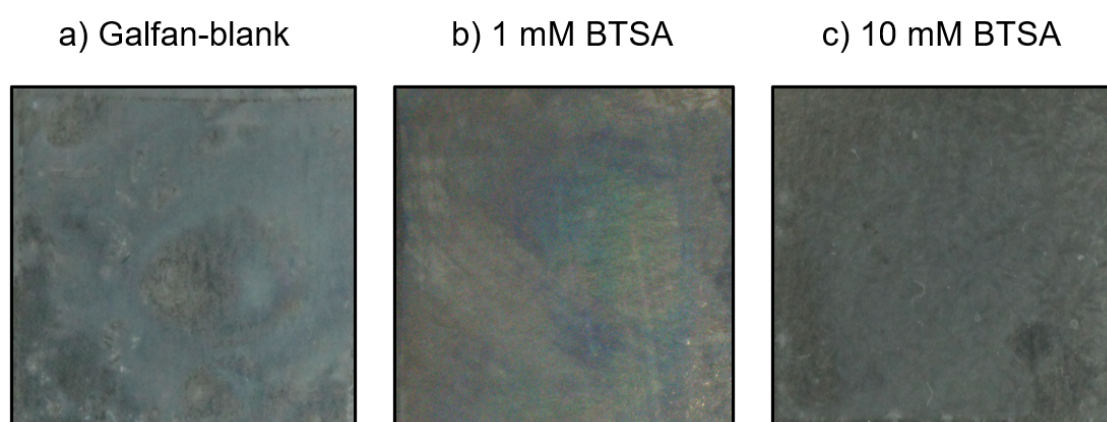


**Figure 4.8:** *Post-SVET photographs of the 100 mm<sup>2</sup> exposed surfaces of Galfan immersed in 1% w/v NaCl<sub>(aq)</sub> pH 7 containing BTSA concentrations of a) uninhibited, b) 1 mM, and c) 10 mM.*

Table 4.3 presents the time-dependent cumulative  $J_a$  and  $\eta$  values derived from SVET current density maps. In the case of 1 mM BTSA, a maximum  $\eta$  value of 86% is recorded after 2 h of immersion, which decreases modestly to 78% after 6 h. For 10 mM BTSA,  $\eta$  values over 97% are achieved during the first 3 h of immersion, demonstrating the suppression of localised activity as observed in its current density maps (Figure 4.7). Similarly to 1 mM BTSA, a minor decline in performance is recorded for 10 mM BTSA at later immersion times, with an  $\eta$  value of 86% recorded after 6 h of immersion.

**Table 4.3:** SVET-derived time-dependent values of cumulative  $J_a$  and corresponding inhibitor efficiency,  $\eta$ , of Galfan immersed in 1% w/v  $\text{NaCl}_{(aq)}$  at pH 7 containing BTSA concentrations of a) uninhibited, b) 1 mM, and c) 10 mM.

| Galfan SVET | Uninhibited   | 1 mM BTSA   |            | 10 mM BTSA  |            |
|-------------|---|---|------------|---|------------|
| Time / h    | Cumulative<br>anodic current<br>density / $\text{A m}^{-2}$ | Cumulative<br>anodic current<br>density / $\text{A m}^{-2}$ | $\eta$ / % | Cumulative<br>anodic current<br>density / $\text{A m}^{-2}$ | $\eta$ / % |
| 0.5         | 0.17  | 0.03  | 82         | 0.01  | 97         |
| 1.0         | 0.35  | 0.05  | 85         | 0.01  | 98         |
| 1.5         | 0.52  | 0.07  | 86         | 0.01  | 99         |
| 2.0         | 0.68  | 0.10  | 86         | 0.01  | 99         |
| 2.5         | 0.80  | 0.12  | 85         | 0.01  | 99         |
| 3.0         | 0.89  | 0.15  | 83         | 0.04  | 96         |
| 3.5         | 1.16  | 0.18  | 84         | 0.09  | 92         |
| 4.0         | 1.26  | 0.21  | 83         | 0.16  | 87         |
| 4.5         | 1.37  | 0.25  | 82         | 0.18  | 87         |
| 5.0         | 1.46  | 0.28  | 81         | 0.20  | 86         |
| 5.5         | 1.56  | 0.32  | 80         | 0.21  | 86         |
| 6.0         | 1.61  | 0.35  | 78         | 0.22  | 86         |

As conducted on HDG, the action of BTSA introduced to freely corroding Galfan was performed. Figure 4.9 presents the SVET current density maps of the surface 30 minutes before and after adding 10 mM BTSA at 3 h of immersion. The pre-addition current density map shows four established localised anodes, the most intense being the centre-most anode with a peak anodic  $j_z$  of  $12.5 \text{ A m}^{-2}$ . However, upon adding 10 mM BTSA, the anodes can no longer be seen, suggesting an immediate passivation of the localised anodes by BTSA.



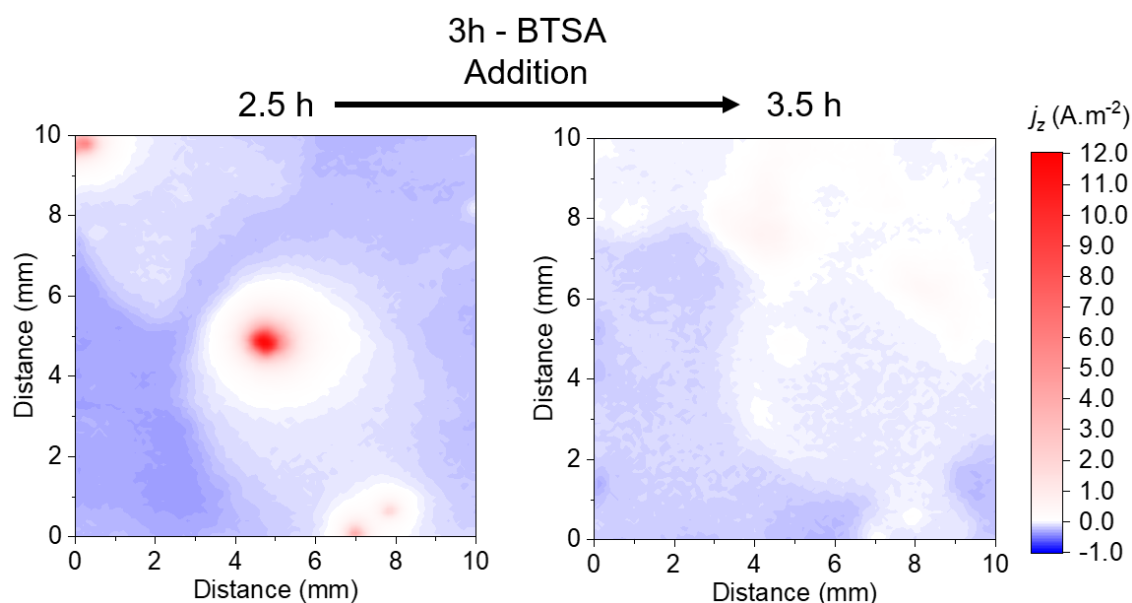


**Figure 4.9:** SVET current density maps of the immersed surface of Galfan a) 0.5 h before, and b) 0.5 h after the addition at 3 h of 10 mM BTSA to an initial 1% w/v  $\text{NaCl}_{(aq)}$  pH 7 solution.

Figure 4.10 shows a plot of the average anodic  $j_z$  emanating from the Galfan surface against time. During the first 2.5 h of uninhibited immersion, the average anodic  $j_z$  values at each 30-minute interval are approximately  $0.8 \text{ A m}^{-2}$ . However, upon adding 10 mM BTSA, the average anodic  $j_z$  falls sharply to  $0.16 \text{ A m}^{-2}$  within 30 minutes, an 80% reduction that indicates an immediate inhibitory effect of BTSA towards the freely corroding Galfan surface. For the remaining immersion time, an average anodic  $j_z$  value of around  $0.1 \text{ A m}^{-2}$  is maintained, an approximate decrease of 85% compared to values prior to the BTSA addition.

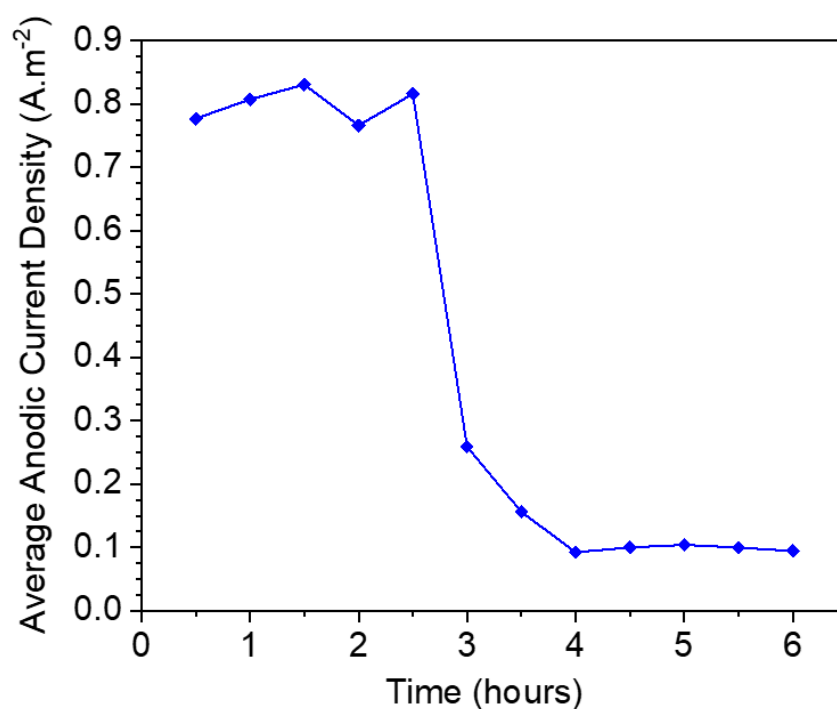


**Figure 4.10:** SVET-derived average anodic current density as a function of time of a 100 mm<sup>2</sup> exposed area of Galfan immersed in 1% w/v NaCl<sub>(aq)</sub> pH 7 solution. After 3 h, 10 mM BTSA was added to the solution.

#### 4.3.2.2 LPR

Table 4.4 shows LPR-derived time-dependent values of  $R_p$  and  $\eta$  of Galfan in the presence of varying concentrations of BTSA. Compared to uninhibited-Galfan, higher  $R_p$  values are recorded in the presence of BTSA at every time interval, corresponding to time-averaged  $\eta$  values of  $81 \pm 4\%$  and  $96 \pm 2\%$  for 1 mM BTSA and 10 mM BTSA, respectively. In both cases, the small uncertainty associated with the  $\eta$  value suggests that inhibition is maintained during immersion.

**Table 4.4:** LPR-derived time-dependent values of polarisation resistance,  $R_p$ , and corresponding inhibitor efficiency,  $\eta$ , of Galfan immersed in 1% w/v  $\text{NaCl}_{(\text{aq})}$  at pH 7 containing BTSA concentrations of a) uninhibited, b) 1 mM, and c) 10 mM.

| Galfan LPR | Uninhibited                               | 1 mM BTSA                                 |             | 10 mM BTSA                                |             |
|------------|---|---|-------------|---|-------------|
| Time / h   | $R_p / \text{k}\Omega\cdot\text{cm}^{-2}$ | $R_p / \text{k}\Omega\cdot\text{cm}^{-2}$ | $\eta / \%$ | $R_p / \text{k}\Omega\cdot\text{cm}^{-2}$ | $\eta / \%$ |
| 0.5        | 1.72                                      | 7.81                                      | 78          | 19.12                                     | 91          |
| 1.0        | 1.76                                      | 7.23                                      | 76          | 27.79                                     | 94          |
| 1.5        | 1.56                                      | 7.04                                      | 78          | 31.5                                      | 95          |
| 2.0        | 1.40                                      | 6.70                                      | 79          | 34.18                                     | 96          |
| 2.5        | 1.27                                      | 6.80                                      | 81          | 34.19                                     | 96          |
| 3.0        | 1.22                                      | 6.65                                      | 82          | 34.44                                     | 96          |
| 3.5        | 1.16                                      | 6.73                                      | 83          | 37.03                                     | 97          |
| 4.0        | 1.11                                      | 6.66                                      | 83          | 27.02                                     | 96          |
| 4.5        | 1.00                                      | 6.64                                      | 85          | 32.6                                      | 97          |
| 5.0        | 0.96                                      | 6.26                                      | 85          | 29.99                                     | 97          |
| 5.5        | 0.99                                      | 6.15                                      | 84          | 29.03                                     | 97          |
| 6.0        | 1.01                                      | 5.94                                      | 83          | 29.71                                     | 97          |

#### 4.3.2.3 OCP and PP

OCP and PP experiments were performed to provide information on how BTSA inhibits Galfan. For uninhibited-Galfan, the OCP is  $-1.011 \pm 0.017$  V vs SCE after 1 h of immersion in 1% w/v  $\text{NaCl}_{(\text{aq})}$ , within the range expected for freely corroding zinc. However, in the presence of BTSA, the OCP after 1 h increases to  $-1.003 \pm 0.008$  V vs SCE and  $-0.997 \pm 0.012$  V vs SCE for 1 mM BTSA and 10 mM BTSA, respectively. The change in OCP in the presence of BTSA is comparable to the uncertainty value of each measurement; therefore, a net positive or negative change in OCP in the presence of BTSA cannot be stated. Given the significant inhibition of Galfan by BTSA in SVET and LPR experiments the OCP measurements suggest mixed inhibition behaviour.

The anodic and cathodic-going PP curves obtained for Galfan immersed in 1% w/v  $\text{NaCl}_{(\text{aq})}$  in the presence of varying concentrations of BTSA are given in Figure 4.11. Compared to

uninhibited-Galfan, the presence of BTSA results in lower current densities for both the anodic and cathodic-going curves (mixed inhibition); however, the main influence appears to be on the anodic branch, with at least an order of magnitude reduction in anodic current density at applied potentials 0.1 V higher than the OCP of uninhibited Galfan. The small decrease in cathodic current density observed contrasts with that of HDG, where there is a more pronounced effect on the cathodic branch.

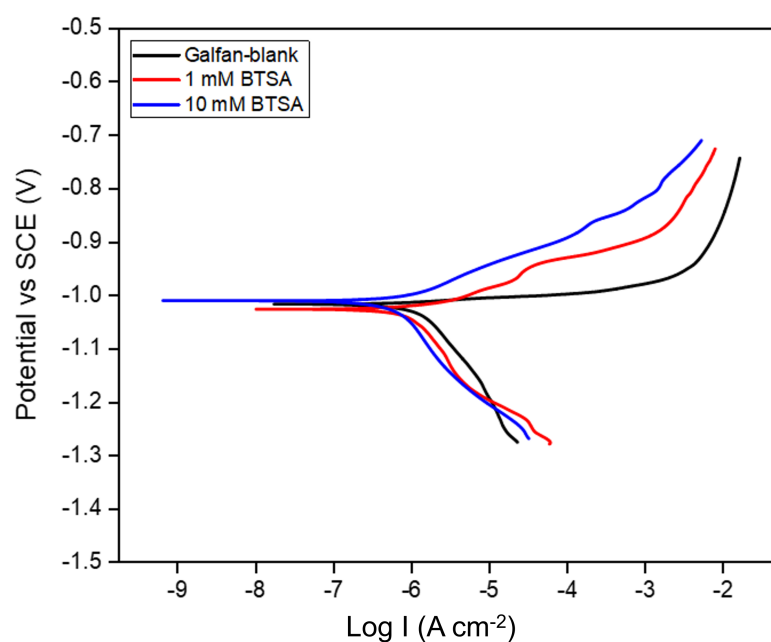


**Figure 4.11:** The anodic and cathodic-going polarisation curves of Galfan immersed in 1% w/v  $\text{NaCl}_{(aq)}$  pH 7 containing BTSA concentrations of a) uninhibited, b) 1 mM, and c) 10 mM.

### 4.3.3 Zn55Al

Figure 4.12 shows SVET-derived current density maps at 2 h, 4 h and 6 h during immersion of Zn55Al in 1% w/v NaCl<sub>(aq)</sub> containing BTSA concentrations of a) uninhibited, b) 1 mM BTSA, and c) 10 mM BTSA. For uninhibited-Zn55Al (Figure 4.12a), current density maps follow the trend of localised corrosion described in Chapter 3: transient (moving) anodes initiating upon immersion, then stabilising to a fixed position at later immersion times. The peak anodic  $j_z$  recorded during immersion is approximately  $2.0 \text{ A m}^{-2}$  and is associated with the transient anodic activity of the top-left corner of the current density map at 4 h. The observed background cathodic current density during immersion is approximately  $-0.1 \text{ A m}^{-2}$ .

In the presence of 1 mM BTSA (Figure 4.12b), the SVET current density maps again show localised activity, as several discrete anodes are observed; however, the recorded peak anodic  $j_z$  of  $0.7 \text{ A m}^{-2}$  during immersion is less than half the value of uninhibited-Zn55Al. This reduction is accompanied by a decreased cathodic  $j_z$  ( $-0.05 \text{ A m}^{-2}$ ), half that of the uninhibited-Zn55Al.

Finally, in the presence of 10 mM BTSA (Figure 4.12c), local anodes are absent from all current density maps, instead, each map shows very low-magnitude general corrosion throughout the immersion time with the associated anodic and cathodic  $j_z$  values being close to  $0 \text{ A m}^{-2}$ .

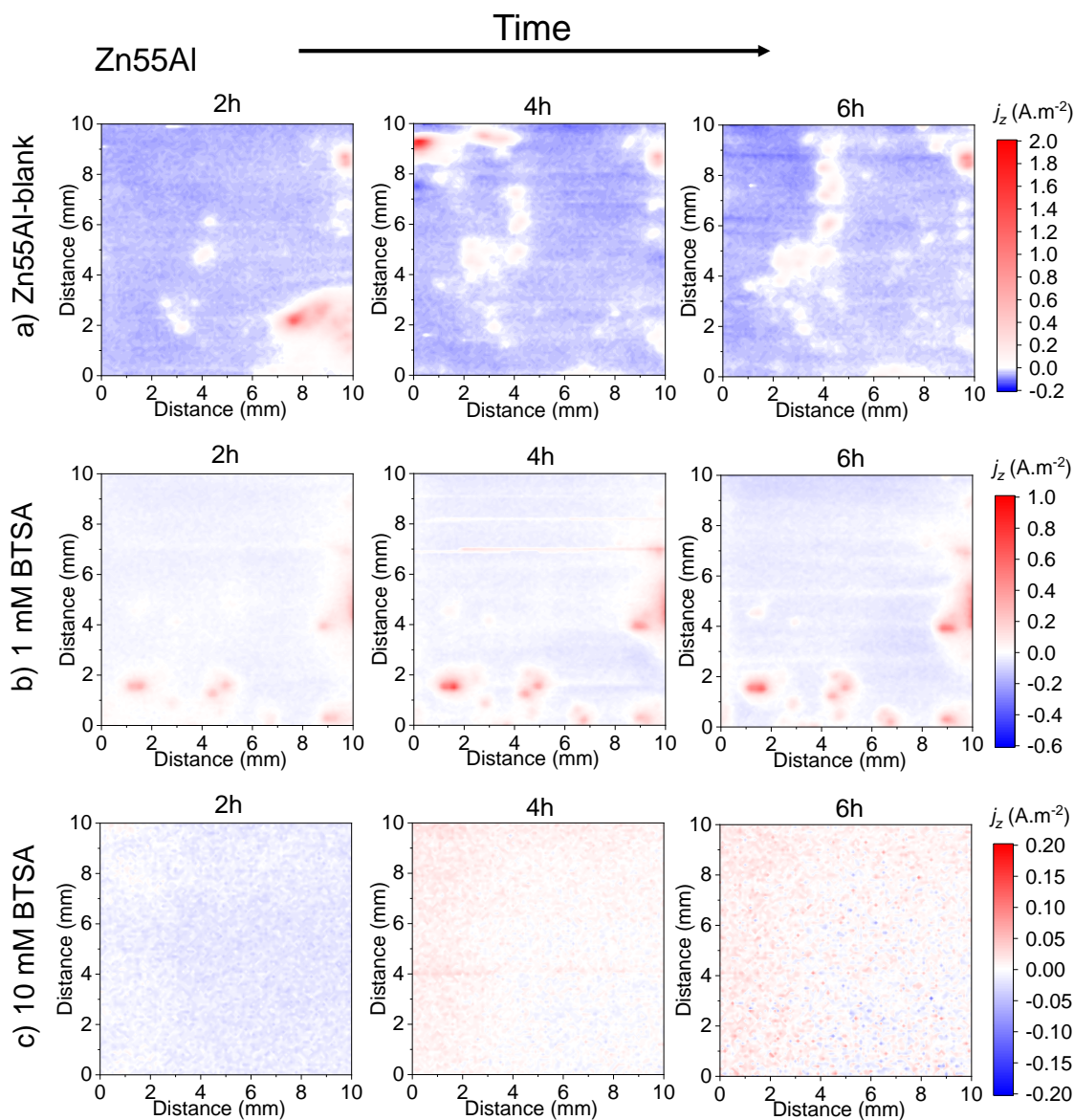


**Figure 4.12:** SVET current density maps at various times during the immersion of a 100 mm<sup>2</sup> area of Zn55Al in 1% w/v NaCl<sub>(aq)</sub> pH 7 containing BTSA concentrations of a) uninhibited, b) 1 mM, and c) 10 mM.

Figure 4.13 displays photographs of the Zn55Al surfaces taken after immersion. In the uninhibited-Zn55Al image (Figure 4.13a), the prominent white-stained regions correspond to localised anodes of the 6 h current density map (Figure 4.12). At the same time, the black-stained, tarnished areas relate to the map's background cathodic activity. For further information on the appearance of Zn55Al post-immersion in aqueous chloride see Chapter 3.

For 10 mM BTSA (Figure 4.13b), the post-immersion image shows no evidence of white or black staining, consistent with the complete absence of localised corrosion in current density maps (Figure 4.12c).

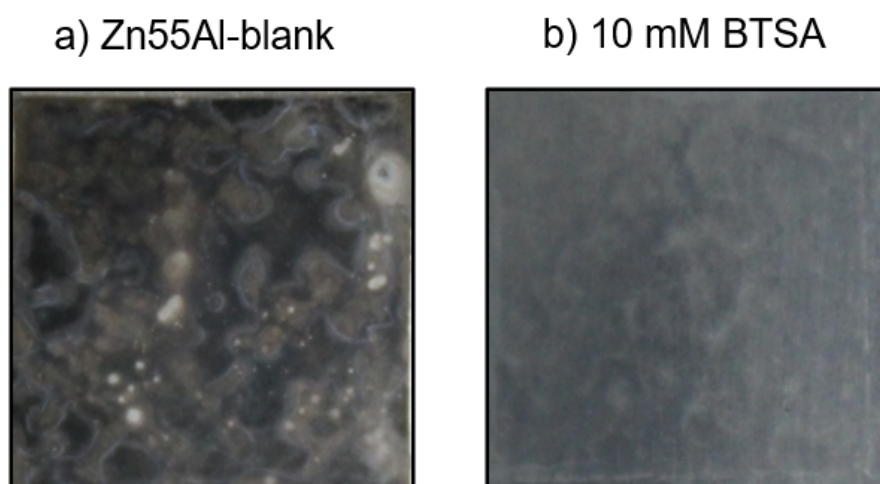


**Figure 4.13:** Post-SVET photographs of the 100 mm<sup>2</sup> exposed surfaces of Zn55Al immersed in 1% w/v NaCl<sub>(aq)</sub> pH 7 containing BTSA concentrations of a) uninhibited, b) 1 mM, and c) 10 mM.

Table 4.5 shows the time-dependent cumulative  $J_a$  and  $\eta$  values derived from SVET current density maps. In the case of 1 mM BTSA, a maximum  $\eta$  value of 43% is achieved 2 h after immersion before falling to 18% at 6 h, consistent with the incomplete inhibition of localised corrosion in its current density map (Figure 4.12b). On the other hand, for 10 mM BTSA, inhibition is significantly improved, with  $\eta$  values above 90% achieved for the first 3 h of immersion before falling modestly to 69% at 6 h immersion.

**Table 4.5:** SVET-derived time-dependent values of cumulative anodic  $J_a$  and corresponding inhibitor efficiency,  $\eta$ , of Zn55Al immersed in 1% w/v  $\text{NaCl}_{(aq)}$  at pH 7 containing BTSA concentrations of a) uninhibited, b) 1 mM, and c) 10 mM.

| Zn55Al SVET | Uninhibited   | 1 mM BTSA   |            | 10 mM BTSA  |            |
|-------------|---|---|------------|---|------------|
| Time / h    | Cumulative<br>anodic current<br>density / $\text{A m}^{-2}$ | Cumulative<br>anodic current<br>density / $\text{A m}^{-2}$ | $\eta$ / % | Cumulative<br>anodic current<br>density / $\text{A m}^{-2}$ | $\eta$ / % |
| 0.5         | 0.01  | 0.01  | 0          | 0.00  | 94         |
| 1.0         | 0.02  | 0.02  | 0          | 0.00  | 94         |
| 1.5         | 0.05  | 0.03  | 40         | 0.00  | 97         |
| 2.0         | 0.07  | 0.04  | 43         | 0.00  | 98         |
| 2.5         | 0.07  | 0.05  | 37         | 0.00  | 95         |
| 3.0         | 0.09  | 0.06  | 36         | 0.01  | 90         |
| 3.5         | 0.10  | 0.07  | 34         | 0.02  | 84         |
| 4.0         | 0.11  | 0.08  | 27         | 0.02  | 79         |
| 4.5         | 0.13  | 0.09  | 34         | 0.03  | 79         |
| 5.0         | 0.14  | 0.10  | 28         | 0.03  | 75         |
| 5.5         | 0.15  | 0.11  | 23         | 0.04  | 72         |
| 6.0         | 0.15  | 0.13  | 18         | 0.05  | 69         |

As conducted on HDG and Galfan, the action of BTSA introduced to freely corroding Zn55Al was performed. Figure 4.14 presents the SVET current density maps of an immersed Zn55Al surface 30 minutes before and 30 minutes after the addition of 10 mM BTSA at 3 h of immersion. The pre-addition current density map shows three discrete established localised anodes, with a peak  $j_z$  of approximately  $3.0 \text{ A m}^{-2}$  belonging to the bottom-most anode. However, upon adding 10 mM BTSA, the three anodes can no longer be seen during immersion, suggesting both an immediate passivation of localised corrosion and continued protection.



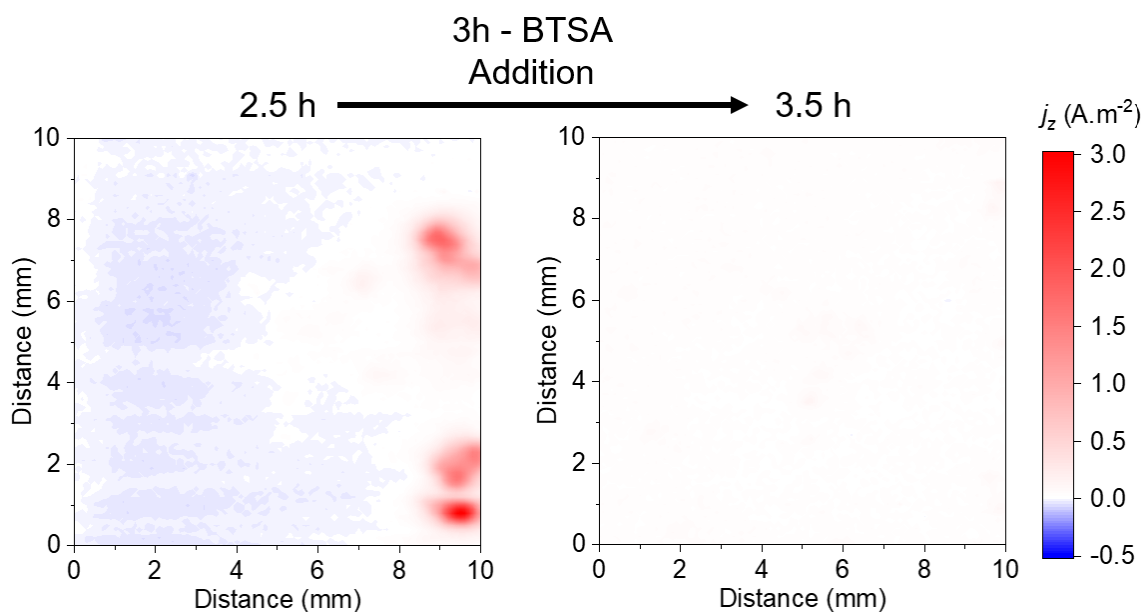


**Figure 4.14:** SVET current density maps of the immersed surface of Zn55Al a) 0.5 h before, and b) 0.5 h after the addition at 3h of 10 mM BTSA to an initial 1% w/v  $\text{NaCl}_{(aq)}$  pH 7 solution.

Figure 4.15 shows a plot of the average anodic  $j_z$  emanating from the Zn55Al surface against time. During the first 2.5 h of uninhibited immersion, the average anodic  $j_z$  increases to a peak of  $0.18 \text{ A m}^{-2}$ . However, upon adding 10 mM BTSA, the average anodic  $j_z$  falls sharply to  $0.037 \text{ A m}^{-2}$ , a 79% reduction that indicates an immediate inhibitory effect of BTSA towards localised corrosion. For the remaining immersion time, average anodic  $j_z$  values of around  $0.030 \text{ A m}^{-2}$  are recorded, an  $\eta$  of 83% compared to the average anodic  $j_z$  recorded 30 minutes before the BTSA addition.

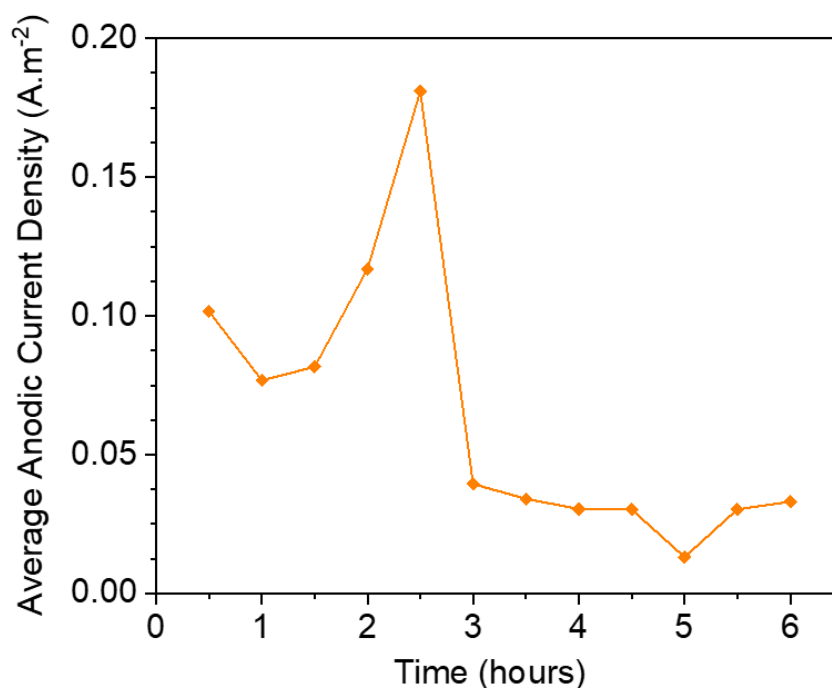


**Figure 4.15:** SVET-derived average anodic current density as a function of time of a 100 mm<sup>2</sup> exposed area of Zn55Al immersed in 1% w/v NaCl<sub>(aq)</sub> pH 7 solution. After 3h, 10 mM BTSA was added to the solution.

#### 4.3.3.1 LPR

Table 4.6 shows LPR-derived time-dependent values of  $R_p$  and  $\eta$  of Zn55Al in the presence of varying concentrations of BTSA. Compared to uninhibited-Zn55Al, higher  $R_p$  values are recorded in the presence of BTSA at every time interval, corresponding to time-averaged  $\eta$  values of  $82\% \pm 4\%$  and  $93\% \pm 2\%$  for 1 mM BTSA and 10 mM BTSA, respectively. In both cases, the small uncertainty associated with the value of  $\eta$  suggests that inhibition is maintained during immersion.

The high  $\eta$  values with low uncertainty suggest that inhibition of Zn55Al by BTSA is high and is maintained throughout immersion, contrary to the SVET results shown in Table 4.5, which show either poor inhibition (1 mM BTSA) or a fall in inhibition over time (10 mM BTSA). The difference can be ascribed to the semi-quantitative nature of the SVET; occasions of low-magnitude corrosion events are beyond the sensitivity limits of

the instrument. Consequently, determining current densities for highly corrosion-resistant surfaces (such as Zn55Al) or highly inhibited surfaces by SVET may not be accurate. On the other hand, the LPR method provides better rate determination during low-level localised or general corrosion, thereby showing value in the performance assessment.

**Table 4.6:** *LPR-derived time-dependent values of polarisation resistance,  $R_p$ , and corresponding inhibitor efficiency,  $\eta$ , of Zn55Al immersed in 1% w/v NaCl<sub>(aq)</sub> at pH 7 containing BTSA concentrations of a) uninhibited, b) 1 mM, and c) 10 mM.*

| Zn55Al LPR | Uninhibited                          | 1 mM BTSA                            |            | 10 mM BTSA                           |            |
|------------|--------------------------------------|--------------------------------------|------------|--------------------------------------|------------|
| Time / h   | $R_p$ / k $\Omega$ .cm <sup>-2</sup> | $R_p$ / k $\Omega$ .cm <sup>-2</sup> | $\eta$ / % | $R_p$ / k $\Omega$ .cm <sup>-2</sup> | $\eta$ / % |
| 0.5        | 3.94                                 | 17.87                                | 78         | 49.23                                | 92         |
| 1.0        | 3.99                                 | 19.03                                | 79         | 56.98                                | 93         |
| 1.5        | 3.70                                 | 19.42                                | 81         | 52.86                                | 93         |
| 2.0        | 3.09                                 | 20.61                                | 85         | 51.48                                | 94         |
| 2.5        | 2.82                                 | 17.63                                | 84         | 45.69                                | 94         |
| 3.0        | 2.95                                 | 20.64                                | 86         | 50.44                                | 94         |
| 3.5        | 2.73                                 | 12.54                                | 78         | 50.40                                | 95         |
| 4.0        | 3.50                                 | 16.35                                | 79         | 54.86                                | 94         |
| 4.5        | 3.65                                 | 21.67                                | 83         | 41.40                                | 91         |
| 5.0        | 3.40                                 | 18.71                                | 82         | 49.77                                | 93         |
| 5.5        | 2.94                                 | 17.60                                | 83         | 50.26                                | 94         |
| 6.0        | 3.47                                 | 17.10                                | 80         | 52.93                                | 93         |

#### 4.3.3.2 OCP and PP

OCP and PP measurements were conducted to provide information on how BTSA inhibits Zn55Al. For uninhibited-Zn55Al, the OCP is  $-0.987 \pm 0.014$  V vs SCE after 1 h of immersion in 1% w/v NaCl<sub>(aq)</sub>, within the range expected for freely corroding zinc. However, in the presence of BTSA, the OCP after 1 h increases to  $-0.980 \pm 0.015$  V vs SCE and  $-0.969 \pm 0.020$  V vs SCE for 1 mM BTSA and 10 mM BTSA, respectively. The change in OCP in the presence of BTSA is comparable to the uncertainty value of each measurement; therefore, a net positive or negative change in OCP in the presence of

BTSA cannot be stated. As such, the inhibition of Zn55Al observed in SVET and LPR tests most likely arises through a mixed inhibition mechanism.

Figure 4.16 shows the cathodic and anodic PP curves obtained for Zn55Al immersed in 1% w/v  $\text{NaCl}_{(\text{aq})}$  in the presence of varying concentrations of BTSA. As observed for Galfan, the inhibitory action of BTSA towards Zn55Al is mixed-type but with a significantly more pronounced effect on the anodic branch. For example, for the anodic branch at applied potentials approximately 0.1 V higher than the OCP of uninhibited Zn55Al, the presence of BTSA produces at least a two order of magnitude reduction in anodic current density, however, the corresponding decrease in the cathodic branch is only a factor of 1.5.

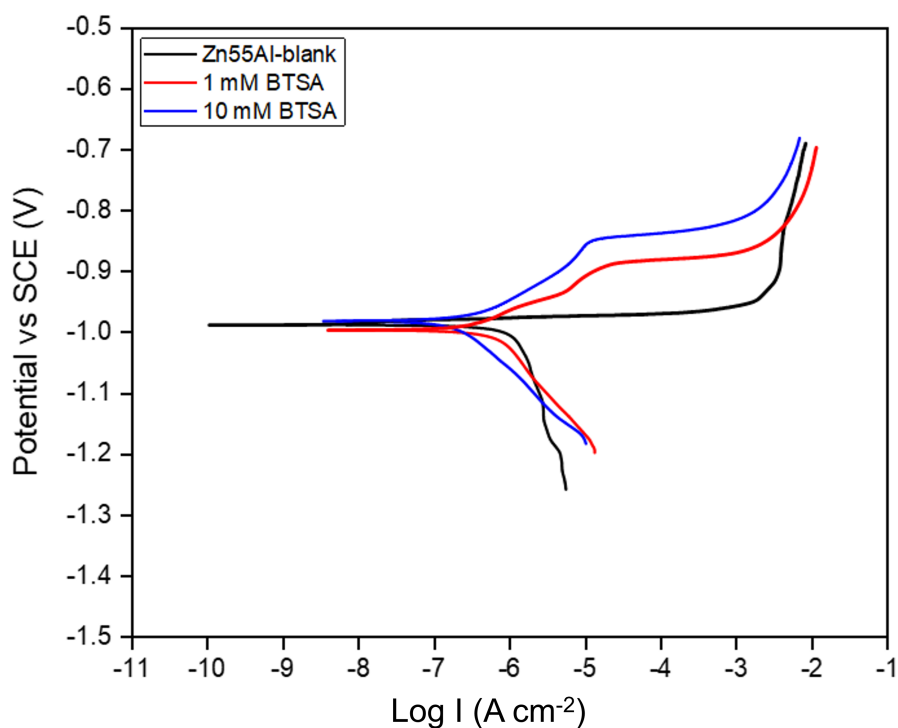


**Figure 4.16:** The anodic-going and cathodic-going polarisation curves of Zn55Al immersed in 1% w/v  $\text{NaCl}_{(\text{aq})}$  pH 7 containing BTSA concentrations of a) uninhibited, b) 1 mM, and c) 10 mM.

## 4.4 Discussion

### 4.4.1 Inhibition via Adsorption

The results of SVET and potentiodynamic polarisation experiments show that BTSA, when added to aqueous chloride solutions reduces both the anodic and cathodic current density for all three ZnAl galvanised steels, indicating that BTSA acts as a mixed-type inhibitor for each substrate. Mixed inhibition is common for organic inhibitors like azole compounds. These inhibitors work by creating a protective film on the metal surface through adsorption that reduce the rates of both anodic and cathodic reactions simultaneously.

When an organic inhibitor is adsorbed, it replaces the water molecules on the metal surface. The effectiveness of adsorption depends on the electrostatic interaction between the inhibitor and the metal [33], which is strongly influenced by the solution's pH. At pH 7, the surface of HDG and Galfan is predicted to be predominantly covered by zinc hydr(oxide), while for Zn55Al, the predominant oxide film will be aluminium hydr(oxide) [34-37]. Both oxide films have isoelectric points greater than pH 7 [38-40]. Therefore, at pH 7, the surfaces of HDG, Galfan, and Zn55Al have positively charged dipoles.

Regarding BTSA, it can exist in different speciation depending on the pH of the solution. It can be fully protonated as  $H_2BTSA$ , singly deprotonated as  $H[BTSA]^-$ , or doubly deprotonated as  $BTSA^{2-}$ . Figure 4.17 illustrates the predicted normalised fraction of each BTSA species concerning solution pH based on literature values for succinic acid [41]. The first and second  $pK_a$  values are approximately 4.2 and 5.6, respectively. This means that at pH 7, the most common form of BTSA is  $BTSA^{2-}$ .

Considering the positive dipoles associated with zinc and aluminium surfaces, it seems plausible that in aqueous solution the negatively charged  $BTSA^{2-}$  dianion adsorbs directly onto the surfaces of each ZnAl coating (Figure 4.17), forming a protective film that suppresses anodic and cathodic reactions.

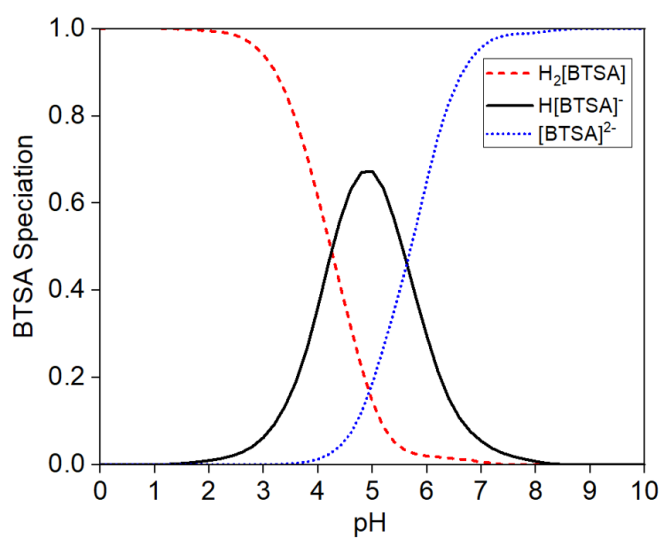


**Figure 4.17:** The relative concentration of BTSA species as a function of pH [41].

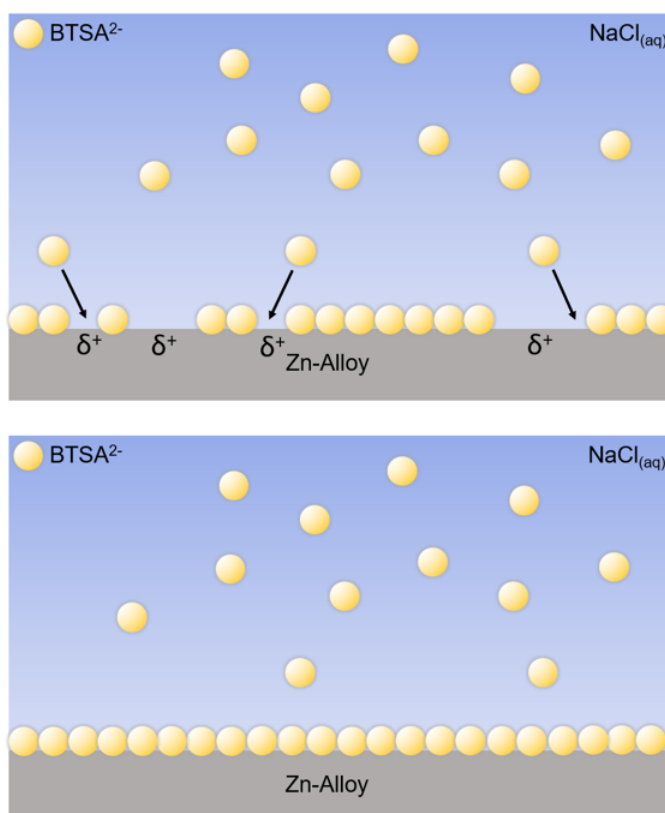
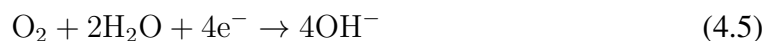


**Figure 4.18:** The adsorption of BTSA<sup>2-</sup> to ZnAl coated steel in near-neutral aqueous chloride solution.

The PP results indicate that the effectiveness of BTSA on ZnAl coatings is likely determined by its ability to adsorb onto zinc rather than aluminium. For example, regarding the cathodic curve at an applied potential of -1.1 V, the presence of 10 mM BTSA reduced the cathodic current of HDG by 68%, Galfan by 49%, and Zn55Al by 17% compared to the control. This suggests that the cathodic kinetics of ZnAl coatings with higher zinc content are more affected by the presence of BTSA. This effect is expected because cathodic oxygen reduction predominantly occurs on zinc-rich microstructural phases [42]. Zn55Al has less surface zinc than HDG and Galfan, so a smaller portion of its surface requires cathodic protection.

#### 4.4.2 Inhibition via Precipitation

As shown in SVET current density maps, the uninhibited surfaces of HDG (Figure 4.2a), Galfan (Figure 4.7a), and Zn55Al (Figure 4.12a) are all susceptible to localised corrosion in aqueous chloride at pH 7. In these circumstances, the possible anodic reactions are Zn and Al dissolution via Reaction 4.3 and 4.4, respectively, while the coupled cathodic response is oxygen reduction via Reaction 4.5 [43].



The observation that the 1 h OCP measurements of all three ZnAl coatings are like that of pure zinc suggests that Reactions 4.3 and 4.5 are the most significant contributors to corrosion, consistent with previous reports of each substrate's initial dissolution of zinc-rich areas [32]. Subsequent hydrolysis of  $\text{Zn}^{2+}$  ions in those areas yields  $\text{H}^{+}$ , generating a low pH proximal to those anodic sites and stabilising them. Conversely, the  $\text{OH}^{-}$  ions

produced by Reaction 4.5 create proximal regions of high pH, which promote the precipitation of insoluble metal hydr(oxide) corrosion products that keep those areas passive. Consequently, areas of cathodic and anodic activity remain separate so localised corrosion ensues [43].

The addition of 10 mM BTSA to freely corroding HDG (Figure 4.4), Galfan (Figure 4.9), and Zn55Al (Figure 4.14) results in the immediate passivation of localised anodes in each case. This passivation is unlikely to be due to adsorption through a film formation mechanism, as cathodic activity creates local alkaline regions with a pH above each substrate's isoelectric point. These regions would be negatively charged, repelling the negatively charged  $\text{BTSA}^{2-}$  anions. Instead, a secondary protection mechanism is proposed. As shown schematically in Figure 4.19,  $\text{BTSA}^{2-}$  in solution may react with  $\text{Zn}^{2+}$  produced at local anodes to form an insoluble ZnBTSA precipitate that prevents further anodic attack. Evidence for this comes from the anodic curves of the PP measurements, where for each substrate BTSA provides a similar degree of passivity, suggesting a specific interaction of  $\text{Zn}^{2+}$  with  $\text{BTSA}^{2-}$  in aqueous solution.

To test this theory, some solubility spot-tests were conducted by mixing different solutions containing equal concentrations of BTSA or  $\text{ZnCl}_2$  at pH 7. At all concentrations  $\geq 1$  mM, a cloudy white precipitate was observed, giving a maximum calculated  $K_{\text{sp}}$  value of  $1 \times 10^{-6} \text{ mol}^2 \text{ dm}^{-6}$ . Notably, the calculated  $K_{\text{sp}}$  value is lower than that of zinc succinate ( $3.75 \times 10^{-4} \text{ mol}^2 \text{ dm}^{-6}$  [45]), likely due the increased hydrophobicity of BTSA from its aromatic heterocyclic moiety. This supports the notion of an insoluble ZnBTSA compound formed when  $\text{Zn}^{2+}$  and  $\text{BTSA}^{2-}$  interact.



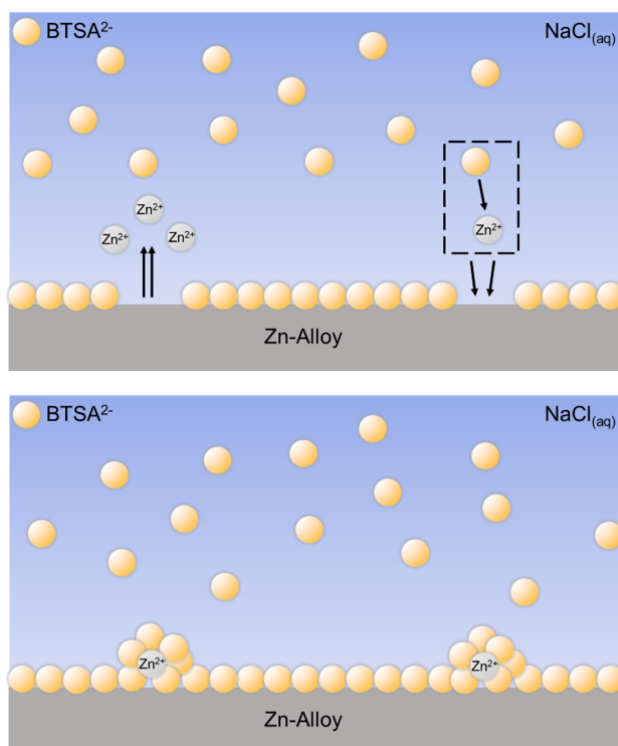


**Figure 4.19:** A proposed mechanism of inhibition of freely corroding ZnAl galvanised steel by BTSA in near-neutral aqueous chloride solution.

## 4.5 Conclusion

A systematic electrochemical study has been completed to establish the inhibitory performance of 2-(1,3-Benzothiazol-2-ylthio) succinic acid (BTSA) towards the localised corrosion ZnAl galvanised steels in aqueous chloride. Time-dependent data from Scanning Vibrating Electrode Technique (SVET) and Linear Polarisation Resistance (LPR) experiments showed that a BTSA addition of 10 mM into the electrolyte achieves an inhibition efficiency over 90% for HDG, Galfan, and Zn55Al surfaces, with inhibition generally being maintained for the entire 6 h of immersion. Further, adding 10 mM of BTSA to all three freely locally corroding ZnAl surfaces was found to provide an instantaneous inhibitory effect, passivating established localised corrosion.

Through the SVET study alongside open circuit potential and potentiodynamic polarisation measurements, a mixed inhibition mechanism is proposed whereby in the near neutral electrolyte, dianionic BTSA<sup>2-</sup> is adsorbed onto ZnAl surfaces due to electrostatic interaction, forming a protective film that simultaneously reduces the rate of anodic and cathodic reactions. A second inhibition mechanism is also proposed, whereby a reaction of BTSA<sup>2-</sup> and metal ions (predominantly Zn<sup>2+</sup>) produces a protective insoluble product that passivates active local anodes. If the mechanism of inhibition were further investigated, the characterisation of any surface films or complexes would be of interest.

Overall, the results presented demonstrate the promise of BTSA as a non-toxic corrosion inhibitor that could be incorporated chromate-free organic coating systems for ZnAl galvanised steels. As such, the following Chapter investigates the performance of in-coating BTSA additives within model organic coatings.

## 4.6 References

1. O.Ø. Knudsen, A. Forsgren, Corrosion control through organic coatings, second edition, Corrosion Control through Organic Coatings, Second Edition. (2017) 1–255.
2. J. Sander, 1. Coil Coating – Principle, Market And Applications, Coil Coating. (2014) 13–30.
3. G. Williams, H.N. McMurray, Chromate Inhibition of Corrosion-Driven Organic Coating Delamination Studied Using a Scanning Kelvin Probe Technique, J. Electrochem. Soc. 148 (2001) B377.
4. R. Berger, U. Bexell, T. Mikael Grehk, S.E. Hörnström, A comparative study of the corrosion protective properties of chromium and chromium free passivation methods, Surf. Coat. Technol. 202 (2007) 391–397.
5. Y.I. Kuznetsov, I.L. Rozenfel'd, T.A. Agalarova, Protection of steel in sea water by chromate inhibitors in conjunction with cathodic polarization, Protection of Metals. 18 (1982) 438–441.
6. I.L. Rozenfeld, Corrosion inhibitors, McGraw Hill, New York. (1981) 327.
7. J. Zhao, G. Frankel, R.L. McCreery, Corrosion Protection of Untreated AA-2024-T3 in Chloride Solution by a Chromate Conversion Coating Monitored with Raman Spectroscopy, J. Electrochem. Soc. 145 (1998) 2258–2264.
8. D.M. Proctor, M. Suh, S.L. Campleman, C.M. Thompson, Assessment of the mode of action for hexavalent chromium-induced lung cancer following inhalation exposures, Toxicology. 325 (2014) 160–179.
9. F.L. Petrilli, S. De Flora, Toxicity and Mutagenicity of Hexavalent Chromium on *Salmonella typhimurium*, Appl. Environ. Microbiol. 33 (1977) 805–809.
10. S.A. Katz, H. Salem, The toxicology of chromium with respect to its chemical speciation: A review, Journal of Applied Toxicology. 13 (1993) 217–224.

11. S.A. Katz, The analytical biochemistry of chromium, *Environ. Health. Perspect.* 92 (1991) 13–16.
12. T. Eicher, S. Hauptmann, A. Speicher, *The Chemistry of Heterocycles.* (2003).
13. L. Chen, Y. He, Q. Yang, R. Yang, L. Zhang, Y. Fan, Z. He, A Glycine Derivative as Corrosion Inhibitor for Carbon Steel in 3.5 wt% NaCl solution: The combined Experimental and Theoretical Calculation, *Int. J. Electrochem. Sci.* 13 (2018) 4640–4660.
14. X. Guo, H. Huang, D. Liu, The inhibition mechanism and adsorption behavior of three purine derivatives on the corrosion of copper in alkaline artificial seawater: Structure and performance, *Colloids. Surf. A. Physicochem. Eng Asp.* 622 (2021) 126644.
15. A. Döner, G. Kardaş, N-Aminorhodanine as an effective corrosion inhibitor for mild steel in 0.5M H<sub>2</sub>SO<sub>4</sub>, *Corros. Sci.* 53 (2011) 4223–4232.
16. Q. Deng, S. Jeschke, B.J. Murdoch, S. Hirth, P. Eiden, J.N. Gorges, P. Keil, X.B. Chen, I. Cole, In-depth insights of inhibitory behaviour of 2-amino-4-methylthiazole towards galvanised steel in neutral NaCl solution, *Corros. Sci.* 199 (2022) 110206.
17. Q. Deng, S. Jeschke, M.R. Jakeria, P. White, S. Hirth, P. Eiden, J.N. Gorges, X.B. Chen, P. Keil, I. Cole, Synergistically and sustainably performed inhibitors for galvanised steel against aqueous corrosion, *Corros. Sci.* 213 (2023) 110984.
18. I.A. Kartsonakis, S.G. Stanciu, A.A. Matei, R. Hristu, A. Karantonis, C.A. Charitidis, A comparative study of corrosion inhibitors on hot-dip galvanized steel, *Corros. Sci.* 112 (2016) 289–307.
19. K. Aramaki, Effects of organic inhibitors on corrosion of zinc in an aerated 0.5 M NaCl solution, *Corros. Sci.* 43 (2001) 1985–2000.
20. T. Kosec, D.K. Merl, I. Milošev, Impedance and XPS study of benzotriazole films formed on copper, copper–zinc alloys and zinc in chloride solution, *Corros. Sci.* 50 (2008) 1987–1997.

21. A.M. Fenelon, C.B. Breslin, An electrochemical study of the formation of benzotriazole surface films on copper, zinc and a copper-zinc alloy, *J. Appl. Electrochem.* 31 (2001) 509–516.
22. V. Sirtori, F. Zambon, L. Lombardi, XPS and ellipsometric characterization of zinc-BTA complex, *J. Electron. Mater.* 29 (2000) 463–467.
23. A. Mohamed, D.P. Visco, D.M. Bastidas, Sodium Succinate as a Corrosion Inhibitor for Carbon Steel Rebars in Simulated Concrete Pore Solution, *Molecules.* 27 (2022) 8776.
24. S. Böhm, H.N. McMurray, S.M. Powell, D.A. Worsley, Photoelectrochemical investigation of corrosion using scanning electrochemical techniques, *Electrochim. Acta.* 45 (2000) 2165–2174.
25. G. Williams, H. Neil McMurray, Localized Corrosion of Magnesium in Chloride-Containing Electrolyte Studied by a Scanning Vibrating Electrode Technique, *J. Electrochem. Soc.* 155 (2008) C340.
26. A.C. Bastos, M.C. Quevedo, O. v Karavai, M.G.S. Ferreira, On the Application of the Scanning Vibrating Electrode Technique (SVET) to Corrosion Research, *J. Electrochem. Soc.* 164 (2017) C973–C990.
27. H.S. Isaacs, The Effect of Height on the Current Distribution Measured with a Vibrating Electrode Probe, *J. Electrochem. Soc.* 138 (1991) 722–728.
28. H.N. McMurray, S.M. Powell, D.A. Worsley, Mechanistic changes in cut edge corrosion induced by variation of inhibitor pigmentation in organically coated galvanised steel, *British Corrosion Journal.* 36 (2013) 42–48.
29. D.A. Worsley, H.N. McMurray, A. Belghazi, Determination of localised corrosion mechanisms using a scanning vibrating reference electrode technique, *Chemical Communications.* (1997) 2369–2370.
30. G.W.C. Kaye, T.H. Laby, *Tables of Physical and Chemical Constants*, Longman, London, 1986.

31. C.F. Glover, G. Williams, Inhibition of Localized Corrosion of Hot Dip Galvanized Steel by Phenylphosphonic Acid, *J. Electrochem. Soc.* 164 (2017) C407–C417.
32. D.A. Worsley, H.N. McMurray, J.H. Sullivan, I.P. Williams, Quantitative Assessment of Localized Corrosion Occurring on Galvanized Steel Samples Using the Scanning Vibrating Electrode Technique, *Corrosion*. 60 (2004) 437–447.
33. N. Wint, J.H. Sullivan, D.J. Penney, The Role of pH on the Inhibition of Aqueous Zinc Corrosion by L-tryptophan, *J. Electrochem. Soc.* 164 (2017) C356–C366.
34. S. Thomas, N. Birbilis, M.S. Venkatraman, I.S. Cole, Corrosion of zinc as a function of pH, *Corrosion*. 68 (2012) 1–9.
35. D. Persson, D. Thierry, N. LeBozec, Corrosion product formation on Zn55Al coated steel upon exposure in a marine atmosphere, *Corros. Sci.* 53 (2011) 720–726.
36. B. Beverskog, I. Puigdomenech, Revised pourbaix diagrams for zinc at 25–300°C, *Corros. Sci.* 39 (1997) 107–114.
37. P. M., *Atlas of Electrochemical Equilibria in Aqueous Solutions*, (1966).
38. R. Marsalek, Particle Size and Zeta Potential of ZnO, *APCBEE Procedia*. 9 (2014) 13.
39. K. Jurkiewicz, The removal of zinc from solutions by foam separation, II. Precipitate flotation of zinc hydroxide, *Int. J. Miner. Process.* 29 (1990) 1.
40. G. Redmond, A. O’Keeffe, C. Burgess, C. MacHale, D. Fitzmaurice, Spectroscopic determination of the flatband potential of transparent nanocrystalline ZnO films, *J. Phys. Chem.* 97 (1993) 11081.
41. M. Gausmann, A. Jupke, Dynamic Modeling of Electrochemical pH-Swing Extraction, *Chemie Ingenieur Technik*. 92 (2020) 1953–1961.
42. H. Dafydd, D.A. Worsley, H.N. McMurray, The kinetics and mechanism of cathodic oxygen reduction on zinc and zinc–aluminium alloy galvanized coatings, *Corros. Sci.* 47 (2005) 3006–3018.

43. H.N. McMurray, Localized Corrosion Behavior in Aluminum-Zinc Alloy Coatings Investigated Using the Scanning Reference Electrode Technique, *Corrosion*. 57 (2001) 313–322.
44. N. Wint, C.M. Griffiths, C.J. Richards, G. Williams, H.N. McMurray, The role of benzotriazole modified zinc phosphate in preventing corrosion-driven organic coating disbondment on galvanised steel, *Corros. Sci.* 174 (2020) 108839.
45. S. Sobel, A. Haigney, T. Conception, M. Kim, The complexation of aqueous metal ions relevant to biological applications. 1. Poorly soluble zinc salts and enhanced solubility with added amino acid, *Chemical Speciation and Bioavailability*. 20 (2008) 93–97.

## **Chapter 5**

# **Inhibition of Corrosion-Driven Cathodic Delamination of HDG by in-coating BTSA Additives**



## 5.1 Introduction

The study discussed in Chapter 4 revealed that adding BTSA to aqueous electrolyte can effectively reduce the occurrence and severity of localised corrosion on HDG, Galfan, and Zn55Al surfaces through mixed inhibition. While this is a promising result, it does not necessarily mean that it will perform well when incorporated into organic coatings for each substrate, for which corrosion-driven organic coating failure is a significant challenge. Therefore, for BTSA to be considered a viable and non-toxic alternative to chromate in primer coating systems, it must demonstrate efficacy against such failures.

For HDG, a prevalent corrosion-induced organic failure is cathodic delamination, whereby anodic metal dissolution at a coating defect couples with a front of underfilm cathodic oxygen reduction [1–8]. This process produces underfilm  $\text{OH}^-$ , resulting in an elevated pH underfilm environment that causes coating delamination through a combination of zinc hydr(oxide) dissolution, destruction of interfacial bonding, and base-catalysed polymer degradation [9–13].

To date, chromate-free inhibitor pigments have struggled to match the efficacy of chromate-containing pigments in preventing cathodic delamination [14–17]. For example, while model coating systems containing strontium chromate ( $\text{SrCrO}_4$ ) provided complete prevention of HDG cathodic delamination over 24 hours, the chromate-free industry standard, zinc phosphate ( $\text{Zn}_3(\text{PO}_4)_2$ ), at an equal pigment loading, only reduced the rate by 66% [18–20]. As described in greater detail in (Section 1.3.5), unlike chromate, phosphate cannot compete with the oxygen reduction reaction at cathodic sites. Instead, it reduces the rate of the anodic reaction at defect sites. However, the solubility of phosphate salts is low, so insufficient quantities can leach out of the organic coating to inhibit the anodic reaction. Hence, cathodic delamination continues [18–20].

Considering its mixed inhibition towards HDG, BTSA leaching out of an organic coating may reduce cathodic and anodic activity during cathodic delamination. However, the challenge of incorporating organic compounds such as BTSA within protective coatings is the tendency of heteroatoms to react with organic coating functionalities. As a

result, inhibitory properties can be lost, and cross-linking densities of coating systems are reduced [21]. To alleviate compatibility issues, organic inhibitors have been previously encapsulated within “smart-release” technologies that possess better compatibility with coating systems whilst offering improved anti-corrosion properties [22–26]. Smart-release systems can sequester corrosion-stimulating ions through ionic exchange with their encapsulated inhibitor [22].

A promising smart release system is hydrotalcite (HT), a layered-double hydroxide of the general formula  $\text{Mg}_6\text{Al}_2\text{CO}_3(\text{OH})_{16}\cdot 4(\text{H}_2\text{O})$ . HT consists of positively charged layers of magnesium and aluminium that are electrically neutralised by weakly bound anions, typically carbonate [27,28]. Recently, Ansell et al. showed the effect of several novel HT-based pigments on the cathodic delamination of HDG. It was found that HT intercalated with benzotriazole (BTA) rivalled the performance of HT containing stored chromate ions at equal pigment loadings. The performance was consistent with released  $\text{BTA}^-$  adsorbing onto the underfilm metal surface and forming a barrier to corrosive processes [29].

This chapter investigates and compares the inhibition of cathodic delamination on hot-dip galvanised steel (HDG) using two types of pigments: in-coating BTSA and newly synthesized HT-BTSA. By employing an accelerated cell designed by Stratmann [1-3], the cathodic delamination of model coatings containing dispersions of BTSA and HT-BTSA pigments at varying pigment loadings is monitored. The monitoring is conducted using a combination of time-lapse photography and the scanning Kelvin probe (SKP) technique.

## 5.2 Experimental Details

### 5.2.1 Materials

Hot dip galvanised steel (HDG) substrate was supplied and cleaned in the same way as for Chapter 4. All chemicals, including 2-(1,3-benzothiazol-2-ylthio)succinic acid (BTSA), hydrotalcite (HT, nominal composition:  $\text{Mg}_6\text{Al}_2\text{CO}_3(\text{OH})_{16}\cdot 4(\text{H}_2\text{O})$ ), and polyvinyl butyral-co-vinyl alcohol-co-vinyl acetate (PVB), molecular weight 70,000-100,000, as well as all other reagents and solvents used, were purchased in analytical grade from Merck.

### 5.2.2 Methods

#### 5.2.2.1 Spectrophotometric Determination of BTSA

Optical absorbance measurements were performed in a 1 cm quartz cuvette using a Perkin-Elmer Lambda 750 UV/VIS/NIR Spectrometer. Solutions were adjusted to pH 7 with  $\text{NaOH}_{(\text{aq})}$  so that the dianion of BTSA,  $\text{BTSA}^{2-}$  was measured. Absorbance measurements were taken at  $\lambda_{\text{max}} = 283 \text{ nm}$  in  $\text{BTSA}^{2-}$  concentrations ranging between  $1 \times 10^{-5}$  and  $10 \times 10^{-5} \text{ mol dm}^{-3}$  and plotted in a calibration plot of absorbance vs. BTSA concentration (Figure 5.1). The resulting straight line ( $R^2 = 0.9997$ ) showed that at pH 7, aqueous  $\text{BTSA}^{2-}$  in the stated concentration range obeys the Beer-Lambert law (Equation 5.1) and that  $\text{BTSA}^{2-}$  does not have a significant association, precipitation, or surface absorption.

$$A_{283} = \varepsilon_{283} \cdot c \cdot l \quad (5.1)$$

Where  $\varepsilon_{283}$  is the molar extinction coefficient,  $c$  is the molar concentration, and  $l$  is the optical path length in cm. The least squares analysis of the calibration plot determined an  $\varepsilon_{283}$  value of  $11770 \pm 100 \text{ M}^{-1} \text{ cm}^{-1}$  at  $20^\circ \text{C}$ . The concentration of subsequent aqueous solutions of BTSA were determined by withdrawing aliquots, volumetrically diluting with de-ionised water (if necessary), adding  $\text{NaOH}_{(\text{aq})}$  to neutralise to pH 7, and then measuring the optical absorbance of  $\text{BTSA}^{2-}$  at 283 nm.

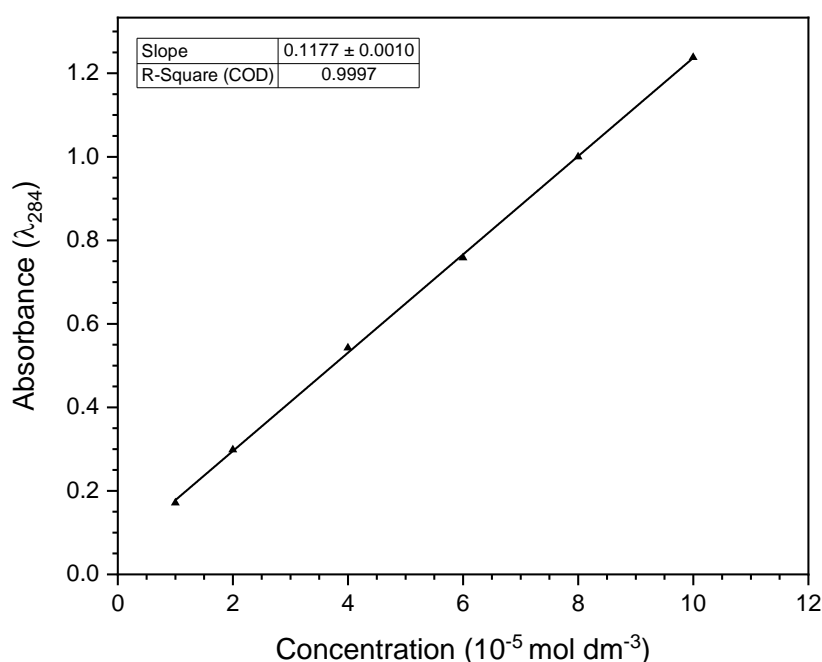


**Figure 5.1:** Calibration plot of  $\text{BTSA}^{2-}$  concentration vs optical absorbance ( $\lambda_{\text{max}} = 283$  nm). All solutions were buffered to pH 7 through dropwise addition of  $\text{NaOH}_{(\text{aq})}$ .

#### 5.2.2.2 Preparation of HT-BTSA

HT-BTSA was prepared via the rehydration method [30]. HT was calcined in air at  $450^\circ\text{C}$  for 3 h, removing intercalated  $\text{CO}_3^{2-}$  and associated  $\text{H}_2\text{O}$  to produce an  $\text{Al}_2\text{O}_3$ -MgO mixed oxide, which was allowed to cool to room temperature [31-33]. 10 g quantities of  $\text{Al}_2\text{O}_3$ -MgO were then dispersed into 3 L aliquots of deaerated, 10 mmol solutions of BTSA at pH 7 and stirred at a constant speed for 18 h. The resulting HT-BTSA pigment was washed by repeated cycles of centrifugation and re-dispersion in fresh deionised water until BTSA was not observed in the washed filtrate, as determined by its UV-Vis optical absorbance. The washed pigment was collected using Buchner filtration and dried for 6 h under a vacuum. The resulting pigment was milled using a Retch planetary ball mill at 350 RPM for 1 h and sieved through a  $20\ \mu\text{m}$  mesh, yielding a finely divided HT-BTSA pigment of particle size  $<20\ \mu\text{m}$  [29,34].

### 5.2.2.3 HT-BTSA Back-Exchange

The quantity of stored inhibitor within HT-BTSA was determined by the following method. 1 g quantities of HT-BTSA were dispersed in 100 mL of either 1% w/v NaOH<sub>(aq)</sub> at pH 10 or deionised water. After 10 minutes of magnetic stirring, 1 mL aliquots of the supernatant solution were withdrawn, diluted to 100 mL with deionised water, adjusted to pH 7 by adding NaOH<sub>(aq)</sub>, and its UV-VIS absorbance at 283 nm recorded. Four successive back-exchange cycles were performed, using fresh aqueous solutions on each occasion. Figure 5.2 shows how the quantity of BTSA<sup>2-</sup> released upon each exchange cycle in 1% w/v NaOH<sub>(aq)</sub> at pH 10 decreased from 0.23 mmol g<sup>-1</sup> on the first cycle to 0.03 mmol g<sup>-1</sup> on the fourth cycle. In comparison, the maximum quantity exchanged in a cycle in deionised water was 0.02 mmol g<sup>-1</sup>. The total exchangeable BTSA<sup>2-</sup>, obtained by adding up quantities released over all four cycles, was 0.35 mmol g<sup>-1</sup>, corresponding to a pigment anion-exchange capacity of 0.7 meq g<sup>-1</sup>. This value is consistent with previous quantification of the exchange capacity of HT intercalated with a dianionic species [35].

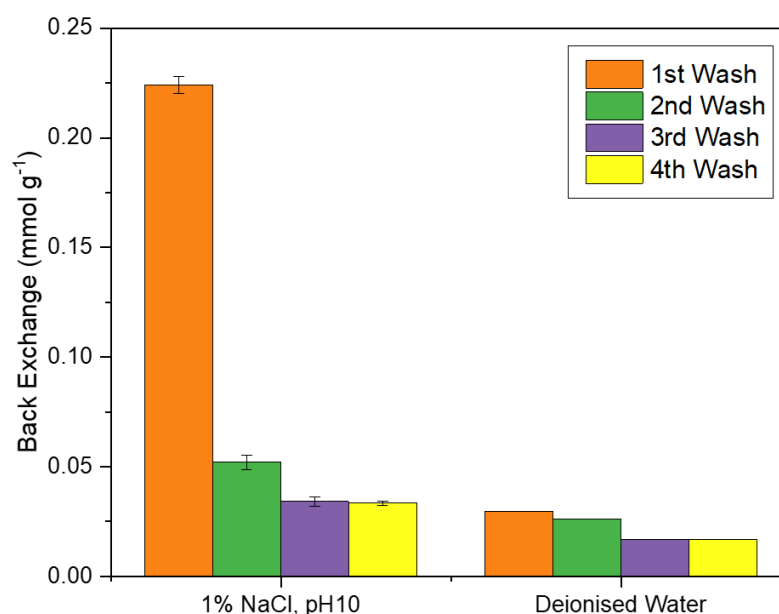


**Figure 5.2:** The back-exchanged concentration of BTSA<sup>2-</sup> after four successive cycles in a) 1% w/v NaOH<sub>(aq)</sub>, pH 10, and b) deionised water.

#### 5.2.2.4 Stratmann Cell Preparation

Accelerated cathodic delamination samples were prepared for HDG following a method described by Stratmann et al. [1–3] and in Section 2.2.2.2.

#### 5.2.2.5 Cathodic Delamination Inhibition by in-coating BTSA Species

Model organic coatings containing varying pigment volume fractions,  $\Phi$  of HT-BTSA were prepared according to Equation 5.2:

$$\Phi = \left( 1 + \frac{M_{\text{PVB}} \cdot \rho_{\text{HT-BTSA}}}{M_{\text{HT-BTSA}} \cdot \rho_{\text{PVB}}} \right)^{-1} \quad (5.2)$$

where  $M_{\text{PVB}}$  is the mass of PVB used in the coating formulation,  $M_{\text{HT-BTSA}}$  is the mass of the HT-BTSA pigment,  $\rho_{\text{HT-BTSA}}$  is the density of the HT-BTSA pigment ( $2.06 \text{ g cm}^{-3}$ ) [36], and  $\rho_{\text{PVB}}$  is the density of PVB ( $0.8 \text{ g cm}^{-3}$ ). By way of comparison, non smart-release model-coatings were made via dispersion of varying BTSA loadings into ethanolic solutions of 15.5% w/w PVB via a w/w calculation.

Stratmann cells of the model coatings on HDG were prepared, and cathodic delamination was initiated by adding 2 mL of  $0.86 \text{ mol dm}^{-3} \text{ NaCl}_{(\text{aq})}$ , pH 7 into the defect. The kinetics of cathodic delamination for the pigmented coatings were determined using time-lapse photography experiments described by Wint et al. [37] and in Chapter 2. Additionally, insights into the mechanism of inhibition were provided by the SKP. A full description of the SKP instrumentation, calibration, experimental set-up, and analysis can be found in Chapter 2 and elsewhere [1,2,18]. In this work, the SKP reference probe was scanned along a 12 mm line normal and adjacent to the defect boundary, 100  $\mu\text{m}$  from the sample surface. Scans were conducted immediately after initiation and then at 1 h intervals for up to 72 h, giving rise to time-dependent  $E_{\text{corr}}$ -distance(x) profiles with 20 points per mm. The SKP chamber was kept at a constant temperature of 25 °C and relative humidity (RH) of 95%.

## 5.3 Results and Discussion

### 5.3.1 Effects of in-coating BTSA

Time-lapse photography was used to provide a preliminary evaluation of the influence of BTSA incorporated either directly into a PVB coating or as the stored inhibitor within a dispersion of HT-BTSA pigment. A comparison of delamination kinetics, provided as plots of  $X_{\text{del}}$  against time for varying loadings of BTSA and HT-BTSA, are shown in Figure 5.3 and Figure 5.4, respectively. In both cases, an increase in inhibitor loading produces a progressive decrease in the extent of visual coating delamination and increasingly delays the onset of underfilm corrosion initiation. Notably, the time-dependent behaviour of delamination distance for all loadings of BTSA (Figure 5.3) and HT-BTSA (Figure 5.4) is linear, a clear contrast to the parabolic kinetics shown for unpigmented PVB. The latter observation for the unpigmented case is consistent with previous findings for unpigmented PVB coatings applied to HDG substrates, where in-situ SKP analysis showed that delamination kinetics depend on the square root of holding time at high humidity [8,18,20].

The transition from parabolic to linear kinetics observed for all BTSA-inhibited PVB coatings is consistent with previous findings for a range of in-coating inhibitive pigment technologies applied to HDG surfaces [8,20,29,38–40]. In that research, it was observed that the linear kinetics for inhibited PVB coatings can be attributed to a change in the rate-limiting step; instead of cation migration from the defect region to the delamination front being rate-limiting [2,41], the delamination rate is controlled by the rate of interfacial electron transfer. However, recently published work involving PVB-coated iron has proposed an alternative theory. This theory suggests a rate-limiting cation insertion step at the intact coating-metal interface immediately ahead of the cathodic delamination front [42]. The authors argue that the cation insertion step can remain rate-controlling, regardless of whether the observed delamination kinetics are constant with time or dependent on the square root of time. They suggest that the change in kinetics is derived from differences in the IR drop along the delaminated interface. Considering this new alternative

theory, the influence of in-coating BTSA on delamination kinetics is further discussed in Section 5.3.3.

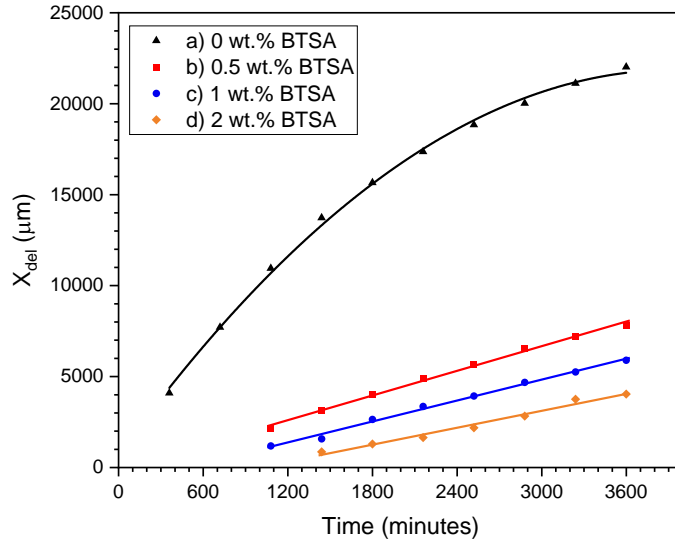


**Figure 5.3:** Time lapse photography derived plots of delamination distance ( $X_{del}$ ) as a function of time for PVB films containing (a) 0 wt.%, b) 0.5 wt.%, c) 1 wt.% and d) 2 wt.% BTSA.

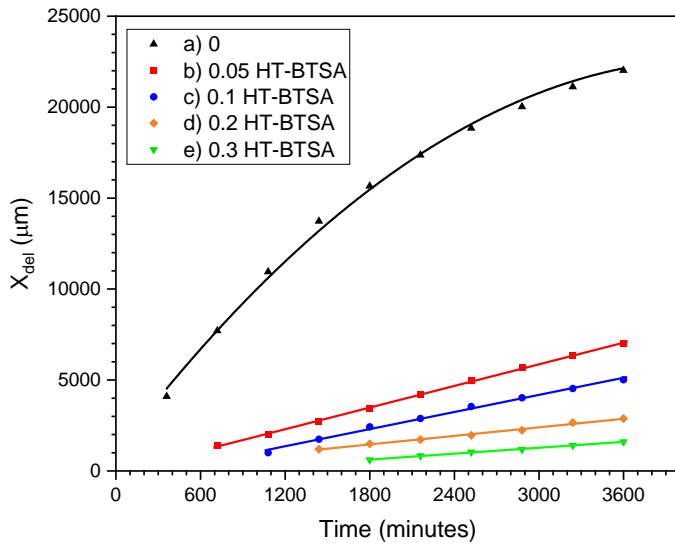


**Figure 5.4:** Time lapse photography derived plots of delamination distance ( $X_{del}$ ) as a function of time for PVB films containing a  $\Phi_{HT-BTSA}$  of (a) 0, b) 0.05, c) 0.1, d) 0.2 and e) 0.3.



Examining the kinetics of cathodic delamination, an initial visual inspection of each plot appears to show that BTSA and HT-BTSA provide similar levels of inhibition of cathodic delamination. However, a linear regression analysis of the slopes of the  $X_{\text{del}}$  versus time plot to calculate the delamination rate ( $k_{\text{del}}$ ) reveals that the in-coating HT-BTSA pigment is a more effective inhibitor of cathodic delamination. The results are summarised in Figure 5.5, where  $k_{\text{del}}$  (in  $\mu\text{m min}^{-1}$ ) is plotted as a function of the loading of each inhibitor. It should be noted that the comparison of BTSA loading (in wt.%) and HT-BTSA pigment volume fraction is made based on mmol of available BTSA per  $\text{cm}^2$  of PVB coating, assuming that the smart release pigment contains 0.35 mmol of exchangeable BTSA<sup>2-</sup> anions per gram of HT-BTSA pigment. Furthermore, to compare with the control experiment, the  $k_{\text{del}}$  of the uninhibited PVB coating is estimated from the first 10 h of the experiment, where the relationship between  $X_{\text{del}}$  and time is initially linear.

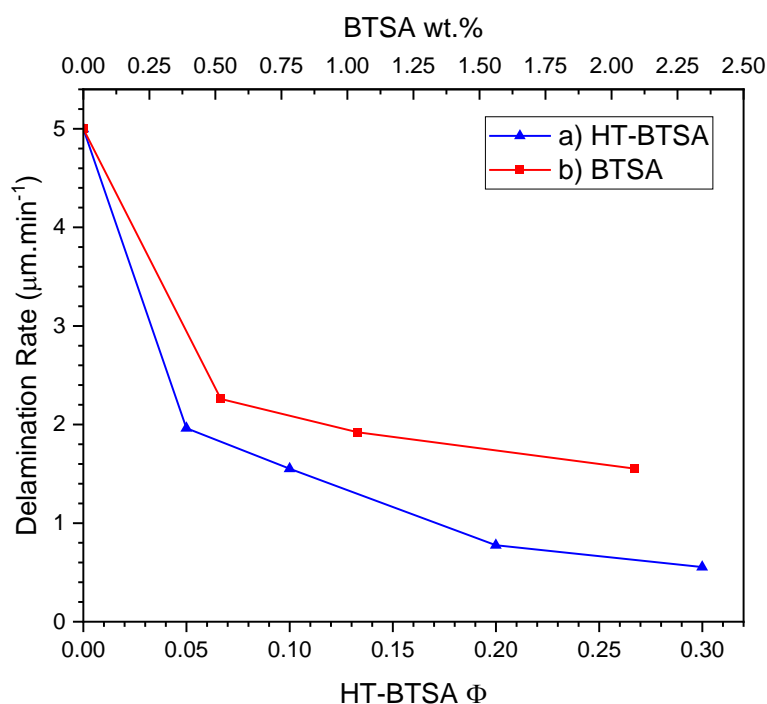


**Figure 5.5:** Time-lapse derived rate of cathodic delamination ( $k_{\text{del}}$ ) as a function of HT-BTSA  $\Phi$  and BTSA wt.% for a) PVB coatings containing HT-BTSA and b) PVB coatings containing BTSA.

As shown in the Figure, the superior performance of HT-BTSA pigment becomes increasingly evident with higher pigment loading. Using Equation 5.3 below to calculate inhibitor efficiency ( $\eta$ ), a value of 70% is calculated for a 2 wt.% BTSA direct addition, significantly lower than the equivalent  $\eta$  of 89% determined for the highest HT-BTSA pigment volume fraction used. This indicates that despite the equivalent availability of BTSA per unit area of coating, the inhibitory performance of HT-BTSA is better than that of BTSA dissolved into the PVB coating. This superior performance of HT-BTSA may be due to the enhanced delivery of BTSA anions to both the cathodic delamination front and the underfilm electrolyte layer within the delaminated zone.

$$\eta = \left( \frac{k_{\text{PVB}} - k_{\text{inh}}}{k_{\text{PVB}}} \right) \times 100\% \quad (5.3)$$

In Equation 5.3, the term  $k_{\text{PVB}}$  represents the coating delamination rate measured for uninhibited PVB, while  $k_{\text{inh}}$  refers to delamination rates measured in the presence of in-coating BTSA or HT-BTSA.

Having established that the HT-BTSA inhibitor is a more effective inhibitor of cathodic delamination than direct additions of BTSA, further experiments designed to elucidate the possible mechanism of inhibition were performed exclusively on the former.

### 5.3.2 SKP Investigation of Unpigmented PVB

A preliminary SKP experiment was conducted to study the cathodic delamination of the HDG substrate. The experiment produced time-dependent  $E_{\text{corr}}$ -distance( $x$ ) profiles, which are shown in Figure 5.6. This particular case, in the absence of inhibitor pigments has been presented in several previous publications, therefore it will only be briefly discussed.

After equilibrium with humid air, the surface of the PVB-coated HDG (intact) obtains a high and uniform potential of around -350 mV vs SHE, similar to the passive state of a zinc surface [18]. Within 1-2 h of applying 0.86 mol dm<sup>-3</sup> NaCl<sub>(aq)</sub> electrolyte to the defect region of the specimen, PVB coating delamination is initiated, resulting in distinctive

$E_{\text{corr}}$ -distance(x) profiles as the delamination propagates under the influence of a differential aeration cell. The  $E_{\text{corr}}$ -distance(x) profiles are characterised by a sharp potential drop of ca. 300 mV, indicating the position of the cathodic delamination front, and a gradual decrease in potential within the delaminated region that connects the underfilm cathode (Reaction 5.4) to a net anode located at the defect region (Reaction 5.5). Measured at a distance of 0 mm, potential values ranging from -700 mV to -800 mV vs SHE reflect the  $E_{\text{corr}}$  of a zinc surface freely corroding in a chloride-containing aqueous electrolyte.

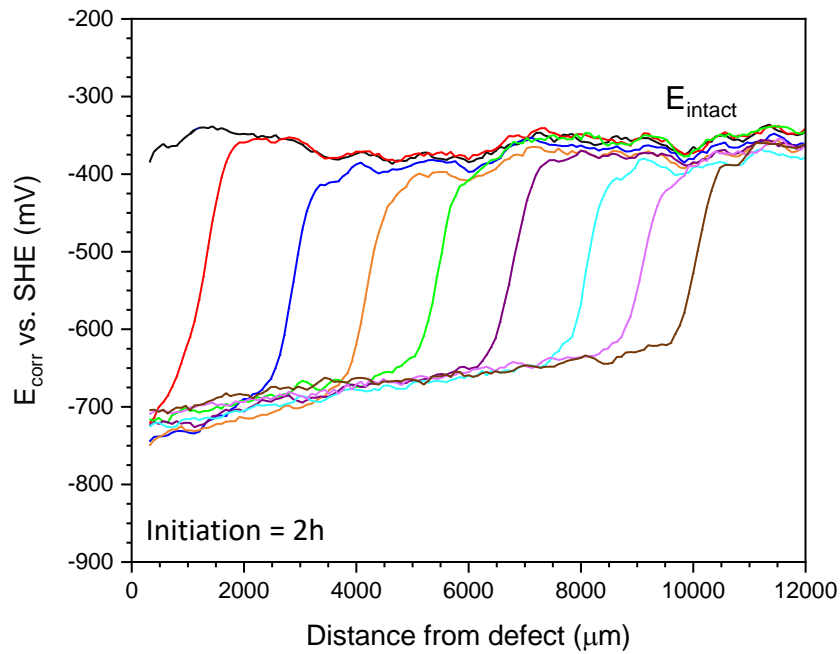
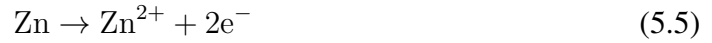
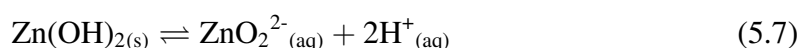
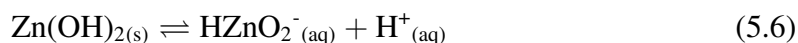


**Figure 5.6:** SKP derived  $E_{\text{corr}}$  as a function of distance from defect profile for the delamination of unpigmented PVB coating on HDG steel shown at a) 2h, b) 4h, c) 6h, d) 8h, e) 10h, f) 12h, g) 14h, h) 16h, and i) 18h.

The underfilm generation of hydroxide ions via Reaction 5.4, produces an alkaline un-

derfilm environment with a pH >10. As such, delamination of the PVB coating results from a combination of the dissolution of the amphoteric zinc hydr(oxide) layer at the polymer coating interface (Reactions 5.6 and 5.7) and base catalysed hydrolysis of PVB vinyl acetate functions.



The delamination kinetics, determined by the time-dependent position of the sharp drop in  $E_{\text{corr}}$ , marking the location of the cathodic delamination front, is similar to that observed previously for time-lapse imaging experiments (Figure 5.4). Furthermore, the parabolic nature of the kinetics for unpigmented PVB is confirmed by a linear relationship of delamination distance versus  $t^{1/2}$ , producing a slope of  $460 \mu\text{m min}^{-1/2}$ .

To examine how the presence of BTSA inhibitor in the initial electrolyte affects the cathodic delamination rate, a 10 mM concentration of BTSA was dissolved in  $0.86 \text{ mol dm}^{-3}$   $\text{NaCl}_{(\text{aq})}$  and adjusted to pH 7. Subsequently, a further SKP was conducted with the BTSA dosed electrolyte solution. The corresponding time-dependent  $E_{\text{corr}}$ -distance(x) profiles using BTSA inhibited electrolyte are provided in Figure 5.7, showing a significant reduction in delamination rate compared to the uninhibited control experiment (Figure 5.6). Linear kinetics are established, with the inhibited electrolyte yielding a  $k_{\text{PVB}}$  value of  $1.3 \mu\text{m min}^{-1}$ , a reduction by an order of magnitude from the uninhibited case, where an initial  $k_{\text{PVB}}$  of approximately  $12 \mu\text{m min}^{-1}$  is established.

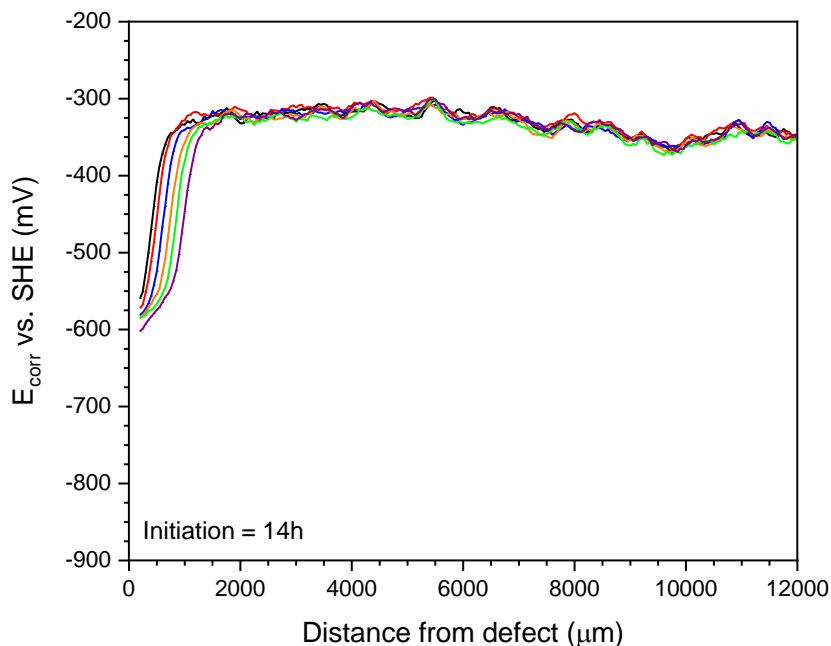


**Figure 5.7:** SKP derived  $E_{corr}$  as a function of distance from defect for the delamination of a PVB film on HDG steel with 10 mM BTSA doped into the well electrolyte shown at a) 14h, b) 16h, c) 18h, d) 20h, e) 22h, and f) 24h.

The marked effect of BTSA on the delamination rate contrasts with previous studies that used various ionic inorganic inhibitors dosed into defect electrolytes applied to PVB-coated HDG [18,39,43]. In those studies, anodic inhibition was not sufficient to prevent cathodic delamination. As explained in Chapter 4, assuming that the pKa values of BTSA are similar to that of succinic acid ( $pK_a(1) = 4.16$  and  $pK_a(2) = 5.61$ ) [44], at pH 7, most dissolved BTSA exists as its di-anionic species,  $BTSA^{2-}$ . Therefore, on an electrostatic basis,  $BTSA^{2-}$  should not migrate into the underfilm electrolyte in the delaminated region and affect the rate of underfilm cathodic oxygen reduction. Thus, in the case of BTSA dissolved in the defect electrolyte, it seems that sufficient inhibition of anodic zinc dissolution (Reaction 5.5) is achieved, especially in the vicinity of the defect-coating boundary, to limit the progress of the underfilm cathodic delamination front.

In reference to the investigation of anodic inhibition by dissolved BTSA on ZnAl surfaces in Chapter 4, spot tests found that mixing different solutions containing equal concentrations of either BTSA or  $ZnCl_{2(aq)}$  at pH 7 produced a cloudy white precipitate at all

concentrations  $\geq 10^{-3}$  M. Therefore it seems plausible to suggest that the formation of an insoluble film of Zn(BTSA) at sites of anodic Zn dissolution near, or at the defect-coating interface contributes to the significant reduction in  $k_{\text{PVB}}$  when dissolved BTSA is present in the defect electrolyte. Additional evidence to support this theory is obtained from Figure 5.7, where measured  $E_{\text{corr}}$  values immediately adjacent to the defect are approximately 100 mV more positive than the case where the defect contains an uninhibited  $\text{NaCl}_{(\text{aq})}$  electrolyte (Figure 5.6).

### 5.3.3 SKP Investigation of HT-BTSA Pigmented PVB

Further SKP experiments were conducted using PVB coatings dispersed with varying HT-BTSA pigment volume fractions. Figure 5.8 and Figure 5.9 show typical examples of  $E_{\text{corr}}$ -distance(x) profiles obtained for low (0.05) and high (0.2) pigment volume fractions, respectively. The delamination kinetics obtained from the relevant  $E_{\text{corr}}$ -distance(x) data for the varying HT-BTSA loadings are consistent with the  $k_{\text{del}}$  vs pigment loading range reported in Section 5.3.1. Nevertheless, the influence of in-coating HT-BTSA additions on the distribution of  $E_{\text{corr}}$  values determined over the underfilm delamination cell provides valuable evidence on the modes by which the cathodic delamination process may become inhibited. A comparison of the potentials measured over regions where the coating remains adherent to the HDG substrate ( $E_{\text{intact}}$ ) shows that the in-coating HT-BTSA depresses potentials by up to 150 mV compared to the unpigmented case ( $E_{\text{intact}}$  approx. -350 mV vs SHE). It is also noteworthy that progressive increases in HT-BTSA loading produce a greater depression in  $E_{\text{intact}}$ , from -450 mV vs SHE for  $\Phi = 0.05$  to -500 mV vs SHE for  $\Phi = 0.2$ . In turn, this progressive depression of  $E_{\text{intact}}$  with increasing availability of in-coating inhibitive pigment, coupled with a change from parabolic to linear delamination kinetics (Figure 5.4) implies that inhibition of underfilm cathodic oxygen reduction via Reaction 5.4 may contribute to the observed decrease in rates of corrosion-driven delamination.

The question arises of how the in-coating BTSA suppresses underfilm cathodic oxygen reduction (Reaction 5.4), as indicated by the previously discussed decrease in  $E_{\text{intact}}$  and

the notable decrease in delamination rate observed with increasing inhibitor pigment loading. Previous research on other organic anions stored within an HT smart-release pigment system has highlighted the efficacy of aromatic species such as salicylaldoximate and benzotrizolate as effective inhibitors of cathodic delamination on a HDG surface [29]. These compounds, once released from their ion-exchanger exhibited strong adsorption on the oxide-covered zinc, impeding electron transfer at the coating-substrate interface. Additionally, it was previously shown in potentiodynamic polarisation experiments in Chapter 4 that BTSA, also an anionic heterocyclic species reduces cathodic current densities on zinc surfaces. As such, it seems plausible that BTSA adsorbs onto the hydr(oxide)-covered zinc surface in the underfilm region and operates similarly to stifle oxygen reduction.

Furthermore, it is conceivable that the ion-exchange properties of the pigment allow for better adsorption and subsequent performance. Firstly, when an ethanolic solution of PVB containing dispersed HT-BTSA is initially applied to the HDG surface, it is expected that some of the stored  $\text{BTSA}^{2-}$  ions are released via ion exchange with surface  $\text{OH}^-$  groups and are adsorbed. However, once cathodic delamination initiates, ion exchange with further  $\text{OH}^-$  ions that are liberated as a result of Reaction 5.4 releases more  $\text{BTSA}^{2-}$  into the delamination zone electrolyte to reinforce the adsorbed layer.

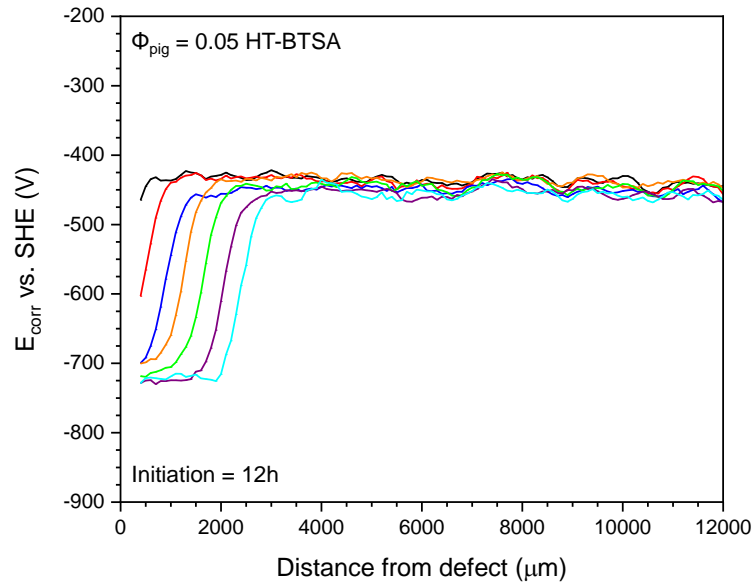


**Figure 5.8:** SKP derived  $E_{corr}$  as a function of distance from defect for the delamination of a PVB film containing a  $\Phi_{HT-BTSA}$  of 0.05 on HDG steel shown at a) 12h, b) 14h, c) 16h, d) 18h, e) 20h, f) 22h, and g) 24h.

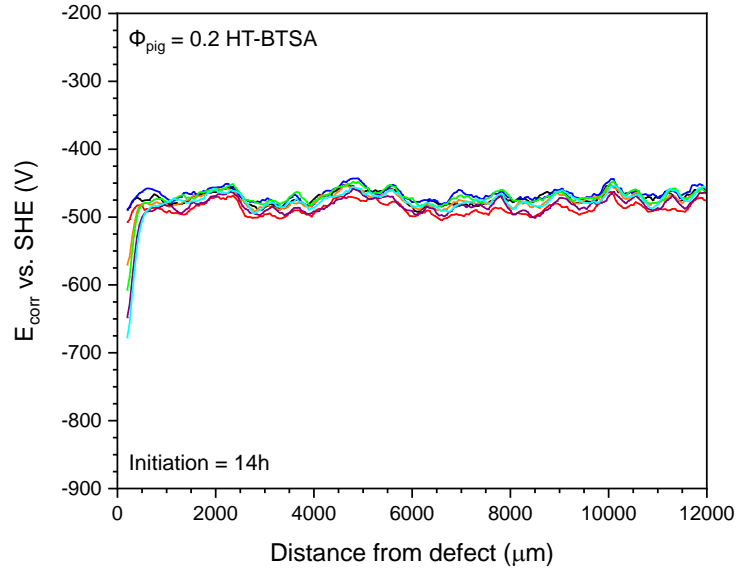


**Figure 5.9:** SKP derived  $E_{corr}$  as a function of distance from defect for the delamination of a PVB film containing a  $\Phi_{HT-BTSA}$  of 0.2 on HDG steel shown at a) 14h, b) 16h, c) 18h, d) 20h, e) 22h, and f) 24h.



It is also evident from the results presented in Figure 5.7 that any release of  $\text{BTSA}^{2-}$  anions from the in-coating HT pigment via ion exchange into the underfilm electrolyte, particularly adjacent to the coating-defect boundary, will provide anodic inhibition. Under the influence of the polarity of the underfilm corrosion cell, any  $\text{BTSA}^{2-}$  anions released into the delaminated zone will migrate towards the principal anode, eventually being transported to the chloride rich-electrolyte present at the defect. Observations of the formation of a white film in the defect region immediately adjacent to the coating using HT-BTSA-pigmented PVB at  $\Phi = 0.2$  support the hypothesis that an inhibitive film is formed at the point where  $\text{BTSA}^{2-}$  anions, transported from the underfilm region, meets a counter-current of  $\text{Zn}^{2+}$  cations produced by Reaction 5.5. However, this process of anodic inhibition is likely to be secondary to the affects of cathodic inhibition considering the relatively high concentration of  $\text{BTSA}^{2-}$  that would be required for complete anodic inhibition of the large model defect area. For instance, even 10 mM of BTSA dosed directly into the initiating electrolyte did not completely prevent cathodic delamination (Figure 5.7).

### 5.3.4 Mechanism of HT-BTSA Inhibition

The proposed mixed-inhibition of cathodic delamination of HDG by in-coating HT-BTSA is represented schematically in Figure 5.10. Through ion-exchange with  $\text{OH}^-$ ,  $\text{BTSA}^{2-}$  is released into the underfilm region and is adsorbed on to the hydr(oxide) zinc surface. This adsorption stifles underfilm cathodic oxygen reduction, thus reducing the rate of cathodic delamination. Additionally, under the influence of the polarity of the underfilm corrosion cell,  $\text{BTSA}^{2-}$  anions released into the underfilm electrolyte may migrate to the defect, inhibiting the anodic dissolution of zinc through formation of an insoluble  $\text{Zn}(\text{BTSA})$  product. However, this anodic protection mechanism is likely less influential compared to the cathodic inhibition.

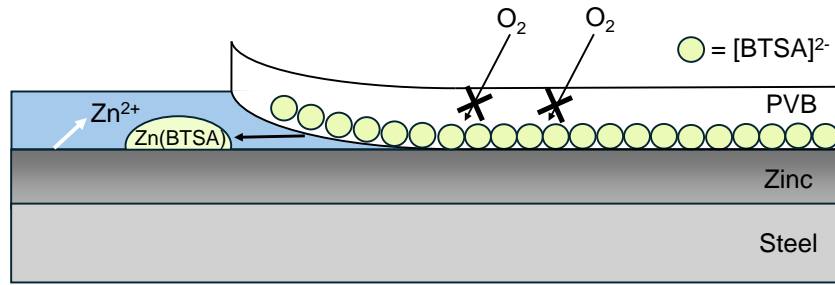
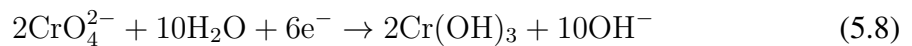


**Figure 5.10:** Schematic representation of the inhibitory influence of in-coating BTSA on the underfilm corrosion-delamination cell.

### 5.3.5 Comparison of HT-BTSA to HT-Chromate

The results presented have shown the promise of HT-BTSA as an in-coating inhibitor against the cathodic delamination of HDG. However, despite its effective performance, it does not offer the values of inhibition afforded by HT intercalated with chromate (HT- $\text{CrO}_4^{2-}$ ). For instance, at a  $\Phi$  of 0.2, HT-BTSA decreases  $k_{\text{del}}$  by 84% in comparison to unpigmented PVB, but HT- $\text{CrO}_4^{2-}$  at an equivalent loading entirely prevents cathodic delamination [29]. Unlike  $\text{CrO}_4^{2-}$ ,  $\text{BTSA}^{2-}$  is not redox active, meaning it can't directly compete with the oxygen reduction reaction whereas chromate can (Reaction 5.8). It can only slow down rates of oxygen reduction through adsorption and precipitation.



## 5.4 Conclusions

The ability of BTSA to mitigate corrosion-driven organic coating failure within model coatings applied to hot-dip galvanised steel has been investigated. A combination of time-lapse imaging and in-situ scanning Kelvin probe (SKP) potentiometry was employed to quantify the cathodic delamination rates of model polyvinyl butyral (PVB) coatings containing varying loadings of BTSA. It was demonstrated that in-coating BTSA, both added

directly to PVB or stored as an exchangeable anion in a layered double hydroxide “smart-release” pigment, was able to reduce rates of cathodic delamination by up to a factor of 20. For both methods of incorporating in-coating BTSA, an increased loading produced a progressive decrease in delamination rates and a transition from linear to parabolic coating failure kinetics. In addition, it was also demonstrated that BTSA dissolved in the aqueous  $\text{NaCl}_{(\text{aq})}$  electrolyte applied to a defect could also significantly reduce the rate of cathodic delamination observed for an unpigmented PVB coating.

In-coating BTSA appears to stifle cathodic delamination by adsorbing strongly on the intact organic-coated metal, which in turn hinders underfilm oxygen reduction. Additionally, the release of dissolved BTSA anions from the underfilm delaminated zone into the chloride-rich region immediately adjacent to the coating-defect boundary is shown to produce anodic inhibition, which further slows the progress of the delamination front.

## 5.5 References

1. A. Leng, H. Streckel, M. Stratmann, The delamination of polymeric coatings from steel. Part 1: Calibration of the Kelvinprobe and basic delamination mechanism, *Corros. Sci.* 41 (1998) 547.
2. A. Leng, H. Streckel, M. Stratmann, The delamination of polymeric coatings from steel. Part 2: First stage of delamination, effect of type and concentration of cations on delamination, chemical analysis of the interface, *Corros. Sci.* 41 (1998) 579.
3. A. Leng, H. Streckel, K. Hofmann, M. Stratmann, The delamination of polymeric coatings from steel Part 3: Effect of the oxygen partial pressure on the delamination reaction and current distribution at the metal/polymer interface, *Corros. Sci.* 41 (1998) 599.
4. E.L. Koehler, The Oxide Film on Steel and Cathodic Disbondment of a Protective Organic Coating, *J. Electrochem. Soc* 132 (1985) 1005–1009.
5. N.W. Khun, G.S. Frankel, Effects of surface roughness, texture and polymer degradation on cathodic delamination of epoxy coated steel samples, *Corros. Sci.* 67 (2013) 152.
6. S.J. Caraguay, T.S. Pereira, R.O. Giacomelli, A. Cunha, M. Pereira, F.A. Xavier, The effect of laser surface textures on the corrosion resistance of epoxy coated steel exposed to aggressive environments for offshore applications, *Surf. Coatings. Technol.* 437 (2022) 128371.
7. W. Fürbeth, M. Stratmann, Delamination of polymeric coatings from electrogalvanized steel - a mechanistic approach. Part 2: Delamination from a defect down to steel, *Corros. Sci.* 43 (2001) 229.
8. C.M. Griffiths, N. Wint, G. Williams, H.N. McMurray, The contribution of Zn(II) and phosphate anions to the inhibition of organic coating cathodic disbondment on galvanised steel by zinc phosphate pigment, *Corros. Sci.* 198 (2022) 110111.
9. H. Dafydd, D.A. Worsley, H.N. McMurray, The kinetics and mechanism of cathodic

- oxygen reduction on zinc and zinc–aluminium alloy galvanized coatings, *Corros. Sci.* 47 (2005) 3006–3018.
10. R. Hausbrand, M. Stratmann, M. Rohwerder, Delamination Resistant Zinc Alloys: Simple Concept and Results on the System Zinc-Magnesium, *Steel. Res. Int.* 74 (2003) 453–458.
  11. M. Stratmann, R. Feser, A. Leng, Corrosion protection by organic films, *Electrochim. Acta.* 39 (1994) 1207–1214.
  12. E.L. Koehler, The Influence of Contaminants on the Failure of Protective Organic Coatings on Steel, *Corrosion.* 33 (1977) 209–217.
  13. H. Leidheiser, W. Wang, L. Igetoft, The mechanism for the cathodic delamination of organic coatings from a metal surface, *Prog. Org. Coat.* 11 (1983) 19–40.
  14. R. Berger, U. Bexell, T. Mikael Grehk, S.E. Hörnström, A comparative study of the corrosion protective properties of chromium and chromium free passivation methods, *Surf. Coat. Technol.* 202 (2007) 391–397.
  15. P. Puomi, H.M. Fagerholm, A. Sopanen, Parameters affecting long-term performance of painted galvanised steels, *Anti-Corrosion Methods and Materials.* 48 (2001) 160–170.
  16. P. Puomi, H.M. Fagerholm, J.B. Rosenholm, K. Jyrkäs, Comparison of different commercial pretreatment methods for hot-dip galvanized and Galfan coated steel, *Surf. Coat. Technol.* 115 (1999) 70–78.
  17. M.F. Montemor, Functional and smart coatings for corrosion protection: A review of recent advances, *Surf. Coat. Technol.* 258 (2014) 17–37.
  18. G. Williams, H.N. McMurray, Chromate Inhibition of Corrosion-Driven Organic Coating Delamination Studied Using a Scanning Kelvin Probe Technique, *J. Electrochem. Soc.* 148 (2001) B377.
  19. O.Ø. Knudsen, A. Forsgren, Corrosion control through organic coatings, second edition, *Corrosion Control through Organic Coatings, Second Edition* (2017) 1–255.

20. N. Wint, C.M. Griffiths, C.J. Richards, G. Williams, H.N. McMurray, The role of benzotriazole modified zinc phosphate in preventing corrosion-driven organic coating disbondment on galvanised steel, *Corros. Sci.* 174 (2020) 108839.
21. B. Ramezanzadeh, E. Ghasemi, F. Askari, M. Mahdavian, Synthesis and characterization of a new generation of inhibitive pigment based on zinc acetate/benzotriazole: Solution phase and coating phase studies, *Dyes and Pigments*. 122 (2015) 331–345.
22. D.G. Evans, X. Duan, Preparation of layered double hydroxides and their applications as additives in polymers, as precursors to magnetic materials and in biology and medicine, *Chemical Communications*. (2006) 485–496.
23. D.A. Leal, A. Kuznetsova, G.M. Silva, J. Tedim, F. Wypych, C.E.B. Marino, Layered materials as nanocontainers for active corrosion protection: A brief review, *Appl. Clay. Sci.* 225 (2022) 106537.
24. A. Ouarga, N. Lebaz, M. Tarhini, H. Noukrati, A. Barroug, A. Elaissari, H. Ben Youcef, Towards smart self-healing coatings: Advances in micro/nano-encapsulation processes as carriers for anti-corrosion coatings development, *J. Mol. Liq.* 354 (2022) 118862.
25. M.F. Montemor, Functional and smart coatings for corrosion protection: A review of recent advances, *Surf. Coat. Technol.* 258 (2014) 17–37.
26. Y. Cao, D. Zheng, F. Zhang, J. Pan, C. Lin, Layered double hydroxide (LDH) for multi-functionalized corrosion protection of metals: A review, *J. Mater. Sci. Technol.* 102 (2022) 232–263.
27. S.J. Mills, A.G. Christy, J.-M.R. Génin, T. Kameda, F. Colombo, Nomenclature of the hydrotalcite supergroup: natural layered double hydroxides, *Mineral. Mag.* 76 (2012) 1289–1336.
28. S. Miyata, Anion-exchange properties of hydrotalcite-like compounds, *Clay. Miner.* 31 (1983) 305–311.
29. P. Ansell, L. Berry, J. McGettrick, J. Searle, N. Wint, H.N. McMurray, G. Williams, Role of Smart-Release Pigments in Preventing Corrosion Driven Cathodic Dis-

- bondment of Organically Coated Hot Dip Galvanised Steel, *J. Electrochem. Soc.* 170 (2023) 011502.
30. F. Kovanda, E. Kováčsová, D. Koloušek, Removal of Anions from Solution by Calcined Hydrotalcite and Regeneration of Used Sorbent in Repeated Calcination-Rehydration-Anion Exchange Processes, *Chem. Commun.* 64 (1999) 1517–1528.
31. D.G. Evans, X. Duan, Preparation of layered double hydroxides and their applications as additives in polymers, as precursors to magnetic materials and in biology and medicine, *Chem. Commun.* (2006) 485–496.
32. S. Miyata, Anion-exchange properties of hydrotalcite-like compounds, *Clay. Miner.* 31 (1983) 305–311.
33. F. Cavani, F. Trifirò, A. Vaccari, Hydrotalcite-type anionic clays: Preparation, properties and applications, *Catal. Today.* 11 (1991) 173–301.
34. G. Williams, H.N. McMurray, Inhibition of filiform corrosion on organic-coated AA2024-T3 by smart-release cation and anion-exchange pigments, *Electrochim. Acta.* 69 (2012) 287–294.
35. G. Williams, H.N. McMurray, Anion-exchange inhibition of filiform corrosion on organic coated AA2024-T3 aluminum alloy by hydrotalcite-like pigments, *Electrochem. Solid-State. Lett.* 6 (2003) B9.
36. N. Wint, D. Eaves, G. Williams, H.N. McMurray, The use of anion exchange pigments to inhibit the filiform corrosion of zinc-aluminium-magnesium coated steel, *Corros. Sci.* 193 (2021) 109886.
37. N. Wint, P. Ansell, J. Edy, G. Williams, H.N. McMurray, A Method for Quantifying the Synergistic Inhibitory Effect of Corrosion Inhibitors When Used in Combination: A ‘Chromate Generating Coating’, *J. Electrochem. Soc.* 166 (2019) C580–C588.
38. R.J. Holness, G. Williams, D.A. Worsley, H.N. McMurray, Polyaniline Inhibition of Corrosion-Driven Organic Coating Cathodic Delamination on Iron, *J. Electrochem. Soc.* 152 (2005) B73.

39. G. Williams, H.N. McMurray, M.J. Loveridge, Inhibition of corrosion-driven organic coating disbondment on galvanised steel by smart release group II and Zn(II)-exchanged bentonite pigments, *Electrochim. Acta.* 55 (2010) 1740–1748.
40. C.A.J. Richards, H.N. McMurray, G. Williams, Smart-release inhibition of corrosion driven organic coating failure on zinc by cationic benzotriazole based pigments, *Corros. Sci.* 154 (2019) 101–110.
41. H. Leidheiser, W. Wang, L. Igetoft, The mechanism for the cathodic delamination of organic coatings from a metal surface, *Prog. Org. Coat.* 11 (1983) 19.
42. N. Khayatan, M. Rohwerder, A new insight into the rate determining step of cathodic delamination, *Corros. Sci.* 202 (2022) 110311.
43. G. Williams, H.N. McMurray, D.A. Worsley, Cerium(III) inhibition of corrosion-driven organic coating delamination studied using a scanning Kelvin probe technique, *J. Electrochem. Soc.* 149 (2002) B154–B162.
44. R. Weast, ed., *CRC Handbook of Chemistry and Physics*, 62nd Edition, CRC Press, Boca Raton, FL, 1982.



## **Chapter 6**

# **A Novel Accelerated Anodic Undermining Cell for ZnAl Coated Steels**

## 6.1 Introduction

The work presented in Chapter 5 demonstrated the effectiveness of in-coating BTSA and "smart release" HT-BTSA pigments in inhibiting the corrosion-driven cathodic delamination of HDG. This chapter added to the substantial body of research on the corrosion-driven organic coatings failure mechanisms of HDG and its protection through in-coating inhibitor pigments [1–6]. Notably, however, the chapter did not include Galfan and Zn55Al since they are not susceptible to cathodic delamination [7,8]. This resistance arises because both alloys contain microstructural phases rich in Al that are ineffective in oxygen-reduction reactions [9]. Consequently, both surfaces are cathodically inactive, preventing the advancement of a cathodic delamination front due to the absence of a continuous cathodic surface.

Instead, for Galfan and Zn55Al, the primary corrosion-driven organic coating failure is anodic undermining. Here, cathodic activity at a defect in the coating is coupled with an underfilm front of anodic activity that destroys the interface between the ZnAl substrate and causes delamination. A common anodic undermining defect is a cut edge, produced during manufacturing when the pre-finished product is cut to size. At cut edges, the underlying steel, ZnAl galvanised coating, and organic coating layers are exposed to the environment. In the presence of an electrolyte, the ZnAl coating acts as a sacrificial anode to protect the exposed steel, and underfilm anodic dissolution propagates.

Several studies on the anodic undermining of other Zn and Al-containing steel coatings, such as ZAM (Zn-Al-Mg), have been published [10-12]. However, relatively little has been published on Galfan and Zn55Al. To date, the resistance of both organically coated substrates to anodic-driven coating failure has been determined through either long-term outdoor exposure or accelerated weathering tests that simulate the aggressive environments the product is exposed to during its lifetime [13]. In accelerated weathering tests, coated samples are scribed, positioned inside a sealed cabin, and sprayed with electrolyte either continuously (salt spray testing), or in cycles (prohesion testing). The coating's performance is assessed in terms of the subsequent degree of coating deadhesion, blistering, and underlying corrosion.

Regarding the development of in-coating inhibitor pigments to suppress anodic undermining, performance evaluation through long-term exposure and accelerated weathering tests often requires their incorporation into fully formulated coated systems. This requirement complicates and prolongs the inhibition assessment process. Therefore, a method that allows the rapid screening of inhibitors against anodic undermining would enable more efficient selection of inhibitor pigments for inclusion in coating formulations and further assessment.

Previously, for another anodic undermining mechanism, namely filiform corrosion (FFC), the effect of in-coating inhibitor pigments has been systematically measured in accelerated tests using a modified Lockheed Filiform Corrosion Test [14-16]. This test involves adding controlled amounts of aqueous acid to a penetrative coating defect and holding the sample at a fixed relative humidity. For ZAM-coated steel, the test has provided insights into the mechanism of FFC corrosion on the substrate with the penetrative defect exposing the underlying steel [10-12]. Considering that the defect is similar to a cut-edge defect in that the underlying steel is exposed, the test may be applicable to model and assess the cut-edge corrosion of organically coated ZnAl and for in-coating inhibitor studies.

To this end, this chapter presents a preliminary investigation of cut-edge anodic undermining of unpigmented PVB on Zn55Al using a FFC Test viewed by time-lapse photography. The results of the test are used to inform the engineering of a second, newly designed anodic undermining test cell. The second test method is assessed visually with time-lapse photography and electrochemically using the Scanning Kelvin Probe (SKP). Both the FFC test and the novel cell are performed with a view to being used to assess in-coating inhibitor performance in the future.

## 6.2 Experimental Details

### 6.2.1 Materials

Zn55Al substrate was supplied and prepared in the same way as for Chapter 3. All reagents and solvents used were purchased in analytical grade from Merck.

### 6.2.2 Method

#### 6.2.2.1 FFC Assessment

The as-received Zn55Al galvanised steel was cleaned and polished as described in Section 2.1.2 and cut into 50 x 50 mm coupons using a guillotine. Two parallel strips of insulating tape were applied to the coupons, onto which a 15% w/v ethanolic solution of PVB was bar-cast and allowed to dry in air [14,17-21]. This procedure produced a dry film thickness of 30  $\mu\text{m}$ , as measured using a micrometer screw gauge. A linear scribed penetrative coating defect of 10 mm in length was then created perpendicular to the rolling direction of the substrate using a scalpel blade. The defect was scribed to the steel surface. To the defect, a 2  $\mu\text{L}$  aliquot of 4  $\text{mol dm}^{-3}$   $\text{HCl}_{(\text{aq})}$  was introduced using a micro-syringe.

Following the initiation of corrosion, the coupon was placed in a humidity chamber that contained a reservoir of saturated  $\text{Na}_2\text{SO}_4 \cdot 10\text{H}_2\text{O}$ , maintaining a relative humidity (RH) of 93% [14,17-21]. Every week for four weeks, digital optical images of the scribed area were taken using a Canon EOS Camera, with the chamber air also being refreshed. The area of underfilm corrosion was determined from the photos using ImageJ.

#### 6.2.2.2 Novel Anodic Undermining Cell

Figure 6.1 depicts the preparation of the novel anodic undermining cell on Zn55Al. The as-received Zn55Al was cleaned and polished as described in Section 2.1.2 and cut into 25 x 50 mm coupons using a guillotine. To act as height guides for subsequent coating, strips of insulating tape were applied to the 25 mm long edges of the substrate, covering 10 mm

x 25 mm of the coupon surface on both sides. A strip of PTFE tape was applied to one of the remaining edges to allow a platform from which an unpigmented ethanolic solution of 15.5% w/v PVB could be dropped onto and bar-cast across the substrate. After 30 minutes of drying in air, a 30  $\mu\text{m}$  thick dry film was produced, as measured by a micrometer screw gauge. PTFE tape was then applied to the underside of the coupon and approximately 10% of the exposed cut edge to ensure the protection of the underside Zn55Al coating from the experimental conditions. Then, a 26 x 76 mm glass microscope slide was stuck to the underside of the coated substrate with cyanoacrylate glue to allow subsequent deposition of non-corrosive silicone to create a reservoir for aqueous electrolyte next to the coupon's cut edge.

To induce anodic undermining, 2 mL of 1 mol dm<sup>-3</sup> HCl<sub>(aq)</sub> was added to the reservoir so that only the exposed cut edge of the cell was in contact with the electrolyte. The sample was then contained in an enclosed, air-containing environment with a constant relative humidity of 93%, and subsequent anodic undermining followed either visually by time-lapse photography or electrochemically by the SKP.

In time-lapse photography experiments, the humidity chamber was itself placed in an Ortery Photosimile 200 software-operated photography studio in which the lighting conditions were controlled. A transparent window in the container allowed images of the samples to be taken using a Canon EOS 600D SLR camera. Photos were taken immediately after initiation and then at five-minute intervals for 20 hours. The time dependent area of underfilm corrosion was determined from the photos using Image J.

For SKP experiments, measurement of  $E_{\text{corr}}$  of the Zn55Al surface underneath the PVB film was determined as a function of distance from the cut-edge electrolyte reservoir.  $E_{\text{corr}}$  measurements were made immediately after immersion then at four hour intervals for 26 hours. The samples used for both techniques post-experiment were removed from the humidity chamber, their electrolyte wells drained and the cell allowed to air dry.

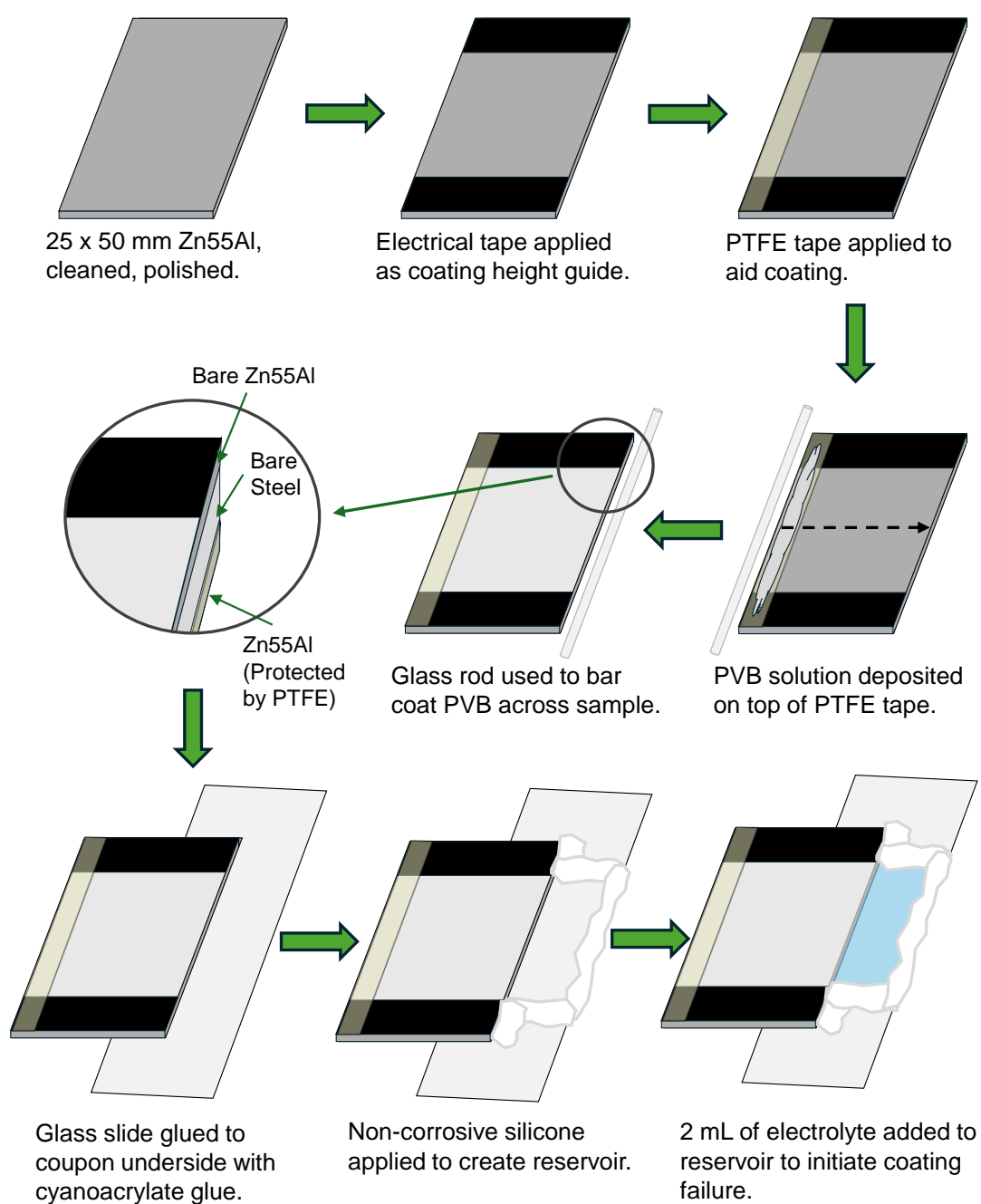


**Figure 6.1:** Preparation of the novel anodic undermining cell.

## 6.3 Results and Discussion

### 6.3.1 FFC

Figure 6.2 shows the optical images obtained for the preliminary FFC experiment on Zn55Al over 28 days following initiation using 2  $\mu\text{m}$  of 4 mol dm<sup>-3</sup> HCl<sub>(aq)</sub>. After 7 days, several areas of underfilm corrosion initiated and propagated perpendicular to the scribed defect, appearing dark against the lighter substrate. As time progressed, narrow filaments of underfilm corrosion were observed to propagate away from the defect but often merged into a larger front.

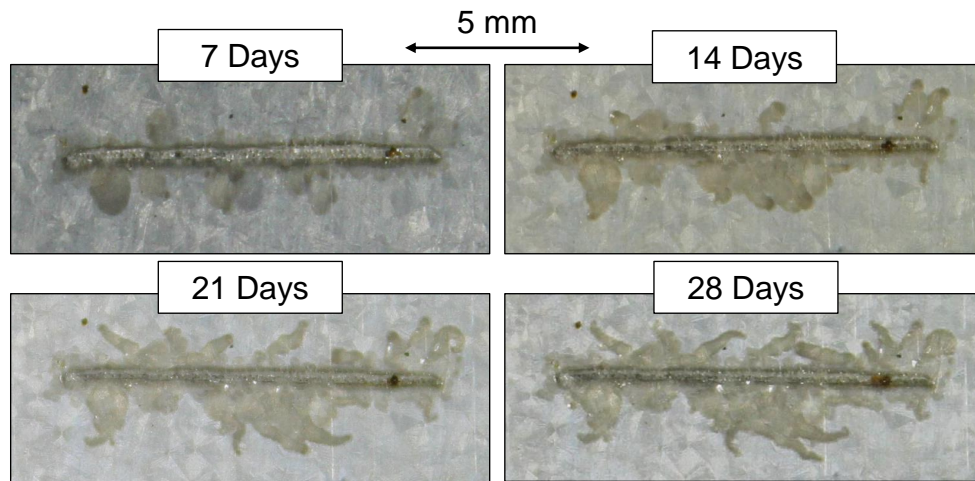


**Figure 6.2:** Optical images of the FFC experiment on Zn55Al over a 4-week period. Underfilm corrosion was initiated by injection of 2  $\mu\text{L}$  of 4 mol dm<sup>-3</sup> into a scribed defect that penetrated to the underlying steel substrate.

In previous studies of FFC corrosion of aluminium alloy and ZAM substrates, the kinetics of underfilm corrosion were calculated from time-lapse images by measuring and averaging the length of individual filaments [12,20]. However, in this case, the filaments merged into a more prominent front over time, making this method inapplicable. Furthermore, the underfilm corrosion develops very slowly so an in-situ study (such as SKP used in the case of ZAM and AA2024 [12,14]) is impossible. Instead, the area of underfilm corrosion

was used as an alternative measure of propagation. The total area of underfilm corrosion at each time interval was quantified using ImageJ and plotted over time (Figure 6.3). As shown by the trendline in Figure 6.3, the corroded area increased linearly with the square root of time, indicating that underfilm corrosion propagation followed parabolic kinetics.

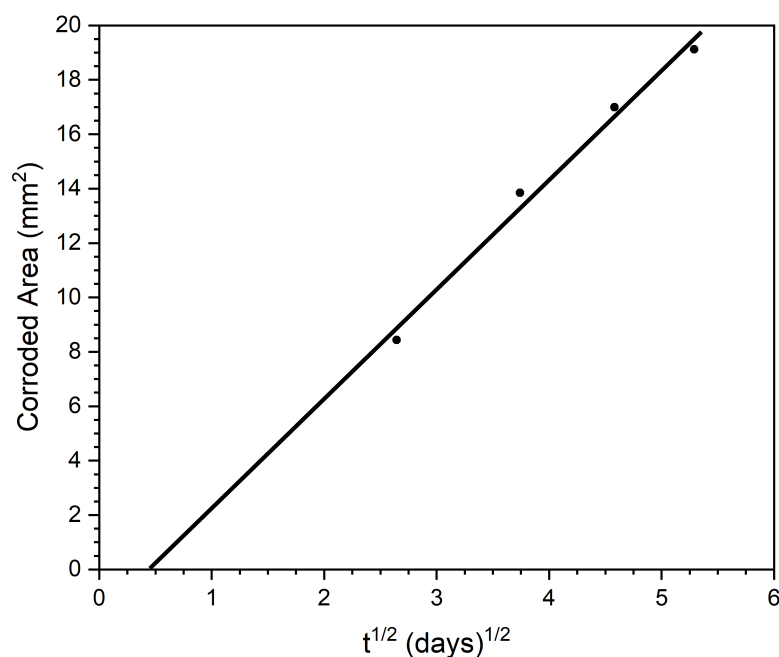


**Figure 6.3:** Time-lapse photography derived plot of underfilm corroded area as a function of  $t^{1/2}$  for the preliminary FFC experiment on Zn55Al.

In FFC, filaments are made up of a distinguishable "head" and "tail". Filament heads are filled with electrolyte consisting of metal cations and aggressive anions (such as  $\text{Cl}^-$ ), typically exhibiting a low pH at their leading edge due to cation hydrolysis [14,22,23]. In contrast, filament tails are filled with dry, porous corrosion product. For iron and aluminium substrates, it is believed that anodic dissolution occurs at the front of the filaments' head [22-24], while its coupled cathodic reaction (oxygen reduction) occurs at the rear of the head, subsequently precipitating insoluble metal oxides and hydroxides by alkalization. Facile  $\text{O}_2$  diffusion along the porous corrosion product tail then drives the filament head forward through differential aeration [22-28]. For ZAM, a secondary driving force has been identified, wherein the preferential anodic dissolution of magnesium-rich



eutectic phases creates pathways for  $O_2$  to diffuse to the underlying iron substrate to form a galvanic couple that contributes to filament advance [12].

For organically coated iron, aluminium alloys, or ZAM, FFC propagation is ultimately self-sustaining as the aqueous electrolyte is conserved within their filament heads. This results in linear kinetics with rates controlled by the IR drop between the leading (anodic) edge and the cathode at the rear of the filament head [12,20]. However, the parabolic kinetics observed for Zn55Al indicate that the underfilm corrosion on Zn55Al does not align with classical FFC behavior. Instead, it appears that for Zn55Al, the FFC experiment led to underfilm corrosion similar to that seen on a cut-edge, characterised by sacrificial underfilm anodic activity coupled with stationary cathodic oxygen reduction on the exposed steel at the defect.

This hypothesis is supported by previous kinetic studies on corrosion-driven organic coating failure. The observed kinetics of Zn55Al resemble those of cathodic delamination (Chapter 5), where parabolic kinetics arise due to rate-limiting underfilm ion migration between a stationary anode at the defect and an outward-moving underfilm front of cathodic activity. Consequently, it is plausible that the parabolic kinetics observed in the Zn55Al FFC experiment are due to an increasing separation of sacrificial underfilm anodic activity and cathodic activity over time. This separation is likely caused by Zn55Al's microstructure, where over 70% of the coating's volume is occupied by passive Al-rich dendrites, which are poor sites for oxygen reduction meaning cathodic activity on the underfilm coating is not supported. Furthermore, due to the large volume of passive dendrites, unlike ZAM, it is improbable that the preferential dissolution of Zn55Al's most susceptible phase (Zn-rich interdendritic regions) would create a continuous pathway to the underlying iron, preventing it from contributing significantly to oxygen reduction.

### 6.3.2 Novel Anodic Undermining Cell

Overall, the FFC experiments produced results on Zn55Al resembling cut-edge corrosion, characterised by sacrificial underfilm anodic activity of the Zn55Al coating coupled to stationary cathodic activity on the exposed steel at the scribed defect. These findings suggest its potential use as an accelerated method for assessing in-coating inhibitor pigments against cut-edge corrosion. Unfortunately, the main drawback is that its propagation is slow and does not extend very far (<3 mm in 28 days), making it unsuitable for accelerated comparisons of in-coating inhibitors.

The likely reason for the slow kinetics of the FFC experiment is that at the scribed defect, a small area of steel was exposed relative to the larger exposed area of the Zn55Al coating. Consequently, extensive dissolution of the Zn55Al coating perpendicular to the scribe was not required to maintain sacrificial protection to the exposed steel. Additionally, only a small volume of electrolyte could be introduced to the defect, thereby limiting the rate of anodic activity as only a finite amount of anions ( $\text{Cl}^-$ ) can migrate in the underfilm electrolyte to the site of anodic activity and balance the positive charge of dissolved cations.

In an attempt to accelerate anodic undermining kinetics, an alternative anodic undermining cell was created. As shown in Figure 6.4, the cell introduces  $\text{HCl}_{(\text{aq})}$  directly to the cut-edge of a PVB-coated Zn55Al coupon, thus exposing a larger area of steel to electrolyte than in the FFC experiment. Further, through the use of an external silicone well, a larger volume of  $\text{HCl}_{(\text{aq})}$  is contained, therefore alleviating the problem of insufficient electrolyte being available for adequate underfilm ion migration.

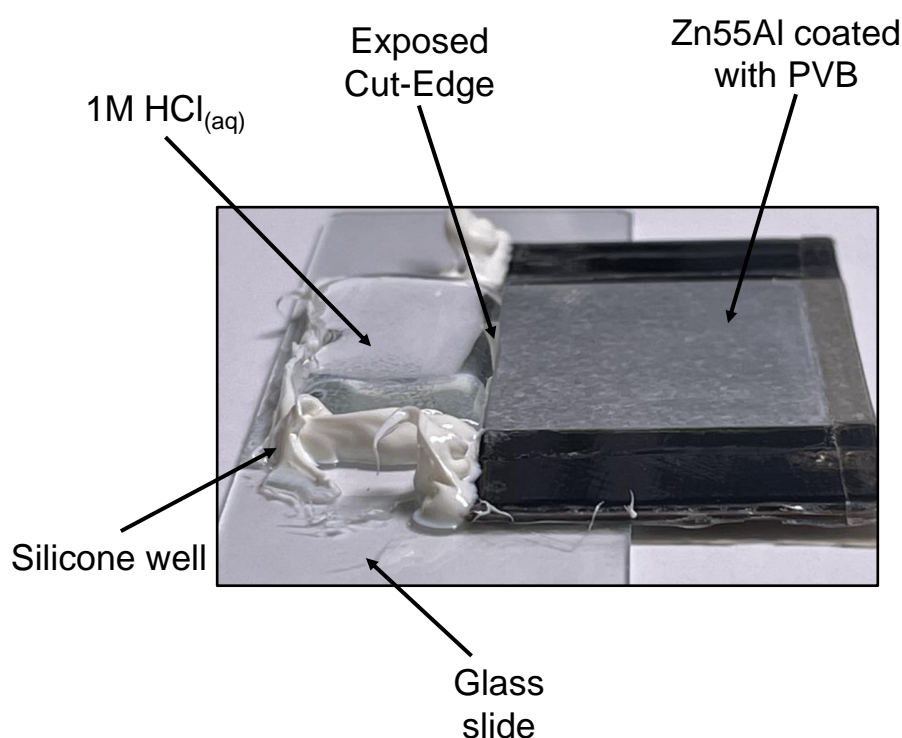


**Figure 6.4:** Photo of the anodic undermining cell for Zn55Al.

### 6.3.2.1 Assessment by Time-Lapse Photography

Figure 6.5 shows photographs of the anodic undermining cell for unpigmented PVB on Zn55Al at different time intervals. Upon initiation with  $1 \text{ mol dm}^{-3} \text{ HCl}_{(\text{aq})}$ , two distinct features were immediately observed. First, bubbles emerged directly from the cut-edge surface. Second, a section of the Zn55Al surface became tarnished and black, starting from the cut edge and progressively spreading outward over time to the interior surface area of the substrate coupon.

After the experiment, it was observed that the exposed steel of the cut-edge had retained its silvery-grey colour and showed no visible brown iron corrosion products, suggesting that the steel was protected from dissolution. Given the acidic (pH 0) reservoir electrolyte and the observation of an effervescence at the cut-edge, it is likely that the exposed steel was the site of cathodic activity, reducing  $\text{H}^+$  to hydrogen gas (Equation 6.1):

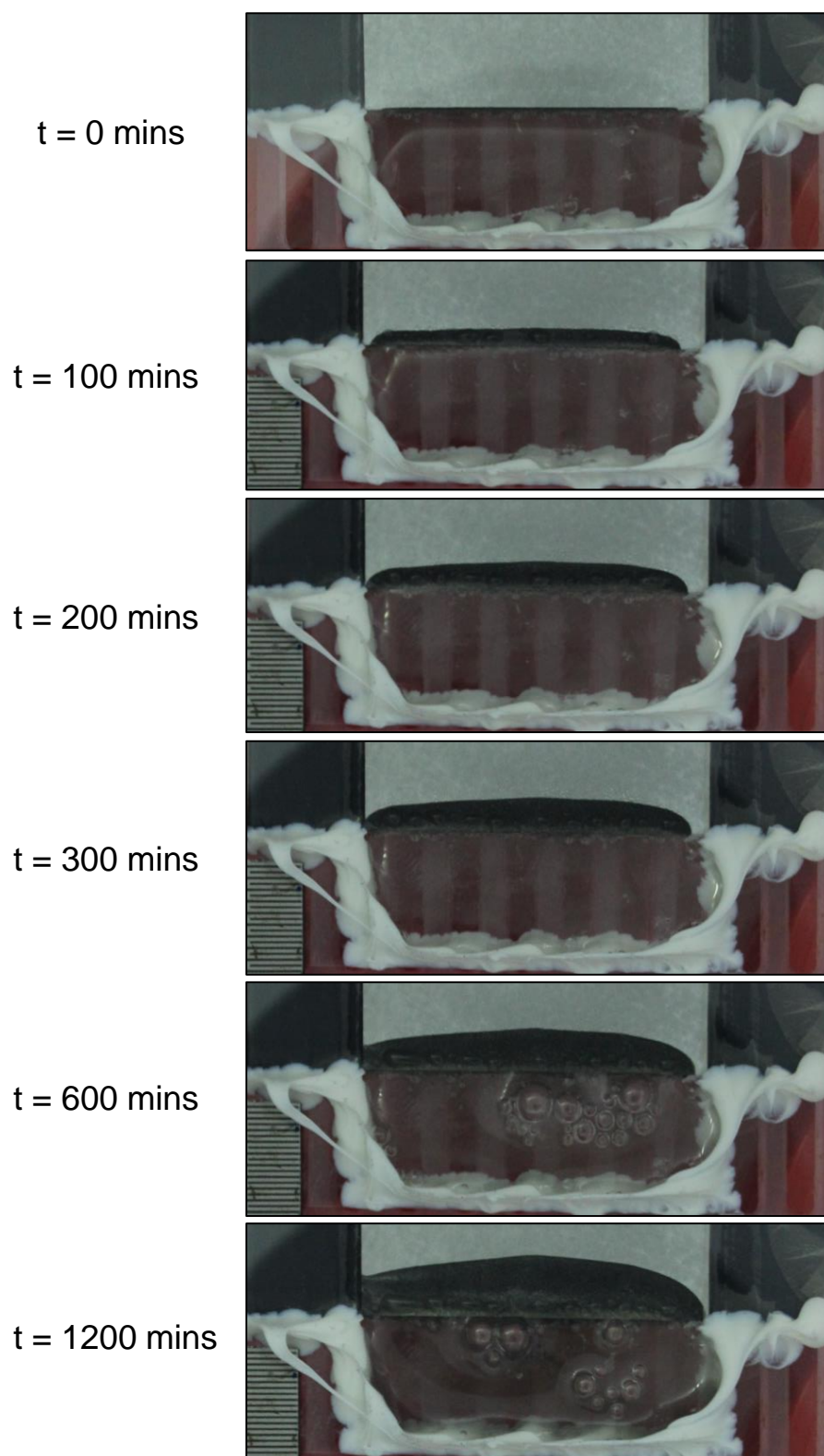


**Figure 6.5:** Time-lapse photos at selected intervals of the novel anodic undermining cell of unpigmented PVB on Zn55Al.



The black tarnishing of the Zn55Al galvanised coating underneath the unpigmented PVB coating suggests that the coating behaved as a sacrificial anode, dissolving preferentially to protect the exposed steel. In acidic electrolyte (pH 0), both Zn and Al are active, so will dissolve via Reactions 6.2 and 6.3, respectively.



As observed in Figure 6.5, over time, the black tarnishing progressed as a front from the exposed cut-edge towards the interior of the coupons' PVB-coated surface. Following the experiment, it was found that after draining and drying of the cell, the PVB overlying the tarnished region could be easily detached from the Zn55Al surface with tweezers, while the remaining dry coating over the seemingly intact Zn55Al coating required significantly more force to be removed. These results indicate anodic dissolution of the Zn55Al as the probable cause of PVB delamination.

A possible explanation for the moving delamination front is that, upon initiation, the Zn55Al coating on the cut edge comes into contact with the electrolyte and dissolves. This process destroys the interface between the Zn55Al surface and the PVB, causing the coating to delaminate at the cut edge. As a result, the reservoir electrolyte infiltrates underneath the PVB coating and reaches the intact top surface of the Zn55Al coupon, leading to an underfilm anodic attack. This anodic attack further promotes coating delamination at the leading edge and more anodic dissolution. The driving force behind this propagation is the maintenance of sacrificial protection of the exposed steel.

As the moving anodic front is associated with coating delamination, time-dependent values of delamination distance ( $X_{\text{del}}$ ) were determined by measuring the distance from the cut-edge to the leading edge of the anodic front over time. As observed in Figure 6.5, the

anodic front was not uniform, resulting in varying  $X_{\text{del}}$  values across it. Despite this variability, the geometry of the anodic front remained constant. Thus, three measurements were taken at different points along the front and averaged at each time interval.

The resulting plot of  $X_{\text{del}}$  as a function of time for unpigmented PVB on Zn55Al is shown in Figure 6.6. This plot reveals that the propagation of anodic undermining of the cell increased linearly with the square root of time, indicating parabolic kinetics. Like the FFC experiment, the parabolic kinetics suggest an increased separation of cathodic and anodic sites over time. However, the kinetics of this cell is significantly faster, achieving over 5 mm of anodic undermining within 20 hours of initiation, compared to less than 3 mm in 28 days in the FFC experiment.

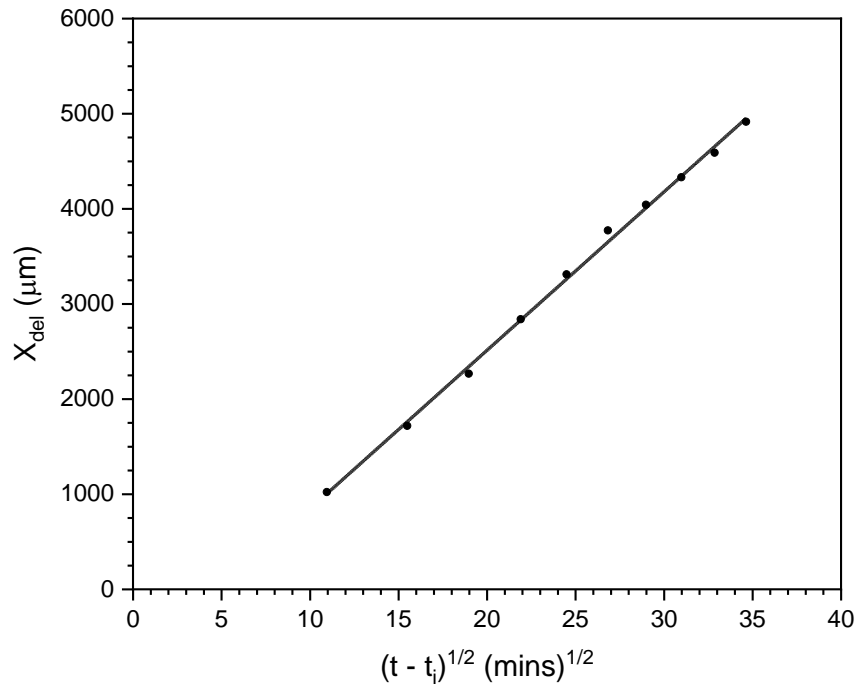


**Figure 6.6:** Time lapse photography derived plot of delamination distance ( $X_{\text{del}}$ ) as a function of  $t^{1/2}$ , for an unpigmented PVB coated Zn55Al sample using the accelerated anodic undermining cell.

### 6.3.2.2 Assessment by SKP

An SKP experiment of the test cell was conducted to provide electrochemical and mechanistic information. Figure 6.7 shows the SKP-derived, time-dependent  $E_{\text{corr}}$  values as a function of distance from the defect of the unpigmented PVB film coated on Zn55Al after adding  $1 \text{ mol dm}^{-3} \text{ HCl}_{(\text{aq})}$  into the cell's reservoir. For clarity, a simplified schematic plot is also provided.

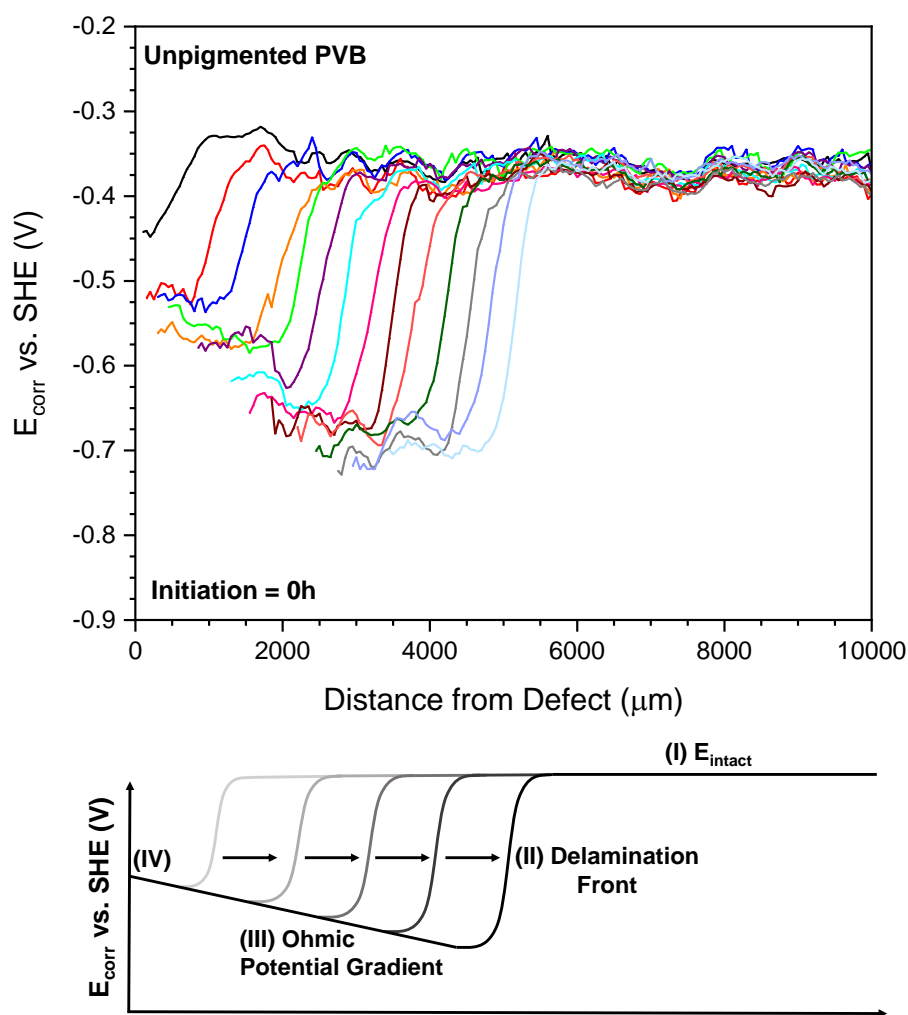


**Figure 6.7:** SKP derived time-dependent profiles of  $E_{\text{corr}}$  as a function of distance from the defect for an unpigmented PVB coated Zn55Al sample using the accelerated anodic undermining cell. The profiles are shown at 2h intervals.

The plot possesses four distinct regions:

- I. A region of high relative  $E_{\text{corr}}$  that represents the  $E_{\text{intact}}$  of Zn55Al, i.e. the open circuit potential of Zn55Al coated with an adherent, non-conducting polymer. A uniform value of approximately -380 mV is recorded in this case.
- II. A sharp drop from  $E_{\text{intact}}$  to more negative (active) potentials; its position moving further away from the defect at each time interval suggesting that it characterises the position of the delamination front. In this region, the potentials recorded are as low as -720 mV, a value expected during dissolution of Zn and Al in acidic electrolyte.
- III. A region between the delamination front and the defect where the PVB film is delaminated and there is a slight increase in potential (approximately 200 mV vs SHE) from the delamination front to the region adjacent to the cut-edge defect. Notably, this slight increase is in direct contrast to the slight decrease in potential seen between the delamination front and the defect in cathodic delamination (Chapter 5). In cathodic delamination, the ohmic potential drop is attributed to the galvanic coupling between the net local anode at the defect and the net local cathodic at the delamination front. Here, an increase in potential suggests the opposite: galvanic coupling between a net cathode at the cut-edge defect and a net local anode at the moving delamination front.
- IV. A region adjacent to the cut-edge defect of high  $E_{\text{corr}}$  (approximately -480 mV vs SHE). Its  $E_{\text{corr}}$  is more positive (i.e. noble) than the  $E_{\text{corr}}$  of the delamination front, highlighting its proximity to the cathodically protected steel.

After the SKP experiment, the test cell was removed from the humidity chamber, its electrolyte drained, and the cell allowed to dry in air. Once dry, tweezers were used to remove the PVB coating from the substrate, enabling characterisation of the post-experiment underfilm surface. Figure 6.8 shows an SEM image and corresponding EDX mapping of the underfilm Zn55Al surface at the boundary (front) between delaminated and intact regions. The EDX elemental maps reveal that, compared to the intact region, the delaminated re-



gion is depleted in Al and Zn, thus indicating that Al and Zn dissolution (Reactions 6.2 and 6.3) occurred in the delaminated region.

Furthermore, the EDX maps also show that the delaminated region became enriched in Cl, suggesting the migration of  $\text{Cl}^-$  from the electrolyte well to the anodic front. This is consistent with anions being required to balance the positive charge of  $\text{Zn}^{2+}$  and  $\text{Al}^{3+}$  cations produced at the anodic front.

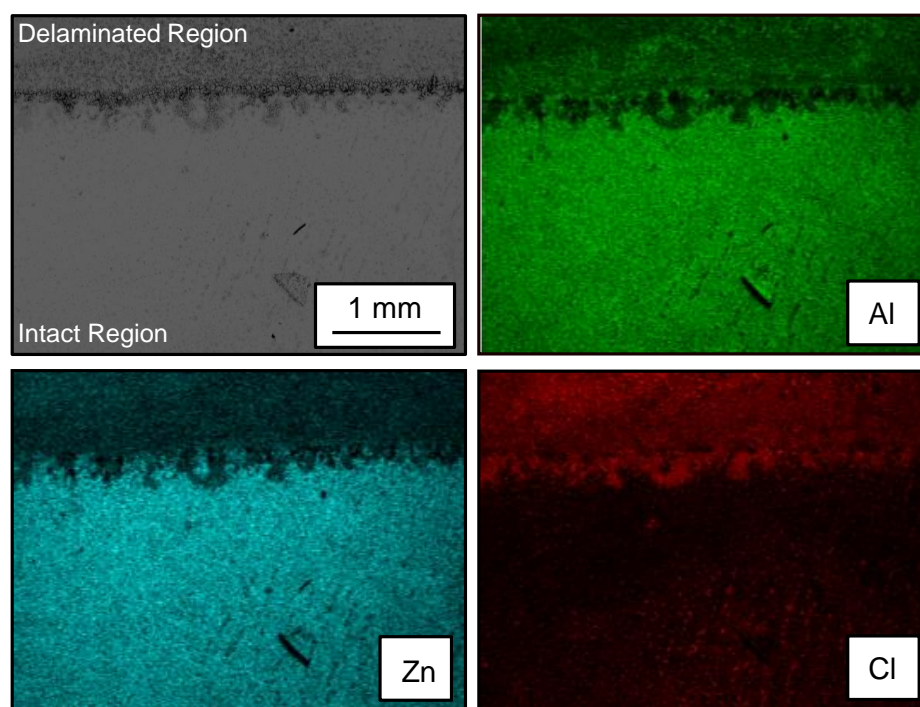


**Figure 6.8:** SEM image and corresponding EDX elemental maps of the post-SKP under-film Zn55Al surface.

### 6.3.2.3 Mechanism

As determined by the time-lapse experiment, the kinetics of anodic undermining of the cell is parabolic, suggesting that the rate limiting step of propagation is a diffusion process. The possible diffusion-related processes are:

1. Diffusion of  $\text{H}^+$ :  $\text{H}^+$  ions migrate from the acidic electrolyte to the steel surface, where they are reduced to  $\text{H}_2$  gas. If the rate at which  $\text{H}^+$  diffuses to the steel surface

is slower than the rate of the hydrogen evolution reaction, the cathodic reaction rate is reduced. Consequently, the rate of its coupled underfilm anodic reaction will be reduced.

2. Ion migration: In the underfilm anodic front, Zn and Al are oxidised to aqueous  $\text{Zn}^{2+}$  and  $\text{Al}^{3+}$ , respectively. Since these ions carry positive charges and will migrate towards the cathode, negatively charged anions from the defect electrolyte must move towards the anodic front to maintain electrical neutrality. The only available anions to balance the charge are  $\text{Cl}^-$  ions present in the reservoir; therefore, as suggested by their presence in the delaminated region (Figure 6.8) they migrate to the anodic front. This means that if the migration rate of  $\text{Cl}^-$  towards the anodic front is slow, the anodic reaction rate must slow to ensure the site remains electrically neutral. As a result, the velocity of the forward movement of the anodic front will progressively decrease as its distance from the cathodic cut-edge increases.

In this case, the concentration of  $\text{H}^+$  in the electrolyte reservoir is high ( $1 \text{ mol dm}^{-3}$ ), so it is unlikely that  $\text{H}^+$  diffusion is rate limiting. As such, the likely rate limiting process is the underfilm migration of  $\text{Cl}^-$  to the anodic front.

Figure 6.9 shows a schematic diagram of the proposed mechanism of the novel cell, along with a simplified schematic of the SKP plot. Upon introduction of  $1 \text{ mol dm}^{-3} \text{HCl}_{(\text{aq})}$  to the cell's reservoir, a galvanic couple at the cut-edge between the exposed steel and Zn55Al coating is established. Due to its more noble standard electrode potential relative to the ZnAl coating, steel becomes the site of cathodic hydrogen evolution, with the reaction being provided electrons by sacrificial anodic dissolution of the Zn55Al coating underneath the PVB coating. As a result, the interface between the substrate and the PVB coating is compromised, causing coating delamination at the cut-edge. This allows the reservoir electrolyte to ingress underneath the PVB coating and come into contact with more intact Zn55Al. As a result, further Al and Zn dissolution occurs, establishing a moving front of delamination that propagates to provide continued sacrificial protection to the exposed steel of the cut-edge. This is accompanied by a black, tarnished appearance of the delamination region due to a surface roughening of the micro-scale that scatters

light differently to that of the intact Zn55Al surface. Furthermore, the propagation of the process is controlled by the rate of migration of  $\text{Cl}^-$  from the electrolyte reservoir to the delamination front.

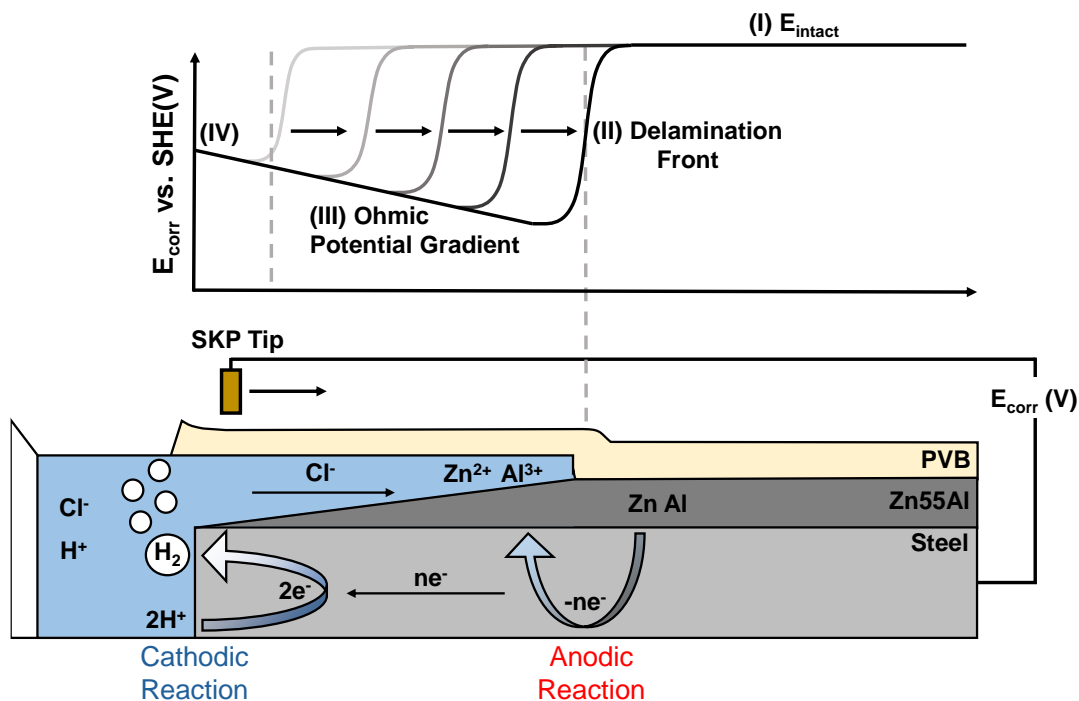


**Figure 6.9:** Schematic of the anodic undermining produced by the test cell, overlaid with representative SKP  $E_{\text{corr}}$  vs distance profiles and the noteworthy regions marked.

## 6.4 Conclusion

This chapter explored two accelerated test methods for producing anodic undermining on organically coated Zn55Al with a view to using these methods as future assessment tools for in-coating inhibitor pigment performance for ZnAl substrates.

The first method was a modified Lockheed FFC test, initiating underfilm corrosion by adding 2  $\mu\text{L}$  of 4  $\text{mol dm}^{-3}$   $\text{HCl}_{(\text{aq})}$  into a steel-penetrating scribed defect of a PVB-coated Zn55Al substrate. Time-lapse photography showed that, under 93% RH, corrosion resembled cut-edge corrosion characterised by sacrificial anodic dissolution of the Zn55Al coating and stationary cathodic activity on the exposed steel. However, the slow propagation of underfilm corrosion ( $<3$  mm in 28 days) made it an unsuitable candidate for accelerated testing of in-coating inhibitors. This was attributed to the large ratio of surface area between anodic and cathodic sites and limited  $\text{Cl}^-$  ion availability to balance the positive ionic charge produced by underfilm anodic dissolution.

To increase the rate of underfilm corrosion, a second test method introduced 2 mL of 1  $\text{mol dm}^{-3}$   $\text{HCl}_{(\text{aq})}$  directly to the cut-edge of PVB-coated Zn55Al, exposing a larger area of steel to corrosive electrolyte and addressing the issue of insufficient  $\text{Cl}^-$  ions. Subsequently, accelerated kinetics were recorded, with over 5 mm of underfilm corrosion achieved within 20 hours of initiation at 93% RH. Time-lapse and SKP experiments indicated that cathodic hydrogen evolution took place on the exposed steel at the cut-edge, while the anodic activity was Al and Zn dissolution of the underfilm Zn55Al coating. This dissolution destroyed the interface between the Zn55Al surface and the PVB coating, leading to delamination. The kinetics of the process were parabolic, suggesting a rate probably limited by  $\text{Cl}^-$  migration. This is in direct contrast to the linear kinetics of anodic undermining observed for FFC corrosion, thereby confirming a novel anodic undermining process for Zn55Al.

Overall, the study demonstrated the promise of the newly designed cell as a future accelerated test method for in-coating inhibitors against anodic undermining of organically coated ZnAl substrates. However, further work is required to validate the method.

## 6.5 References

1. W. Fürbeth, M. Stratmann, The delamination of polymeric coatings from electrogalvanised steel – a mechanistic approach.: Part 1: delamination from a defect with intact zinc layer, *Corros. Sci.* 43 (2001) 207–227.
2. W. Fürbeth, M. Stratmann, Delamination of polymeric coatings from electrogalvanized steel - a mechanistic approach. Part 2: Delamination from a defect down to steel, *Corros. Sci.* 43 (2001) 229.
3. W. Fürbeth, M. Stratmann, The delamination of polymeric coatings from electrogalvanized steel – a mechanistic approach.: Part 3: delamination kinetics and influence of CO<sub>2</sub>, *Corros. Sci.* 43 (2001) 243–254.
4. N. Wint, P. Ansell, J. Edy, G. Williams, H.N. McMurray, A Method for Quantifying the Synergistic Inhibitory Effect of Corrosion Inhibitors When Used in Combination: A ‘Chromate Generating Coating’, *J. Electrochem. Soc.* 166 (2019) C580–C588.
5. P. Ansell, L. Berry, J. McGettrick, J. Searle, N. Wint, H.N. McMurray, G. Williams, Role of Smart-Release Pigments in Preventing Corrosion Driven Cathodic Disbondment of Organically Coated Hot Dip Galvanised Steel, *J. Electrochem. Soc.* 170 (2023) 011502.
6. C.M. Griffiths, N. Wint, G. Williams, H.N. McMurray, The contribution of Zn(II) and phosphate anions to the inhibition of organic coating cathodic disbondment on galvanised steel by zinc phosphate pigment, *Corros. Sci.* 198 (2022) 110111.
7. C. Glover, Thin organic coatings for hot dip galvanised steel and cold rolled products, Swansea University, 2014.
8. C. Gallagher, The corrosion of Zn-4.8%Al sacrificial coatings used for the protection of steel, Swansea University, 2022.

9. H. Dafydd, D.A. Worsley, H.N. McMurray, The kinetics and mechanism of cathodic oxygen reduction on zinc and zinc–aluminium alloy galvanized coatings, *Corros. Sci.* 47 (2005) 3006–3018.
10. N. Wint, D. Eaves, G. Williams, H.N. McMurray, The use of anion exchange pigments to inhibit the filiform corrosion of zinc-aluminium-magnesium coated steel, *Corros. Sci.* 193 (2021) 109886.
11. N. Wint, D. Eaves, G. Williams, H.N. McMurray, The effect of composition and thickness on the mechanism and kinetics of filiform corrosion occurring on zinc-aluminium-magnesium coated steel, *Corros. Sci.* 179 (2021) 109168.
12. N. Wint, D. Eaves, E. Michailidou, A. Bennett, J.R. Searle, G. Williams, H.N. McMurray, The kinetics and mechanism of filiform corrosion occurring on zinc-aluminium-magnesium coated steel, *Corros. Sci.* 158 (2019) 108073.
13. R.L. Howard, S.B. Lyon, J.D. Scantlebury, Accelerated tests for the prediction of cut-edge corrosion of coil-coated architectural cladding: Part I: cyclic cabinet salt spray, *Prog. Org. Coat.* 37 (1999) 91–98.
14. H.N. McMurray, G. Williams, S. O'Driscoll, Chromate Inhibition of Filiform Corrosion on Organic Coated AA2024-T3 Studied Using the Scanning Kelvin Probe, *J. Electrochem. Soc.* 151 (2004) B406.
15. G. Williams, H.N. McMurray, Anion-exchange inhibition of filiform corrosion on organic coated AA2024-T3 aluminum alloy by hydrotalcite-like pigments, *Electrochem. Solid-State. Lett.* 6 (2003) B9.
16. G. Williams, H.N. McMurray, Inhibition of filiform corrosion on polymer coated AA2024-T3 by hydrotalcite-like pigments incorporating organic anions, *Electrochem. Solid-State Lett.* 7 (2004) B13.
17. G. Williams, H.N. McMurray, The mechanism of group (I) chloride initiated filiform corrosion on iron, *Electrochem. Commun.* 5 (2003) 871–877.

18. H.N. McMurray, A. Holder, G. Williams, G.M. Scamans, A.J. Coleman, The kinetics and mechanisms of filiform corrosion on aluminium alloy AA6111, *Electrochim. Acta.* 55 (2010) 7843–7852.
19. G. Williams, R. Grace, Chloride-induced filiform corrosion of organic-coated magnesium, *Electrochim. Acta.* 56 (2011) 1894–1903.
20. G. Williams, H.N. McMurray, The Kinetics of Chloride-Induced Filiform Corrosion on Aluminum Alloy AA2024-T3, *J. Electrochem. Soc.* 150 (2003) B380.
21. W.H. Slabaugh, M. Grotheer, Mechanism of Filiform Corrosion, *Ind. Eng. Chem.* 46 (2002) 1014–1016.
22. R.T. Ruggeri, T.R. Beck, An Analysis of Mass Transfer in Filiform Corrosion, *Corrosion.* 39 (1983) 452–465.
23. A. Bautista, Filiform corrosion in polymer-coated metals, *Prog. Org. Coat.* 28 (1996) 49–58.
24. H.N. McMurray, G. Williams, Under Film/Coating Corrosion, *Shreir's Corrosion.* (2010) 988–1004.
25. G. Grundmeier, W. Schmidt, M. Stratmann, Corrosion protection by organic coatings: electrochemical mechanism and novel methods of investigation, *Electrochim. Acta.* 45 (2000) 2515–2533.
26. W. Schmidt, M. Stratmann, Scanning kelvinprobe investigations of filiform corrosion on aluminum alloy 2024-t3, *Corros. Sci.* 40 (1998) 1441–1443.
27. T.M. Watson, A.J. Coleman, G. Williams, H.N. McMurray, The effect of oxygen partial pressure on the filiform corrosion of organic coated iron, *Corros. Sci.* 89 (2014) 46–58.
28. W.H. Slabaugh, M. Grotheer, Mechanism of Filiform Corrosion, *Ind. Eng. Chem.* 46 (2002) 1014–1016.

## **Chapter 7**

## **Conclusions and Future Work**



The aims of this thesis were to:

- a) Determine the localised corrosion mechanism in aqueous chloride of Zn55Al, a type of ZnAl galvanised steel.
- b) Identify a non-toxic chromate-free inhibitor that can inhibit the aqueous localised corrosion of ZnAl galvanised steels, namely HDG, Galfan and Zn55Al.
- c) Incorporate the identified inhibitor into model coatings systems for testing its effectiveness against cathodic delamination, a corrosion-driven organic coating failure of HDG.
- d) Determine an accelerated method of reproducibly producing anodic undermining, a corrosion-driven organic coating failure observed for ZnAl galvanised steels. Such a method is required so that the performance of in-coating inhibitors against anodic undermining can be assessed on an accelerated time-scale in the future.

**Chapter 3:** The mechanism of localised corrosion of Zn55Al galvanised steel in near-neutral aqueous chloride (0.04% w/v – 5% w/v NaCl<sub>(aq)</sub>) was investigated. Before immersion, the Zn-rich interdendritic of Zn55Al's microstructure was found by SKPFM to be more susceptible to anodic attack than Al-rich dendrites. Indeed, TLM studies showed an initial preferential attack of the interdendritic upon exposure to near-neutral aqueous chloride solutions (0.04% w/v and 5% w/v NaCl<sub>(aq)</sub>) that was also recorded by the SVET as transient (moving) anodes. However, after longer immersion times and the presence of higher aqueous chloride concentrations, TLM showed anodic attack into Al-rich dendrites, producing pit-like features that coincided with the stabilisation of transient anodes in SVET current density maps to anodes of fixed position. It was tentatively suggested that early dezincification leads to surface areas becoming enriched in Al, resulting in localised corrosion behaviour similar to pure Al, where higher chloride concentrations enhance local anode initiation and maintenance.

To further corroborate the results and provide further insights into the localised corrosion mechanism, characterisation of the corrosion products formed by the locally corroded

Zn55Al would be beneficial as there was a clear distinction in appearance between areas that were stable anodes (appearing white) and areas that were net cathodes (appearing tarnished/black). Analysis of corrosion products may be achieved using Fourier Transform Infrared (FTIR) spectroscopy and X-Ray Diffraction (XRD).

**Chapter 4:** A systematic electrochemical assessment of the inhibitory performance of 2-(1,3-Benzothiazol-2-ylthio) succinic acid (BTSA) towards the localised corrosion ZnAl galvanised steels immersed in near neutral aqueous chloride (1% w/v NaCl<sub>(aq)</sub>) was conducted. Time-dependent SVET and LPR studies showed that BTSA at a dosed concentration of 10 mM achieves an inhibition efficiency over 90% for HDG, Galfan and Zn55Al surfaces. Additionally, it was found that an introduction of 10 mM BTSA to all three freely corroding surfaces provides instantaneous passivation of active localised anodes. In addition to the SVET results, open circuit potential and potentiodynamic polarisation measurements suggested that BTSA acts as a mixed inhibitor, simultaneously reducing the rates of anodic and cathodic activity on each ZnAl surface via surface adsorption of anionic BTSA<sup>2-</sup>. However, the results also suggested a possible interaction between BTSA<sup>2-</sup> and Zn<sup>2+</sup> that provides passivation of local anodes.

To improve the work presented in the Chapter, surface characterisation techniques could be used to characterise the nature of adsorption between BTSA and each ZnAl surface. Scanning Electron Microscopy (SEM) could be conducted on the surface of each substrate post immersion in aqueous chloride and in the absence/presence of BTSA. This would allow any differences in topography of the surface in the presence or absence of BTSA to be determined giving an indication of BTSA-substrate interaction. If topological features were observed then Energy-dispersive X-ray Spectroscopy (EDX) could be used to provide a chemical analysis of the feature. In this case, EDX mapping of sulfur would provide further evidence of adsorption of BTSA, and potentially this could be confirmed with X-ray Photoelectron Spectroscopy (XPS) or Time-of-Flight Secondary Ion Mass Spectrometry (ToF-SIMS). Furthermore, the methods could also be used to test the hypothesis of a specific passivating interaction between Zn<sup>2+</sup> and BTSA<sup>2-</sup> through determination of any ZnBTSA compounds.

**Chapter 5:** As a progression from Chapter 4, the ability of in-coating BTSA additives to mitigate the cathodic delamination of HDG was investigated. A combination of timelapse imaging and in-situ scanning Kelvin probe (SKP) potentiometry was employed to quantify the cathodic delamination rates of model polyvinyl butyral (PVB) coatings containing varying loadings of either BTSA or BTSA intercalated into hydrotalcite (HT-BTSA). It was found that both BTSA and HT-BTSA dispersed in model PVB coatings were able to reduce the rate of cathodic delamination by up to a factor of 20 compared to the unpigmented control, with progressive increases in loading achieving lower rates. Of the two, HT-BTSA possessed superior performance, probably due to its ion-exchange properties allowing a faster release of BTSA<sup>2-</sup> ions into the underfilm electrolyte. The released ions likely had the effect of stifling cathodic delamination by adsorbing strongly on the intact organic-coated metal to hinder underfilm oxygen reduction and the dissolution of the amphoteric zinc (hydr)oxide layer at the metal-polymer interface.

Future research stemming from this chapter could follow approaches similar to those discussed in Chapter 4, such as employing surface characterisation techniques to study the nature of adsorption by BTSA on HDG. This research would involve conducting Strathmann Cell experiments using various loadings of BTSA and HT-BTSA. After these experiments, the cell would be drained and allowed to dry completely. Subsequently, the PVB coating would be mechanically removed to expose the underfilm HDG surface, which would then be subjected to surface characterisation to understand the adsorption characteristics of BTSA. Possible instrumentation to do that would be SEM/EDX, XPS, and ToF-SIMS. Furthermore, computational studies such as density functional theory (DFT) could be attempted to see what contributions azole moieties have on the adsorption mechanism.

**Chapter 6:** This work explored two accelerated test methods for producing anodic undermining on organically coated Zn55Al with a view to using those methods as future assessment tools for in-coating inhibitors for ZnAl substrates. The methods were employed on unpigmented PBV-coated Zn55Al. The first method was a modified Lockheed FFC Test, which initiated corrosion with the addition of  $4 \text{ mol dm}^{-3} \text{ HCl}_{(\text{aq})}$  into a scribed defect,

and the second method was a newly designed cell which introduced  $1 \text{ mol dm}^{-3} \text{ HCl}_{(\text{aq})}$  directly to the coated substrates cut-edge. Investigations showed that both methods likely produced anodic undermining akin to cut-edge corrosion, i.e. stationary cathodic activity on exposed steel coupled to a moving front of underfilm anodic activity (undermining). The novel cell recorded the most accelerated kinetics, achieving over 5 mm of underfilm corrosion within 20 hours of initiation. Time-lapse and SKP experiments indicated that cathodic hydrogen evolution took place on the exposed steel at the cut-edge, while the anodic activity was Al and Zn dissolution of underfilm Zn55Al coating. This dissolution destroyed the interface between the Zn55Al surface and the PVB coating, leading to delamination. The kinetics of the process were parabolic, suggesting a rate probably limited by  $\text{Cl}^-$  migration.

Immediate future work should involve validating the novel anodic cell as an appropriate accelerated test method. To show if the test cell can provide an accurate representation of in-coating inhibitor performance, the next step would be to disperse several corrosion inhibitors, ranging in known efficacy against the anodic undermining of Zn55Al, into the model PVB coating and follow the kinetics of each with time-lapse photography. If the relative performance of inhibitors is similar when used as part of the test cell, it can be considered representative. Additionally, the results for each inhibitor could be compared to outdoor exposure or accelerated weathering tests for fully formulated systems containing each inhibitor.

If the test cell proves reliable, it could be used to compare the performance of in-coating BTSA or HT-BTSA to chromate-containing pigments. Additionally, the preliminary tests discussed in this chapter could potentially be attempted on other ZnAl-coated steel substrates, such as Galfan.